Progress in Particle and Nuclear Physics 149 (2026) 104242

Contents lists available at ScienceDirect

Progress in Particle and Nuclear Physics

journal homepage: www.elsevier.com/locate/ppnp

Review

Ab initio description of hypernuclei

Johann Haidenbauer [a], Ulf-G. Meißner [b,a,c,d,*], Andreas Nogga [a,c]

[a] *Institute for Advanced Simulation (IAS-4), Forschungszentrum Jülich, 52428 Jülich, Germany*
[b] *Helmholtz-Institut für Strahlen-und Kernphysik and Bethe Center for Theoretical Physics, Universität Bonn, 53115 Bonn, Germany*
[c] *Centre for Advanced Simulation and Analytics (CASA), Forschungszentrum Jülich, 52428 Jülich, Germany*
[d] *Peng Huanwu Collaborative Center for Research and Education, International Institute for Interdisciplinary and Frontiers, Beihang University, Beijing 100191, China*

ARTICLE INFO

Keywords:
Hypernuclei
Baryon interactions
Chiral effective field theory
ab initio methods

ABSTRACT

Hypernuclei are bound states of neutrons, protons and one or two hyperons, thus extending the nuclear landscape to a third dimension. They also encode information about the baryon–baryon and three-baryon interactions. Here, we review recent work on chiral effective field theory for two- and three-baryon interactions and their application in nuclei based on *ab initio* methods. These include the Faddeev–Yakubovsky equations, the no-core–shell-model (NCSM) and nuclear lattice effective field theory (NLEFT). Besides of providing an overview of the formalisms explicit results for the separation energies of light Λ hypernuclei are provided. Two-body and three-body forces are included consistently, in line with the underlying power counting. Calculations of Λ hypernuclei within the NCSM, performed up to A=7 so far, suggest that agreement with the experimental binding energies can be achieved once appropriate three-body forces are taken into account. Similar conclusions are drawn from the study based on NLEFT, where even hypernuclei up to A=16 can be computed. Additionally, applications of *ab initio* approaches in calculations of $\Lambda\Lambda$ and Ξ hypernuclei are discussed and possible candidates for the lightest systems that could be bound are identified, namely ${}^{5}_{\Lambda\Lambda}$He and ${}^{4}_{\Xi}$H.

Contents

* Corresponding author at: Helmholtz-Institut für Strahlen-und Kernphysik and Bethe Center for Theoretical Physics, Universität Bonn, 53115 Bonn, Germany.
E-mail addresses: j.haidenbauer@fz-juelich.de (J. Haidenbauer), meissner@hiskp.uni-bonn.de (U.-G. Meißner), a.nogga@fz-juelich.de (A. Nogga).

https://doi.org/10.1016/j.ppnp.2026.104242

Available online 19 March 2026

1. Introduction

Conventional atomic nuclei that make up the visible matter in the Universe are made of the light quarks u and d, generating the two-dimensional nuclear landscape that is investigated at radioactive beam and other accelerator facilities worldwide. With the strange quark, that is considerably heavier than the light quarks, a new dimension in the nuclear chart opens. While conventional nuclei have strangeness $S = 0$, adding one, two, ... hyperons (Λ, Σ, Ξ baryons) to a nucleus generates hypernuclei with strangeness $S = -1, -2, ...$ To understand the formation and the properties of these "strange nuclei" is the main goal of strangeness nuclear physics, for an early review see e.g. [1]. A sketch of the hypernuclear landscape for nuclei with atomic number $A \leq 16$ is given in Fig. 1.1.

Hypernuclei constitute an important source of information on the hyperon–nucleon (YN) interaction. Indeed, from the first discovery of a Λ hypernucleus in 1952 [2] up to 1964 the binding (or separation) energies of the observed hypernuclei [3] were practically the only experimental information that could be used to estimate the strength of the YN interaction and to establish appropriate potential models. General conclusions like that the ΛN interaction in the spin-singlet state ($^1S_0$) has to be more attractive than in the triplet state ($^3S_1$) were already drawn in those days, based on the observations that the hypertriton has angular momentum $J = 1/2$ and that the ground state of ${}^4_\Lambda$H has $J = 0$ rather than $J = 1$ [4].

From 1964 onward, with the arrival of a more extended set of Λp cross sections for low momenta [5,6], potentials could be constructed by fitting them directly to scattering data. Subsequently also low-momentum data for $\Sigma^+ p$ and $\Sigma^- p$ became available [7,8] and paved the way for a more refined theoretical treatment of the YN interaction. In particular, exploiting the approximate SU(3) flavor symmetry [9] of the quark model (and of QCD) allowed to interconnect the interaction between octet baryons (N, Λ, Σ, Ξ) and by building on the meson-exchange picture a realistic and physically sound description of the YN interaction could be achieved. The driving force of that development was certainly the Nijmegen group which published various potentials over the years [10–15], later in competition with the Jülich–Bonn group [16–18] and some others [19–22].

Nonetheless, the insight into the properties of the ΛN interaction that one can gain from the presently available scattering experiments [23–28] is still somewhat limited. In particular, essential features like the already mentioned spin dependence cannot be deduced from those data. Therefore, hypernuclei continue to play an essential role in testing and improving our understanding of the YN interaction. Of course, for that aim one needs reliable and efficient tools for evaluating the properties of hypernuclei such as separation energies directly for the underlying YN interaction. Indeed, it took until 1993 for the first microscopic calculation of hypernuclei which utilized realistic meson-exchange YN potentials in their full complexity, i.e. with the tensor coupling between the $^3S_1$ and $^3D_1$ partial waves and with the coupling between the ΛN and ΣN systems. First results for the hypertriton based on the Faddeev approach [29,30] were followed by calculations of ${}^4_\Lambda$H and ${}^4_\Lambda$He by applying the Faddeev–Yakubovsky formalism [31] and variational methods [32,33]. In fact within a cluster model approach the calculations could be even pushed up to A=10–13

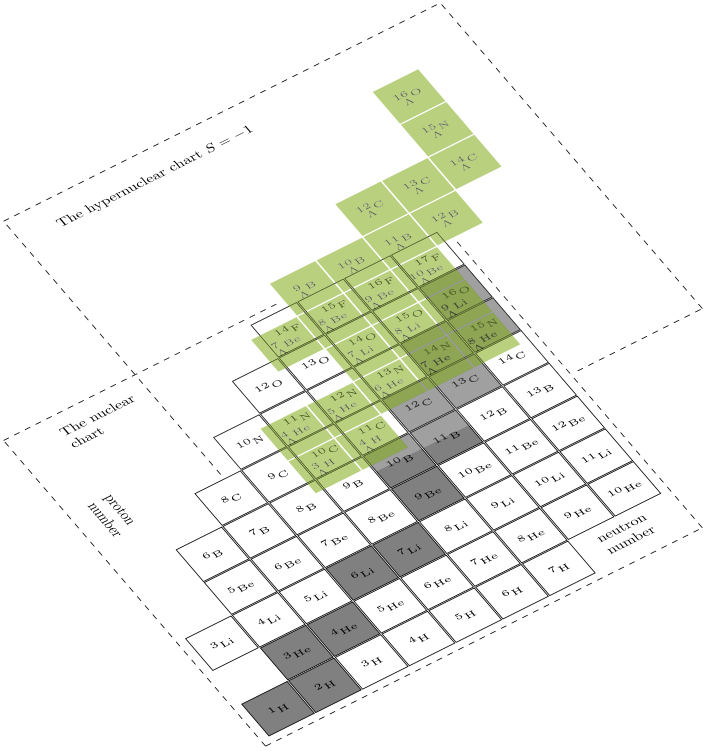

Fig. 1.1. Sketch of the hypernuclear landscape for hypernuclei with strangeness $S = -1$ up to the oxygen region.
Source: Figure courtesy of Fabian Hildenbrand.

Λ hypernuclei [34,35]. However, this was only possible at the expense of having to use simplified phenomenological effective potentials as input.

Fortunately, in the past decade the theoretical and computational tools have been significantly improved. Specifically, new *ab initio* methods like the no-core shell model (NCSM) have been developed [36–38] that allow one to compute binding energies for hypernuclei well beyond the *s*-shell, retaining the full complexity of the YN interaction. So far, studies of hypernuclei up to ${}^{13}_{\Lambda}$C have been reported [36]. Moreover, YN interactions based on modern approaches like chiral effective field theory (EFT) have been employed. Originally suggested for the nucleon–nucleon (NN) interaction, chiral EFT can be easily extended to baryons with strangeness, again by exploiting the approximate SU(3) flavor symmetry of QCD [39–42]. One essential merit of this approach is that two-body forces and three-body forces (3BFs) can be treated/derived consistently [43]. Hypernuclei have been also studied in the framework of nuclear lattice effective field theory (NLEFT) [44]. This framework is a powerful quantum many-body method that combines aspects of effective field theories with lattice (stochastic) methods. Based on it, results for hypernuclei up to ${}^{16}_{\Lambda}$O have been obtained. Other approaches like the auxiliary field diffusion Monte Carlo algorithm allowed to extend the investigations to much heavier hypernuclei [45,46], though only for simplified representations of the YN interaction. Recently, the properties of light hypernuclei have been studied within a variational Monte Carlo method based on neural network quantum states within a pionless EFT framework, showing good agreement with binding energies up to ${}^{16}_{\Lambda}$O [47].

Recent calculations of light hypernuclei within *ab initio* approaches and with realistic ΛN-ΣN potentials as input show that the binding energies and mass spectra can be qualitatively well reproduced [41,48]. But they also revealed noticeable deviations from the experimental values. Whether those point already to shortcomings in the employed YN interactions or rather are a sign for the need to include 3BFs remains unclear at present. But at least a partial answer has been given by investigations that employ NN and YN interactions derived within chiral EFT. In this case, the inherent power counting not only determines the order at which 3BFs start to contribute and, thereby, enables conclusions on their relative importance, but it allows also an explicit estimation for their magnitude [48]. Calculations of Λ hypernuclei up to A=7, guided by such principles, suggest that 3BFs alone could be sufficient to achieve agreement with the experimental binding energies [49]. Similar conclusions can be also drawn from the work based on NLEFT, where even hypernuclei up to A=16 were considered [44].

Another aspect where measured binding energies of hypernuclei play an essential role is charge-symmetry breaking (CSB). Up to now there are no data on Λn scattering, which one could compare to the ones for Λp, or for $\Sigma^- n$, which one could compare to the ones for $\Sigma^+ p$, for establishing a possible CSB in the ΛN and/or ΣN systems. However, already for a long time, there is clear experimental evidence for CSB from the separation energies of the hypernuclei ${}^{4}_{\Lambda}$H and ${}^{4}_{\Lambda}$He, in the ground state (0^+) as well as in the excited state (1^+) [50]. The differences in the separation energies are in the order of 100 to 200 keV and, thus, much larger

than the ones one knows from ordinary nuclei, say ^{3}H and ^{3}He, when disregarding the trivial effect due to the Coulomb interaction. There is also a noticeable CSB in heavier systems like in the isospin triplet ${}^{7}_{\Lambda}$He, ${}^{7}_{\Lambda}$Li*, ${}^{7}_{\Lambda}$Be, and the $I = 1/2$ doublet ${}^{8}_{\Lambda}$Li, ${}^{8}_{\Lambda}$Be [51]. CSB effects in light Λ hypernuclei have been studied in recent times based on a heuristic treatment of CSB [52,53] but also by employing a CSB interaction derived consistently within chiral EFT [54]. In the latter case, the CSB in the energy levels can be well described and leads to the conclusion that the Λn interaction in the $^1S_0$ state must be noticeably more attractive than the one in Λp, whereas the difference in the $^3S_1$ is much smaller and also of opposite sign. An exploration has been made to examine whether the CSB effects established from the ${}^{4}_{\Lambda}$H/${}^{4}_{\Lambda}$He systems are consistent with those in the mentioned $A = 7, 8$ hypernuclei [55]. But firm conclusions are difficult to draw because the present experimental uncertainty is large for the latter. New measurements with improved precision would be highly desirable for those systems but also for other light hypernuclei for which it is still feasible to perform calculations within *ab initio* approaches.

Finally, it should be mentioned that *ab initio* approaches have been also successfully applied in calculations of $\Lambda\Lambda$ and Ξ hypernuclei [56–59]. Candidates for the possible lightest bound systems have been identified, for example ${}^{5}_{\Lambda\Lambda}$He [57,58] or ${}^{4}_{\Xi}$H [59]. They are waiting for an experimental confirmation – or disproof – though it is clear that corresponding experiments are rather challenging.

We should also mention the femtoscopic approach that recently has been used to get information on various YN and YY (as well as other hadronic) interactions and also promises to pin down three-body forces with unprecedented precision, see e.g. [60–66]. While this approach is certainly capable of getting some information on interactions that are otherwise difficult to access, in view of the recent criticism related mostly to the model-dependence of the hadronic source [67] and the frequent use of simplified interaction models [68], we do not consider this approach here in detail but just mention it whenever appropriate.

In this review we summarize the present status of *ab initio* calculations of hypernuclei. Several previous review articles exist focusing more on experimental data [69–72] or describing the historical development of hypernuclear physics [73]. Therefore, in our review we focus specifically on recent developments related to the application of effective field theories and also we include an introduction of the pertinent computational approaches. In Section 2, we introduce the chiral effective field theory (EFT) approach to baryon–baryon interactions. The three-baryon forces from chiral EFT are discussed in Section 3. Then, in Section 4 we discuss the Faddeev–Yakubovsky approach that allows for *ab initio* studies for hypernuclei with atomic number $A = 3, 4$. To tackle heavier hypernuclei, we first consider the No-Core Shell Model (NCSM) approach in Section 5, in particular the Jacobi NCSM, and we present results for p-shell hypernuclei. A different *ab initio* approach is presented in Section 6, namely Nuclear Lattice EFT (NLEFT). We outline how it can be applied to hypernuclei and present result for hypernuclei up-to-and including $A = 16$. We end with a summary and outlook in Section 7.

2. Baryon–baryon interaction in chiral effective field theory

The baryon–baryon (BB) interactions considered in the present review are all constructed within SU(3) chiral effective field theory (EFT), an approach which exploits the symmetries of the underlying fundamental theory of strong interactions, quantum chromodynamics (QCD), and the breaking of those symmetries. In that approach a potential is established via an expansion in terms of small momenta, subject to an appropriate power counting, so that the results can be improved systematically by going to higher orders, while at the same time theoretical uncertainties can be estimated [74,75]. Furthermore, two- and three-baryon forces can be constructed in a consistent way. The resulting interaction potentials can be readily employed in standard two- and few-body calculations. They consist of contributions from an increasing number of pseudoscalar-meson exchanges, determined by the underlying chiral symmetry, and of contact terms which encode the unresolved short-distance dynamics and whose strengths are parameterized by a priori unknown low-energy constants (LECs). The latter need to be determined by a fit to experimental data.

In the following we describe the construction of the potential within the Weinberg power counting. So far the Jülich–Bonn (and partly Jülich–Bonn–TUM) group has established YN potentials at leading order (LO) [39], up to next-to-leading order (NLO) [40,41], and, recently, even up to next-to-next-to-leading order (N2LO) [42] in the chiral expansion. We note that alternative approaches have been pursued in [76], where the so-called Kaplan–Savage–Weise (KSW) resummation scheme [77] has been applied, and in [78–80] where calculations are performed in covariant chiral EFT, but so far only at LO. The ΛN and $\Lambda\Lambda$ interactions have been also treated within pion-less EFT [57,81–83].

We would like to mention that there are also ongoing efforts to compute the YN interaction within lattice QCD, spearheaded by the NPLQCD [84] and HAL QCD [85] collaborations. In fact, over the past few years, it has become possible to perform such lattice simulations for quark (pion) masses close to the physical point and the HAL QCD collaboration has published corresponding results for ΛN [86] and ΣN [87], and also for $S = -2$ systems [88].

2.1. Formalism

The application of chiral effective field theory to the NN system is thoroughly documented in various reviews, see e.g. [74,75]. Details on the derivation of the chiral baryon–baryon potentials for the strangeness sector at LO using the Weinberg power counting can be found in Refs. [39,89]. The LO potential consists of four-baryon contact terms without derivatives and of one-pseudoscalar-meson exchanges, see Fig. 2.1 (top).

The LO SU(3) invariant contact terms for the octet baryon–baryon interactions that are Hermitian and invariant under Lorentz transformations follow from the Lagrangians

$$\mathcal{L}^1 = C_i^1 \left\langle \bar{B}_a \bar{B}_b \left(\Gamma_i B\right)_b \left(\Gamma_i B\right)_a \right\rangle ,$$

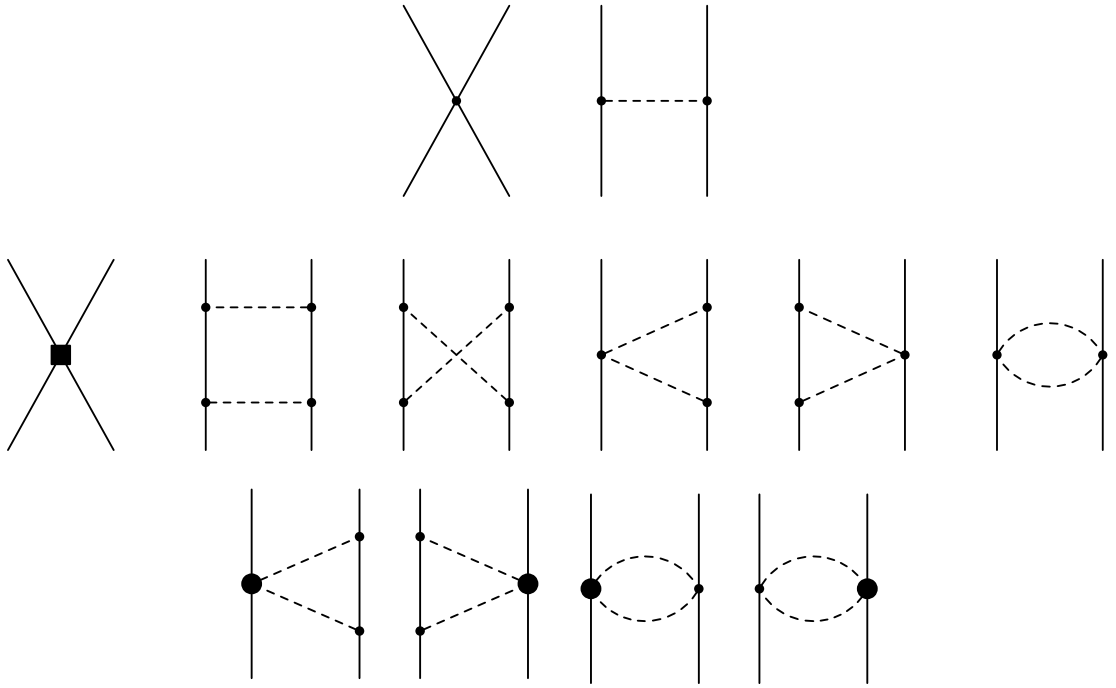

Fig. 2.1. Diagrams contributing at LO (top), NLO (center), and N2LO (bottom) in chiral EFT. Solid and dashed lines denote octet baryons and pseudoscalar mesons, respectively. For the meson–baryon interaction, the small (fat) circle denotes a one-(two-)derivative vertex, whereas for the four-baryon contact terms the small circle (big square) represents a zero-(two-)derivative interaction.

$$\begin{aligned}\mathcal{L}^2 &= C_i^2 \left\langle \bar{B}_a \left(\Gamma_i B\right)_a \bar{B}_b \left(\Gamma_i B\right)_b \right\rangle \ , \\ \mathcal{L}^3 &= C_i^3 \left\langle \bar{B}_a \left(\Gamma_i B\right)_a \right\rangle \left\langle \bar{B}_b \left(\Gamma_i B\right)_b \right\rangle \ . \end{aligned} \tag{2.1}$$

Here a and b denote the Dirac indices of the particles, B is the irreducible octet representation of $\mathrm{SU(3)_f}$, in form of a traceless 3×3 matrix,

$$B = \begin{pmatrix} \frac{\Sigma^0}{\sqrt{2}} + \frac{\Lambda}{\sqrt{6}} & \Sigma^+ & p \\ \Sigma^- & -\frac{\Sigma^0}{\sqrt{2}} + \frac{\Lambda}{\sqrt{6}} & n \\ -\Xi^- & \Xi^0 & -\frac{2\Lambda}{\sqrt{6}} \end{pmatrix} . \tag{2.2}$$

and the Γ_i are the usual elements of the Clifford algebra [39]. Further, $\langle ... \rangle$ denotes the trace in flavor space.

As described in Ref. [39], to LO the Lagrangians in Eq. (2.1) give rise to only six independent low-energy coefficients (LECs) – C_S^1, C_T^1, C_S^2, C_T^2, C_S^3 and C_T^3 – due to SU(3) constraints. The subscripts S and T refer to the central and spin–spin parts of the potential, respectively. The spin- and momentum structure of the potentials to LO is given by

$$V^{(0),CT} = C_S + C_T(\boldsymbol{\sigma}_1 \cdot \boldsymbol{\sigma}_2). \tag{2.3}$$

For concrete applications it is convenient to re-express the LECs C_S^i and C_T^i in terms of LECs that correspond to the SU(3) irreducible representations, C^{27}, C^{10}, C^{10^*}, C^{8_s}, C^{8_a}, C^1, according to the decomposition of the tensor product for two octet baryons, $\mathbf{8} \otimes \mathbf{8} = \mathbf{27} \oplus \mathbf{10} \oplus \overline{\mathbf{10}} \oplus \mathbf{8}_s \oplus \mathbf{8}_a \oplus \mathbf{1}$, see e.g. [9,90]. Then the contact interaction can be written in the practical form

$$V^{(0),CT} = \frac{1}{4}(1 - \boldsymbol{\sigma}_1 \cdot \boldsymbol{\sigma}_2)\, C_{1S0} + \frac{1}{4}(3 + \boldsymbol{\sigma}_1 \cdot \boldsymbol{\sigma}_2)\, C_{3S1} \ , \tag{2.4}$$

where the LECs for the ${}^1S_0$ and ${}^3S_1$ partial waves in the various baryon–baryon channels are linear combinations of C^{27}, C^{8_s}, C^1 and C^{10}, C^{10^*}, C^{8_a}, respectively. The explicit relations which express the constraints imposed by the assumed SU(3) flavor symmetry are summarized in Table 2.1.

Table 2.1
SU(3) relations for the various contact potentials in the isospin basis for strangeness $S = 0$, -1, and -2. C_α^{27} etc. refers to the corresponding irreducible SU(3) representation for a particular partial wave α, see text and Ref. [40]. The isospin is denoted by I. The actual potential still needs to be multiplied by pertinent powers of the momenta p and p'.

S	Channel	I	$V(\alpha)$			
			$\alpha = {}^1S_0, {}^3P_0, {}^3P_1, {}^3P_2$	$\alpha = {}^3S_1, {}^3S_1\text{-}{}^3D_1, {}^1P_1$	${}^1S_0\ \chi$	${}^3S_1\ \chi$
0	$NN \to NN$	0	–	$C_\alpha^{10^*}$	–	$\frac{1}{2}C_\chi^7$
	$NN \to NN$	1	C_α^{27}	–	$\frac{1}{2}C_\chi^1$	–
-1	$\Lambda N \to \Lambda N$	$\frac{1}{2}$	$\frac{1}{10}\left(9C_\alpha^{27} + C_\alpha^{8_s}\right)$	$\frac{1}{2}\left(C_\alpha^{8_a} + C_\alpha^{10^*}\right)$	C_χ^2	C_χ^8
	$\Lambda N \to \Sigma N$	$\frac{1}{2}$	$\frac{3}{10}\left(-C_\alpha^{27} + C_\alpha^{8_s}\right)$	$\frac{1}{2}\left(-C_\alpha^{8_a} + C_\alpha^{10^*}\right)$	$-C_\chi^3$	$-C_\chi^9$
	$\Sigma N \to \Sigma N$	$\frac{1}{2}$	$\frac{1}{10}\left(C_\alpha^{27} + 9C_\alpha^{8_s}\right)$	$\frac{1}{2}\left(C_\alpha^{8_a} + C_\alpha^{10^*}\right)$	C_χ^4	C_χ^{10}
	$\Sigma N \to \Sigma N$	$\frac{3}{2}$	C_α^{27}	C_α^{10}	$\frac{1}{4}C_\chi^1$	$-\frac{1}{4}C_\chi^7$
-2	$\Lambda\Lambda \to \Lambda\Lambda$	0	$\frac{1}{40}\left(27C_\alpha^{27} + 8C_\alpha^{8_s} + 5C_\alpha^1\right)$	–	$\frac{1}{2}C_\chi^5$	–
	$\Lambda\Lambda \to \Xi N$	0	$\frac{-1}{40}\left(18C_\alpha^{27} - 8C_\alpha^{8_s} - 10C_\alpha^1\right)$	–	$\frac{3}{4}C_\chi^1 - 3C_\chi^2 - C_\chi^3 + \frac{3}{4}C_\chi^5$	–
	$\Lambda\Lambda \to \Sigma\Sigma$	0	$\frac{\sqrt{3}}{40}\left(-3C_\alpha^{27} + 8C_\alpha^{8_s} - 5C_\alpha^1\right)$	–	–	–
	$\Xi N \to \Xi N$	0	$\frac{1}{40}\left(12C_\alpha^{27} + 8C_\alpha^{8_s} + 20C_\alpha^1\right)$	$C_\alpha^{8_a}$	$\frac{2}{3}C_\chi^1 - 3C_\chi^2 + \frac{1}{3}C_\chi^4 + \frac{9}{8}C_\chi^5$	C_χ^{11}
	$\Xi N \to \Sigma\Sigma$	0	$\frac{\sqrt{3}}{40}\left(2C_\alpha^{27} + 8C_\alpha^{8_s} - 10C_\alpha^1\right)$	–	$-\frac{1}{4\sqrt{3}}C_\chi^1 + \sqrt{3}C_\chi^3 + \frac{1}{\sqrt{3}}C_\chi^4$	–
	$\Sigma\Sigma \to \Sigma\Sigma$	0	$\frac{1}{40}\left(C_\alpha^{27} + 24C_\alpha^{8_s} + 15C_\alpha^1\right)$	–	–	–
	$\Xi N \to \Xi N$	1	$\frac{1}{5}\left(2C_\alpha^{27} + 3C_\alpha^{8_s}\right)$	$\frac{1}{3}\left(C_\alpha^{10} + C_\alpha^{10^*} + C_\alpha^{8_a}\right)$	C_χ^6	C_χ^{12}
	$\Xi N \to \Sigma\Lambda$	1	$\frac{\sqrt{6}}{5}\left(C_\alpha^{27} - C_\alpha^{8_s}\right)$	$\frac{\sqrt{6}}{6}\left(C_\alpha^{10} - C_\alpha^{10^*}\right)$	$-\frac{\sqrt{2}}{3\sqrt{3}}C_\chi^1 + \sqrt{\frac{3}{2}}C_\chi^2 - \frac{1}{3\sqrt{6}}C_\chi^4 - \sqrt{\frac{2}{3}}C_\chi^6$	$-\frac{1}{\sqrt{6}}C_\chi^{10} + \sqrt{\frac{2}{3}}C_\chi^{12} + \frac{1}{2\sqrt{6}}C_\chi^7 - \sqrt{\frac{3}{2}}C_\chi^8 + \sqrt{\frac{2}{3}}C_\chi^9$
	$\Xi N \to \Sigma\Sigma$	1	–	$\frac{\sqrt{2}}{6}\left(C_\alpha^{10} + C_\alpha^{10^*} - 2C_\alpha^{8_a}\right)$	–	$\sqrt{2}C_\chi^{10} - \frac{1}{2\sqrt{2}}C_\chi^7 - \sqrt{2}C_\chi^9$
	$\Sigma\Lambda \to \Sigma\Lambda$	1	$\frac{1}{5}\left(3C_\alpha^{27} + 2C_\alpha^{8_s}\right)$	$\frac{1}{2}\left(C_\alpha^{10} + C_\alpha^{10^*}\right)$	$-\frac{1}{9}C_\chi^1 + \frac{4}{3}C_\chi^3 + \frac{4}{9}C_\chi^4 + \frac{2}{3}C_\chi^6$	$\frac{4}{3}C_\chi^{10} + \frac{2}{3}C_\chi^{12} - \frac{1}{3}C_\chi^7 - \frac{4}{3}C_\chi^9$
	$\Sigma\Lambda \to \Sigma\Sigma$	1	–	$\frac{\sqrt{3}}{6}\left(C_\alpha^{10} - C_\alpha^{10^*}\right)$	–	–
	$\Sigma\Sigma \to \Sigma\Sigma$	1	–	$\frac{1}{6}\left(C_\alpha^{10} + C_\alpha^{10^*} + 4C_\alpha^{8_a}\right)$	–	–
	$\Sigma\Sigma \to \Sigma\Sigma$	2	C_α^{27}	–	–	–

The lowest order SU(3) invariant pseudoscalar-meson–baryon interaction Lagrangian with the appropriate symmetries was discussed in [39,40]. Introducing the matrix ϕ representing the pseudoscalar mesons,

$$\phi = \begin{pmatrix} \frac{\pi^0}{\sqrt{2}} + \frac{\eta}{\sqrt{6}} & \pi^+ & K^+ \\ \pi^- & -\frac{\pi^0}{\sqrt{2}} + \frac{\eta}{\sqrt{6}} & K^0 \\ K^- & \bar{K}^0 & -\frac{2\eta}{\sqrt{6}} \end{pmatrix}, \tag{2.5}$$

it can be written in the form

$$\mathcal{L}_{BB\phi} = -\frac{\sqrt{2}}{2F_0}\left\langle D\bar{B}\gamma^\mu\gamma_5\left\{\partial_\mu\phi, B\right\} + F\bar{B}\gamma^\mu\gamma_5\left[\partial_\mu\phi, B\right]\right\rangle, \tag{2.6}$$

which leads to a vertex between two baryons and one meson. Here, F_0 is the pseudoscalar-meson decay constant in the chiral limit. F and D are coupling constants which satisfy the relation $F + D = g_A \simeq 1.26$, where g_A is the axial–vector strength measured in neutron β–decay.

In the isospin basis the Lagrangian reads

$$\begin{aligned}
\mathcal{L} \;=\; & -f_{NN\pi}\bar{N}\gamma^\mu\gamma_5\boldsymbol{\tau}N\cdot\partial_\mu\boldsymbol{\pi} + if_{\Sigma\Sigma\pi}\bar{\boldsymbol{\Sigma}}\gamma^\mu\gamma_5\times\boldsymbol{\Sigma}\cdot\partial_\mu\boldsymbol{\pi} \\
& - f_{\Lambda\Sigma\pi}\left[\bar{\Lambda}\gamma^\mu\gamma_5\boldsymbol{\Sigma} + \bar{\boldsymbol{\Sigma}}\gamma^\mu\gamma_5\Lambda\right]\cdot\partial_\mu\boldsymbol{\pi} - f_{\Xi\Xi\pi}\bar{\Xi}\gamma^\mu\gamma_5\boldsymbol{\tau}\Xi\cdot\partial_\mu\boldsymbol{\pi} \\
& - f_{\Lambda NK}\left[\bar{N}\gamma^\mu\gamma_5\Lambda\partial_\mu K + \bar{\Lambda}\gamma^\mu\gamma_5 N\partial_\mu K^\dagger\right] \\
& - f_{\Xi\Lambda K}\left[\bar{\Xi}\gamma^\mu\gamma_5\Lambda\partial_\mu K_c + \bar{\Lambda}\gamma^\mu\gamma_5\Xi\partial_\mu K_c^\dagger\right] \\
& - f_{\Sigma NK}\left[\bar{\boldsymbol{\Sigma}}\cdot\gamma^\mu\gamma_5\partial_\mu K^\dagger\boldsymbol{\tau}N + \bar{N}\gamma^\mu\gamma_5\boldsymbol{\tau}\partial_\mu K\cdot\boldsymbol{\Sigma}\right] \\
& - f_{\Xi\Sigma K}\left[\bar{\boldsymbol{\Sigma}}\cdot\gamma^\mu\gamma_5\partial_\mu K_c^\dagger\boldsymbol{\tau}\Xi + \bar{\Xi}\gamma^\mu\gamma_5\boldsymbol{\tau}\partial_\mu K_c\cdot\boldsymbol{\Sigma}\right] \\
& - f_{NN\eta_8}\bar{N}\gamma^\mu\gamma_5 N\partial_\mu\eta \\
& - f_{\Lambda\Lambda\eta_8}\bar{\Lambda}\gamma^\mu\gamma_5\Lambda\partial_\mu\eta - f_{\Sigma\Sigma\eta_8}\bar{\boldsymbol{\Sigma}}\cdot\gamma^\mu\gamma_5\boldsymbol{\Sigma}\partial_\mu\eta \\
& - f_{\Xi\Xi\eta_8}\bar{\Xi}\gamma^\mu\gamma_5\Xi\partial_\mu\eta\ .
\end{aligned} \tag{2.7}$$

The vertices $\Lambda\Lambda\pi$ and $\Lambda\Sigma\eta_8$ are not allowed by isospin conservation.

The interaction Lagrangian in Eq. (2.7) is invariant under SU(3) transformations if the various coupling constants fulfill specific relations which can be expressed in terms of the coupling constant f and the $F/(F+D)$-ratio α as [9],

$$\begin{array}{llll} f_{NN\pi} = & f, & f_{NN\eta_8} = & \frac{1}{\sqrt{3}}(4\alpha-1)f, \quad f_{\Lambda NK} = -\frac{1}{\sqrt{3}}(1+2\alpha)f, \\ f_{\Xi\Xi\pi} = & -(1-2\alpha)f, & f_{\Xi\Xi\eta_8} = & -\frac{1}{\sqrt{3}}(1+2\alpha)f, \quad f_{\Xi\Lambda K} = \frac{1}{\sqrt{3}}(4\alpha-1)f, \\ f_{\Sigma\Sigma\pi} = & 2\alpha f, & f_{\Sigma\Sigma\eta_8} = & \frac{2}{\sqrt{3}}(1-\alpha)f, \quad f_{\Xi\Sigma K} = -f, \\ f_{\Lambda\Sigma\pi} = & \frac{2}{\sqrt{3}}(1-\alpha)f, & f_{\Lambda\Lambda\eta_8} = & -\frac{2}{\sqrt{3}}(1-\alpha)f \quad f_{\Sigma NK} = (1-2\alpha)f\,, \end{array} \tag{2.8}$$

where $f \equiv g_A/(2F_0)$. In the actual calculations F_0 was fixed to the weak pion decay constant, $F_\pi = 92.4$ MeV (LO and NLO). In the N2LO potential the explicit SU(3) breaking of the decay constant was taken into account by using the empirical values for F_π, F_K, and F_η [42]. For the $F/(F+D)$-ratio the SU(6) value ($\alpha = 0.4$) was adopted in the LO, NLO, and N2LO studies.

The spin-space part of the LO one-pseudoscalar-meson-exchange potential is similar to the static one-pion-exchange potential in [91] (recoil and relativistic corrections give higher order contributions),

$$V^{(0),OBE}_{B_1B_2\to B_3B_4} = -f_{B_1B_3\phi} f_{B_2B_4\phi} \frac{(\boldsymbol{\sigma}_1\cdot\mathbf{q})\,(\boldsymbol{\sigma}_2\cdot\mathbf{q})}{\mathbf{q}^2+M_\phi^2}\,, \tag{2.9}$$

where M_ϕ is the mass of the exchanged pseudoscalar meson. The transferred and average momentum, $\mathbf{q}$ and $\mathbf{k}$, are defined in terms of the final and initial center-of-mass (c.m.) momenta of the baryons, $\mathbf{p}'$ and $\mathbf{p}$, as $\mathbf{q} = \mathbf{p}' - \mathbf{p}$ and $\mathbf{k} = (\mathbf{p}' + \mathbf{p})/2$. Note that we use the physical masses of the exchanged pseudoscalar mesons. Thus, the explicit SU(3) breaking reflected in the mass splitting between the pseudoscalar mesons is taken into account. The η meson was identified with the octet η (η_8) and its physical mass was used.

In next-to-leading order (NLO) contributions from (non-iterative) two-pseudoscalar-meson exchange diagrams arise [40,92]. Those involve the leading meson–baryon Lagrangian

$$\mathcal{L}_{\phi B} = \frac{1}{4F_0^2}\left\langle i\bar{B}\gamma^\mu\left[\left[\phi,\partial_\mu\phi\right],B\right]\right\rangle\,, \tag{2.10}$$

which describes a (Weinberg–Tomozawa) vertex between two baryons and two mesons. Explicit expressions for the resulting NLO potential can be found in the appendix of Ref. [40]. A graphical representation of the contributions is provided in the middle line of Fig. 2.1 and consists of (irreducible) planar box, crossed box, triangle, and football diagrams. In addition there are four-baryon contact terms with two derivatives, which can be constructed analogous to Eq. (2.1). The spin- and momentum structure of the latter is given by

$$\begin{aligned} V^{(2),CT} &= C_1\mathbf{q}^2 + C_2\mathbf{k}^2 + (C_3\mathbf{q}^2 + C_4\mathbf{k}^2)(\boldsymbol{\sigma}_1\cdot\boldsymbol{\sigma}_2) \\ &+ iC_5(\boldsymbol{\sigma}_1+\boldsymbol{\sigma}_2)\cdot(\mathbf{q}\times\mathbf{k}) + C_6(\mathbf{q}\cdot\boldsymbol{\sigma}_1)(\mathbf{q}\cdot\boldsymbol{\sigma}_2) \\ &+ C_7(\mathbf{k}\cdot\boldsymbol{\sigma}_1)(\mathbf{k}\cdot\boldsymbol{\sigma}_2) + iC_8(\boldsymbol{\sigma}_1-\boldsymbol{\sigma}_2)\cdot(\mathbf{q}\times\mathbf{k}). \end{aligned} \tag{2.11}$$

The C_i's are additional LECs. Performing a partial wave projection and imposing again SU(3) symmetry, one finds that in case of the YN interaction there are ten new coefficients entering the S waves and S-D transitions, respectively, and eight coefficients in the P waves. The potential up to NLO can then be written in the form

$$\begin{aligned} V^{CT}_{B_1B_2\to B_3B_4} &= \tilde{C}_\alpha + C_\alpha\,(p^2+p'^2) \quad (\alpha = {}^1S_0,\,{}^3S_1), \\ &= C_\beta\,p^2\,,\; C_\beta\,p'^2 \qquad (\beta = {}^3S_1 - {}^3D_1,\,{}^3D_1 - {}^3S_1), \\ &= C_\gamma\,p\,p' \qquad (\gamma = {}^3P_0,\,{}^1P_1,\,{}^3P_1,\,{}^3P_2), \end{aligned} \tag{2.12}$$

with $p = |\mathbf{p}|$ and $p' = |\mathbf{p}'|$. $\tilde{C}_\alpha$ and C_α, etc. are appropriate combinations of the C_i's appearing in Eqs. (2.4) and (2.11), see Ref. [40]. As before, for each partial wave the contact interactions in the various BB channels are interrelated with each other by the imposed SU(3) symmetry, see Table 2.1. Note that, at NLO, additional contact terms arise from an insertion of the external field χ [93],

$$\chi = 2B_0\begin{pmatrix} m_u & 0 & 0 \\ 0 & m_d & 0 \\ 0 & 0 & m_s \end{pmatrix} \approx \begin{pmatrix} M_\pi^2 & 0 & 0 \\ 0 & M_\pi^2 & 0 \\ 0 & 0 & 2M_K^2 - M_\pi^2 \end{pmatrix}, \tag{2.13}$$

into the Lagrangians in Eq. (2.1). The parameter B_0 is related to the vacuum quark condensate. Those introduce an explicit SU(3) symmetry breaking [40,93] and lead to a modification of the S-wave contact potentials given in Eq. (2.12):

$$V^{CT}_{B_1B_2\to B_3B_4} = \tilde{C}_\alpha + C_\alpha\,(p^2+p'^2) + C_{\alpha,\chi}\,(M_K^2 - M_\pi^2)\,. \tag{2.14}$$

The pertinent LECs $C_{\alpha,\chi}$ are likewise constrained by SU(3) symmetry and the relations are given in the last two columns of Table 2.1.

Finally, at next-to-next-to-leading order (N2LO), contributions involving the subleading meson–baryon Lagrangian [42] arise and are depicted at the bottom of Fig. 2.1. Explicit expressions for those contributions can be found in Ref. [42].

The presently available YN scattering data do not allow any conclusions on possible effects from charge symmetry breaking (CSB), say regarding Λp versus Λn or $\Sigma^+ p$ versus $\Sigma^- n$. However, the experimentally established difference of the Λ separation energies in the mirror nuclei ${}^4_\Lambda$He and ${}^4_\Lambda$H provides clear evidence for a CSB between the Λp and Λn interactions. CSB effects can

be included in the YN interaction [54] following the arguments and the power counting outlined for the NN system in Ref. [92]. According to that work (and notation) at LØ CSB forces are due to the Coulomb interaction and due to the mass differences of the exchanged pseudoscalar mesons. However, in case of ΛN, the former is absent while the latter is rather small, since the mass difference between the K^0 and $K^\pm$ mesons is small compared to their averaged mass. More important are CSB contributions to the ΛN potential at NLØ which are given by [54]

$$V^{CSB}_{\Lambda N\to\Lambda N} = \left[-f^{(\Lambda-\Sigma^0)}_{\Lambda\Lambda\pi} f_{NN\pi} \frac{(\boldsymbol{\sigma}_1\cdot\mathbf{q})\,(\boldsymbol{\sigma}_2\cdot\mathbf{q})}{\mathbf{q}^2+M^2_{\pi^0}} - f^{(\eta-\pi^0)}_{\Lambda\Lambda\pi} f_{NN\pi}\,(\boldsymbol{\sigma}_1\cdot\mathbf{q})\,(\boldsymbol{\sigma}_2\cdot\mathbf{q}) \left(\frac{1}{\mathbf{q}^2+M^2_{\pi^0}} - \frac{1}{\mathbf{q}^2+M^2_{\eta}}\right) + \frac{1}{4}(1-\boldsymbol{\sigma}_1\cdot\boldsymbol{\sigma}_2)\,C^{CSB}_{^1S_0} + \frac{1}{4}(3+\boldsymbol{\sigma}_1\cdot\boldsymbol{\sigma}_2)\,C^{CSB}_{^3S_1} \right] \tau_N \ . \tag{2.15}$$

These CSB contributions arise from a non-zero $\Lambda\Lambda\pi$ coupling constant which can be estimated from $\Lambda-\Sigma^0$ ($f^{(\Lambda-\Sigma^0)}_{\Lambda\Lambda\pi}$) and $\eta-\pi^0$ ($f^{(\eta-\pi^0)}_{\Lambda\Lambda\pi}$) mixing [94], respectively, and from two contact terms, $C^{CSB}_{^1S_0}$ and $C^{CSB}_{^3S_1}$, that represent short-ranged CSB forces. Note that $\tau_p=1$ and $\tau_n=-1$.

The reaction amplitudes are obtained from the solution of a coupled-channels Lippmann–Schwinger (LS) equation for the interaction potentials:

$$T^{\nu''\nu',J}_{\rho''\rho'}(p'',p';E) = V^{\nu''\nu',J}_{\rho''\rho'}(p'',p') + \sum_{\rho,\nu}\int_0^\infty \frac{dpp^2}{(2\pi)^3}\, V^{\nu''\nu,J}_{\rho''\rho}(p'',p)\frac{2\mu_\nu}{q^2_\nu-p^2+i\eta} T^{\nu\nu',J}_{\rho\rho'}(p,p';E) \ . \tag{2.16}$$

The label ν indicates the particle channels and the label ρ the partial wave. μ_ν is the pertinent reduced mass. The on-shell momentum in the intermediate state, q_ν, is defined by $E=E_{B_{1,\nu}}+E_{B_{2,\nu}}=\sqrt{m^2_{B_{1,\nu}}+q^2_\nu}+\sqrt{m^2_{B_{2,\nu}}+q^2_\nu}$. Relativistic kinematics is used for relating the laboratory energy $T_{\rm lab}$ of the hyperons to the c.m. momentum. We solve the LS equation in the particle basis, in order to incorporate the correct physical thresholds. Depending on the specific values of strangeness and charge up to six baryon–baryon channels can couple. For the $S=-1$ sector, where a detailed comparison with scattering data is possible, the Coulomb interaction is taken into account appropriately.

When the chiral potentials are inserted into the LS equation a regulator has to be introduced in order to remove high-momentum components of the baryon and pseudoscalar meson fields [92]. In the chiral YN potentials of the Jülich–Bonn group up to 2019 [39–41] a non-local regulator function of the form $\exp\left[-\left(p'^4+p^4\right)/\Lambda^4\right]$ has been applied, analogous to the procedure used for chiral NN potentials [92]. In particular, values for the cut-off mass Λ in a comparable range, i.e. 550, ..., 700 MeV, were considered. Please note that there are two variants of the NLO interaction, which are denoted according to the year of publication, i.e. NLO13 [40] and NLO19 [41], respectively. These yield practically equivalent results for ΛN and ΣN scattering observables, but they differ in "non-observable" properties like the strength of the ΛN→ΣN transition potential [41]. The impact of this difference on predictions for light hypernuclei is instructive and will be discussed below.

In the extension of the YN potentials to N2LO in [42] a novel regularization scheme has been adopted, following the development in the NN sector [95]. Specifically, now a local regulator is applied to the meson-exchange contributions and only the contact terms, being non-local by themselves, are regularized with a non-local function. Following Reinert et al. [95] we call the resulting interactions semilocal momentum-space (SMS) regularized potentials. Here the considered cut-off masses Λ are in the range of 500, ..., 600 MeV, i.e. slightly larger than those used in the NN sector. This choice reflects the requirement that the cutoff mass has to be larger than the mass of the exchanged meson and that in SU(3) chiral EFT not only pions are exchanged but also K- and η mesons. Regarding two-meson exchange, only contributions from $\pi\pi$ have been taken into account in the SMS potentials. For those involving a K and/or η (πK, KK, etc.) the combined masses exceed the cutoff value so that they should be strongly suppressed, see the pertinent discussion in Ref. [42]. Note that, in the SMS potentials, deviations of the meson–baryon coupling constants from the SU(3) values are taken into account. Specifically, the explicit SU(3) symmetry breaking in the empirical values of the decay constants [96],

$$F_\pi = 92.4 \text{ MeV}, \quad F_K=(1.19\pm0.01)F_\pi, \quad F_\eta=(1.30\pm0.05)F_\pi \ . \tag{2.17}$$

is implemented. Furthermore, following the practice in chiral NN potentials [95], we use $g_A=1.29$, which is slightly larger than the experimental value, in order to account for the Goldberger–Treiman discrepancy [97].

2.2. Results

In order to establish the potentials, the involved LECs have to be fixed by a fit to data. For that the Jülich–Bonn group considered the "standard" set of 35 ΛN and ΣN cross sections at low momenta that have also been used in studies based on the conventional meson-exchange framework in the past [10–18]. These data consists of two sets of cross sections for Λp [23,24] (6 data points each), and single sets for Σ^+p [8] (4 data points), Σ^-p [8] (7 data points), and for the transitions $\Sigma^-p\to\Lambda n$ [7] (6 data points) and $\Sigma^-p\to\Sigma^0 n$ [7] (6 data points). In addition, the inelastic capture ratio at rest [98,99] is taken into account. Besides these YN data, the empirical binding energy of the hypertriton ${}^3_\Lambda$H was used as a further constraint. Otherwise it would not be possible to fix the

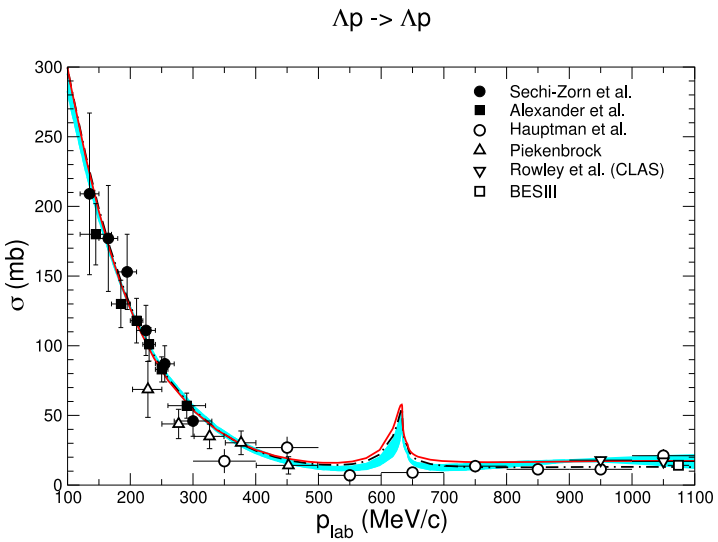

Fig. 2.2. Λp cross section. Results are shown for the chiral YN potentials NLO19 [41] (cyan band) and the SMS potentials NLO (550) (black dash-dotted line) and N2LO (550) (red solid line) [42]. Data shown as open symbols have not been included in the fitting procedure. Data are taken from Refs. [23,24,26–28].

relative strength of the spin-singlet and spin-triplet S-wave contributions to the Λp interaction. See also the discussion in Section 4 below.

In practice, the LECs in the S-waves can be fixed fairly well from the data. Those in the P-waves could be only determined qualitatively, namely by imposing more general restrictions like that the partial-wave cross sections for Λp remain small at higher energies [40], so that the total cross section remains small as well, as indicated by the measurements. Luckily, when the extension to N2LO was in progress, the first extended measurements of differential cross sections for $\Sigma^+ p$ and $\Sigma^- p$ away from the threshold region became available from the E40 experiment at J-PARC [100–102]. This allowed one to pin down the P-wave LECs better than before [42]. Still some ambiguities remain and, because of that, two scenarios for the P-waves of the N2LO potential with cutoff 550 MeV were explored in that work which were denoted by the superscripts a and b, see the discussion in Section 3.1 in Ref. [42].

As expected, at LO only the bulk properties of the YN interaction can be reproduced [39]. However, already at NLO, the description of the YN system achieved is on the same level of quality as the one by the most advanced meson-exchange YN interactions [14]. In terms of the χ^2 its values are around 15–16 for the total of 36 ΛN and ΣN data included. It amounts to $\approx$ 30 for the LO interactions.

Interestingly, with the NLO interactions NLO13 and NLO19, it was possible to achieve a combined description of the Λp and ΣN systems without any explicit SU(3) symmetry breaking in the contact interactions. Of course, SU(3) symmetry is broken by the used physical masses of the involved pseudoscalar mesons in the potential and of the hyperons when solving the LS equation. On the other hand, a unified description of other BB interactions, for example, in the NN system or of $\Lambda\Lambda$ and ΞN, with contact terms fulfilling strict SU(3) symmetry turned out to be not possible [103]. In particular, the strength of the contact interaction in the **27** representation of SU(3), see Table 2.1, that is needed to reproduce the pp (or np) $^1S_0$ phase shifts is simply not compatible with what is required for the description of the empirical Σ^+p cross section [104].

2.2.1. ΛN and ΣN systems

In the following, we focus on a comparison with cross section data at low energies. Here the results are dominated by the S-wave interactions, which are also the most relevant ones for the predictions of hypernuclei that will be discussed below.

Cross sections for Λp are shown in Fig. 2.2, while those for $\Sigma^- p$ and $\Sigma^+ p$ can be found in Fig. 2.3. Data that have been considered in the fitting procedure are indicated by filled symbols. We include results for the NLO19 YN potential (the variation with the cutoff is indicated by the band) and those for the SMS potentials up to NLO and N2LO, respectively. In the latter case the results correspond to the cutoff of 550 MeV, and to variant a. As mentioned above, the variants a and b differ only in the P-wave interaction. They yield almost identical results for integrated cross sections [42]. Note that the results for the NLO13 and NLO19 potentials for Λp and ΣN scattering are very similar [41] and, therefore, the former ones are not included/discussed here.

The results for Λp are shown over an extended momentum range so that we can also include the very recent data from CLAS [27] and from BESIII [28]. Interestingly, the predictions from the chiral potentials are quite well in line with those measurements. Nonetheless, one should keep in mind that, strictly speaking, the potentials are only valid for momenta below the $\pi\Lambda$N threshold, i.e. for $p_{\rm lab} < 890$ MeV/c.

The most striking feature in the Λp cross section is certainly the large cusp-like structure at the ΣN threshold, which is predicted by all considered potentials. In fact, it appears in all coupled-channel treatments which provide a realistic description of the Λp and

Table 2.2
Scattering lengths (a) and effective ranges (r) for singlet (s) and triplet (t) S-waves (in fm), for ΛN, ΣN with isospin $I = 1/2$, $3/2$, and for $\Sigma^+ p$ with inclusion of the Coulomb interaction.

Λ [MeV]	SMS NLO			SMS N2LO			NLO13	NLO19
	500	550	600	500	550	600	600	600
$a_s^{\Lambda N}$	−2.80	−2.79	−2.79	−2.80	−2.79	−2.80	−2.91	−2.91
$r_s^{\Lambda N}$	2.87	2.72	2.63	2.82	2.89	2.68	2.78	2.78
$a_t^{\Lambda N}$	−1.59	−1.57	−1.56	−1.56	−1.58	−1.56	−1.54	−1.41
$r_t^{\Lambda N}$	3.10	2.99	3.00	3.16	3.09	3.17	2.72	2.53
Re $a_s^{\Sigma N\ (I=1/2)}$	1.14	1.15	1.10	1.03	1.12	1.06	0.90	0.90
Im $a_s^{\Sigma N}$	0.00	0.00	0.00	0.00	0.00	0.00	0.00	0.00
Re $a_t^{\Sigma N\ (I=1/2)}$	2.58	2.42	2.31	2.60	2.38	2.53	2.27	2.29
Im $a_t^{\Sigma N}$	−2.60	−2.95	−3.09	−2.56	−3.26	−2.64	−3.29	−3.39
$a_s^{\Sigma N\ (I=3/2)}$	−4.21	−4.05	−4.11	−4.37	−4.19	−4.03	−4.45	−4.55
$r_s^{\Sigma N}$	3.93	3.89	3.75	3.73	3.89	3.74	3.68	3.65
$a_t^{\Sigma N\ (I=3/2)}$	0.46	0.47	0.47	0.38	0.44	0.41	0.44	0.43
$r_t^{\Sigma N}$	−5.08	−4.74	−4.82	−5.70	−4.96	−5.72	−4.59	−5.27
$a_s^{\Sigma^+ p}$	−3.41	−3.30	−3.44	−3.47	−3.39	−3.25	−3.56	−3.62
$r_s^{\Sigma^+ p}$	3.75	3.73	3.59	3.61	3.73	3.65	3.54	3.50
$a_t^{\Sigma^+ p}$	0.51	0.52	0.52	0.41	0.48	0.45	0.49	0.47
$r_t^{\Sigma^+ p}$	−5.46	−5.12	−5.19	−6.74	−5.50	−6.41	−5.08	−5.77

$\Sigma^- p$ data including the $\Sigma^- p$ capture ratio at rest [14–18]. Unfortunately, as one can see, the two Λp data points available in the pertinent momentum region suffer from a poor momentum resolution and do not allow any conclusions. However, the presence of a pronounced ΣN threshold effect is well established in measurements of the Λp invariant-mass spectrum in reactions like $K^- d \to \pi^- \Lambda p$, $\pi^+ d \to K^+ \Lambda p$, or $pp \to K^+ \Lambda p$, see the overview given by Machner et al. [105]. More recent observations, in the reaction $pp \to K^+ \Lambda p$, are documented in Refs. [106,107].

We refrain from showing more results here. Further observables, specifically Σ^+p and Σ^-p cross sections at higher momenta, differential cross sections [100–102], and S- and P-wave phase shifts in the ΛN and ΣN channels can be found in Refs. [40–42]. However, we list results for the effective range parameters, see Table 2.2. Those parameters provide a simple and illuminating view on the strength of the S-wave interactions in the various ΛN and ΣN channels.

2.2.2. $\Lambda\Lambda$ and ΞN systems

Chiral potentials up to NLO for the BB interaction in the strangeness $S = -2$ systems $\Lambda\Lambda$ and ΞN have already been established in 2016 [104]. Thereby constraints from the $\Lambda\Lambda$ scattering length in the $^1S_0$ state together with experimental upper bounds on the cross sections for ΞN scattering and for the transition $\Xi N \to \Lambda\Lambda$ have been exploited. This allowed us to fix the additional LECs that arise in the **1** irreducible representation of SU(3) [104], see Table 2.1. Furthermore, the consideration of those empirical constraints necessitated to add SU(3) symmetry breaking contact terms (cf. Eq. (2.13)) in other irreps (**27**, **10**, $\overline{\mathbf{10}}$, $\mathbf{8_s}$, $\mathbf{8_a}$), with regard to those determined from the ΛN and ΣN data, as already mentioned above. In 2019, a modified version has been suggested [108] which only differs from the one in Ref. [104] by a more attractive interaction in the $^3S_1$ partial wave with isospin $I = 1$. That potential yields a moderately attractive (in-medium) Ξ-nuclear interaction [108] and supports the existence of bound Ξ-hypernuclei as will be discussed below. In both variants, a non-local regulator is applied throughout. An extension of the S=−2 interaction up to N2LO based on the SMS scheme has not been attempted yet. This would be only meaningful once more extensive and more quantitative experimental information becomes available.

Results for the $\Lambda\Lambda$ cross sections are presented in Fig. 2.4 while those for the ΞN cross sections (based on the ΞN potential from 2019 [108]) are presented in Fig. 2.5. Interestingly, for the $\Xi^- p$ cross sections a cusp effect is predicted at the threshold of the $\Lambda\Sigma^0$ channel, similar to though somewhat less pronounced than in case of the Λp system at the ΣN threshold, cf. Fig. 2.2.

Unfortunately, so far there is no experimental information for low momenta. Moreover, in some cases only upper limits for the cross sections are available. We include here recent additions to the data base. One is from the BESIII Collaboration [109,110] who deduced the $\Xi^0 n$ inelastic and charge-exchange cross sections from the Ξ^0+^{9}Be reaction. The others are new Ξ^-p cross sections from the J-PARC E42 experiment [111], estimated from the production of Ξ^- and $\Lambda\Lambda$ in the reaction $^{12}C(K^-, K^+)$ at an incident beam momentum of 1.8 GeV/c using the eikonal approximation. As one can see in Fig. 2.4, the cross section for $\Xi^- p \to \Lambda\Lambda$ is well in line with older empirical information [112] and with results from chiral EFT. The same can be said about the $\Xi^0 n \to \Xi^- p$ cross section, cf. Fig. 2.5. On the other hand, there is a striking discrepancy in the $\Xi^- p$ inelastic cross section in comparison to previous experimental evidence [113] and also to theory. Note that such large values as suggested by the new experimental estimate would

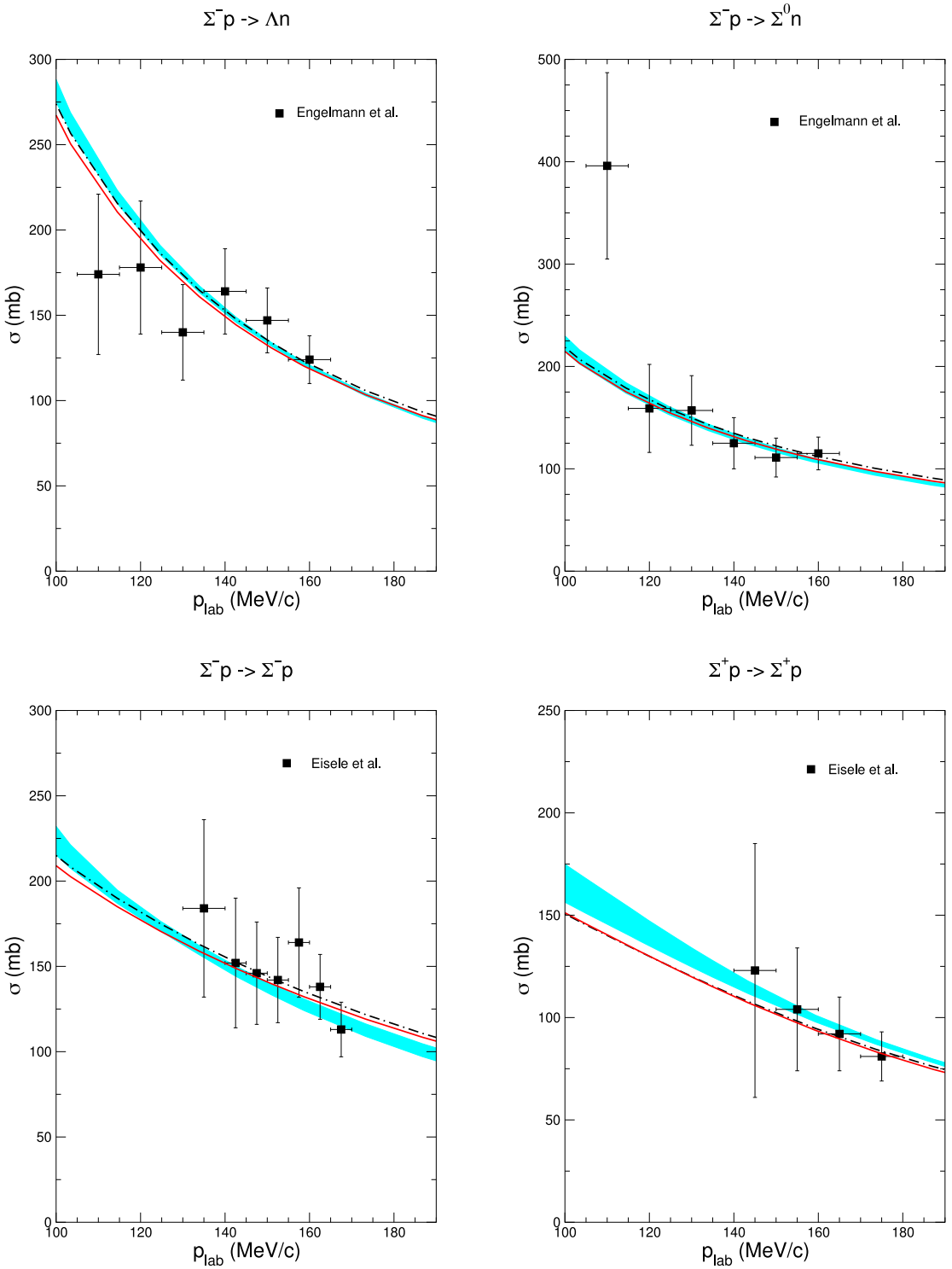

Fig. 2.3. $\Sigma^- p$ and $\Sigma^+ p$ cross sections. Results are shown for the chiral YN potentials NLO19 [41] (cyan band) and SMS [42] NLO (550) (dash-dotted/black line) and N2LO (550) (solid/red line).
Source: Data are taken from Refs. [7,8].

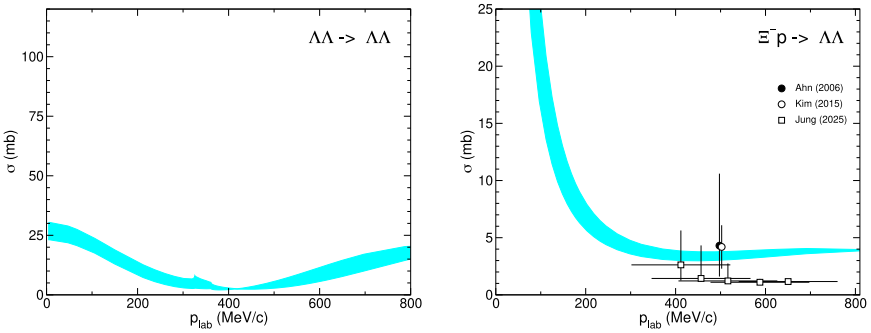

Fig. 2.4. Results for the $\Lambda\Lambda$ cross sections of the NLO potential from Ref. [104].
Source: Data are from Refs. [111,112].

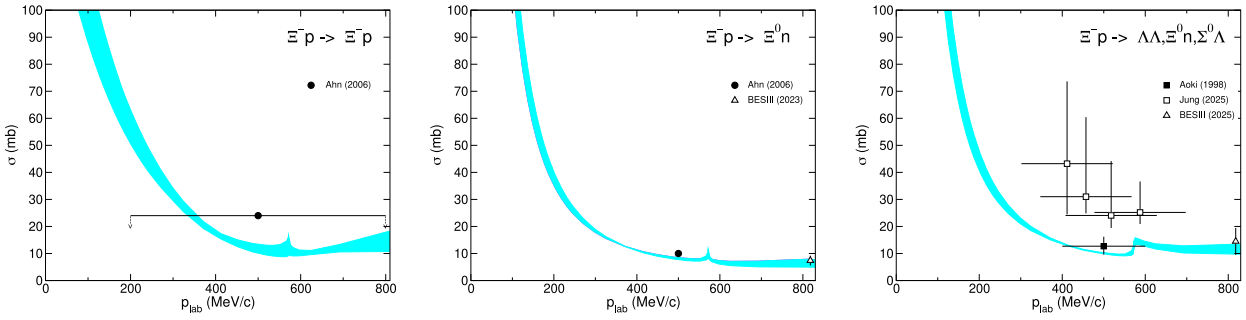

Fig. 2.5. Results for the ΞN cross sections of the NLO potential from Ref. [108].
Source: Data are from Refs. [109–113].

require a much stronger attractive ΞN interaction, likely even a bound state in one of the $^3S_1$ partial waves, see Ref. [104], for which, however, there is no empirical evidence.

An interesting and independent test for the ΞN interaction is provided by two-particle momentum correlation functions. The ones for $\Xi^- p$ have been measured recently by the ALICE Collaboration in p-Pb collisions at 5.02 TeV [114] and in pp collisions at 13 TeV [61]. As has been shown in Refs. [115,116], those data are nicely reproduced by the chiral ΞN interaction from 2019 [108].

2.3. Large-N_c constraints

We end this section by discussing constraints from large-N_c QCD. It was introduced by 't Hooft [117] as a means of studying QCD amplitudes in a systematic way using the inverse number of colors, $1/N_c$, as the expansion parameter. Witten [118] developed a Hartree-like picture of large-N_c baryons. Shortly after this, not only the connection to the Skyrme model [119,120] could be uncovered [121,122], but also the fact that baryons with an $\mathrm{SU}(N_f) \times \mathrm{SU}(2)_{\mathrm{spin}}$ symmetry come with an exact contracted $\mathrm{SU}(2N_f)$ spin-flavor symmetry in the large-N_c limit leading to a tower of degenerate $\mathrm{SU}(N_f)$ baryon multiplets [123–125]. The investigation of the NN interaction was pioneered in Refs. [126,127] and the SU(3) BB interaction was studied first in this framework focusing on the leading order chiral contact interactions in [128]. Note that the basis of the BB interaction in the large-N_c scenario was already spelled out in Ref. [127]. Here, we follow the more recent and more detailed work of Ref. [129] and refer to that paper for calculational details.

First, we summarize the large-N_c scaling of the various ingredients entering the BB potential. These are

$$m_B \sim N_c, \quad |\mathbf{q}|^2 \sim 1, \quad q_0 \sim N_c^{-1}, \quad \Delta m_B \sim N_c^{-1}, \quad |\mathbf{k}|^2 \sim 1, \quad (\mathbf{k}\cdot\mathbf{q}) \sim 1. \tag{2.18}$$

Here, m_B denotes the baryon mass, Δm_B the splitting within a given multiplet, $\mathbf{q} = \mathbf{p}' - \mathbf{p}$ is the three-momentum transfer, $\mathbf{k} = \mathbf{p}' + \mathbf{p}$ the momentum sum, and $q_0 = \Delta m_B + (\mathbf{k}\cdot\mathbf{q})/(2m_B)$ the energy transfer in the non-relativistic limit. Moreover, expanding the BB potential in a Taylor series of the above momenta leads to the second source of $1/N_c$ suppressions due to factors of $1/m_B$. As argued in [127], this suppression follows the general rule that terms proportional to $\mathbf{q}^m\,\mathbf{k}^n$ are suppressed by

$$1/N_c^{\min(m,n)}. \tag{2.19}$$

Restricting ourselves to the pure octet baryon sector, the resulting BB potential takes the form

$$
\begin{aligned}
V_{B^\alpha B^\beta \to B^\gamma B^\delta} = N_c \Bigg\{ & v_{0,0} + v_{0,1}^{(T)} \frac{\left(\hat{\mathcal{T}}_1 \cdot \hat{\mathcal{T}}_2\right)}{2N_c^2} + v_{0,1}^{(S)} \frac{\left(\hat{\mathcal{S}}_1 \cdot \hat{\mathcal{S}}_2\right)}{3N_c^2} + 2v_{0,1}^{(G)} \frac{\left(\hat{\mathcal{G}}_1 \cdot \hat{\mathcal{G}}_2\right)}{N_c^2} \\
& + \left[\left(v_{1,0} + v_{1,1}^{(T)} \frac{\left(\hat{\mathcal{T}}_1 \cdot \hat{\mathcal{T}}_2\right)}{2N_c^2} \right) \frac{\left(\hat{\mathcal{S}}_1^i + \hat{\mathcal{S}}_2^i\right)}{\sqrt{3}N_c} + v_{2,0} \frac{\left(\hat{\mathcal{G}}_2^{ia} \hat{\mathcal{T}}_1^a + \hat{\mathcal{G}}_1^{ia} \hat{\mathcal{T}}_2^a\right)}{N_c^2} \right] (\mathbf{q} \times \mathbf{k})^i \\
& + \left[v_{4,0} \left(\mathbf{q}^i \mathbf{q}^j - \frac{1}{3} |\mathbf{q}|^2 \delta^{ij} \right) + v_{5,0} \left(\mathbf{k}^i \mathbf{k}^j - \frac{1}{3} |\mathbf{k}|^2 \delta^{ij} \right) \right] \frac{2\left(\hat{\mathcal{G}}_1^{ia} \hat{\mathcal{G}}_2^{ja}\right)}{N_c^2} \Bigg\} + \mathcal{O}\left(1/N_c^3\right) ,
\end{aligned}
\tag{2.20}
$$

in terms of the generators of the contracted SU(6) spin-flavor symmetry.

$$
\hat{\mathcal{S}}^i = q^\dagger \left(\frac{\sigma^i}{2} \otimes \mathbb{1} \right) q , \quad \hat{\mathcal{T}}^a = q^\dagger \left(\mathbb{1} \otimes \frac{\lambda^a}{2} \right) q , \quad \hat{\mathcal{G}}^{ai} = q^\dagger \left(\frac{\sigma^i}{2} \otimes \frac{\lambda^a}{2} \right) q .
\tag{2.21}
$$

Here, $q = (u, d, s)$ represents a three flavor bosonic quark operator that carries no color, the σ_i's are the three Pauli spin matrices and the λ_a's are the eight Gell-Mann matrices. Furthermore, the coefficients $v_{n,k}$ are scalar functions of $|\mathbf{q}|^2$ and $|\mathbf{k}|^2$. Also, we have used the abbreviations $\hat{\Lambda}_1 \cdot \hat{\Lambda}_2 = \hat{\Lambda}_{\gamma\alpha}^M \hat{\Lambda}_{\delta\beta}^M$ and correspondingly for $\hat{\mathcal{S}}$, $\hat{\mathcal{T}}$, and $\hat{\mathcal{G}}$. It is instructive to compare this to the generic formulation of the SU(3) BB potential with flavor labels $a \ldots d$, which can be written as

$$
V_{B^a B^b \to B^c B^d} = V_0^0 + V_\sigma^0 \left(\boldsymbol{\sigma}_1 \cdot \boldsymbol{\sigma}_2\right) + V_{\mathrm{LS}}^0 \left(\mathbf{L} \cdot \mathbf{S}\right) + V_{\mathrm{T}}^0 S_{12} + V_0^1 \rho_0^{abcd} + V_\sigma^1 \left(\boldsymbol{\sigma}_1 \cdot \boldsymbol{\sigma}_2\right) \rho_\sigma^{abcd} + V_{\mathrm{LS}}^1 \left(\mathbf{L} \cdot \mathbf{S}\right) \rho_{\mathrm{LS}}^{abcd} + V_{\mathrm{T}}^1 S_{12} \rho_{\mathrm{T}}^{abcd},
\tag{2.22}
$$

where $S_{12}(\hat{\mathbf{r}}) = 3\left(\hat{\mathbf{r}} \cdot \boldsymbol{\sigma}_1\right)\left(\hat{\mathbf{r}} \cdot \boldsymbol{\sigma}_2\right) - \left(\boldsymbol{\sigma}_1 \cdot \boldsymbol{\sigma}_2\right)$, with $\hat{\mathbf{r}} = \mathbf{r}/|\mathbf{r}|$, and the $\rho_{\{0,\sigma,\mathrm{LS,T}\}}^{abcd}$ represent some appropriate structure in accordance with SU(3) flavor symmetry not important at this stage. Here, we have deliberately mimicked the generic NN potential given in Ref. [127] in order to facilitate the comparison. For the NN interaction, the $\rho_{\{0,\sigma,\mathrm{LS,T}\}}^{abcd}$ are simply given by $\left(\boldsymbol{\tau}_1 \cdot \boldsymbol{\tau}_2\right)$, with $\boldsymbol{\tau}$ being the isospin operator. What the authors of Ref. [127] have shown is that, in this case only, V_0^0, V_σ^1, and V_{T}^1 are of leading $\mathcal{O}\left(N_c\right)$, while all other contributions are of $\mathcal{O}\left(1/N_c\right)$. Similarly, one finds for the SU(3) BB interaction considering baryons of strangeness of $\mathcal{O}(1)$

$$
V_0^0 \sim V_0^1 \sim V_\sigma^1 \sim V_{\mathrm{T}}^1 \sim N_c, \quad V_\sigma^0 \sim V_{\mathrm{LS}}^0 \sim V_{\mathrm{LS}}^1 \sim V_{\mathrm{T}}^0 \sim 1/N_c,
\tag{2.23}
$$

which is basically the same as for the NN case except for the lifting of V_0^1, which is related to the terms $\sim \left(\hat{\mathcal{T}}_1 \cdot \hat{\mathcal{T}}_2\right)$ which in the corresponding NN potential are suppressed by a relative factor of $1/N_c^2$ but in general are not suppressed in the BB case. Note that, in the most general case, the BB potential Eq. (2.22) can also have an antisymmetric spin–orbit term $\sim \mathbf{L} \cdot \left(\boldsymbol{\sigma}_1 - \boldsymbol{\sigma}_2\right)$ [40]. This force describing spin singlet–triplet transitions is absent in isospin-symmetric NN potentials but is in accordance with SU(3) symmetry. However, in the large-N_c case this contribution comes with the same suppression that also showed up in the V_{LS}^i case above due to Eq. (2.19). As none of the contributions at LO and NLO in $1/N_c$ does actually generate such antisymmetric spin–orbit interactions, this term is excluded from the analysis and from Eq. (2.22). We further note that the large-N_c results for the potential are not RG-invariant and that there is a preferred scale, see e.g. Ref. [130] (and references therein). However, the extraction of this preferred scale as discussed in the NN case [130] cannot be performed at present as corresponding data are either absent or too imprecise.

The contact terms of leading order in chiral perturbation theory, see Section 2.1, generate a potential that includes central, spin–spin, spin–orbit, and tensorial parts. However, only the central and spin–spin parts of this potential are indeed of $\mathcal{O}\left(N_c\right)$, while all other contributions are suppressed by a factor $1/m_B^2$. The contact terms alone hence do not generate the full leading $\mathcal{O}\left(N_c\right)$ potential, but only terms corresponding to V_0^0, V_0^1, and V_σ^1 in Eq. (2.22), while an $\mathcal{O}\left(N_c\right)$ tensorial part is missing. Moreover, the spin–orbit part is of subleading $\mathcal{O}\left(1/N_c\right)$ as expected. What these contact terms also add is a partial expansion of the large-N_c coefficients in Eq. (2.20) in the momenta, which cannot be determined from the large-N_c Hartree scenario. The leading $\mathcal{O}\left(N_c\right)$ contact contributions $\sim C_S^{abcd}$ and $\sim C_T^{abcd}$, where a, b, c, d are flavor indices, consist of linear combinations of six of the original 15 low-energy constants of the contact Lagrangian. One can derive sum rules valid at leading order in $1/N_c$ allowing to reduce the number of independent parameters to three. These read

$$
\begin{aligned}
C_{1S0}^{\Sigma\Sigma} &\approx \frac{1}{9}\left(20\, C_{1S0}^{\Lambda\Lambda} - 11\, C_{3S1}^{\Lambda\Lambda} - 7\, C_{3S1}^{\Lambda\Sigma}\right) , \\
C_{3S1}^{\Sigma\Sigma} &\approx -12\, C_{1S0}^{\Lambda\Lambda} + 13\, C_{3S1}^{\Lambda\Lambda} + 9\, C_{3S1}^{\Lambda\Sigma} .
\end{aligned}
\tag{2.24}
$$

These large-N_c sum rules of the leading order contact terms are indeed fulfilled to a good accuracy as can be seen from Table 2.3. Especially for small cutoff masses, the agreement is formidable with deviations just within what is expected from $1/N_c$ corrections.[1]

A BB potential derived from SU(3) Chiral Perturbation Theory (CHPT) must include one-meson exchange contributions in order to fully reproduce the leading order large-N_c potential, as the tensorial part V_T^1 of $\mathcal{O}\left(N_c\right)$ cannot be generated by the contact terms alone, which only generate a tensorial part of $\mathcal{O}\left(1/N_c\right)$. This is in accordance with chiral power counting. Matching the one-meson exchange contributions with the large-N_c potential yields the already known ratio $F/D = 2/3\left(1 + \mathcal{O}\left(1/N_c^2\right)\right)$, see e.g. [131]. One can further derive an effective coupling $g_{BB\Phi}$ in terms of $g_A = F + D$ that is valid at leading order in $1/N_c$. In the literature, it

[1] Note that these sum rules differ from the ones given in [128], from the details given in that paper we were not able to arrive at their results.

Table 2.3
Comparing best fit YN potentials from Ref. [39] and corresponding large-N_c predictions (in units of 10^4 GeV^{-2}). The bold values of $C_{1S0}^{\Sigma\Sigma}$ and $C_{3S1}^{\Sigma\Sigma}$ are obtained using the large-N_c sum rules Eq. (2.24).

Cutoff	$C_{1S0}^{\Lambda\Lambda}$	$C_{3S1}^{\Lambda\Lambda}$	$C_{3S1}^{\Lambda\Sigma}$	$C_{1S0}^{\Sigma\Sigma}$		$C_{3S1}^{\Sigma\Sigma}$	
550 MeV	−0.0466	−0.0222	−0.0016	−0.0766	**−0.0751**	0.2336	**0.2562**
600 MeV	−0.0403	−0.0163	−0.0019	−0.0763	**−0.0682**	0.2391	**0.2546**
650 MeV	−0.0322	−0.0097	0.0000	−0.0757	**−0.0597**	0.2392	**0.2603**
700 MeV	−0.0304	−0.0022	0.0035	−0.0744	**−0.0676**	0.2501	**0.3677**

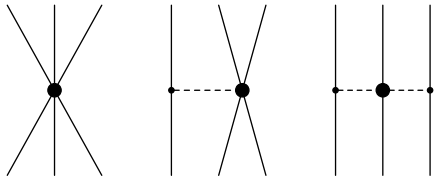

Fig. 3.1. Leading three-baryon interactions: contact term, one-meson exchange and two-meson exchange. Filled circles and solid dots denote vertices with dimension $\Delta_i = 1$ and $\Delta_i = 0$, respectively [43].

is common to use YN and YY couplings $f_{BB\Phi}$ expressed in terms of $f_{NN\pi} = g_A/(2F_0)$ and $\alpha = F/(F+D)$ based on Ref. [9]. The effective large-N_c coupling $g_{BB\Phi}$ just reproduces these $f_{BB\Phi}$ after forming appropriate isospin combinations and setting $\alpha = 2/5$. It is also of relevance that the full large-N_c scaling of $\mathcal{O}\left(N_c\right)$ in the one-meson exchange case is only achieved by exchanging pions, while exchanging kaons are of $\mathcal{O}(1)$ and exchanging η's are even more suppressed and of $\mathcal{O}\left(1/N_c\right)$ which is a consequence of the choice to match real-world baryons with those large-N_c baryons that have strangeness of $\mathcal{O}(1)$. At the level of quarks and gluons, this is just a result of combinatorics, as, with this choice, there are about N_c choices to pick up an up or down quark, but only $\mathcal{O}(1)$ choices to find a strange quark.

Finally, we note that the large-N_c scalings of many-meson exchange contributions cannot be assessed by means of a naive power counting of the involved meson–baryon couplings alone, as this might lead to results that contradict the assumption that the BB potential is of $\mathcal{O}\left(N_c\right)$. However, imposing spin-flavor symmetry and considering all diagrams of a given type including the full baryon tower retains consistency. Summing over all n-meson exchange diagrams of a given type yields a contribution that at most scales as $\mathcal{O}\left(N_c^{2-n}\right)$. For the two-meson exchange contributions in SU(3) CHPT, this is explicitly shown in [129]. In this case, the inclusion of the decuplet baryons is mandatory, and a cancellation between the deceptive $\mathcal{O}\left(N_c^2\right)$ contributions of the box and crossed box diagrams appears if the large-N_c ratio $C/D = 2$ in addition to the ratio $F/D = 2/3$, where C is the leading baryon octet-baryon decuplet-Goldstone boson coupling constant (often also denoted as H). To leading order, it is thus possible to describe one-meson and two-meson exchange diagrams by a single parameter, e.g. by setting $D = 3/5\, g_A$, $F = 2/5\, g_A$, and $C = 6/5\, {g_A}^2$.

3. Three-baryon forces in chiral effective field theory

One of the merits of chiral EFT is that two-body forces and three-body forces (3BFs) can be derived in a consistent way. Given the importance of three-nucleon forces (3NFs) for an accurate description of nuclei, one expects that 3BFs play likewise an important role in nuclear systems with strangeness. Specifically, the ΛNN interaction could play a decisive role for reproducing the separation energies of Λ hypernuclei, which are experimentally well established.

In this section, we review the derivation of the leading irreducible three-baryon interactions from SU(3) chiral effective field theory following Ref. [43]. We introduce the minimal effective Lagrangian required for the pertinent vertices. Furthermore, the estimation of the corresponding LECs through decuplet saturation will be covered [132]. According to the power counting the 3BFs arise formally at N2LO in the chiral expansion. Three types of diagrams contribute: three-baryon contact terms, one-meson and two-meson exchange diagrams, cf. Fig. 3.1. Note that a two-meson exchange diagram, such as on the right of Fig. 3.1, with a (LO) Weinberg–Tomozawa vertex in the middle, would formally be an NLO contribution. However, as in the nucleonic sector, this contribution is kinematically suppressed due to the fact that the involved meson energies are differences of baryon kinetic energies. Anyway, parts of these N2LO contributions get promoted to NLO by the introduction of intermediate decuplet baryons.

3.1. Contact interaction

In this subsection, we consider the leading three-baryon contact interaction. The corresponding Lagrangian involves six baryon fields and has been constructed in Ref. [43], where the following possible structures in flavor space have been considered

$$\langle \bar{B}\bar{B}\bar{B}BBB\rangle, \langle \bar{B}\bar{B}B\bar{B}BB\rangle, \langle \bar{B}\bar{B}BB\bar{B}B\rangle, \langle \bar{B}B\bar{B}B\bar{B}B\rangle, \tag{3.1}$$

[2] Note that the conventions in Ref. [129] and [132] differ from each other. Therefore, the numerical value of C here and in Section 3.5 are not comparable.

$$\langle \bar{B}\bar{B}BB\rangle\langle \bar{B}B\rangle\,,\langle \bar{B}B\bar{B}B\rangle\langle \bar{B}B\rangle\,,\langle \bar{B}\bar{B}\bar{B}B\rangle\langle BB\rangle\,, \tag{3.2}$$

$$\langle \bar{B}\bar{B}\bar{B}\rangle\langle BBB\rangle\,,\langle \bar{B}\bar{B}B\rangle\langle B\bar{B}B\rangle\,, \tag{3.3}$$

$$\langle \bar{B}B\rangle\langle \bar{B}B\rangle\langle \bar{B}B\rangle\,,\langle \bar{B}\bar{B}\rangle\langle \bar{B}B\rangle\langle BB\rangle\,. \tag{3.4}$$

The possible Dirac structures are

$$\mathbb{1}\otimes\mathbb{1}\otimes\mathbb{1}\,,\ \mathbb{1}\otimes\gamma_5\gamma^\mu\otimes\gamma_5\gamma_\mu\,,\ \gamma_5\gamma^\mu\otimes\mathbb{1}\otimes\gamma_5\gamma_\mu\,, \tag{3.5}$$

$$\gamma_5\gamma^\mu\otimes\gamma_5\gamma_\mu\otimes\mathbb{1}\,,\ \gamma_5\gamma_\mu\otimes \mathrm{i}\,\sigma^{\mu\nu}\otimes\gamma_5\gamma_\nu\,, \tag{3.6}$$

which lead to the following operators in the three-body spin space

$$\mathbb{1}\,,\ \boldsymbol{\sigma}_1\cdot\boldsymbol{\sigma}_2\,,\ \boldsymbol{\sigma}_1\cdot\boldsymbol{\sigma}_3\,,\ \boldsymbol{\sigma}_2\cdot\boldsymbol{\sigma}_3\,,\ \mathrm{i}\,\boldsymbol{\sigma}_1\cdot(\boldsymbol{\sigma}_2\times\boldsymbol{\sigma}_3)\,. \tag{3.7}$$

All combinations of these possibilities leads to a (largely overcomplete) set of terms for the leading covariant Lagrangian. Note that in [43] the starting point is a covariant Lagrangian, but the goal is the minimal non-relativistic Lagrangian. Therefore, only Dirac structures leading to independent (non-relativistic) spin operators are relevant.

Let us consider the process $B_1B_2B_3\to B_4B_5B_6$, where the B_i are baryons in the particle basis, $B_i\in\{n,p,\Lambda,\Sigma^+,\Sigma^0,\Sigma^-,\Xi^0,\Xi^-\}$. The contact potential V has to be derived within a threefold spin space for this process. The operators in spin-space 1 is defined to act between the two-component Pauli spinors of B_1 and B_4. In the same way, spin-space 2 belongs to B_2 and B_5, and spin-space 3 to B_3 and B_6. For a fixed spin configuration the potential can be calculated from

$$\chi^{(1)^\dagger}_{B_4}\chi^{(2)^\dagger}_{B_5}\chi^{(3)^\dagger}_{B_6}\,V\,\chi^{(1)}_{B_1}\chi^{(2)}_{B_2}\chi^{(3)}_{B_3}\,, \tag{3.8}$$

where the superscript of a spinor denotes the spin space and the subscript denotes the baryon to which the spinor belongs. The potential is obtained as $V=-\langle B_4B_5B_6|\,\mathscr{L}\,|B_1B_2B_3\rangle$, where the contact Lagrangian $\mathscr{L}$ has to be inserted, and the 36 Wick contractions need to be performed. The number 36 corresponds to the $3!\times3!$ possibilities to arrange the three initial and three final baryons into Dirac bilinears. One obtains six direct terms, where the baryon bilinears combine the baryon pairs 1–4, 2–5 and 3–6, as shown in Eq. (3.8). For the other 30 Wick contractions, the resulting potential is not fitting to the form of Eq. (3.8), because the wrong baryon pairs are connected in a separate spin space. Hence, an appropriate exchange of the spin wave functions in the final state has to be performed. This is achieved by multiplying the potential with the well-known spin-exchange operators $P^{(\sigma)}_{ij}=\frac{1}{2}(\mathbb{1}+\boldsymbol{\sigma}_i\cdot\boldsymbol{\sigma}_j)$. Furthermore additional minus signs arise from the interchange of anticommuting baryon fields. The full potential is then obtained by adding up all 36 contributions to the potential. One obtains a potential that fulfills automatically the generalized Pauli principle and that is fully antisymmetrized.

In order to obtain a minimal set of Lagrangian terms of the final potential matrix, redundant terms have been eliminated until the rank of the final potential matrix (consisting of multiple flavor structures, see Eqs. (3.1)–(3.4), and the spin structures in Eq. (3.7)) matches the number of terms in the Lagrangian. The minimal non-relativistic six-baryon contact Lagrangian is [43]

$$\begin{aligned}
\mathscr{L} =& -C_1\langle \bar{B}_a\bar{B}_b\bar{B}_cB_aB_bB_c\rangle + C_2\langle \bar{B}_a\bar{B}_b\bar{B}_aB_c\bar{B}_cB_bB_c\rangle\\
&-C_3\langle \bar{B}_a\bar{B}_bB_aB_b\bar{B}_cB_c\rangle + C_4\langle \bar{B}_aB_a\bar{B}_b\bar{B}_bB_c\bar{B}_cB_c\rangle\\
&-C_5\langle \bar{B}_a\bar{B}_bB_aB_b\rangle\,\langle \bar{B}_cB_c\rangle\\
&-C_6\Big(\langle \bar{B}_a\bar{B}_bB_c\bar{B}_aB_a(\sigma^iB)_b(\sigma^iB)_c\rangle+\langle \bar{B}_c\bar{B}_b\bar{B}_a(\sigma^iB)_c(\sigma^iB)_bB_a\rangle\Big)\\
&+C_7\Big(\langle \bar{B}_a\bar{B}_bB_a\bar{B}_c(\sigma^iB)_b(\sigma^iB)_c\rangle+\langle \bar{B}_c\bar{B}_b(\sigma^iB)_c\bar{B}_a(\sigma^iB)_bB_a\rangle\Big)\\
&-C_8\Big(\langle \bar{B}_a\bar{B}_bB_a(\sigma^iB)_b\bar{B}_c(\sigma^iB)_c\rangle+\langle \bar{B}_b\bar{B}_a(\sigma^iB)_bB_a\bar{B}_c(\sigma^iB)_c\rangle\Big)\\
&+C_9\langle \bar{B}_aB_a\bar{B}_b(\sigma^iB)_b\bar{B}_c(\sigma^iB)_c\rangle\\
&-C_{10}\Big(\langle \bar{B}_a\bar{B}_bB_a(\sigma^iB)_b\rangle\,\langle \bar{B}_c(\sigma^iB)_c\rangle+\langle \bar{B}_b\bar{B}_a(\sigma^iB)_bB_a\rangle\,\langle \bar{B}_c(\sigma^iB)_c\rangle\Big)\\
&-C_{11}\langle \bar{B}_a\bar{B}_b\bar{B}_c(\sigma^iB)_aB_b(\sigma^iB)_c\rangle + C_{12}\langle \bar{B}_a\bar{B}_b(\sigma^iB)_a\bar{B}_cB_b(\sigma^iB)_c\rangle\\
&-C_{13}\langle \bar{B}_a\bar{B}_b(\sigma^iB)_a(\sigma^iB)_b\bar{B}_cB_c\rangle - C_{14}\langle \bar{B}_a\bar{B}_b(\sigma^iB)_a(\sigma^iB)_b\rangle\,\langle \bar{B}_cB_c\rangle\\
&-\mathrm{i}\,\epsilon^{ijk}C_{15}\langle \bar{B}_a\bar{B}_b\bar{B}_c(\sigma^iB)_a(\sigma^jB)_b(\sigma^kB)_c\rangle + \mathrm{i}\,\epsilon^{ijk}C_{16}\langle \bar{B}_a\bar{B}_b(\sigma^iB)_a\bar{B}_c(\sigma^jB)_b(\sigma^kB)_c\rangle\\
&-\mathrm{i}\,\epsilon^{ijk}C_{17}\langle \bar{B}_a\bar{B}_b(\sigma^iB)_a(\sigma^jB)_b\bar{B}_c(\sigma^kB)_c\rangle + \mathrm{i}\,\epsilon^{ijk}C_{18}\langle \bar{B}_a(\sigma^iB)_a\bar{B}_b(\sigma^jB)_b\bar{B}_c(\sigma^kB)_c\rangle\,,
\end{aligned} \tag{3.9}$$

with vector indices i,j,k and two-component spinor indices a,b,c. In total 18 low-energy constants $C_1\ldots C_{18}$ are present. The low-energy constant E of the six-nucleon contact term (see [133]) can be expressed through these LECs by $E=2(C_4-C_9)$.

As in the two-body sector, group theoretical considerations can deliver valuable constrains on the resulting potentials. In flavor space, the three octet baryons form the 512-dimensional tensor product $\mathbf{8}\otimes\mathbf{8}\otimes\mathbf{8}$, which decomposes into the following irreducible SU(3) representations

$$\mathbf{8}\otimes\mathbf{8}\otimes\mathbf{8}=\mathbf{64}\oplus(\mathbf{35}\oplus\overline{\mathbf{35}})_2\oplus\mathbf{27}_6\oplus(\mathbf{10}\oplus\overline{\mathbf{10}})_4\oplus\mathbf{8}_8\oplus\mathbf{1}_2\,, \tag{3.10}$$

where the multiplicity of an irreducible representations is denoted by subscripts. In spin space, one obtains for the product of three doublets

$$\mathbf{2}\otimes\mathbf{2}\otimes\mathbf{2}=\mathbf{2}_2\oplus\mathbf{4}\,. \tag{3.11}$$

Table 3.1
Irreducible representations for three-baryon states with strangeness S and isospin I in partial waves $|^{2S+1}L_J\rangle$, with the total spin $S = \frac{1}{2}, \frac{3}{2}$, the angular momentum $L = 0$ and the total angular momentum $J = \frac{1}{2}, \frac{3}{2}$ [43].

states	(S, I)	$^2S_{1/2}$	$^4S_{3/2}$
NNN	$(0, \frac{1}{2})$	$\overline{\mathbf{35}}$	
$\Lambda NN, \Sigma NN$	$(-1, 0)$	$\overline{\mathbf{10}}, \overline{\mathbf{35}}$	$\overline{\mathbf{10}}_a$
$\Lambda NN, \Sigma NN$	$(-1, 1)$	$\mathbf{27}, \overline{\mathbf{35}}$	$\mathbf{27}_a$
ΣNN	$(-1, 2)$	$\mathbf{35}$	
$\Lambda\Lambda N, \Sigma\Lambda N, \Sigma\Sigma N, \Xi NN$	$(-2, \frac{1}{2})$	$\mathbf{8}, \overline{\mathbf{10}}, \mathbf{27}, \overline{\mathbf{35}}$	$\mathbf{8}_a, \overline{\mathbf{10}}_a, \mathbf{27}_a$
$\Sigma\Lambda N, \Sigma\Sigma N, \Xi NN$	$(-2, \frac{3}{2})$	$\mathbf{10}, \mathbf{27}, \mathbf{35}, \overline{\mathbf{35}}$	$\mathbf{10}_a, \mathbf{27}_a$
$\Sigma\Sigma N$	$(-2, \frac{5}{2})$	$\mathbf{35}$	
$\Lambda\Lambda\Lambda, \Sigma\Sigma\Lambda, \Sigma\Sigma\Sigma, \Xi\Lambda N, \Xi\Sigma N$	$(-3, 0)$	$\mathbf{8}, \mathbf{27}$	$\mathbf{1}_a, \mathbf{8}_a, \mathbf{27}_a$
$\Sigma\Lambda\Lambda, \Sigma\Sigma\Lambda, \Sigma\Sigma\Sigma, \Xi\Lambda N, \Xi\Sigma N$	$(-3, 1)$	$\mathbf{8}, \mathbf{10}, \overline{\mathbf{10}}, \mathbf{27}, \mathbf{35}, \overline{\mathbf{35}}$	$\mathbf{8}_a, \mathbf{10}_a, \overline{\mathbf{10}}_a, \mathbf{27}_a$
$\Sigma\Sigma\Lambda, \Sigma\Sigma\Sigma, \Xi\Sigma N$	$(-3, 2)$	$\mathbf{27}, \mathbf{35}, \overline{\mathbf{35}}$	$\mathbf{27}_a$
$\Xi\Lambda\Lambda, \Xi\Sigma\Lambda, \Xi\Sigma\Sigma, \Xi\Xi N$	$(-4, \frac{1}{2})$	$\mathbf{8}, \mathbf{10}, \mathbf{27}, \mathbf{35}$	$\mathbf{8}_a, \mathbf{10}_a, \mathbf{27}_a$
$\Xi\Sigma\Lambda, \Xi\Sigma\Sigma, \Xi\Xi N$	$(-4, \frac{3}{2})$	$\overline{\mathbf{10}}, \mathbf{27}, \mathbf{35}, \overline{\mathbf{35}}$	$\overline{\mathbf{10}}_a, \mathbf{27}_a$
$\Xi\Sigma\Sigma$	$(-4, \frac{5}{2})$	$\overline{\mathbf{35}}$	
$\Xi\Xi\Lambda, \Xi\Xi\Sigma$	$(-5, 0)$	$\mathbf{10}, \mathbf{35}$	$\mathbf{10}_a$
$\Xi\Xi\Lambda, \Xi\Xi\Sigma$	$(-5, 1)$	$\mathbf{27}, \mathbf{35}$	$\mathbf{27}_a$
$\Xi\Xi\Sigma$	$(-5, 2)$	$\overline{\mathbf{35}}$	
$\Xi\Xi\Xi$	$(-6, \frac{1}{2})$	$\mathbf{35}$	

Transitions are only allowed between irreducible representations of the same type. Analogous to [134] for the two-baryon sector, the contributions of different irreducible representations to three-baryon multiplets can be established, which is summarized in Table 3.1. At LO only transitions between S-waves are possible, since the potentials are momentum-independent. Due to the Pauli principle, the totally symmetric spin-quartet **4** must combine with the totally antisymmetric part of $\mathbf{8} \otimes \mathbf{8} \otimes \mathbf{8}$ in flavor space,

$$\mathrm{Ant}_3(\mathbf{8}) = \mathbf{56}_a = \mathbf{27}_a + \mathbf{10}_a + \overline{\mathbf{10}}_a + \mathbf{8}_a + \mathbf{1}_a\,. \tag{3.12}$$

It follows, that these totally antisymmetric irreducible representations are present only in states with total spin 3/2. The totally symmetric part of $\mathbf{8} \otimes \mathbf{8} \otimes \mathbf{8}$ leads to

$$\mathrm{Sym}_3(\mathbf{8}) = \mathbf{120}_s = \mathbf{64}_s + \mathbf{27}_s + \mathbf{10}_s + \overline{\mathbf{10}}_s + \mathbf{8}_s + \mathbf{1}_s\,. \tag{3.13}$$

However, the totally symmetric flavor part has no totally antisymmetric counterpart in spin space, hence these representations do not contribute to the potential. In Table 3.1, the restrictions obtained by the generalized Pauli principle have already been incorporated. The potentials of [43] (decomposed in isospin basis and partial waves) fulfill the restrictions of Table 3.1. For example the combination of LECs related to the representation $\overline{\mathbf{35}}$ is present in the NNN interaction as well as in the $\Xi\Xi\Sigma$ (strangeness, isospin) $= (S, I) = (-5, 2)$ interaction.

3.2. One-meson exchange component

The meson–baryon couplings in the one-meson exchange diagram of Fig. 3.1 emerge from the LO chiral Lagrangian $\mathscr{L}_{\mathrm{BBP}}$ given in Eq. (2.6). It specifies the $BB\phi$ vertices where $\phi = \{\pi^0, \pi^+, \pi^-, K^+, K^-, K^0, \bar{K}^0, \eta\}$. The other vertex involves four baryon fields and one pseudoscalar-meson field. In [43] first an overcomplete set of terms for the corresponding Lagrangian has been constructed. Subsequently, in order to obtain the complete minimal Lagrangian from the overcomplete set of terms, the matrix elements of the process $B_1 B_2 \to B_3 B_4 \phi_1$ have been evaluated. The corresponding spin operators in the potential are

$$\boldsymbol{\sigma}_1 \cdot \boldsymbol{q}\,, \quad \boldsymbol{\sigma}_2 \cdot \boldsymbol{q}\,, \quad \mathrm{i}\,(\boldsymbol{\sigma}_1 \times \boldsymbol{\sigma}_2) \cdot \boldsymbol{q}\,, \tag{3.14}$$

where $\boldsymbol{q}$ denotes the momentum of the emitted meson. Redundant term are removed until the rank of the potential matrix formed by all transitions and spin operators matches the number of terms in the Lagrangian. One ends up with the minimal non-relativistic chiral Lagrangian

$$\begin{aligned}
\mathscr{L} = {} & D_1/F_0 \langle \bar{B}_a (\nabla^i \phi) B_a \bar{B}_b (\sigma^i B)_b \rangle \\
& + D_2/F_0 \Big(\langle \bar{B}_a B_a (\nabla^i \phi) \bar{B}_b (\sigma^i B)_b \rangle + \langle \bar{B}_a B_a \bar{B}_b (\sigma^i B)_b (\nabla^i \phi) \rangle \Big) \\
& + D_3/F_0 \langle \bar{B}_b (\nabla^i \phi) (\sigma^i B)_b \bar{B}_a B_a \rangle \\
& - D_4/F_0 \Big(\langle \bar{B}_a (\nabla^i \phi) \bar{B}_b B_a (\sigma^i B)_b \rangle + \langle \bar{B}_b \bar{B}_a (\sigma^i B)_b (\nabla^i \phi) B_a \rangle \Big) \\
& - D_5/F_0 \Big(\langle \bar{B}_a \bar{B}_b (\nabla^i \phi) B_a (\sigma^i B)_b \rangle + \langle \bar{B}_b \bar{B}_a (\nabla^i \phi) (\sigma^i B)_b B_a \rangle \Big) \\
& - D_6/F_0 \Big(\langle \bar{B}_b (\nabla^i \phi) \bar{B}_a (\sigma^i B)_b B_a \rangle + \langle \bar{B}_a \bar{B}_b B_a (\nabla^i \phi) (\sigma^i B)_b \rangle \Big)
\end{aligned}$$

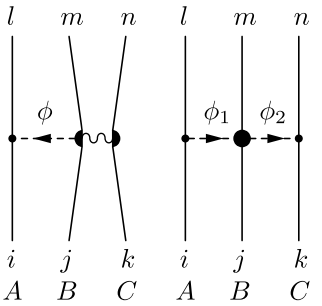

(a) Generic one-meson exchange diagram

(b) Generic two-meson exchange diagram

Fig. 3.2. Generic meson-exchange diagrams. The wiggly line symbolized the four-baryon contact vertex, to illustrate the baryon bilinears.

$$
\begin{aligned}
&- D_7/F_0\Big(\langle \bar{B}_a \bar{B}_b B_a (\sigma^i B)_b (\nabla^i \phi)\rangle + \langle \bar{B}_b \bar{B}_a (\sigma^i B)_b B_a (\nabla^i \phi)\rangle\Big)\\
&+ D_8/F_0 \langle \bar{B}_a (\nabla^i \phi) B_a\rangle \langle \bar{B}_b (\sigma^i B)_b\rangle + D_9/F_0 \langle \bar{B}_a B_a (\nabla^i \phi)\rangle \langle \bar{B}_b (\sigma^i B)_b\rangle\\
&+ D_{10}/F_0 \langle \bar{B}_b (\nabla^i \phi)(\sigma^i B)_b\rangle \langle \bar{B}_a B_a\rangle\\
&+ \mathrm{i}\,\epsilon^{ijk} D_{11}/F_0 \langle \bar{B}_a (\sigma^i B)_a (\nabla^k \phi) \bar{B}_b (\sigma^j B)_b\rangle\\
&- \mathrm{i}\,\epsilon^{ijk} D_{12}/F_0\Big(\langle \bar{B}_a (\nabla^k \phi) \bar{B}_b (\sigma^i B)_a (\sigma^j B)_b\rangle - \langle \bar{B}_b \bar{B}_a (\sigma^j B)_b (\nabla^k \phi)(\sigma^i B)_a\rangle\Big)\\
&- \mathrm{i}\,\epsilon^{ijk} D_{13}/F_0 \langle \bar{B}_a \bar{B}_b (\nabla^k \phi)(\sigma^i B)_a (\sigma^j B)_b\rangle - \mathrm{i}\,\epsilon^{ijk} D_{14}/F_0 \langle \bar{B}_a \bar{B}_b (\sigma^i B)_a (\sigma^j B)_b (\nabla^k \phi)\rangle\,,
\end{aligned}
\tag{3.15}
$$

for the processes $BB \to BB\phi$, with two-component spinor indices a and b and 3-vector indices i, j and k. For all possible strangeness sectors $S = -4 \ldots 0$ one obtains in total 14 low-energy constants $D_1 \ldots D_{14}$. The low-energy constant of the corresponding vertex in the nucleonic sector D [133] is related to the LECs above by $D = 4(D_1 - D_3 + D_8 - D_{10})$.

To obtain the 3BF one-meson-exchange diagram, the generic one-meson-exchange diagram in Fig. 3.2(a) has to be evaluated. It involves the baryons i, j, k in the initial state, the baryons l, m, n in the final state and an exchanged meson ϕ. The contact vertex on the right is pictorially separated into two parts to indicate that baryon j–m and k–n are in the same bilinear. The spin spaces corresponding to the baryon bilinears are denoted by A, B, C.

One obtains a generic potential of the form

$$
V = \frac{1}{2F_0^2} \frac{\boldsymbol{\sigma}_A \cdot \boldsymbol{q}_{li}}{\boldsymbol{q}_{li}^2 + M_\phi^2} \Big(N_1 \boldsymbol{\sigma}_C \cdot \boldsymbol{q}_{li} + N_2 \mathrm{i}\,(\boldsymbol{\sigma}_B \times \boldsymbol{\sigma}_C) \cdot \boldsymbol{q}_{li} \Big)\,,
\tag{3.16}
$$

with the momentum transfer $\boldsymbol{q}_{li} = \boldsymbol{p}_l - \boldsymbol{p}_i$ carried by the exchanged meson. The constants N_1 and N_2 are linear combinations of low-energy constants.

The complete one-meson exchange three-baryon potential for the process $B_1 B_2 B_3 \to B_4 B_5 B_6$ is finally obtained by summing up the 36 permutations of initial-state and final-state baryons for a fixed meson and by summing over all mesons $\phi \in \{\pi^0, \pi^+, \pi^-, K^+, K^-, K^0, \bar{K}^0, \eta\}$. As defined before, the baryons B_1, B_2 and B_3 belong to the spin-spaces 1, 2 and 3, respectively.

3.3. Two-meson exchange component

The two-meson exchange diagram of Fig. 3.1 includes the vertices arising from the $BB\phi$ Lagrangian. Furthermore, we need the well-known $\mathcal{O}(q^2)$ meson–baryon (ϕB) Lagrangian [135]. The relevant terms are [136]

$$
\begin{aligned}
\mathscr{L} = {} & b_D \langle \bar{B}\{\chi_+, B\}\rangle + b_F \langle \bar{B}[\chi_+, B]\rangle + b_0 \langle \bar{B} B\rangle \langle \chi_+\rangle\\
&+ b_1 \langle \bar{B}[u^\mu, [u_\mu, B]]\rangle + b_2 \langle \bar{B}\{u^\mu, \{u_\mu, B\}\}\rangle + b_3 \langle \bar{B}\{u^\mu, [u_\mu, B]\}\rangle + b_4 \langle \bar{B} B\rangle \langle u^\mu u_\mu\rangle\\
&+ \mathrm{i} d_1 \langle \bar{B}\{[u^\mu, u^\nu], \sigma_{\mu\nu} B\}\rangle + \mathrm{i} d_2 \langle \bar{B}[[u^\mu, u^\nu], \sigma_{\mu\nu} B]\rangle + \mathrm{i} d_3 \langle \bar{B} u^\mu\rangle \langle u^\nu \sigma_{\mu\nu} B\rangle\,,
\end{aligned}
\tag{3.17}
$$

with $u_\mu = -\frac{1}{F_0}\partial_\mu \phi + \mathcal{O}(\phi^3)$ and $\chi_+ = 2\chi - \frac{1}{4F_0^2}\{\phi, \{\phi, \chi\}\} + \mathcal{O}(\phi^4)$, and χ given in Eq. (2.13). The terms proportional to b_D, b_F, b_0 break explicitly SU(3) flavor symmetry, because of different meson masses $M_K \neq M_\pi$. The LECs of Eq. (3.17) are related to the conventional LECs of the nucleonic sector by [137,138]

$$
\begin{aligned}
c_1 &= \frac{1}{2}(2b_0 + b_D + b_F)\,,\\
c_3 &= b_1 + b_2 + b_3 + 2b_4\,,\\
c_4 &= 4(d_1 + d_2)\,.
\end{aligned}
\tag{3.18}
$$

Note, however, that these are not the matching relations when going from SU(3) to SU(2) but rather the relations that are generated when one compares the dimension-two meson–baryon operators in the two- and the three-flavor representations. The matching relations are discussed in Refs. [137,138].

To obtain the potential of the two-meson exchange diagram of Fig. 3.1, the generic diagram of Fig. 3.2(b) can be considered. It includes the baryons i, j, k in the initial state, the baryons l, m, n in the final state, and two exchanged mesons ϕ_1 and ϕ_2. The spin spaces corresponding to the baryon bilinears are denoted by A, B, C and they are aligned with the three initial baryons. The momentum transfers carried by the virtual mesons are $\boldsymbol{q}_{li} = \boldsymbol{p}_l - \boldsymbol{p}_i$ and $\boldsymbol{q}_{nk} = \boldsymbol{p}_n - \boldsymbol{p}_k$. One obtains the generic transition amplitude

$$V = -\frac{1}{4F_0^4}\frac{\boldsymbol{\sigma}_A\cdot\boldsymbol{q}_{li}\;\boldsymbol{\sigma}_C\cdot\boldsymbol{q}_{nk}}{(\boldsymbol{q}_{li}^2+M_{\phi_1}^2)(\boldsymbol{q}_{nk}^2+M_{\phi_2}^2)}\left(N_1' + N_2'\,\boldsymbol{q}_{li}\cdot\boldsymbol{q}_{nk} + N_3'\,\mathrm{i}\,(\boldsymbol{q}_{li}\times\boldsymbol{q}_{nk})\cdot\boldsymbol{\sigma}_B\right), \tag{3.19}$$

with N_i' linear combinations of the low-energy constants of the three involved vertices. The complete three-body potential for a transition $B_1B_2B_3 \to B_4B_5B_6$ can be calculated by summing up the contributions of all 18 distinguishable Feynman diagrams and by summing over all possible exchanged mesons. If the baryon lines are not in the configuration 1–4, 2–5 and 3–6 additional (negative) spin-exchange operators have to be included.

3.4. ΛNN and NNN three-baryon potentials

In order to give concrete examples, the explicit expressions for the ΛNN three-body potentials in spin-, isospin- and momentum-space are presented for the contact interaction and one- and two-pion exchange contributions [43]. In addition, we provide those for the corresponding NNN forces for the ease of comparison.

3.4.1. Contact interaction

The ΛNN contact interaction is described by the following potential

$$\begin{aligned} V_{\Lambda NN}^{\rm CT} = \;& C_1'\;(\mathbb{1}-\boldsymbol{\sigma}_2\cdot\boldsymbol{\sigma}_3)(3+\boldsymbol{\tau}_2\cdot\boldsymbol{\tau}_3) \\ &+ C_2'\;\boldsymbol{\sigma}_1\cdot(\boldsymbol{\sigma}_2+\boldsymbol{\sigma}_3)\,(\mathbb{1}-\boldsymbol{\tau}_2\cdot\boldsymbol{\tau}_3) \\ &+ C_3'\;(3+\boldsymbol{\sigma}_2\cdot\boldsymbol{\sigma}_3)(\mathbb{1}-\boldsymbol{\tau}_2\cdot\boldsymbol{\tau}_3), \end{aligned} \tag{3.20}$$

where the primed constants are linear combinations of $C_1 \ldots C_{18}$ of Eq. (3.9). The symbols $\boldsymbol{\sigma}$ and $\boldsymbol{\tau}$ denote the usual Pauli matrices in spin and isospin space. The constant C_1' appears only in the transition with total isospin $I = 1$. The constants C_2' and C_3' contribute for total isospin $I = 0$.

For comparison, the NNN contact potential of [133] in its antisymmetrized form is

$$V_{NNN}^{\rm CT} = \frac{1}{2}E\,\mathcal{A}\sum_{j\neq k}\boldsymbol{\tau}_j\cdot\boldsymbol{\tau}_k\,, \tag{3.21}$$

where $\mathcal{A}$ denotes the three-body antisymmetrization operator, $\mathcal{A} = (\mathbb{1}-\mathcal{P}_{12})(\mathbb{1}-\mathcal{P}_{13}-\mathcal{P}_{23})$. Each two-particle exchange operator $\mathcal{P}_{ij} = P_{ij}^{(\sigma)}P_{ij}^{(\tau)}P_{ij}^{(p)}$ is the product of an exchange operator in spin space $P_{ij}^{(\sigma)} = \frac{1}{2}(\mathbb{1}+\boldsymbol{\sigma}_i\cdot\boldsymbol{\sigma}_j)$, in isospin space $P_{ij}^{(\tau)} = \frac{1}{2}(\mathbb{1}+\boldsymbol{\tau}_i\cdot\boldsymbol{\tau}_j)$ and in momentum space $P_{ij}^{(p)}$. However, the latter has no effect here, since the LO NNNN contact potential is momentum-independent.

Note that the NNN force is usually written in terms of the dimensionless coupling $c_E = EF_\pi^4\Lambda_\chi$, where c_E is then in the order of one. Here Λ_χ is the chiral symmetry breaking scale assumed to be of the order of the ρ meson mass, i.e. $\Lambda_\chi \approx 700$ MeV [133].

3.4.2. One-pion exchange

Isospin conservation implies that the $\Lambda\Lambda\pi$ coupling constant is zero. This reduces the number of possible diagrams that can contribute to the ΛNN one-pion exchange three-body potentials. One obtains the following potential

$$\begin{aligned} V_{\Lambda NN}^{\rm OPE} = -\frac{g_A}{2F_0^2}\Bigg(\;& \frac{\boldsymbol{\sigma}_2\cdot\boldsymbol{q}_{52}}{\boldsymbol{q}_{52}^2+M_\pi^2}\boldsymbol{\tau}_2\cdot\boldsymbol{\tau}_3\Big[(D_1'\boldsymbol{\sigma}_1+D_2'\boldsymbol{\sigma}_3)\cdot\boldsymbol{q}_{52}\Big] + \frac{\boldsymbol{\sigma}_3\cdot\boldsymbol{q}_{63}}{\boldsymbol{q}_{63}^2+M_\pi^2}\boldsymbol{\tau}_2\cdot\boldsymbol{\tau}_3\Big[(D_1'\boldsymbol{\sigma}_1+D_2'\boldsymbol{\sigma}_2)\cdot\boldsymbol{q}_{63}\Big] \\ &+ P_{23}^{(\sigma)}P_{23}^{(\tau)}P_{13}^{(\sigma)}\frac{\boldsymbol{\sigma}_2\cdot\boldsymbol{q}_{62}}{\boldsymbol{q}_{62}^2+M_\pi^2}\boldsymbol{\tau}_2\cdot\boldsymbol{\tau}_3\Big[-\frac{D_1'+D_2'}{2}(\boldsymbol{\sigma}_1+\boldsymbol{\sigma}_3)\cdot\boldsymbol{q}_{62} + \frac{D_1'-D_2'}{2}\,\mathrm{i}\,(\boldsymbol{\sigma}_3\times\boldsymbol{\sigma}_1)\cdot\boldsymbol{q}_{62}\Big] \\ &+ P_{23}^{(\sigma)}P_{23}^{(\tau)}P_{12}^{(\sigma)}\frac{\boldsymbol{\sigma}_3\cdot\boldsymbol{q}_{53}}{\boldsymbol{q}_{53}^2+M_\pi^2}\boldsymbol{\tau}_2\cdot\boldsymbol{\tau}_3\Big[-\frac{D_1'+D_2'}{2}(\boldsymbol{\sigma}_1+\boldsymbol{\sigma}_2)\cdot\boldsymbol{q}_{53} - \frac{D_1'-D_2'}{2}\,\mathrm{i}\,(\boldsymbol{\sigma}_1\times\boldsymbol{\sigma}_2)\cdot\boldsymbol{q}_{53}\Big]\;\Bigg), \end{aligned} \tag{3.22}$$

with only two constants D_1' and D_2', which are linear combinations of the constants $D_1 \ldots D_{14}$. Exchange operators in spin space $P_{ij}^{(\sigma)} = \frac{1}{2}(\mathbb{1}+\boldsymbol{\sigma}_i\cdot\boldsymbol{\sigma}_j)$ and in isospin space $P_{ij}^{(\tau)} = \frac{1}{2}(\mathbb{1}+\boldsymbol{\tau}_i\cdot\boldsymbol{\tau}_j)$ have been introduced.

The corresponding result for the NNN potential is equal to the antisymmetrization of the expression given in [133],

$$V_{NNN}^{\rm OPE} = -\frac{g_A}{8F_\pi^2}D\mathcal{A}\sum_{i\neq j\neq k}\frac{\boldsymbol{\sigma}_j\cdot\boldsymbol{q}_j}{\boldsymbol{q}_j^2+m_\pi^2}\boldsymbol{\tau}_i\cdot\boldsymbol{\tau}_j\;\boldsymbol{\sigma}_i\cdot\boldsymbol{q}_j\,, \tag{3.23}$$

inserting the momentum transfers $\boldsymbol{q}_1 = \boldsymbol{q}_{41} = \boldsymbol{p}_4 - \boldsymbol{p}_1$, $\boldsymbol{q}_2 = \boldsymbol{q}_{52} = \boldsymbol{p}_5 - \boldsymbol{p}_2$, $\boldsymbol{q}_3 = \boldsymbol{q}_{63} = \boldsymbol{p}_6 - \boldsymbol{p}_3$. In this case the momentum part of each two-body exchange operator, $P_{ij}^{(p)}$, exchanges also the momenta in the final state.[3]

[3] For example, $P_{23}^{(p)}$ leads to the replacements $q_{41}, q_{52}, q_{63} \to q_{41}, q_{62}, q_{53}$ and $P_{12}^{(p)}P_{13}^{(p)}$ to $q_{41}, q_{52}, q_{63} \to q_{61}, q_{42}, q_{53}$.

Also here it is standard to rewrite the NNN forces in terms of dimensionless couplings, namely in the form $c_D = DF_\pi^2 \Lambda_\chi$ [133].

3.4.3. Two-pion exchange

The ΛNN three-body interaction generated by two-pion exchange is given by

$$V_{\Lambda NN}^{\rm TPE} = \frac{g_A^2}{3F_0^4} \frac{\boldsymbol{\sigma}_3 \cdot \boldsymbol{q}_{63}\ \boldsymbol{\sigma}_2 \cdot \boldsymbol{q}_{52}}{(\boldsymbol{q}_{63}^2 + M_\pi^2)(\boldsymbol{q}_{52}^2 + M_\pi^2)} \boldsymbol{\tau}_2 \cdot \boldsymbol{\tau}_3 \left(-(3b_0 + b_D) M_\pi^2 + (2b_2 + 3b_4)\, \boldsymbol{q}_{63} \cdot \boldsymbol{q}_{52} \right)$$
$$- P_{23}^{(\sigma)} P_{23}^{(\tau)} \frac{g_A^2}{3F_0^4} \frac{\boldsymbol{\sigma}_3 \cdot \boldsymbol{q}_{53}\ \boldsymbol{\sigma}_2 \cdot \boldsymbol{q}_{62}}{(\boldsymbol{q}_{53}^2 + M_\pi^2)(\boldsymbol{q}_{62}^2 + M_\pi^2)} \boldsymbol{\tau}_2 \cdot \boldsymbol{\tau}_3 \left(-(3b_0 + b_D) M_\pi^2 + (2b_2 + 3b_4)\, \boldsymbol{q}_{53} \cdot \boldsymbol{q}_{62} \right). \tag{3.24}$$

Due to the vanishing of the $\Lambda\Lambda\pi$ vertex, only those two diagrams contribute, where the (final and initial) Λ hyperon are attached to the central baryon line, see Fig. 3.2(b).

Regarding the NNN case the result is equal to the antisymmetrization of the expression given in [133]:

$$V_{\rm NNN}^{\rm TPE} = \frac{g_A^2}{8F_\pi^2} \mathcal{A} \sum_{i \neq j \neq k} \frac{\boldsymbol{\sigma}_i \cdot \boldsymbol{q}_i\ \boldsymbol{\sigma}_j \cdot \boldsymbol{q}_j}{(\boldsymbol{q}_i^2 + M_\pi^2)(\boldsymbol{q}_j^2 + M_\pi^2)} F_{ijk}^{\alpha\beta} \tau_i^\alpha \tau_j^\beta, \tag{3.25}$$

with

$$F_{ijk}^{\alpha\beta} = \frac{\delta^{\alpha\beta}}{F_\pi^2} (-4c_1 M_\pi^2 + 2c_3 \boldsymbol{q}_i \cdot \boldsymbol{q}_j) + \sum_\gamma \frac{c_4}{F_\pi^2} \epsilon^{\alpha\beta\gamma} \tau_k^\gamma\ \boldsymbol{\sigma}_k \cdot (\boldsymbol{q}_i \times \boldsymbol{q}_j), \tag{3.26}$$

where the c_i are given in Eq. (3.18).

3.5. Three-baryon force through decuplet saturation

As should be clear from the discussion above, the number of LECs of the leading YNN 3BF is by far too large as compared to the available experimental constraints from light hypernuclei which could be used to pin them down. Of course, the rather large number of unknown LECs presented in the previous subsections is related to the whole multitude of three-baryon multiplets, with strangeness S ranging from 0 to −6. But the number is not that much reduced if we restrict ourselves to the S=−1 sector, i.e. to ΛNN and ΣNN. Even if one considers the ΛNN 3BF alone (and disregards K and η exchanges), as done in Section 3.4, one would have to deal with 5 LECs (3 for the contact terms and 2 from the one-pion exchange 3BF) to be compared with only 2 LECs in the NNN case.

Varying all LECs or setting some of them arbitrarily to zero is neither practical nor a sound procedure for concrete few-body calculations. Therefore, in a first application of the chiral 3BFs in studying hypernuclei [49] a different strategy was followed. In that work, the mechanism of resonance saturation via decuplet baryons (Δ, Σ^*, Ξ^*) was exploited to estimate the strengths of chiral 3BFs [132,139,140]. Moreover, meson-exchange contributions were restricted to those from pion-exchange, in line with the SMS YN potential [42] where two-meson contributions involving the K and/or η were neglected. As already discussed at the end of Section 2.1, the contributions from K and η exchanges should be substantially suppressed, because of their larger mass, and possible residual effects can be well represented by the YNN contact interaction.

The utilization of decuplet saturation is well motivated by corresponding observations/studies in the purely nucleonic sector [141]. There, some of the a priori unknown LECs turned out to be fairly large compared to their order of magnitude as expected from the hierarchy of nuclear forces in chiral EFT, when fitted to, say, NN scattering data and 3N observables such as 3-body binding energies [133]. The physical origin of this behavior is obviously the strong coupling of the π-system to the low-lying $\Delta(1232)$-resonance. It is therefore natural to include the $\Delta(1232)$-isobar as an explicit degree of freedom in the chiral Lagrangian (see [141–144]). The small mass difference between nucleons and Δ (293 MeV) introduces a small scale, which can be included consistently in the chiral power counting scheme and the hierarchy of nuclear forces. The dominant parts of the three-nucleon interaction mediated by two-pion exchange at N2LO are then promoted to NLO through the Δ contributions. The appearance of the inverse mass splitting explains the large numerical values of the corresponding LECs [74,141,145].

In SU(3) χEFT the situation is similar. In systems with strangeness $S = -1$ like ΛNN, resonances such as the $\Sigma^*(1385)$ play a comparable role to that of the Δ in the NNN system. The small decuplet–octet mass splitting (in the chiral limit), $\tilde{\Delta} := m_{10} - m_8$, is counted together with external momenta and meson masses as $\mathcal{O}(q)$ and, thus, parts of the N2LO three-baryon interaction are promoted to NLO by the explicit inclusion of the baryon decuplet, as illustrated in Fig. 3.3. Therefore, in principle, one could incorporate those contributions to the three-baryon interaction already together with the NLO YN interaction. Note that in the nucleonic sector, only the two-pion exchange diagram with an intermediate Δ-isobar is allowed. Other diagrams are forbidden due to the Pauli principle, as we will show later. For three flavors more particles are involved and, in general, also the other diagrams (contact and one-meson exchange) with intermediate decuplet baryons in Fig. 3.3 appear. In the following we review the estimation of these LECs by resonance saturation which has been worked out in [132].

The LO non-relativistic interaction Lagrangian between octet and decuplet baryons (see, e.g., [147]) is

$$\mathscr{L} = \frac{C}{F_0} \sum_{a,b,c,d,e=1}^{3} \epsilon_{abc} \left(\bar{T}_{ade} \boldsymbol{S}^\dagger \cdot \left(\boldsymbol{\nabla} \phi_{db} \right) B_{ec} + \bar{B}_{ce} \boldsymbol{S} \cdot \left(\boldsymbol{\nabla} \phi_{bd} \right) T_{ade} \right), \tag{3.27}$$

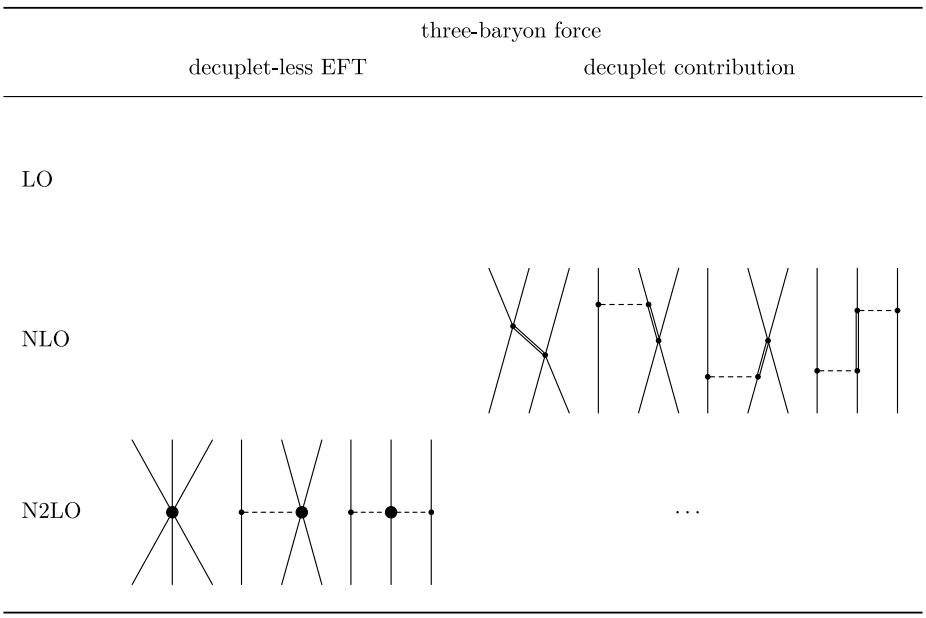

Fig. 3.3. Hierarchy of three-baryon forces with explicit introduction of the baryon decuplet (represented by double lines) [132,146].

where the decuplet baryons are represented by the totally symmetric three-index tensor T, see [132]. At this order only a single LEC C appears. Typically the (large-N_c) value $C = \frac{3}{4} g_A \approx 1$ is used, as it leads to a decay width $\Gamma(\Delta \to \pi N) = 110.6$ MeV that is in good agreement with the empirical value of $\Gamma(\Delta \to \pi N) = (115 \pm 5)$ MeV [143]. The spin $\frac{1}{2}$ to $\frac{3}{2}$ transition operators $\boldsymbol{S}$ connect the two-component spinors of octet baryons with the four-component spinors of decuplet baryons (see e.g., [148]). In their explicit form they are given as 2×4 transition matrices

$$
\begin{aligned}
S_1 &= \begin{pmatrix} -\frac{1}{\sqrt{2}} & 0 & \frac{1}{\sqrt{6}} & 0 \\ 0 & -\frac{1}{\sqrt{6}} & 0 & \frac{1}{\sqrt{2}} \end{pmatrix}, \\
S_2 &= \begin{pmatrix} -\frac{i}{\sqrt{2}} & 0 & -\frac{i}{\sqrt{6}} & 0 \\ 0 & -\frac{i}{\sqrt{6}} & 0 & -\frac{i}{\sqrt{2}} \end{pmatrix}, \\
S_3 &= \begin{pmatrix} 0 & \sqrt{\frac{2}{3}} & 0 & 0 \\ 0 & 0 & \sqrt{\frac{2}{3}} & 0 \end{pmatrix}.
\end{aligned}
\tag{3.28}
$$

These operators fulfill the relation $S_i {S_j}^\dagger = \frac{1}{3}(2\delta_{ij} - \mathrm{i}\epsilon_{ijk}\sigma_k)$.

A non-relativistic $B^* BBB$ Lagrangian with a minimal set of terms is given by [132]:

$$
\begin{aligned}
\mathscr{L} = \quad & H_1 \sum_{\substack{a,b,c,\\ d,e,f=1}}^{3} \epsilon_{abc} \left[\left(\bar{T}_{ade} \boldsymbol{S}^\dagger B_{db} \right) \cdot \left(\bar{B}_{fc} \boldsymbol{\sigma} B_{ef} \right) + \left(\bar{B}_{bd} \boldsymbol{S}\, T_{ade} \right) \cdot \left(\bar{B}_{fe} \boldsymbol{\sigma} B_{cf} \right) \right] \\
& + H_2 \sum_{\substack{a,b,c,\\ d,e,f=1}}^{3} \epsilon_{abc} \left[\left(\bar{T}_{ade} \boldsymbol{S}^\dagger B_{fb} \right) \cdot \left(\bar{B}_{dc} \boldsymbol{\sigma} B_{ef} \right) + \left(\bar{B}_{bf} \boldsymbol{S}\, T_{ade} \right) \cdot \left(\bar{B}_{fe} \boldsymbol{\sigma} B_{cd} \right) \right],
\end{aligned}
\tag{3.29}
$$

with the LECs H_1 and H_2. Again one can employ group theory to justify the number of two constants for a transition $BB \to B^* B$. In flavor space the two initial octet baryons form the tensor product $\mathbf{8} \otimes \mathbf{8}$, and in spin space they form the product $\mathbf{2} \otimes \mathbf{2}$. These tensor products can be decomposed into irreducible representations:

$$
\begin{aligned}
\mathbf{8} \otimes \mathbf{8} &= \underbrace{\mathbf{27} \oplus \mathbf{8}_s \oplus \mathbf{1}}_{\text{symmetric}} \oplus \underbrace{\mathbf{10} \oplus \overline{\mathbf{10}} \oplus \mathbf{8}_a}_{\text{antisymmetric}}, \\
\mathbf{2} \otimes \mathbf{2} &= \mathbf{1}_a \oplus \mathbf{3}_s .
\end{aligned}
\tag{3.30}
$$

In the final state, having a decuplet and an octet baryon, the situation is similar:

$$
\mathbf{10} \otimes \mathbf{8} = \mathbf{35} \oplus \mathbf{27} \oplus \mathbf{10} \oplus \mathbf{8},
$$

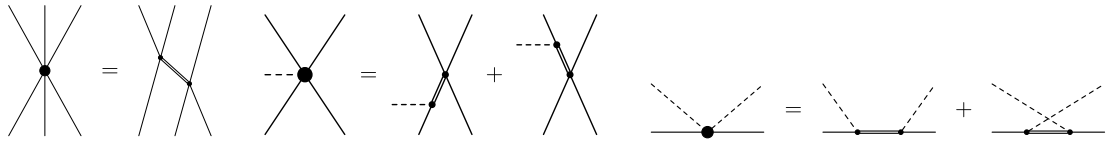

(a) Saturation of the six-baryon contact interaction

(b) Saturation of the $BB \to BB\phi$ vertex

(c) Saturation of the NLO baryon–meson vertex

Fig. 3.4. Saturation via decuplet resonances.

$$\mathbf{4} \otimes \mathbf{2} = \mathbf{3} \oplus \mathbf{5}\,. \tag{3.31}$$

As seen in the previous sections, at LO only S-wave transitions occur, as no momenta are involved. Transitions are only allowed between the same types of irreducible (flavor and spin) representations. Therefore, in spin space the representation **3** has to be chosen. Because of the Pauli principle in the initial state, the symmetric **3** in spin space combines with the antisymmetric representations $\mathbf{10}, \overline{\mathbf{10}}, \mathbf{8}_a$ in flavor space. But only **10** and $\mathbf{8}_a$ have a counterpart in the final state flavor space. This number of two allowed transitions matches the number of two LECs in the minimal Lagrangian. Another interesting observation can be made from Eqs. (3.30) and (3.31). For NN states only the representations **27** and $\overline{\mathbf{10}}$ can contribute. But these representations combine either with the wrong spin, or have no counterpart in the final state. Therefore, NN→ΔN transitions in S-waves are not allowed because of the Pauli principle.

Having the above two interaction types at hand, one can estimate the low-energy constants of the leading three-baryon interaction by decuplet saturation using the diagrams shown in Fig. 3.3. At this order, where no loops are involved, one just needs to evaluate the diagrams with an intermediate decuplet baryon and the diagrams without decuplet baryons and compare them with each other.

In order to estimate the LECs of the six-baryon contact Lagrangian of Eq. (3.9), one can consider the process $B_1 B_2 B_3 \to B_4 B_5 B_6$ as depicted in Fig. 3.4(a). The left side of Fig. 3.4(a) has already been introduced in the previous subsection and can be obtained by performing all 36 Wick contractions. For the diagrams on the right side of Fig. 3.4(a) the procedure is similar. After summing over all intermediate decuplet baryons B^*, the full three-body potential of all possible combinations of baryons on the left side of Fig. 3.4(a) can be compared with the ones on the right side. In the end the 18 LECs of the six-baryon contact Lagrangian $C_1, \ldots, C_{18}$ of Eq. (3.9) can be expressed as linear combinations of the combinations H_1^2, H_2^2 and $H_1 H_2$ and are proportional to the inverse average decuplet–octet baryon mass splitting $1/\tilde{\Delta}$ [132].

Since we are at LO only, tree-level diagrams are involved and we can estimate the LECs of the one-meson-exchange part of the 3BFs already on the level of the vertices, as depicted in Fig. 3.4(b). We consider the transition matrix elements of the process $B_1 B_2 \to B_3 B_4 \phi$ and start with the left side of Fig. 3.4(b). After doing all possible Wick contractions, summing over all intermediate decuplet baryons, and comparing the left side of Fig. 3.4(b) with the right hand side for all combinations of baryons and mesons, the LECs can be estimated. The LECs of the minimal non-relativistic chiral Lagrangian for the four-baryon vertex including one meson of Eq. (3.15) $D_1, \ldots, D_{14}$ are then proportional to $C/\tilde{\Delta}$ and to linear combinations of H_1 and H_2 [132].

The last class of diagrams is the three-body interaction with two-meson exchange. As done for the one-meson exchange, the unknown LECs can be saturated directly on the level of the vertex and one can consider the process $B_1 \phi_1 \to B_2 \phi_2$ as shown in Fig. 3.4(c). A direct comparison of the transition matrix elements for all combinations of baryons and mesons after summing over all intermediate decuplet baryons B^* leads to the following contributions to the LECs of the meson–baryon Lagrangian in Eq. ((3.17)):

$$\begin{aligned}
&b_D = 0\,,\ b_F = 0\,,\ b_0 = 0\,,\\
&b_1 = \frac{7C^2}{36\tilde{\Delta}}\,,\ b_2 = \frac{C^2}{4\tilde{\Delta}}\,,\ b_3 = -\frac{C^2}{3\tilde{\Delta}}\,,\ b_4 = -\frac{C^2}{2\tilde{\Delta}}\,,\\
&d_1 = \frac{C^2}{12\tilde{\Delta}}\,,\ d_2 = \frac{C^2}{36\tilde{\Delta}}\,,\ d_3 = -\frac{C^2}{6\tilde{\Delta}}\,,
\end{aligned} \tag{3.32}$$

These findings are consistent with the $\Delta(1232)$ contribution to the LECs c_1, c_3, c_4 (see Eq. (3.18)) in the nucleonic sector [141]:

$$c_1 = 0\,, \qquad c_3 = -2c_4 = -\frac{g_A^2}{2\tilde{\Delta}}\,. \tag{3.33}$$

Applying decuplet saturation to the ΛNN interaction (contact interaction, one-pion and two-pion exchange) of Section 3.4 one obtains:

$$\begin{aligned}
&C_1' = C_3' = \frac{(H_1 + 3H_2)^2}{72\tilde{\Delta}}\,, \quad C_2' = 0\,,\\
&D_1' = 0\,, \quad D_2' = \frac{2C(H_1 + 3H_2)}{9\tilde{\Delta}}\,,\\
&3b_0 + b_D = 0\,, \quad 2b_2 + 3b_4 = -\frac{C^2}{\tilde{\Delta}}\,.
\end{aligned} \tag{3.34}$$

Evidently, there is only one unknown constant here, namely the combination $H_1 + 3H_2$. It is also interesting to see that the sign of the constants C_i' for the contact interaction is already fixed, independently of the values of the two LECs H_1 and H_2. The fact that it is positive implies that the ΛN 3BF from the contact interaction is always repulsive. Estimates for the order of magnitude of the parameters H_1 and H_2, based on dimensional scaling arguments, have been given in Ref. [132]. These suggest $H_1 \approx H_2 \approx \pm 1/F_0^2$. Those estimates can be compared with the ones for the NNN forces, $E = 2(C_4 - C_9) = c_E/(F_\pi^4 \Lambda_\chi)$ and $D = 4(D_1 - D_3 + D_8 - D_{10}) = c_D/(F_\pi^2 \Lambda_\chi)$ where c_E and c_D are in the order of one. Obviously, the decuplet saturation mechanism promotes the constants C_i and D_i to $\mathcal{O}(1/(F_\pi^4 \tilde{\Delta}))$ and $\mathcal{O}(1/(F_\pi^2 \tilde{\Delta}))$, respectively.

4. Faddeev–Yakubovsky approach

In order to test and improve the two- and three-baryon interactions, solutions of the Schrödinger equation for few-baryon systems are helpful. Properties like the separation energies of hypernuclear systems do not only reflect the overall strength of the interactions but they are also sensitive to their angular and spin dependence and even to their isospin or charge dependence. Various methods exist that allow one to solve the Schrödinger equation for realistic BB interactions. The probably most direct way consists in solving Faddeev or Yakubovsky equations in momentum space. This approach is very flexible with respect to the interaction used and gives high accuracy solutions even for interactions that induce strong correlations between the baryons. The $A = 3$ Faddeev equations for bound states of the hypertriton have been formulated in [29,30] taking Λ-Σ conversion into account. This method has been applied to the phenomenological interactions of the Nijmegen [13,14] and Jülich [17,18] groups and also to the chiral interactions discussed before. Importantly, it was realized early on [149,150] that the hypertriton binding energy depends very sensitively on the ΛN interaction in the $^1S_0$ channel. Therefore, the spin dependence of the YN interactions is usually adjusted to reproduce the hypertriton binding energy. The Faddeev equations of the ΛNN system have also been implemented for scattering states. They were applied to Λ-d scattering by Kohno and Kamada [151] using realistic YN and NN forces. The possibly earliest example of a Λ-d calculation within a Faddeev-type approach has been reported already in 1965 [152]. For references to further works see [153].

Extending to $A = 4$, the Schrödinger equation can be rewritten in a set of Yakubovsky equations. For the strangeness $S = -1$ hypernuclei ${}^4_\Lambda$He and ${}^4_\Lambda$H, one finds a set of five Yakubovsky equations for five independent Yakubovsky components (see below). The equations were likewise solved for the phenomenological interactions of the Nijmegen und Jülich groups [31] and for chiral interactions in LO [154], NLO [40,41] and N2LO [42]. It turns out that the predictions strongly depend on the interaction and even the regulator used. The older models of the Jülich group result in the wrong ordering of the 0^+ and 1^+ states. Some of the Nijmegen interactions lead to an almost unbound 1^+ state. The separation energies for these hypernuclei are significantly influenced by off-shell properties of the YN interactions, and specifically by the strength of the Λ-Σ conversion. As has been discussed in [41], such properties of the YN interaction are linked to corresponding contributions of 3BFs that have usually not been taken into account. Therefore, the deviations of the different interactions can be explained by the incompleteness of the underlying Hamiltonian. We discuss results including such 3BFs later in Section 5.5.

An issue practically unaffected by the problem of missing 3BFs are predictions for the charge-symmetry breaking (CSB) of the $A = 4$ hypernuclei. Experiments suggest that the difference of the Λ-separation energies is quite large, of the order of 200–300 keV and strongly depend on the spin of the nucleus. These values could not be explained by the phenomenological models [31]. We will come back to this issue in the subsection of CSB in the context of chiral interactions that provide much more freedom to determine the CSB contributions.

In the following, we will start with a brief derivation of the pertinent equations.

4.1. Derivation of the Yakubovsky equations

The aim is to obtain solution of the Schrödinger equation for a four-baryon bound state in momentum space. Using momentum space naturally allows for the application of non-local interactions. For a bound state, it is also simple to use long-ranged interactions like the Coulomb force. Therefore, this method has been used regularly to obtain high accuracy solutions for few-baryon problems [29,31,155,156]. Practical calculations show that the few-baryon wave functions converge only slowly with respect to a partial wave decomposition although the interactions themselves usually only require small angular momenta for an accurate representation. This is due to the need to also represent correlations of the baryon pairs in Jacobi coordinates that to do not single out these pairs. This problem can be tamed by rewriting the Schrödinger equation into Faddeev or Yakubovsky equations. Different Faddeev and Yakubovsky components then represent the various correlations efficiently and lead to an improved convergence with respect to partial waves.

We start with the Schrödinger equation for a system of three nucleons and a hyperon with pair interactions V_{ij}, 3BFs V_{ijk} and, to be most general, with the four-baryon force (4BF) V_{1234}

$$\left(E - H_0\right)|\Psi\rangle = \sum_{i<j} V_{ij}\ |\Psi\rangle + \sum_{i<j<k} V_{ijk}\ |\Psi\rangle + V_{1234}\ |\Psi\rangle\ . \tag{4.1}$$

The indices $i, j, k = 1, \ldots, 3$ thereby refer to the nucleons and 4 to the hyperon (Λ or Σ). H_0 is the intrinsic kinetic energy of the four-baryon system and E the energy of the system. Note that H_0 also includes the rest masses of the baryons. Usually an overall shift of the energy is applied so that $E = 0$ corresponds to the mass of the baryons in the lightest particle channel involved. When Λ-Σ conversion is included, the kinetic energy of the Σ channel includes the mass difference of the Λ and Σ. In order to define Faddeev components in presence of the three-baryon interactions, we split each of them into three different parts

$$V_{ijk} = V_{ijk}^{(i)} + V_{ijk}^{(j)} + V_{ijk}^{(k)} \tag{4.2}$$

Table 4.1
Connection between the different Yakubovsky components. The transpositions have to be applied to the Yakubovsky components in the first row.

	$\psi_{1A}=\psi_{(12)3,4}$	$\psi_{1B}=\psi_{(12)4,3}$	$\psi_{1C}=\psi_{(14)2,3}$	$\psi_{2A}=\psi_{(12)34}$	$\psi_{2B}=\psi_{(34)12}$
$\psi_{(12)3,4}$	1	–	–	–	–
$\psi_{(23)1,4}$	$P_{12}P_{23}$	–	–	–	–
$\psi_{(31)2,4}$	$P_{13}P_{23}$	–	–	–	–
$\psi_{(12)4,3}$	–	1	–	–	–
$\psi_{(23)4,1}$	–	$P_{12}P_{23}$	–	–	–
$\psi_{(31)4,2}$	–	$P_{13}P_{23}$	–	–	–
$\psi_{(14)2,3}$	–	–	1	–	–
$\psi_{(24)3,1}$	–	–	$P_{12}P_{23}$	–	–
$\psi_{(34)1,2}$	–	–	$P_{12}P_{13}$	–	–
$\psi_{(14)3,2}$	–	–	$-P_{23}$	–	–
$\psi_{(34)2,1}$	–	–	$-P_{13}$	–	–
$\psi_{(24)1,3}$	–	–	$-P_{12}$	–	–
$\psi_{(12)34}$	–	–	–	1	–
$\psi_{(23)14}$	–	–	–	$P_{12}P_{23}$	–
$\psi_{(31)24}$	–	–	–	$P_{13}P_{23}$	–
$\psi_{(14)23}$	–	–	–	–	$P_{12}P_{23}$
$\psi_{(24)31}$	–	–	–	–	$P_{13}P_{23}$
$\psi_{(34)12}$	–	–	–	–	1

such that the interaction is symmetrical under the exchange of two nucleons ij in $V^{(k)}_{ijk}$. For three-nucleon forces (3NFs), such a decomposition is usually already done when generating the interactions. For the YNN forces, each of the parts can be defined as $V^{(k)}_{ijk} = 1/3\ V_{ijk}$. Similarly, we decompose the 4BF into 12 components $V^{(ij)k,l}_{1234}$ which are also symmetric under the exchange of particles i and j

$$V_{1234} = V^{(12)3,4}_{1234} + V^{(12)4,3}_{1234} + V^{(23)1,4}_{1234} + V^{(23)4,1}_{1234} + V^{(31)2,4}_{1234} + V^{(31)4,2}_{1234} + V^{(14)2,3}_{1234} + V^{(14)3,2}_{1234} + V^{(24)3,1}_{1234} + V^{(24)1,3}_{1234} + V^{(34)1,2}_{1234} + V^{(34)2,1}_{1234} \ . \quad (4.3)$$

A possible decomposition is just $V^{(ij)k,l}_{1234} = \frac{1}{12} V_{1234}$. With this definition, one can define Faddeev components

$$|\psi_{ij}\rangle = G_0 \ \left(V_{ij} + V^{(k)}_{ijk} + V^{(l)}_{ijl} + V^{(ij)k,l}_{1234} + V^{(ij)l,k}_{1234} \right) |\Psi\rangle \quad (4.4)$$

where $G_0 = \left(E - H_0\right)^{-1}$. This definition ensures that

$$|\Psi\rangle = \sum_{i<j} |\psi_{ij}\rangle \quad (4.5)$$

and that the Faddeev components fulfill the Faddeev equations

$$|\psi_{ij}\rangle = G_0\, t_{ij} \left(|\Psi\rangle - |\psi_{ij}\rangle \right) + \left(1 + G_0\, t_{ij}\right)\ G_0 \ \left(V^{(k)}_{ijk} + V^{(l)}_{ijl} + V^{(ij)k,l}_{1234} + V^{(ij)l,k}_{1234} \right) |\Psi\rangle \ . \quad (4.6)$$

For the Faddeev equations, we introduced the two-baryon off-shell t-matrices t_{ij} that are solutions of the Lippmann–Schwinger equations

$$t_{ij} = V_{ij} + V_{ij}\, G_0\, t_{ij} \ . \quad (4.7)$$

Now we are ready to further decompose the Faddeev components into Yakubovsky components

$$|\psi_{ij}\rangle = |\psi_{(ij)k,l}\rangle + |\psi_{(ij)l,k}\rangle + |\psi_{(ij)kl}\rangle \quad (4.8)$$

defined by

$$\begin{aligned} |\psi_{(ij)k,l}\rangle &= G_0\, t_{ij} \left(|\psi_{ik}\rangle + |\psi_{jk}\rangle \right) + \left(1 + G_0\, t_{ij}\right)\ G_0 \ \left(V^{(k)}_{ijk} + V^{(ij)k,l}_{1234} \right) |\Psi\rangle \\ |\psi_{(ij)kl}\rangle &= G_0\, t_{ij}\, |\psi_{kl}\rangle \ . \end{aligned} \quad (4.9)$$

Inserting the decomposition of the Faddeev components leads to the set of Yakubovsky equations that we use for bound state calculations[4]

$$\begin{aligned} |\psi_{(ij)k,l}\rangle &= G_0\, t_{ij} \left(|\psi_{(ik)j,l}\rangle + |\psi_{(ik)l,j}\rangle + |\psi_{(ik)jl}\rangle + |\psi_{(jk)i,l}\rangle + |\psi_{(jk)l,i}\rangle + |\psi_{(jk)il}\rangle \right) \\ &\quad + \left(1 + G_0\, t_{ij}\right)\ G_0 \ \left(V^{(k)}_{ijk} + V^{(ij)k,l}_{1234} \right) |\Psi\rangle \\ |\psi_{(ij)kl}\rangle &= G_0\, t_{ij} \left(|\psi_{(kl)i,j}\rangle + |\psi_{(kl)j,i}\rangle + |\psi_{(kl)ij}\rangle \right) \ . \end{aligned} \quad (4.10)$$

[4] Note that these equations are still not connected when iterated. For a scattering problem, a resummation of parts involving connected clusters is necessary.

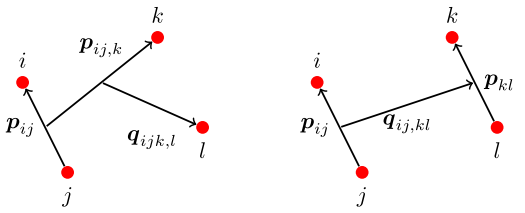

Fig. 4.1. "3+1" and "2+2" Jacobi coordinates to represent Yakubovsky components.

So far, we have not made use of the antisymmetry of the wave function under permutation of the three nucleons. Introducing the permutation operators P_{ij} that commute the momenta and quantum numbers of the ith and jth nucleon, we can relate the 18 different Yakubovsky components to each other leading to a set of five independent Yakubovsky components fulfilling a set of five Yakubovsky equations. The relation of the different Yakubovsky components is shown in Table 4.1 and the resulting set of equations reads

$$\begin{aligned}
|\psi_{1A}\rangle &= |\psi_{(12)3,4}\rangle = G_0\, t_{12}\, P\, \left(|\psi_{1A}\rangle + |\psi_{1B}\rangle + |\psi_{2A}\rangle\right) + \left(1 + G_0\, t_{12}\right)\, G_0\, \left(V^{(3)}_{123} + V^{(12)3,4}_{1234}\right) |\Psi\rangle \\
|\psi_{1B}\rangle &= |\psi_{(12)4,3}\rangle = G_0\, t_{12}\, \left(\left(1 - P_{12}\right)\left(1 - P_{23}\right)|\psi_{1C}\rangle + P\,|\psi_{2B}\rangle\right) + \left(1 + G_0\, t_{12}\right)\, G_0\, \left(V^{(4)}_{124} + V^{(12)4,3}_{1234}\right) |\Psi\rangle \\
|\psi_{1C}\rangle &= |\psi_{(14)2,3}\rangle = G_0\, t_{14}\, \left(|\psi_{1A}\rangle + |\psi_{1B}\rangle + P_{12}\left(P_{23} - 1\right)\,|\psi_{1C}\rangle + |\psi_{2A}\rangle + P_{13}P_{23}\,|\psi_{2B}\rangle\right) \\
&\qquad + \left(1 + G_0\, t_{14}\right)\, G_0\, \left(V^{(2)}_{124} + V^{(14)2,3}_{1234}\right) |\Psi\rangle \\
|\psi_{2A}\rangle &= |\psi_{(12)34}\rangle = G_0\, t_{12}\, \left(\left(P_{12} - 1\right) P_{13}\,|\psi_{1C}\rangle + |\psi_{2B}\rangle\right) \\
|\psi_{2B}\rangle &= |\psi_{(34)12}\rangle = G_0\, t_{34}\, \left(|\psi_{1A}\rangle + |\psi_{1B}\rangle + |\psi_{2A}\rangle\right)
\end{aligned} \tag{4.11}$$

where the combination of permutation operators $P = P_{12}P_{23} + P_{13}P_{23}$ was introduced. Using Eqs. (4.5) and (4.8), the wave function is the sum of all Yakubovsky components which can be simplified to

$$|\Psi\rangle = (1 + P)\left(|\psi_{1A}\rangle + |\psi_{1B}\rangle + |\psi_{2A}\rangle + |\psi_{2B}\rangle\right) + \left(1 - P_{12}\right)(1 + P)\,|\psi_{1C}\rangle \tag{4.12}$$

In order to fully exploit that the Yakubovsky components converge faster than the wave functions, we need to define different sets of Jacobi coordinates for each Yakubovsky component. The natural coordinates for $|\psi_{1A}\rangle$, $|\psi_{1B}\rangle$ and $|\psi_{1C}\rangle$ are of the "3+1" type shown in Fig. 4.1, the ones for $|\psi_{2A}\rangle$ and $|\psi_{2B}\rangle$ are of the "2+2" type. Thereby, the particles i, j, k and l are selected such that they single out the same pairs and triplets as the Yakubovsky component. The corresponding momenta are define as

$$\begin{aligned}
\boldsymbol{p}_{ij} &= \frac{1}{m_i + m_j}\left(m_j\,\boldsymbol{k}_i - m_i\,\boldsymbol{k}_j\right) \\
\boldsymbol{p}_{ij,k} &= \frac{1}{m_i + m_j + m_k}\left(\left(m_i + m_j\right)\boldsymbol{k}_k - m_k\,\left(\boldsymbol{k}_i + \boldsymbol{k}_j\right)\right) \\
\boldsymbol{q}_{ijk,l} &= \frac{1}{m_i + m_j + m_k + m_l}\left(\left(m_i + m_j + m_k\right)\boldsymbol{k}_l - m_l\,\left(\boldsymbol{k}_i + \boldsymbol{k}_j + \boldsymbol{k}_k\right)\right) \\
\boldsymbol{p}_{kl} &= \frac{1}{m_k + m_l}\left(m_l\,\boldsymbol{k}_k - m_k\,\boldsymbol{k}_l\right) \\
\boldsymbol{q}_{ij,kl} &= \frac{1}{m_i + m_j + m_k + m_l}\left(\left(m_k + m_l\right)\,\left(\boldsymbol{k}_i + \boldsymbol{k}_j\right) - \left(m_i + m_j\right)\,\left(\boldsymbol{k}_k + \boldsymbol{k}_l\right)\right)
\end{aligned} \tag{4.13}$$

For a more efficient representation, we expand the angular dependencies in orbital angular momenta which are then coupled with the spins to a fixed total angular momentum. The "3+1" and "2+2" basis states then read

$$\begin{aligned}
|(ij)k,l\rangle &= |p_{ij}p_{ij,k}q_{ijk,l}\left[\left(\left(l_{ij}s_{ij}\right)j_{ij}\,\left(l_k 1/2\right)I_k\right)j_k\,\left(l_l 1/2\right)I_l\right]J\,\left[\left(\left(t_i t_j\right)t_{ij}t_k\right)\tau_k\right]TM_T\rangle\,, \\
|(ij)kl\rangle &= |p_{ij}p_{kl}q_{ij,kl}\left[\left(\left(l_{ij}s_{ij}\right)j_{ij}\lambda\right)I\,\left(\left(l_{kl}s_{kl}\right)j_{kl}\right)\right]J\,\left[\left(\left(t_i t_j\right)t_{ij}\,\left(t_k t_l\right)t_{kl}\right)\right]TM_T\rangle\,.
\end{aligned} \tag{4.14}$$

p_{ij}, $p_{ij,k}$, $q_{ijk,l}$, p_{kl} and $q_{ij,kl}$ are the magnitude of the momenta. Their angular dependence is expanded in orbital angular momenta l_{ij}, l_k, l_l, l_{kl} and λ, respectively. The spin 1/2 of the baryons couple to two-baryon spin s_{ij} and s_{kl} and these couple with the orbital angular momenta to intermediate angular momenta j_{ij}, I_k, I_l, j_k, j_{kl}, and I to the total angular momentum J as indicated. Since isospin symmetry is preserved rather accurately, the states are formulated in the isospin basis. The baryon isospins t_i, t_j, t_k, and t_l are coupled to two-baryon isospins t_{ij} and t_{kl} and three-baryon isospins τ_k and finally to the total isospin T and its third component M_T. Following the standard notation, we use here t for isospins and the I for a coupled angular momentum which differs from the notation of $A = 2$ systems used in Section 2. Note that the inclusion of the isospin quantum numbers allows one to distinguish N, Λ and Σ baryons by their isospin. Depending on the Yakubovsky component, states with different positions of the hyperon, the fourth particle in our convention, are used. E.g., for $|\psi_{1A}\rangle$, '3+1' states with $l = 4$ are used and, for $|\psi_{2B}\rangle$, '2+2' states with $j = 4$.

Since we use different sets of basis states for the different Yakubovsky components, coordinate transformations between the different states are necessary. These are not explicitly shown in the Eqs. (4.11) but are in fact equivalent to the permutation operators. To obtain energies converged up to the keV level, still a very large number of partial waves of the order or several thousands is necessary. Using approximately 40 momentum grid points for each of the momenta, the discretized set of equations can become as large as 10^8 dimensional. Clearly, storing and applying a $10^8 \times 10^8$ matrix is impossible even on today's supercomputers. But fortunately, the Yakubovsky equations can be decomposed in a series of sparse matrices that can be handled on massively parallel systems. To achieve this form, we apply coordinate transformations and permutation operators such that either particle i and j are not affected, or, for "3+1" coordinates,we leave the outer lth particle unaffected, or, for "2+2" coordinates, we only change the subsystems. In these cases, the two-baryon subsystem(s) or lth particle quantum numbers and momenta are conserved and the transformation becomes sparse. The application of the two-baryon t-matrix is sparse since it only changes quantum numbers of the particles i and j. Note however that the possibility of Λ-Σ conversion changes the rest masses of the ij subsystem. This induces a shift of the other momenta when using "3+1" coordinates. In order to end up with sparse matrices, we only apply the t-matrices using "2+2" coordinates where such a shift of Jacobi momenta shows up. The application of the three-baryon interaction is implemented in "3+1" coordinates. In this case, all momenta and quantum numbers of particle l are conserved.

Including the different transformations and the different sets of coordinates, Eqs. (4.11) become more lengthy

$$
\begin{aligned}
\left\langle (12)3,4\middle|\psi_{1A}\right\rangle =& \left\langle (12)3,4\middle|G_0 t_{12}\middle|(12)3,4'\right\rangle \left\langle (12)3,4'\middle|P\middle|(12)3,4''\right\rangle \\
&\left[\left\langle (12)3,4''\middle|\psi_{1A}\right\rangle + \left\langle (12)3,4''\middle|(12)4,3'''\right\rangle \left\langle (12)4,3'''\middle|\psi_{1B}\right\rangle + \left\langle (12)3,4''\middle|(12)34'''\right\rangle \left\langle (12)34'''\middle|\psi_{2A}\right\rangle\right] \\
&+ \left\langle (12)3,4\middle|1+G_0 t_{12}\middle|(12)3,4'\right\rangle \left\langle (12)3,4'\middle|V^{(3)}_{123}+V^{(12)3,4}_{1234}\middle|(12)3,4''\right\rangle \left\langle (12)3,4''\middle|\Psi\right\rangle, \\
\left\langle (12)4,3\middle|\psi_{1B}\right\rangle =& 2\left\langle (12)4,3\middle|G_0 t_{12}\middle|(12)4,3'\right\rangle \left\langle (12)4,3'\middle|(14)2,3''\right\rangle \left[\left\langle (14)2,3''\middle|1-P_{23}\middle|(14)2,3'''\right\rangle \left\langle (14)2,3'''\middle|\psi_{1C}\right\rangle \right. \\
&\left. + \left\langle (34)1,2''\middle|(34)12'''\right\rangle \left\langle (34)12'''\middle|\psi_{2B}\right\rangle\right] \\
&+ \left\langle (12)4,3\middle|1+G_0 t_{12}\middle|(12)4,3'\right\rangle \left\langle (12)4,3'\middle|V^{(4)}_{124}+V^{(12)4,3}_{1234}\middle|(12)4,3''\right\rangle \left\langle (12)4,3''\middle|\Psi\right\rangle, \\
\left\langle (14)2,3\middle|\psi_{1C}\right\rangle =& \left\langle (14)2,3\middle|(14)23'\right\rangle \left\langle (14)23'\middle|G_0 t_{14}\middle|(14)23''\right\rangle \left\langle (14)23''\middle|(14)2,3'''\right\rangle \\
&\left[\left\langle (14)2,3'''\middle|(12)4,3^{IV}\right\rangle \left(\left\langle (12)4,3^{IV}\middle|\psi_{1B}\right\rangle + \left\langle (12)4,3^{IV}\middle|(12)3,4^{V}\right\rangle \left\langle (12)3,4^{V}\middle|\psi_{1A}\right\rangle \right.\right. \\
&\left.\left. + \left\langle (12)4,3^{IV}\middle|(12)34^{V}\right\rangle \left\langle (12)34^{V}\middle|\psi_{2A}\right\rangle\right) \right. \\
&+ \left\langle (14)2,3'''\middle|P_{12}\middle|(14)2,3^{IV}\right\rangle \left(-\left\langle (14)2,3^{IV}\middle|\psi_{1C}\right\rangle + \left\langle (14)2,3^{IV}\middle|P_{23}\middle|(14)2,3^{V}\right\rangle \left\langle (14)2,3^{V}\middle|\psi_{1C}\right\rangle \right. \\
&\left.\left. + \left\langle (34)2,1^{IV}\middle|(34)12^{V}\right\rangle \left\langle (34)12^{V}\middle|\psi_{2B}\right\rangle\right)\right] \\
&+ \left\langle (14)2,3\middle|(14)23'\right\rangle \left\langle (14)23'\middle|1+G_0 t_{14}\middle|(14)23''\right\rangle \left\langle (14)23''\middle|(14)2,3'''\right\rangle \\
&\left\langle (14)2,3'''\middle|V^{(2)}_{124}+V^{(14)2,3}_{1234}\middle|(14)2,3^{IV}\right\rangle \left\langle (14)2,3^{IV}\middle|\Psi\right\rangle, \\
\left\langle (12)34\middle|\psi_{2A}\right\rangle =& \left\langle (12)34\middle|G_0 t_{12}\middle|(12)34'\right\rangle \left\langle (12)34'\middle|(34)12''\right\rangle \left[-2\left\langle (34)12''\middle|(34)2,1'''\right\rangle \left\langle (14)2,3'''\middle|\psi_{1C}\right\rangle + \left\langle (34)12''\middle|\psi_{2B}\right\rangle\right], \\
\left\langle (34)12\middle|\psi_{2B}\right\rangle =& \left\langle (34)12\middle|G_0 t_{34}\middle|(34)12'\right\rangle \left\langle (34)12'\middle|(12)34''\right\rangle \\
&\left[\left\langle (12)34''\middle|(12)3,4'''\right\rangle \left\langle (12)3,4'''\middle|\psi_{1A}\right\rangle + \left\langle (12)34''\middle|(12)4,3'''\right\rangle \left\langle (12)4,3'''\middle|\psi_{1B}\right\rangle + \left\langle (12)34''\middle|\psi_{2A}\right\rangle\right]. \qquad (4.15)
\end{aligned}
$$

This form can be achieved using the antisymmetry of the basis states for two-nucleon subsystems and the fact that permutation operators relate different sets of Jacobi coordinates with each other. Summation and integration of the quantum numbers and coordinates of intermediate states are omitted to shorten the notation. Using the equivalence of permutation operators and coordinate transformations is also used to replace permutation operators by using different sets of coordinates for bra and ket vectors in some of the expressions above. For the application of the 3BFs, we need the wave function defined in Eq. (4.12) in different Jacobi coordinates. Also these can be obtained by appropriate coordinate transformations. In the following, we do not consider the 4BFs anymore since they are, at this point, usually neglected.

Note that our requirements on the sparsity of the different matrices are fulfilled in this form and the YN t-matrix is always applied in "2+2" coordinates to avoid a momentum shift due to particle conversion.

Due to the distribution of different parts of the 3BFs to different Yakubovsky components, the coordinates used are the ones naturally used for these interactions. The improved convergence is primarily enforced by the suppression of high orbital angular momenta due to t_{ij} and $V^{(k)}_{ijk}$. Similarly, the expectation values $\langle\Psi|\,V_{ij}\,|\Psi\rangle$ and $\langle\Psi|\,V_{ijk}\,|\Psi\rangle$ only require a limited range of partial waves if evaluated in the appropriate Jacobi coordinates. The kinetic energy can be easily expressed in arbitrary Jacobi coordinates. In this case, it is advantageous to use the antisymmetry under exchange of the nucleons to rewrite the expectation value using Eq. (4.12) as

$$
\left\langle \Psi\middle|H_0\middle|\Psi\right\rangle = 3\langle\Psi|H_0|\psi_{1A}\rangle + 3\langle\Psi|H_0|\psi_{1B}\rangle + 6\langle\Psi|H_0|\psi_{1C}\rangle + 3\langle\Psi|H_0|\psi_{2A}\rangle + 3\langle\Psi|H_0|\psi_{2B}\rangle\ . \qquad (4.16)
$$

When different parts are then calculated using the appropriate Jacobi coordinate so that again, due to the Yakubovsky components, the contributing number of partial waves is restricted. In order to check the numerical accuracy of our calculations, we compare

Table 4.2
Λ-separation energies and binding for ${}^{3}_{\Lambda}$H and the 0^+ and 1^+ states of ${}^{4}_{\Lambda}$He compared to the experimental values [50]. Besides the chiral interactions, results are shown for selected combinations of phenomenological YN interactions: SC89 [13], SC97d-e [14], Jülich Ã [17] and Jülich '04 [18]. As NN interaction also Nijm 93 [157] was used. Additionally, the corresponding binding energies and the expectation values $\langle H \rangle$ are given. Energies are given in MeV. The experimental values for the separation energy in the last row are taken from the Mainz database [50]. *Value as of August 7, 2025, see discussion in Section 4.2.

YN	NN	3NF	${}^{3}_{\Lambda}$H			${}^{4}_{\Lambda}$He(0^+)			${}^{4}_{\Lambda}$He(1^+)		
			E_Λ	E	$\langle H \rangle$	E_Λ	E	$\langle H \rangle$	E_Λ	E	$\langle H \rangle$
LO(700)	N4LO$^+$(450)	N2LO	0.135	−2.359	−2.360	3.088	−10.827	−10.803	2.275	−10.015	−9.992
NLO13(500)	N4LO$^+$(450)	N2LO	0.134	−2.357	−2.358	1.654	−9.394	−9.367	0.778	−8.518	−8.495
NLO19(500)	N4LO$^+$(450)	N2LO	0.100	−2.323	−2.324	1.630	−9.370	−9.349	1.221	−8.960	−8.940
NLO19(550)	N4LO$^+$(450)	N2LO	0.093	−2.317	−2.317	1.534	−9.274	−9.243	1.238	−8.978	−8.949
NLO19(600)	N4LO$^+$(450)	N2LO	0.091	−2.314	−2.314	1.444	−9.183	−9.136	1.055	−8.795	−8.755
NLO19(650)	N4LO$^+$(400)	N2LO	0.098	−2.321	−2.322	1.553	−9.289	−9.232	0.929	−8.664	−8.622
NLO19(650)	N4LO$^+$(450)	N2LO	0.095	−2.318	−2.319	1.525	−9.265	−9.201	0.917	−8.657	−8.608
NLO19(650)	N4LO$^+$(500)	N2LO	0.090	−2.313	−2.314	1.480	−9.223	−9.153	0.891	−8.635	−8.581
NLO19(650)	N4LO$^+$(550)	N2LO	0.085	−2.308	−2.308	1.429	−9.176	−9.102	0.856	−8.604	−8.547
NLO(500)	N4LO$^+$(450)	N2LO	0.127	−2.350	−2.351	2.009	−9.749	−9.701	1.041	−8.781	−8.746
NLO(550)	N4LO$^+$(450)	N2LO	0.124	−2.347	−2.348	2.102	−9.841	−9.788	1.102	−8.842	−8.800
NLO(600)	N4LO$^+$(450)	N2LO	0.122	−2.345	−2.346	2.021	−9.761	−9.681	0.927	−8.667	−8.602
NLONM(550)	N4LO$^+$(550)	N2LO	0.105	−2.328	−2.328	1.910	−9.657	−9.595	1.017	−8.765	−8.718
N2LO(500)	N4LO$^+$(450)	N2LO	0.147	−2.371	−2.371	2.001	−9.741	−9.686	1.002	−8.741	−8.706
N2LO(550^a)	N4LO$^+$(400)	N2LO	0.137	−2.360	−2.361	1.995	−9.731	−9.673	1.249	−8.985	−8.944
N2LO(550^a)	N4LO$^+$(450)	N2LO	0.139	−2.362	−2.363	2.004	−9.743	−9.677	1.251	−8.990	−8.943
N2LO(550^a)	N4LO$^+$(500)	N2LO	0.138	−2.362	−2.362	1.990	−9.734	−9.661	1.230	−8.974	−8.924
N2LO(550^a)	N4LO$^+$(550)	N2LO	0.136	−2.359	−2.360	1.962	−9.710	−9.633	1.205	−8.953	−8.901
N2LO(600)	N4LO$^+$(450)	N2LO	0.172	−2.395	−2.396	2.263	−10.002	−9.933	1.181	−8.921	−8.872
N2LO(550^b)	N4LO$^+$(450)	N2LO	0.125	−2.348	−2.349	1.969	−9.709	−9.643	1.188	−8.928	−8.881
Jülich Ã	Nijm 93	–	–	–	–	0.430	−7.400		0.480	−7.450	
Jülich '04	Nijm 93	–	0.13			1.9			2.3		
SC89	Nijm 93	–	0.143	−2.367	−2.366	2.140	−9.140		0.020	−6.990	
SC97d	Nijm 93 –	–	–	–	–	1.3			0.8		
SC97e	Nijm 93	–	0.023	−2.247	−2.246	1.540	−8.550		0.720	−7.690	
SC97e	Nijm 93	TM	0.023	−2.247	−2.246	1.560	−9.320		0.700	−8.350	
Experiment			0.164(43)*			2.347(36) (${}^{4}_{\Lambda}$He) 2.169(42) (${}^{4}_{\Lambda}$H) 2.258(55) (average)			0.942(36) (${}^{4}_{\Lambda}$He) 1.081(46) (${}^{4}_{\Lambda}$H) 1.012(58) (average)		

the energy values E entering the Yakubovsky equations to the value of the expectation value calculated as outlined above. The presence of the wave function still limits the accuracy of the expectation value. But we find that our energies for the most recent calculations are converged to 20 keV and the expectation values to 50 keV. Both results generally agree within these uncertainties.

4.2. Application of chiral baryon–baryon interactions

Results for the light hypernuclei for the different chiral interactions and some selected phenomenological interactions are compiled in Table 4.2 and summarized in Fig. 4.2. The usual notation for the chiral NN and YN interactions is adopted which specifies the various potentials by their chiral order and by the employed cutoff mass. Regarding the predominantly used N2LO YN interaction with cutoff 550 MeV there are two variants, denoted by N2LO(550^a) and N2LO(550^b), see Section 2.2 and specifically Ref. [42] for details.

Before starting a discussion on the physical implications, let us note that it has been checked that the separation energies are numerically converged up to 1 keV for ${}^{3}_{\Lambda}$H and up to 20 keV for ${}^{4}_{\Lambda}$He except for the older calculations based on phenomenological interactions. In those calculations, the accuracy is about 50 keV. The expectation values require the calculation of the wave functions. Therefore, their uncertainty is slightly larger, 2 keV for ${}^{3}_{\Lambda}$H and up to 100 keV for ${}^{4}_{\Lambda}$He. It is reassuring to see that the energy and the expectation value agree within these uncertainties in all case. In order to get the most accurate expectation values, the kinetic energy has been evaluated using Eq. (4.16). The expectation value for the NN and 3N interactions was calculated using the coordinates $|(12)3,4\rangle$. For the evaluation of the YN interaction, it turned out that $|(34)12\rangle$ coordinates lead to the fastest convergence with respect to partial waves.

The results for ${}^{4}_{\Lambda}$H are not given in the table since the YN interactions used here do not include charge-symmetry breaking (CSB). The separation energies therefore only show a negligible difference between ${}^{4}_{\Lambda}$He and ${}^{4}_{\Lambda}$H. CSB will be discussed in the next section in detail.

Light hypernuclei are an important source of information on the YN and YNN interactions. Thereby, the ${}^{3}_{\Lambda}$H is of similar importance for the YN interaction as the deuteron for the NN interaction. First of all, it is the lightest bound hypernucleus and therefore the simplest bound system that can be studied. Second, it has been realized very early that the angular momentum $J = 1/2$ and isospin $T = 0$ of the only bound state in this system implies that the ΛN interaction is more attractive in the ${}^1S_0$ than in the ${}^3S_1$

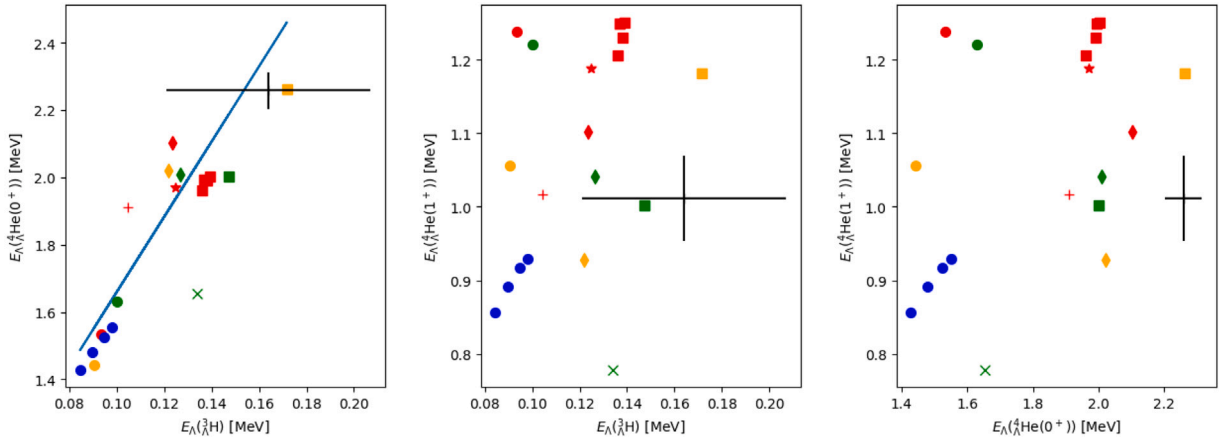

Fig. 4.2. Correlation of the separation energies of the ${}^3_\Lambda$H, ${}^4_\Lambda$He(0^+) and ${}^4_\Lambda$He(1^+) states for different orders and cutoffs. The symbols distinguish the different orders or versions of the chiral interactions: NLO13 (stars), NLO19 (crosses), and the SMS YN potentials NLONM (diamonds), NLO (squares), N2LO (circles), and N2LO(550^b)(+). Colors distinguish different cutoffs of the YN interaction: 500 MeV (green), 550 MeV (red), 600 MeV (orange), 650 MeV (blue). The different cutoffs of the NN and 3N interaction are not distinguished. The black cross indicates the experimental values and their uncertainties.

channel [4]. In absence of any polarization data, this information is a key element to fix the spin dependence of the ΛN interaction. In order to better constrain this spin dependence, one can exploit a series of YN interactions provided by the Nijmegen group (SC97a-f) that essentially differ by their prediction for the ΛN ${}^1S_0$ scattering length while keeping the description of the unpolarized cross sections unaltered [14]. It was found that the hypertriton is only bound by the last two variants of these interactions [155]. This information suggests that the ΛN ${}^1S_0$ scattering length should be larger (in magnitude) than -2.10 fm to ensure that the hypertriton is bound. Unfortunately, there is still no experimental consent on the actual value of the ${}^3_\Lambda$H separation energy. For a long time the value given by Jurič et al. [158], $B_\Lambda = 0.13 \pm 0.05$ MeV, has been accepted as the standard. However, over the past few years many new experimental values have been published, see the hypernuclear data base maintained by the Mainz Group [50], with some results significantly above (0.523 MeV [159]) or below (0.063 MeV [160]) the Jurič value. As a consequence, the average (recommended value) by the Mainz Group changed noticeably after practically each addition. For example, when the calculations of light hypernuclei reviewed here were performed the recommendation was 0.164 ± 0.043 MeV. Now (March 2026) the average from the Mainz Group is $0.105^{+0.037}_{-0.028}$ MeV [50].

Nonetheless, with a Λ separation energy of ${}^3_\Lambda$H in the order of 0.1 MeV, this nucleus represents the lightest halo nucleus and contributions of YNN forces should be effectively suppressed. Based on power counting arguments [48] and explicit calculation of the YNN contribution [49], one can expect that the YNN force contribution is smaller than the experimental uncertainty of the separation energy. This motivates using the separation energy as a guide line for constraining YN interactions, although, for the reasons discussed above, one cannot use it as direct and quantitative input in the fitting procedure. This strategy has been followed in the construction of all chiral YN interactions of the Jülich–Bonn group [18,39,41,42]. Without using charge-symmetry breaking (CSB), all interactions lead to singlet scattering lengths between -2.5 and -2.9 fm except the result of the LO chiral interaction [39] which predicted -1.90 fm because its momentum dependence is too weak to get a reasonable description of the ΛN cross section for all momenta below the opening of the Σ channel. An overview of the correlation between the Λp scattering lengths and the existence of a bound ${}^3_\Lambda$H is provided in Fig. 4.3, based on the YN potentials of the Jülich–Bonn group and for several YN potentials from the literature where bound-state calculations have been performed [20–22,162]. Besides the (a_s, a_t) region where a bound hypertriton has been found for the corresponding YN potentials, one can also see the clear correlation between a_s and a_t that result from fitting to the Λp cross-section data [23,24], and a very similar though slightly shifted correlation when considering recent femtoscopic data by the ALICE Collaboration [60,161]. Indeed, also femtoscopic measurements of the Λp interaction do not allow to disentangle the spin dependence. However, the analysis of such experiments in Ref. [161] indicates that the ΛN interaction could be overall slightly weaker than what follows from the available Λp cross sections. Of course, one should keep in mind that the systematic uncertainty due to the employed theoretical tools (Koonin–Pratt formalism, source function) [67] has not yet been accounted for.

The resulting separation energies can be seen in Table 4.2. Note that the ${}^3_\Lambda$H energies are not exactly the same even if the values were used to fit the interaction. First of all, the separation energy has recently changed due to new data leading to a slightly larger world average [163,164]. However, and more important, because of the rather large experimental uncertainty of this datum, it was only used as guideline and not as a stringent fitting constraint. Moreover, the fit was usually only done for one of the cutoffs of the interaction and the other cases where adjusted to the resulting scattering lengths leading to small variations of the separation energy for the different orders and cutoffs.

The results for the $A = 4$ hypernuclei show much more dependence on the interaction. Especially, the separation energies for the LO interaction are unrealistically large which can be already expected from the overprediction of the Λp cross sections around

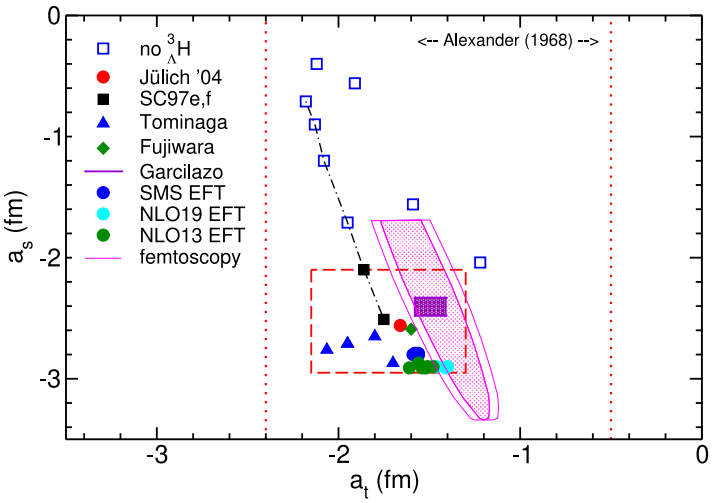

Fig. 4.3. Correlation between the ΛN $^1S_0$ and $^3S_1$ scattering lengths (a_s and a_t) and the existence of a bound $^3_\Lambda$H. Results are shown for various YN potentials from the literature where bound-state calculations have been performed. The region where the $^3_\Lambda$H is bound is indicated by a dashed rectangle. Open symbols correspond to results of potentials for which the $^3_\Lambda$H is not bound. The squares connected by a dash-dotted line correspond to the series of YN interactions by the Nijmegen group [14], see text. The filled (violet) rectangle summarizes the results from Garcilazo et al. [22]. In addition, estimates for the scattering lengths from the measured Λp cross section [23] (dotted lines) and from femtoscopic data [161] (hatched area) are indicated.

the ΣN threshold. In the following, we will not consider the LO results since they are affected by an unrealistic description of YN data.

For the rest of the interactions, the available YN data is generally well described. Nevertheless, one observes significant variations of the $A = 4$ energies. Some insight can be gained by considering the energies from the chiral interactions, summarized in Fig. 4.2. The plots show that there is a correlation of the $^3_\Lambda$H and the $^4_\Lambda$He 0^+ energies. The energy of the 1^+ state is less related to the other two. Assuming only S-wave interactions and neglecting possible contributions from the Λ-Σ transitions, it can be shown that the 1^+ state is driven by the $^3S_1$ interaction [41,149,150] whereas the $J^\pi = 1/2^+$ state of $^3_\Lambda$H is mostly affected by the $^1S_0$ state and the $J^\pi = 0^+$ state of $^4_\Lambda$He gets approximately equal contributions from both partial waves. Those observations taken together suggest that contributions of the $^3S_1$ state to the separation energies are much more dependent on the detailed realization of the YN interactions. This assessment is in line with the observed effects from the difference of the Λ-Σ conversion strength documented in [41], by comparing the NLO13 and NLO19 interactions. Since both interactions are phase-shift equivalent to a high degree, it is clear that the actual Λ-Σ conversion strength in the potential, which is basically an "off-shell" property of the YN interaction, cannot be fixed uniquely by YN data. Different realizations of the YN interaction will need different additional YNN interactions (see Section 5.5 for first results including such interactions). The variation of the separation energies seen in Fig. 4.2 is therefore also a measure of the size of the YNN forces. Note that none of the interactions can describe the 0^+ and 1^+ state simultaneously indicating that YNN forces, that are able to resolve this discrepancy, need to be spin dependent.

Recently, it has been discussed that also differences in the NN interactions could affect the separation energies of Λ hypernuclei [165,166]. In these works, a family of NN interactions and corresponding 3NFs were used to investigate this aspect in more detail. The results show a significant dependence of the order of several hundred keV for $A = 4$ hypernuclei and still 100 keV for $^3_\Lambda$H. This is in contradiction to earlier observations that the NN interaction dependence is minor [155]. It is however also seen that the dependence is systematically linked to the cutoff of the interaction (40 keV for $^3_\Lambda$H [165]) and also to the maximal kinetic energy of the NN data that was used in the fit of the employed NN interaction (60 keV for $^3_\Lambda$H [165]). The numbers are based on LO chiral interactions [39]. The two contributions to the NN-force dependence have clearly a different theoretical origin. The dependence on the NN data used is related to an inaccuracy of the NN interaction that is irrelevant when high order and high accuracy NN interactions are used as is by now standard in any calculations for hypernuclei. The cutoff dependence indicates a sensitivity to the realization of the interaction that should be absorbed by higher order contributions, i.e. 3BFs. Therefore, the results of Refs. [165,166] indicate a contribution of YNN interactions of the order of 20 keV for $^3_\Lambda$H and 100 keV for $^4_\Lambda$He which is in better agreement with previous assessments. Table 4.2 and Fig. 4.2 include a series of calculations for NLO19(650) and N2LO(550) that show that the dependence on the NN interactions is even lower for $^3_\Lambda$H than estimated above. This can be traced back to using higher order YN interactions instead of LO, which seems to strongly reduce the sensitivity to the short range properties of the NN interaction. For these higher order interactions, the estimate for the YNN contribution necessary is less than 10 keV (30 keV) for $^3_\Lambda$H ($^4_\Lambda$He) which is smaller (comparable) to the experimental uncertainty. Certainly, the dependence on the realization of the YN interaction is much larger.

Table 4.3
CSB of the $A = 4$ hypernuclear separation energies in MeV, based on the scenario CSB1 considered in Ref. [54]. For completeness also the ${}^{3}_{\Lambda}$H separation energy is given. The predicted singlet a_s and triplet a_t are given in fm. In the last row the experimental values for the separation energy from the Mainz database [50] are given (the fit used slightly different values). *Value as of August 7, 2025, see discussion in Section 4.2. For the scattering length the averaged scattering length from non-CSB versions of NLO13 and NLO19 is added.

Interaction	$E_\Lambda({}^{3}_{\Lambda}\mathrm{H})$	$E_\Lambda({}^{4}_{\Lambda}\mathrm{He})$		$E_\Lambda({}^{4}_{\Lambda}\mathrm{H})$		a_s		a_t	
		$J^\pi = 0^+$	$J^\pi = 1^+$	$J^\pi = 0^+$	$J^\pi = 1^+$	Λp	Λn	Λp	Λn
NLO13(500)	0.14	1.82	0.76	1.56	0.82	−2.604	−3.267	−1.647	−1.561
NLO13(550)	0.10	1.62	0.56	1.36	0.61	−2.586	−3.291	−1.551	−1.469
NLO13(600)	0.09	1.59	0.55	1.34	0.60	−2.588	−3.291	−1.573	−1.487
NLO13(650)	0.09	1.61	0.59	1.36	0.64	−2.592	−3.271	−1.538	−1.452
NLO19(500)	0.10	1.77	1.19	1.52	1.27	−2.649	−3.202	−1.580	−1.467
NLO19(550)	0.10	1.67	1.21	1.42	1.28	−2.640	−3.205	−1.524	−1.407
NLO19(600)	0.09	1.58	1.03	1.34	1.09	−2.632	−3.227	−1.473	−1.362
NLO19(650)	0.10	1.65	0.89	1.40	0.96	−2.620	−3.225	−1.464	−1.365
Expt.	0.164(43)*	2.347(36)	0.942(36)	2.169(42)	1.081(46)	−2.906(5)		−1.496(65)	

One of the remarkable things one can learn from Table 4.2 is that some of the phenomenological interactions predict vast deviations from the experimental value. For example, the Jülich '04 interaction leads to reversed ordering of the 0^+ and 1^+ states although the ΛN scattering lengths and the ${}^{3}_{\Lambda}$H energy are quite comparable to the other interactions. The origin of this failure is most likely related to the rather weak ΛN-ΣN transition potential that characterizes this YN model. Actually, it is so weak that even the $\Sigma^-\mathrm{p}\to\Lambda\mathrm{n}$ transition cross section is somewhat underestimated, see the results and the discussion in Ref. [41]. One would need large YNN force effects to reproduce the experimental separation energies which, however, cannot be systematically obtained due to the phenomenological character of the interaction. For the Nijmegen SC97 interactions, the ${}^{3}_{\Lambda}$H and ${}^{4}_{\Lambda}$He energies are generally too small. The SC89 is quite different since it describes the ${}^{3}_{\Lambda}$H and the 0^+ state well but barely binds the excited state. Also these deviations are probably mostly due to missing YNN forces that cannot be systematically obtained in the framework of these models.

4.3. Charge-symmetry breaking of $A = 4$ hypernuclei

One important motivation to study hypernuclear interactions is the possible contribution of hyperons to the equation of state (EOS) of neutron matter. It is discussed quite extensively that a possible softening of the EOS due to the appearance of hyperons would be in contradiction to the observation of neutron stars with masses around or larger than two solar masses [167–171]. Since the Λ is expected to be the most relevant hyperon admixture to neutron matter, good knowledge of the Λ-neutron (Λn) interaction is highly desired. YN data is only available for the Λ-proton (Λp) system (except for ΛN-ΣN transition cross sections). Therefore, usually, isospin symmetry is assumed leading to practically equal Λn and Λp interactions.

However, CSB of the YN interaction has already been noted and discussed in the 1960's [94,172]. The data at the time showed that the separation energies of ${}^{4}_{\Lambda}$He and ${}^{4}_{\Lambda}$H are significantly different. Since there is no direct contribution to the ΛN interaction from the Coulomb interaction much smaller differences were expected. Dalitz and von Hippel realized that there is definitely a pion-ranged CSB interaction due to the Λ-Σ^0 mixing. Their estimate of this contribution is still part of many YN interaction models and also of the chiral interactions. More details can be found around Eq. (2.15) above.

Since then many investigations have been performed to better understand this mechanism and to explain the data. Three main contributions have been identified. First, as mentioned above, the Coulomb interaction has been shown to contribute only a small fraction of the difference and this contribution even goes into the wrong direction [31,173]. In addition there is an effect associated with the Λ-Σ conversion which generates a CSB contribution to the kinetic energy due to the mass difference of Σ^+ and Σ^-. The main part of this contribution is just related to the probabilities to find the various charge states of Σ's in the wave function [31]. Since this is a non-observable property of the wave function that can be changed by unitary transformations, it should in principle be linked to other contributions that accommodate any changes in the Σ probabilities. In practical calculations, for YN potentials that predict the $A = 4$ state realistically, this contribution is of the order of 50 keV [174]. The last contribution is due to the CSB interaction which is usually driven by the mechanism of Dalitz and von Hippel.

Unfortunately, the actual comparison of calculations to experiment is hindered by the large uncertainty of the data. In fact, the central values of the currently accepted values [50] of the difference of the separation energies of the 0^+ and 1^+ states

$$\begin{aligned}\Delta E_\Lambda\left(0^+\right) &= E_\Lambda\left(0^+,{}^{4}_{\Lambda}\mathrm{He}\right) - E_\Lambda\left(0^+,{}^{4}_{\Lambda}\mathrm{H}\right) = 178 \pm 55\ \mathrm{keV}\\ \Delta E_\Lambda\left(1^+\right) &= E_\Lambda\left(1^+,{}^{4}_{\Lambda}\mathrm{He}\right) - E_\Lambda\left(1^+,{}^{4}_{\Lambda}\mathrm{H}\right) = -139 \pm 58\ \mathrm{keV}\end{aligned} \tag{4.17}$$

are quite different from the long-term accepted CSB based on Refs. [158,175] of 340 keV (240 keV) for the 0^+ (1^+) states (see experimental values in Table 4.3) used up to 2015. Not only the overall size changed but also the spin dependence is now much more significant. Therefore, many studies were hampered by the goal to explain partly misleading data.

The mechanism of Dalitz and von Hippel promises a straight forward explanation of the CSB. However, many models implementing this contribution did not properly describe the data [31,174] and studies based on different realizations of the LO

chiral YN interaction showed a large regulator dependence [52,53] which could also not be resolved by using the complete Λ-Σ conversion potential to fix the CSB interaction [53]. The reason for this confusing results was that all these interactions were missing the two LO CSB contact interactions that are necessary to properly renormalize the 1π exchange (see Eq. (2.15)). Indeed, a proper application of effective field theory requires these two contact interaction that have to be determined from hypernuclear data. In absence of any Λn data, the two constants can only be determined using hypernuclei and the CSB of the ${}^{4}_{\Lambda}\mathrm{He}/{}^{4}_{\Lambda}\mathrm{H}$ nuclei are probably the best observables to fit the interactions since the experimental uncertainties for other hypernuclear isospin multiplets are even larger and lattice QCD predictions for differences of Λp and Λn scattering will not be available in the foreseeable future. Using these two hypernuclei for the determination, the interactions can be used to predict the Λn interaction. This was performed in Ref. [54] in 2021 based on the NLO13 and NLO19 interactions. Knowing that the experimentally accepted values are still changing, the fit was performed for the central values of three scenarios. The first one, labeled as CSB1, assumes that the $A = 4$ hypernuclei have splitting of 233 ± 92 keV (-83 ± 94 keV) for the 0^+ (1^+) states. These numbers reflect the experimental situation after new data from J-PARC [176] and Mainz [177] became available and was the experimental status when the study was performed. The second one, CSB2, is based on the old data mentioned above 340 keV (240 keV) [158,175] used up to 2015. This scenario requires a very different spin dependence than CSB1. The third one, CSB3, is based on the experimental situation before the Mainz experiment was finished but taking the J-PARC result into account: 350 ± 50 keV (30 ± 50 keV). The scenario is similar to CSB1 since there is only a spin independent shift between them. The overall size is still comparable to the older values. Note that the most recent measurement, from the STAR Collaboration [178], suggests again different values for the CSB splittings, $160 \pm 140(\mathrm{stat}) \pm 100(\mathrm{syst})$ keV ($-160 \pm 140(\mathrm{stat}) \pm 100(\mathrm{syst})$ keV), albeit with rather large uncertainties. The results for the scenario CSB1 are summarized in Table 4.3.

The study in Ref. [54] only took the central values into account and aimed at investigating whether predictions for the Λn scattering length can be made once reliable data for the CSB of the $A = 4$ hypernuclei is available. Therefore, the experimental uncertainties of the difference scenarios were not considered. For CSB1 and CSB3, the determination of the LECs of the CSB contact interactions are straight forward. The adjustment to the $A = 4$ energies only leads to small variations of the predictions. For CSB2, the changes were more significant so that a refit of the YN interaction was necessary. In this case, the final values were obtained in a multi-step process. For CSB1, the fit was done for all cutoffs and both interactions, NLO13 and NLO19. Since both interactions differ by a significantly different strength of Λ-Σ conversion, one can expect that the choice of interactions covers a wider range of possible predictions. As can be seen in the table, the results for singlet Λn scattering length only vary by 3% and the one for the triplet by 15%. The larger variation for the triplet is not surprising since there is more dependence on the realization of the interaction even for the standard non-CSB interactions. For CSB2 and CSB3, fits have only been performed for a cutoff of $\Lambda = 600$ MeV but still for both versions, NLO13 and NLO19. As can be seen in the table, also for the other two scenarios the dependence on the realization is small compared to the shifts of the Λp and Λn scattering length. CSB2 is quite different to the other two. First of all, due to the necessity of refitting the interaction, the shift compared to the original NLO interactions is unsymmetrical and, even more interesting, the shift is opposite to the other two and also affects the triplet. CSB2 was mainly included to exemplify that accurate $A = 4$ separation energies are relevant to determine the Λn interaction. Since the experimental values used for this scenario are updated, we will not consider it further. CSB1 and CSB3 are qualitatively similar to each other. The CSB of the triplet is smaller than the singlet one and the Λn interaction becomes more attractive in the singlet. The larger size of the CSB of the separation energies in CSB3 shows up in a more visible shift of the triplet. It has been argued based on pionless EFT calculations and $\mathrm{SU}(3)_f$ that the CSB in the singlet and triplet can be related to each other [179]. Such considerations could provide arguments that the effect is more pronounced in the singlet. Under these assumptions, only one CSB datum is required to determine the interaction. Since the excitation energies of the hypernuclei can be measured with high accuracy, the determinations are not so much limited by the experimental uncertainty anymore. However, this approach requires model assumptions and an EFT that has a lower break down scale than chiral EFT.

As mentioned above, these results do not take the experimental uncertainty into account. Also the averaged experimental results have shifted again since this study was completed. Fortunately, at the same time, the uncertainty has been reduced. Therefore, in near future, the work of Ref. [54] should be repeated using the new data, the updated interactions [42] and taking experimental uncertainties into account. One can expect that model-independent determinations of the strength of the Λn interaction can be obtained using the $A = 4$ data.

The application of CSB interactions to p-shell hypernuclei will be discussed in Section 5.4.

4.4. Estimate of YNN interactions

Separation energies, at least for light hypernuclei, can be calculated with high numerical accuracy. Besides these purely numerical discretization errors or uncertainties due to the truncation of the partial wave representation, one can expect also uncertainties due to our incomplete knowledge of the hypernuclear interactions. In order to better understand these uncertainties, the chiral EFT approach to (hyper-)nuclear interactions is very useful. By power counting, higher orders of the interaction are expected to contribute less to the result. An arbitrary observable X can therefore be expanded as

$$X = X_{\mathrm{ref}} \sum_{k=0}^{\infty} c_k Q^k \ . \tag{4.18}$$

X_{ref} is dimensionful and sets a scale for the observable that is considered. Often this value is obtained based on the LO result, experiment or any other estimate. c_k are dimensionless expansion coefficients. Assuming a valid power countering, c_k should be of the order of 1. Q is the expansion parameter. For nuclear bound states and chiral EFT, it is usually given by $M_\pi^{\mathrm{eff}}/\Lambda_b$. Λ_b is the

breakdown scale of chiral EFT of the order of 600 MeV and $M_\pi^{\rm eff} \approx 200$ MeV captures typical momenta in nuclei and the expansion in the pion mass [180]. The actual value of Q can be determined using the sizes of the coefficients c_k. From a number of calculations using different orders of the interaction, the first few coefficients c_k ($k \le K$) can be determined. Assuming that the probability distribution for all other c_k, $k > K$ is equal, one can obtain a probability distribution for

$$\delta X_K = X_{\rm ref} \sum_{k=K+1}^{\infty} c_k Q^k \quad \text{with} \quad X = X_K + \delta X_K \text{ where } X_K = X_{\rm ref} \sum_{k=0}^{K} c_k Q^k \ . \tag{4.19}$$

Based on this probability, it is straightforward to obtain an uncertainty estimate for the Kth order prediction X_K of the observable within a Bayesian analysis [181,182].

In Ref. [48], this was done for hypernuclei with $A \le 5$. The calculations used the SMS YN interactions up to N2LO omitting YNN interactions. Although the highest order calculations were not complete because of the missing YNN forces, it was possible to reliably estimate the size of the N2LO contribution which represents the uncertainty at order NLO. Also the expected uncertainty once the calculations include a complete set of the leading YNN forces has been estimated. Fig. 4.4 shows the results at different order of the SMS YN interactions for a high order NN interaction. Obviously, the uncertainty shrinks for higher orders. The gray bands show the NLO uncertainty of the N2LO result where the YNN forces are still omitted. The experimental values are within the estimated uncertainties. The NLO uncertainty, e.g. given by the 68% degree of believe (DoB) interval, also provides an estimate of the YNN force contribution which is 20 keV, 240 keV, and 900 keV for ${}^{3}_{\Lambda}$H, ${}^{4}_{\Lambda}$He/${}^{4}_{\Lambda}$H, and ${}^{5}_{\Lambda}$He, respectively. This clearly shows the importance to include YNN interactions in the calculations for $A \ge 4$. First calculations will be discussed in Section 5.5.

The analysis is also instructive to better understand how different realizations of the NN interaction change the Λ separation energies. Based on phenomenological calculations, the NN force dependence was estimated to be 120 keV for $A = 4$ [31]. Similar calculations for ${}^{3}_{\Lambda}$H indicated that the NN force dependence is only 10 keV for this hypernucleus. This estimate has recently been criticized [165,166]. Based on a series of N2LO NN interactions called NNLO$_{\rm sim}$ [183], the Λ separation energies for $A = 3 - 5$ hypernuclei were calculated. The results suggest that the NN force dependence is much larger than previously estimated: 100 keV for ${}^{3}_{\Lambda}$H and 250 keV ${}^{4}_{\Lambda}$He/${}^{4}_{\Lambda}$H. The dependence is systematically related to the NN data taken into account for fitting the NN interaction and to the cutoff. Therefore, a statistical interpretation that reduces the nominal values of the uncertainty is not possible. On the other hand, standard NN interactions (also chiral ones at high order, say up to N3LO or N4LO) describe the NN data up to the pion production threshold with high accuracy. This is not the case for some variants of the NNLO$_{\rm sim}$ interactions. It turns out that restricting the interactions to the ones that describe the NN data up to higher energies, the NN force dependence shrinks to 50 and 130 keV. For $A = 4$, this is in line with previous estimates. Still, the uncertainty for $A = 3$ is uncomfortably large since it becomes comparable to the experimental uncertainty and this would therefore cast doubt on the use of the ${}^{3}_{\Lambda}$H binding energy for constraining the singlet ΛN scattering length, as usually done by the Jülich–Bonn group. In order to obtain a similar estimate of the uncertainty due to the NN interaction, we also studied explicitly the convergence with respect to the order of the NN interactions and due to cutoff variations of the NN interactions on the left hand side of Fig. 4.4. The uncertainties due to missing higher orders of the NN interaction are generally smaller than the ones due to YN interactions as can be expected because part of the variation will be similar in the core nucleus and the hypernucleus and will drop out for the separation energies. Due to the larger order, the contributions of missing higher orders are tiny as can be seen for the DoB intervals at order N4LO$^+$. Interestingly, the cutoff variation is much larger. Clearly, the missing YNN forces need to be adjusted consistently with the NN and YN force. This also leads to an absorption of cutoff dependencies. Since YNN forces are still missing in these calculations, the cutoff dependence can be expected to be of order N2LO and the results are consistent with this expectation as can be seen when comparing the NLO DoB intervals with the results for the different cutoffs. The NN interaction dependence is therefore linked to interactions involving the hyperon in this case. It is therefore already included in the uncertainty estimates shown on the right hand side of Fig. 4.4. In the future, a similar analysis of the uncertainty needs to be done including YNN interactions. This is still work in progress.

5. No-core shell model approach

The no-core shell model (NCSM) (see [184]) is one of the ab-initio approaches that is suitable for predicting properties of nuclei and hypernuclei beyond $A = 4$. For this method, the Schrödinger equation is solved using a harmonic oscillator (HO) basis. In contrast to the shell-model, the approach does not single out an inert core and valence nucleons but assumes that all nucleons and hyperons are active. Over the years several variants have been developed. Most calculations are performed within the so-called m-scheme where the basis states are build from single particle HO states. This allows one to easily antisymmetrize the states. However, the model spaces used for the basis states are usually large since the center-of-mass (CM) coordinate cannot be separated and because the basis states are not eigenstates of total angular momentum and isospin. The original NCSM uses a complete set of basis states up to a total HO excitation $N_{\rm tot}$. The completeness of the model spaces insures that the CM motion can be exactly separated. The importance truncated NCSM (IT-NCSM) [185] does not included a complete set of states up to a definite HO excitation. Instead, the states are preselected using a perturbative estimate of their importance. This reduces the number of basis states significantly and allows to extend NCSM calculations to medium mass nuclei.

Most of the calculations that will be presented here, have been obtained using the Jacobi NCSM (J-NCSM). In this approach, the basis states are given in terms of relative Jacobi coordinates. By construction, this separates out the CM coordinate and also allows one to define basis states with well-defined total angular momentum and isospin. Therefore, the number of basis states for a given maximal HO excitation is much smaller than in the m-scheme. The drawback of this variant is that it is difficult to define antisymmetric states. This has only been achieved using numerical diagonalization as described below. The J-NCSM was already

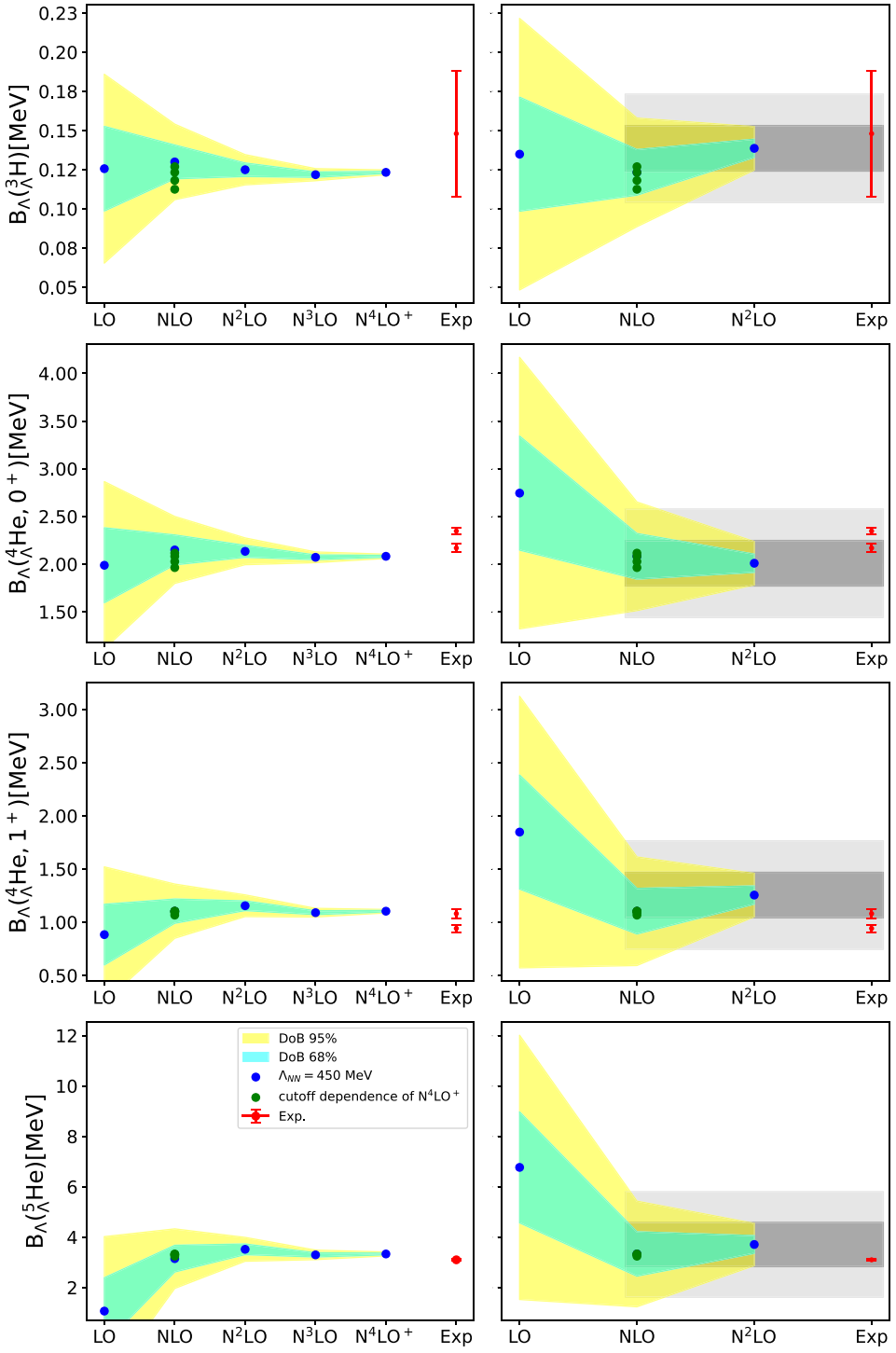

Fig. 4.4. Predictions for the separation energies of ${}^3_\Lambda$H, ${}^4_\Lambda$He(0^+), ${}^4_\Lambda$He(1^+), and ${}^5_\Lambda$He (from top to bottom) based of different orders of the SMS YN interactions for Λ_{YN} = 550 MeV and using the SMS NN interactions for Λ_{NN} = 450 MeV (blue circles). On the left hand side, the order of the NN interaction is increased using the YN interaction at NLO. On the right hand side, the order of the YN interaction is increased keeping the order of the NN interaction at N4LO$^+$. Green circles show results for Λ_{NN} = 400-550 MeV. The red crosses show the experimental values including the error bars. For $A = 4$, the two experimental values correspond to ${}^4_\Lambda$H and ${}^4_\Lambda$He. The yellow and cyan bands show the 95% and 68% degree of believe intervals (DoBs) from the Bayesian analysis. The light and dark gray band are the NLO DoBs plotted around the N2LO result. Energies are in MeV.

applied in [186] to s-shell nuclei but has only recently been extended to p-shell nuclei [187]. The direct application of the NCSM is only suitable for bound state calculations because of its basis states are square-integrable. Nevertheless, several extensions have been devised to gain insight into scattering processes [188–190]. Such approaches can also help to improve the numerical accuracy for calculations of bound states close to threshold.

5.1. Brief overview of NCSM calculations for hypernuclei

The first and pioneering applications of the NCSM to hypernuclei have been accomplished by the Darmstadt group around Wirth and Roth and are documented in a series of publications [36,37,191–193]. Already in the initial work from 2014 results for p-shell Λ hypernuclei up to ${}^{13}_{\Lambda}$C were presented, based on the IT-NCSM scheme, as well as a comparison of results of the J-NCSM to the m-scheme for s-shell Λ hypernuclei [36]. A first application of the J-NCSM to the CSB of the $A = 4$ system was reported by Gazda and Gal [52,53]. With increasing model space sizes, it also became possible to study the barely bound ${}^{3}_{\Lambda}$H leading to an investigation of the lifetime of this hypernucleus [194]. Finally, the J-NCSM has been applied to s-shell hypernuclei for an analysis of theoretical uncertainties [165,166]. In the m-scheme, the NCSM extended calculations to p-shell hypernuclei [37].

Since the HO states are not well suited for representing correlations of baryons induced by the short-range repulsion which is typical for baryonic interactions, usually interactions are unitarily transformed to soften them. The most commonly used approach for such a transformation is the similarity renormalization group (SRG) [195]. The unitary transformation is obtained by an evolution of the interaction that starts from the bare BB or 3B interaction. Thereby, besides the desired softening of the interactions, higher-body interactions are generated, the so-called induced interactions. Hypernuclear calculations where the transformation was performed up to the three-baryon level were first published by Wirth and Roth [191] and are nowadays the standard. The size of the missing four- and higher-body interactions is then estimated using the dependence on the SRG evolution parameter. On the other hand, a restriction of the SRG evolution up to the two-baryon level is problematic, as became clear very quickly. It leads to an unexpectedly large SRG parameter dependence of the binding energies for hypernuclei since the induced YNN forces are quite large [191,193]. Therefore, realistic calculations can only be done using special choices for the SRG parameter [38]. Fortunately, extending the calculations to the 3B level reduced the SRG parameter dependence drastically and leads to results that agree with bare calculations [55,193] for a wider range of the SRG parameters.

The J-NCSM was first extended to p-shell hypernuclei in Refs. [38,196] and also used for predictions of $S = -2$ hypernuclei [58, 59]. The details of the approach and the applications are discussed in the following sections.

Initial calculations of hypernuclei with chiral forces within the NCSM [36,37,52,53,191–193] were all based on a leading-order YN potential [39]. Such potentials provide only a fairly rough and qualitative description of the YN force and, in general, lead to a significant overestimation of the separation energies. This is no longer the case for forces at the NLO and N2LO level, as has been shown in Sections 2 and 4, and as will be seen from the results presented below.

5.2. Jacobi NCSM for hypernuclei

We follow here the formulation of the J-NCSM of Refs. [38,58]. The Hamilton operator of an $S = -1$ hypernucleus consisting of $A-1$ nucleons and the Λ or Σ hyperon can be written in the form

$$H = \sum_{i<j=1}^{A-1}\left(\frac{2\boldsymbol{p}_{ij}^2}{M(t_Y)} + V_{ij}^{\rm NN}\right) + \sum_{i=1}^{A-1}\left(\frac{m_N + m(t_Y)}{M(t_Y)}\frac{\boldsymbol{p}_{iY}^2}{2\mu_{NY}} + V_{iY}^{\rm YN} + \frac{1}{A-1}\left(m(t_Y) - m_\Lambda\right)\right) + \sum_{i<j<k=1}^{A-1} V_{ijk}^{\rm 3N} + \sum_{i<j=1}^{A-1} V_{ijY}^{\rm YNN}. \tag{5.1}$$

m_N, $m(t_Y)$ and μ_{NY} are nucleon-, hyperon-, and their reduced masses, respectively. $t_Y = 0$ and $t_Y = 1$ distinguish Λ and Σ masses. The relative kinetic energy is included in terms of pair terms. We include NN ($V^{\rm NN}$), 3N ($V^{\rm 3N}$), YN ($V^{\rm YN}$)and YNN ($V^{\rm YNN}$) interactions and neglect higher-body forces. Because of Λ-Σ conversion, the total rest mass of the system $M(t_Y) = (A-1)m_N + m(t_Y)$ also depends on the isospin of the hyperon. The relative pair momenta are defined as in Eq. (4.13)

$$\boldsymbol{p}_{ij} = \frac{1}{2}(\boldsymbol{k}_i - \boldsymbol{k}_j), \qquad \boldsymbol{p}_{iY} = \frac{m(t_Y)}{m_N + m(t_Y)}\boldsymbol{k}_i - \frac{m_N}{m_N + m(t_Y)}\boldsymbol{k}_Y. \tag{5.2}$$

5.2.1. $S = -1$ basis states

The appropriate basis states for the $S = -1$ hypernucleus are denoted as

$$\left|\alpha^{*(Y)}(\mathcal{N}JT)\right\rangle = |\mathcal{N}JT, \alpha_{A-1}\mathcal{N}_{A-1}J_{A-1}T_{A-1}\, n_Y(l_Y s_Y)I_Y t_Y; (J_{A-1}I_Y)J, (T_{A-1}t_Y)T\rangle \equiv |\bigcirc\!\!-\!\!\bullet\rangle. \tag{5.3}$$

We use α as a index for the A-body state. The basis state has a well defined total HO excitation $\mathcal{N}$, angular momentum J and isospin T. The $*(Y)$ indicates that the hyperon is coupled out of the A-body system. We assume here that we have already defined antisymmetrized states $|\alpha_{A-1}(\mathcal{N}_{A-1}J_{A-1}T_{A-1})\rangle$ of the $A-1$-nucleon subsystem as described in [187] with total HO quantum number $\mathcal{N}_{A-1}$, angular momentum J_{A-1}, and isospin T_{A-1}. The HO oscillator state describes the relative motion of the hyperon with respect to the $A-1$ cluster with HO quantum number n_Y, its orbital, spin and total angular momentum l_Y, s_Y and I_Y and its isospin t_Y. Note that $\mathcal{N} = \mathcal{N}_{A-1} + 2n_Y + l_Y$. The couplings of J_{A-1}, I_Y, T_{A-1} and t_Y to the total angular momentum and isospin is also indicated.

We drop the third component of J and T since the basis states themselves do not depend on them. The graphical representation on the right hand side shows the coupled out hyperon in red and the antisymmetrized $A-1$-nucleon state as gray blob. To complete the definition of the states, we assume that the HO state of the hyperon refers to Jacobi coordinates that are directed to towards the hyperon.

5.2.2. Separation of two- and three-baryon clusters

The basis states are not suitable for the implementation of the Hamilton operator. In Eq. (5.1), the terms are already arranged in a way that indicates the necessary steps for the application. The first part is the nuclear interaction and kinetic energy acting in a pair of nucleons. For this part, we require transition coefficients defined for the $A-1$ subsystem that couple out a pair of nucleons. The corresponding basis states are defined as

$$\left|\left(\alpha^{*(2)}\right)^{*(Y)}(\tilde{\mathcal{N}}\tilde{J}\tilde{T})\right\rangle = \left|\tilde{\mathcal{N}}\tilde{J}\tilde{T},\alpha^{*(2)}_{A-1}\mathcal{N}^{*(2)}_{A-1}J^{*(2)}_{A-1}T^{*(2)}_{A-1}\ \tilde{n}_Y(\tilde{l}_Y\tilde{s}_Y)\tilde{I}_Y\tilde{t}_Y;(J^{*(2)}_{A-1}\tilde{I}_Y)\tilde{J},(T^{*(2)}_{A-1}\tilde{t}_Y)\tilde{T}\right\rangle \equiv \left|\ \right\rangle. \tag{5.4}$$

The hyperon motion is described by the same quantum numbers $\tilde{n}_Y$, $\tilde{l}_Y$, $\tilde{s}_Y$, $\tilde{I}_Y$, and $\tilde{t}_Y$ as in Eq. (5.3). For the $A-1$ subcluster, states are used that couple out two nucleons as defined in Ref. [187]. Here, we identify the states by their total HO quantum number, angular momentum and isospin $\mathcal{N}^{*(2)}_{A-1}$, $J^{*(2)}_{A-1}$, $T^{*(2)}_{A-1}$ and an index $\alpha^{*(2)}_{A-1}$ that summarizes the quantum numbers of the NN subsystem and the $A-3$ subcluster. Eq. (5.4) also indicates the coupling of the different angular momenta and isospin. On the right hand side, we introduce a graphical representation of the states. Important for the application of the Hamilton operator are the transition coefficients between the states of Eqs. (5.3) and (5.4)

$$\langle\alpha^{*(Y)}|\left(\alpha^{*(2)}\right)^{*(Y)}\rangle = \langle\ |\ \rangle = \delta_{n_Y\tilde{n}_Y}\delta_{l_Y\tilde{l}_Y}\delta_{s_Y\tilde{s}_Y}\delta_{I_Y\tilde{I}_Y}\delta_{t_Y\tilde{t}_Y}\delta_{J\tilde{J}}\delta_{T\tilde{T}}\ \langle\ |\ \rangle_{A-1} \tag{5.5}$$

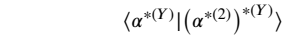

where $\langle\ |\ \rangle_{A-1}$ represent the transition coefficients for coupling out an NN cluster from the $A-1$ nucleon system [187].

For the application of an operator involving a YN pair, like the second term in Eq. (5.1), we need to couple out a YN pair. The corresponding states are defined as

$$\begin{aligned}|\alpha^{*(YN)}(\tilde{\mathcal{N}}\tilde{J}\tilde{T})\rangle &= |\tilde{\mathcal{N}}\tilde{J}\tilde{T},\tilde{n}_{\rm YN}(\tilde{l}_{YN}S_{\rm YN})\tilde{J}_{\rm YN}(\tilde{t}_Y\tilde{t}_N)\tilde{T}_{YN}\ \tilde{n}_\lambda\tilde{\lambda}\ \alpha_{A-2}\mathcal{N}_{A-2}J_{A-2}T_{A-2};(\tilde{J}_{YN}(\tilde{\lambda}J_{A-2})\tilde{I}_\lambda)\tilde{J},(\tilde{T}_{\rm YN}T_{A-2})\tilde{T}\rangle\\ &\equiv |\ \rangle.\end{aligned} \tag{5.6}$$

The state of the YN pair is defined by its HO quantum number $\tilde{n}_{\rm YN}$, the orbital angular momentum and the spin of the baryons $\tilde{l}_{YN}$, $S_{\rm YN}$ that couple to the total two-baryon angular momentum $\tilde{J}_{\rm YN}$. The isospin of the hyperon $\tilde{t}_Y$ and nucleon $\tilde{t}_N = 1/2$ couple to the YN isospin $\tilde{T}_{YN}$. The relative motion of the YN pair and the $A-2$ subcluster is given by its HO quantum number $\tilde{n}_\lambda$ and orbital angular momentum $\tilde{\lambda}$. The $A-2$ state is again given by an index α_{A-2} labeling the state within a block for fixed $\mathcal{N}$, J, and T. As before, we also include the angular momentum and isospin couplings and a graphical representation in Eq. (5.6). Note that coordinates related to the HO state $\tilde{n}_\lambda$, $\tilde{\lambda}$ point towards the $A-2$ subcluster. The calculation of the transition coefficients $\langle\alpha^{*(Y)}|\alpha^{*(YN)}\rangle = \langle\ |\ \rangle$ was outlined in Ref. [38]. The calculation of these coefficients relies on Talmi–Moshinsky (TM) brackets [197–199]. Because of the independence of the TM brackets of the HO frequency, also the transition coefficients and CFPs are independent of the HO frequency. The matrix elements have to be evaluated numerically. The values are publicly available via a python package for downloading the matrix elements in form of HDF5 files [200].

The third part of Eq. (5.1) involves the 3N interaction. For this part, we need to couple out a 3N cluster from our sets of states. In order to match the definition of the J-NCSM for ordinary nuclei [187], we define the states as follows

$$\begin{aligned}|\alpha^{*(A-4)*(Y)}(\tilde{\mathcal{N}}\tilde{J}\tilde{T})\rangle &= |\tilde{\mathcal{N}}\tilde{J}\tilde{T},\alpha^{*(A-4)}_{A-1}\mathcal{N}^{*(A-4)}_{A-1}J^{*(A-4)}_{A-1}T^{*(A-4)}_{A-1}\ \tilde{n}_Y(\tilde{l}_Y\tilde{s}_Y)\tilde{I}_Y\tilde{t}_Y;(J^{*(A-4)}_{A-1}\tilde{I}_\lambda)\tilde{J},(T^{*(A-4)}_{A-1}\tilde{t}_Y)\tilde{T}\rangle\\ &\equiv \left|\ \right\rangle.\end{aligned} \tag{5.7}$$

The notation $*(A-4)$ to couple out a cluster of $A-4$ nucleons leads to a 3N rest cluster and also defines that the $(3N)-(A-4)$ coordinate points towards the $A-4$ system. As before the hyperon is the spectator particle. The states $\alpha^{*(A-4)}_{A-1}$ index the possible combinations of $A=3$ clusters in the $A-1$ nucleon system with a rest cluster with $A-4$ systems. The total angular momentum $J^{*(A-4)}_{A-1}$ and isospin $T^{*(A-4)}_{A-1}$ of the $A-1$ nucleon system couples with the spectator angular momentum and isospin as indicate to the total angular momentum and isospin. The overlap with the basis states is then obtained by

$$\langle\alpha^{*(Y)}|\left(\alpha^{*(A-4)}\right)^{*(Y)}\rangle = \langle\ |\ \rangle = \delta_{n_Y\tilde{n}_Y}\delta_{l_Y\tilde{l}_Y}\delta_{s_Y\tilde{s}_Y}\delta_{I_Y\tilde{I}_Y}\delta_{t_Y\tilde{t}_Y}\delta_{J\tilde{J}}\delta_{T\tilde{T}}\ \langle\ |\ \rangle_{A-1}\ . \tag{5.8}$$

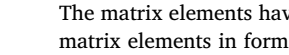

The transition coefficients $\langle\ |\ \rangle_{A-1}$ have been introduced in [187] and can also be obtained from [200].

Finally, for the last part of Eq. (5.1), we require coefficients that couple out a YNN cluster. These are defined for the basis states

$$\begin{aligned}|\alpha^{*(YNN)}(\tilde{\mathcal{N}}\tilde{J}\tilde{T})\rangle &= |\tilde{\mathcal{N}}\tilde{J}\tilde{T},\tilde{\alpha}_{\rm YNN}\tilde{\mathcal{N}}_{\rm YNN}\tilde{J}_{\rm YNN}\tilde{T}_{\rm YNN}\tilde{n}_\lambda\tilde{\lambda}\ \alpha_{A-3}\mathcal{N}_{A-3}J_{A-3}T_{A-3};(J_{\rm YNN}(\tilde{\lambda}J_{A-3})\tilde{I}_\lambda)\tilde{J},(\tilde{T}_{\rm YNN}T_{A-3})\tilde{T}\rangle\\ &\equiv \left|\ \right\rangle.\end{aligned} \tag{5.9}$$

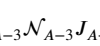

For convenience, we define the YNN states using a single index $\tilde{\alpha}_{\rm YNN}$ and its total HO quantum number $\tilde{\mathcal{N}}_{\rm YNN}$, angular momentum $\tilde{J}_{\rm YNN}$, and isospin $\tilde{T}_{\rm YNN}$. The index labels the different combinations of NN angular momentum and spin and hyperon angular momentum and spin as indicated in the graphical representation of the right hand side. Again the coupling of the different angular momentum and isospins is also given. The corresponding transition coefficients $\langle\ |\ \rangle$ need to be calculated numerically and are available for download at [200].

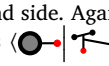

The CFP and transition coefficients are the basic ingredient of any J-NCSM calculations. Because the states are based on HO states, the coefficients conserve the total HO quantum number and are independent of the HO frequency which simplifies the calculations considerably. Unfortunately, HO states are not well suited for a direct solution of the Schrödinger equation for (hyper-)nuclear interactions. Their Gaussian long range behavior does not match the exponential tail of bound state wave functions. For the analysis, this difficulty can be partly overcome by matching the expected exponential behavior to the wave function results [201]. But for the calculation itself, a sufficient number of states is necessary for the tail of the wavefunctions. At the same time, a large number of states is required to represent any short range repulsion that is typical for (hyper-)nuclear interactions. Moreover, different frequency ranges are necessary for an optimal representation of the long- and short-range part of the wave functions. Especially for p-shell (hyper-)nuclei a softening of the chiral interactions is necessary to obtain converged results. The state-of-the-art method to soften the interaction is the SRG evolution described in Section 5.3.

5.2.3. $S = -2$ basis states

The extension to $S = -2$ requires to take into account two cases. First of all, two nucleons are replaced by $S = -1$ hyperons Λ and/or Σ, and second, one nucleon is replaced by a Ξ. In the first case, we need to take the Pauli principle into account for $\Lambda\Lambda$ and $\Sigma\Sigma$ states. We also assume that particle states follow a well defined ordering as defined in the two-baryon systems for the standard interactions [104]. Therefore, we only require $\Lambda\Sigma$ but no $\Sigma\Lambda$ states. The most natural coordinates that allow us to implement these constraints separate a hyperon–hyperon pair from $A-2$ nucleon system. The corresponding basis states read [58]

$$|\alpha^{*(Y_1Y_2)}(\mathcal{N}JT)\rangle = \Big|\mathcal{N}JT, \alpha_{A-2}\mathcal{N}_{A-2}J_{A-2}T_{A-2}\, n_{Y_1Y_2}(l_{Y_1Y_2}S_{Y_1Y_2})J_{Y_1Y_2}(t_{Y_1}t_{Y_2})T_{Y_1Y_2}\, n_\lambda\lambda; (J_{Y_1Y_2}(\lambda J_{A-2})I_\lambda)J,$$
$$(T_{Y_1Y_2}T_{A-2})T\Big\rangle \equiv \Big|$$  $$\Big\rangle\,. \tag{5.10}$$

The two hyperon labels $Y_1, Y_2 = \Lambda, \Sigma$ distinguish the three two-hyperon states $|\Lambda\Lambda\rangle$, $|\Lambda\Sigma\rangle$ and $|\Sigma\Sigma\rangle$. As before the index α_{A-2} labels the antisymmetrized $A-2$ nucleon states with total $\mathcal{N}_{A-2}$ HO excitation and angular momentum and isospin J_{A-2} and T_{A-2}. The YY subsystem is defined by its HO quantum number $n_{Y_1Y_2}$, the orbital angular momentum $l_{Y_1Y_2}$ and its spin and total angular momentum $S_{Y_1Y_2}$ and $J_{Y_1Y_2}$. The isospins of the first and second hyperon t_{Y_1} t_{Y_2} coupled to the YY isospin $T_{Y_1Y_2}$. The relative motion of the two clusters is given by the HO quantum number n_λ and its orbital angular momentum λ. The coupling to the total angular momentum of the $S = -2$ state J and its isospin T is also indicated. As usual, the total HO excitation is given by the sum of each part $\mathcal{N} = \mathcal{N}_{A-2} + 2n_\lambda + \lambda + 2n_{Y_1Y_2} + l_{Y_1Y_2}$

The Ξ states are defined in the same way as the $S = -1$ states of Eq. (5.3)

$$|\alpha^{*(\Xi)}(\mathcal{N}JT)\rangle = |\mathcal{N}JT, \alpha_{A-1}\mathcal{N}_{A-1}J_{A-1}T_{A-1}\, n_\Xi(l_\Xi s_\Xi)I_\Xi t_\Xi; (J_{A-1}I_\Xi)J, (T_{A-1}\, t_\Xi)T\rangle \equiv \Big|$$  $$\Big\rangle \tag{5.11}$$

including analogous definitions of the quantum numbers involved. In both, the hyperon–hyperon and the Ξ ones, the coordinate of the relative motion points towards the hyperon subcluster.

For the solution of the Schrödinger equation, the Hamilton operator needs to be expressed differently for basis states $|$  $\rangle$ and $|$  $\rangle$ and for transitions between these two sets of states. For the $|$  $\rangle$ states, the following terms contribute

$$\Big\langle$$ $$\Big|H\Big|$$  $$\Big\rangle = \sum_{i<j=1}^{A-2}\Big(\frac{2p_{ij}^2}{M(t_{Y_1},t_{Y_2})} + V_{ij}^{\rm NN}\Big) + \sum_{i=1}^{A-2}\Big(\frac{m_N + m(t_{Y_1})}{M(t_{Y_1},t_{Y_2})}\,\frac{p_{iY_1}^2}{2\mu_{iY_1}} + V_{iY_1}^{\rm YN} + \frac{m_N + m(t_{Y_2})}{M(t_{Y_1},t_{Y_2})}\,\frac{p_{iY_2}^2}{2\mu_{iY_2}} + V_{iY_2}^{\rm YN}\Big)$$
$$+ \frac{m(t_{Y_1}) + m(t_{Y_2})}{M(t_{Y_1},t_{Y2})}\,\frac{p_{Y_1Y_2}^2}{2\mu_{Y_1Y_2}} + V_{Y_1Y_2}^{\rm YY} + \big(m(t_{Y_1}) + m(t_{Y_2}) - 2m_\Lambda\big)\,. \tag{5.12}$$

The kinetic energies are expressed in pair particle momenta of two nucleons ($\boldsymbol{p}_{ij}$), a hyperon and a nucleon ($\boldsymbol{p}_{iY_k}$) and two hyperons ($\boldsymbol{p}_{Y_1Y_2}$). The total rest mass of the hypernucleus depends on the isospins of the two hyperons $M(t_{Y_1}, t_{Y_2})$ and the mass of kth hyperon $m(t_{Y_k})$ only on is isospin. The kinetic energies also depend on the reduced masses of the YN and YY system, μ_{iY_k} and $\mu_{Y_1Y_2}$. In this part of the Hamilton operator, the NN, YN and YY interactions contribute. The terms of the interactions and the kinetic energy are already grouped so that they can be applied in coordinates that separate NN, YN and YY pairs. For simplicity, we neglect all 3BFs although 3N and YNN forces are regularly applied. So far, no YYN forces or ΞNN have been included since the chiral ones have not been implemented and the SRG-induced YYN interactions are presumably small [58].

The next part of the Hamilton operator for the $\Big|$ $\Big\rangle$ states is

$$\Big\langle$$ $$\Big|H\Big|$$  $$\Big\rangle = \sum_{i<j=1}^{A-1}\Big(\frac{2p_{ij}^2}{M(\Xi)} + V_{ij}^{\rm NN}\Big) + \sum_{i=1}^{A-1}\Big(\frac{m_N + m_\Xi}{M(\Xi)}\,\frac{p_{\Xi i}^2}{2\mu_{\Xi i}} + V_{\Xi i}^{\Xi\rm N}\Big) + \big(m_\Xi + m_N - 2m_\Lambda\big) \tag{5.13}$$

Table 5.1
Combinatorial factors of the two-body YN interactions embedded in the A-body space with strangeness $S = -2$.

YN / transition	$\tilde{V}_{N\Lambda,N\Lambda}$	$\tilde{V}_{N\Lambda,N\Sigma}$	$\tilde{V}_{N\Sigma,N\Lambda}$	$\tilde{V}_{N\Sigma,N\Sigma}$
$\Lambda\Lambda \to \Lambda\Lambda$	$2(A-2)$	-	-	
$\Lambda\Lambda \to \Lambda\Sigma$	-	$\sqrt{2}(A-2)$	-	
$\Lambda\Sigma \to \Lambda\Sigma$	$A-2$	-	-	$A-2$
$\Lambda\Sigma \to \Sigma\Sigma$	-	$\sqrt{2}(A-2)$	-	-
$\Sigma\Sigma \to \Lambda\Sigma$	-	-	$\sqrt{2}(A-2)$	-
$\Sigma\Sigma \to \Sigma\Sigma$	-	-	-	$2(A-2)$

Table 5.2
Combinatorial factors of the two-body YY interactions embedded in the A-body space with strangeness $S = -2$.

YY / transition	$\tilde{V}_{\Lambda\Lambda,\Lambda\Lambda}$	$\tilde{V}_{\Lambda\Lambda,\Lambda\Sigma}$	$\tilde{V}_{\Lambda\Lambda,\Sigma\Sigma}$	$\tilde{V}_{\Lambda\Sigma,\Lambda\Sigma}$	$\tilde{V}_{\Lambda\Sigma,\Sigma\Sigma}$	$\tilde{V}_{\Sigma\Sigma,\Sigma\Sigma}$	$\tilde{V}_{\Lambda\Lambda,N\Xi}$	$\tilde{V}_{\Lambda\Sigma,N\Xi}$	$\tilde{V}_{\Sigma\Sigma,N\Xi}$	$\tilde{V}_{N\Xi,N\Xi}$
$\Lambda\Lambda \to \Lambda\Lambda$	1	-	-	-	-	-	-	-	-	-
$\Lambda\Lambda \to \Lambda\Sigma$	-	1	-	-	-	-	-	-	-	-
$\Lambda\Lambda \to \Sigma\Sigma$	-	-	1	-	-	-	-	-	-	-
$\Lambda\Sigma \to \Lambda\Sigma$	-	-	-	1	-	-	-	-	-	-
$\Lambda\Sigma \to \Sigma\Sigma$	-	-	-	-	1	-	-	-	-	-
$\Sigma\Sigma \to \Sigma\Sigma$	-	-	-	-	-	1	-	-	-	-
$\Lambda\Lambda \to N\Xi$	-	-	-	-	-	-	$\sqrt{A-1}$	-	-	-
$\Lambda\Sigma \to N\Xi$	-	-	-	-	-	-	-	$\sqrt{A-1}$	-	-
$\Sigma\Sigma \to N\Xi$	-	-	-	-	-	-	-	-	$\sqrt{A-1}$	-
$N\Xi \to N\Xi$	-	-	-	-	-	-	-	-	-	$A-1$

which includes terms that single out NN pairs and ΞN pairs. Additionally to Eq. (5.12), the total mass including the cascade particle $M(\Xi)$ and the reduced mass $\mu_{\Xi i}$ of the ΞN show up. In these coordinates, only the NN and ΞN interactions appear.

For transition matrix elements, only the interactions inducing the ΞN-$\Lambda\Lambda$-$\Lambda\Sigma$-$\Sigma\Sigma$ transitions enter

$$\langle \; \overset{Y_1}{\underset{Y_2}{\bullet\!-\!\bigcirc}} \Big| H \Big| \bigcirc\!-\!\overset{\Xi}{\bullet} \; \rangle = \sum_{i=1}^{A-1} V^{\mathrm{YY},\Xi\mathrm{N}}_{Y_1 Y_2,\Xi i} \,. \tag{5.14}$$

For the $S = -2$ systems, the different clusters have different symmetry properties. This leads to non-trivial combinatorial factors when reformulating the field theoretical interactions in second quantization into an ordinary Schrödinger equation. For a system of $A-2$ identical nucleons and YY or ΞN pairs, the factors for the YN interaction are summarized in Table 5.1 and for the YY interaction in Table 5.2 (see Appendix A of [58]). The factors also replace the sums in Eqs. (5.12), (5.13), and (5.14).

For the evaluation of the matrix elements, we again need transition coefficients to states that single out NN, YN, and YY pairs. Most simple are the transition to YY pairs. For the application of interactions to these states, the basis states Eq. (5.10) are already appropriate. For the NN pairs, we require transitions from both parts of the basis which can be related to the $A-2$ ($\langle \bigcirc\!\!\bullet\!\!-\!\!\bigcirc \rangle_{A-2}$)

and $A-1$ ($\langle$  $\rangle_{A-1}$) transition matrix elements for ordinary nuclei

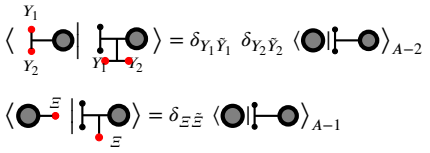

$$= \delta_{Y_1\bar{Y}_1}\ \delta_{Y_2\bar{Y}_2}\ \langle \quad \rangle_{A-2}$$

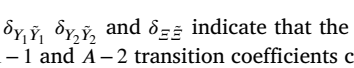

$$= \delta_{\Xi\bar{\Xi}}\ \langle \quad \rangle_{A-1} \tag{5.15}$$

Here, $\delta_{Y_1\bar{Y}_1}\ \delta_{Y_2\bar{Y}_2}$ and $\delta_{\Xi\bar{\Xi}}$ indicate that the quantum numbers related to the relative motion of the Y_1 and Y_2 and Ξ are conserved. The $A-1$ and $A-2$ transition coefficients can be calculated numerically as outlined in [187] and are available for download [200].

The transition for YN pairs is only necessary for  states. We define the two sets of states that either single out Y_1N or Y_2N pairs

$$\left|\left(\alpha^{*(Y_1N)}\right)^{*(Y_2)}(\tilde{\mathcal{N}}\tilde{J}\tilde{T})\right\rangle = |\tilde{\mathcal{N}}\tilde{J}\tilde{T}, \alpha^{*(Y_1N)}_{A-1}\mathcal{N}^{*(Y_1N)}_{A-1}J^{*(Y_1N)}_{A-1}T^{*(Y_1N)}_{A-1}\tilde{n}_{Y_2}(\tilde{l}_{Y_2}\tilde{s}_{Y_2})\tilde{I}_{Y_2}\tilde{t}_{Y_2}; (J^{*(Y_1N)}_{A-1}\tilde{I}_{Y_2})\tilde{J}, (T^{*(Y_1N)}_{A-1}\tilde{t}_{Y_2})\tilde{T}\rangle$$

$$\equiv \left| \quad \right\rangle$$

$$|\left(\alpha^{*(Y_2N)}\right)^{*(Y_1)}(\tilde{\mathcal{N}}\tilde{J}\tilde{T})\rangle = |\tilde{\mathcal{N}}\tilde{J}\tilde{T}, \alpha^{*(Y_2N)}_{A-1}\mathcal{N}^{*(Y_2N)}_{A-1}J^{*(Y_2N)}_{A-1}T^{*(Y_2N)}_{A-1}\tilde{n}_{Y_1}(\tilde{l}_{Y_1}s_{Y_1})\tilde{I}_{Y_1}\tilde{t}_{Y_1}; (J^{*(Y_2N)}_{A-1}\tilde{I}_{Y_1})\tilde{J}, (T^{*(Y_2N)}_{A-1}\tilde{t}_{Y_1})\tilde{T}\rangle$$

$$\equiv \left| \quad \right\rangle \tag{5.16}$$

keeping in mind that our ordering of states and the Pauli principal reduces the number of required YY pairs to $Y_1Y_2 = \Lambda\Lambda$, $\Lambda\Sigma$, and $\Sigma\Sigma$. The YN pair quantum numbers are labeled by an index $\alpha^{*(Y_iN)}_{A-1}$ of states with total HO quantum number $\mathcal{N}^{*(Y_iN)}_{A-1}$, total angular momentum $J^{*(Y_iN)}_{A-1}$, and total isospin $T^{*(Y_iN)}_{A-1}$. The spectator hyperon quantum numbers $\tilde{n}_{Y_i}$, $\tilde{l}_{Y_i}$, $s_{Y_i} = 1/2$, and $\tilde{t}_{Y_i}$ couple as indicated to total angular momentum and isospin. As usual, the coordinates point towards the coupled out baryons. The transition coefficients $\langle$ 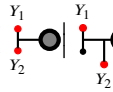 $\rangle$ and $\langle$ 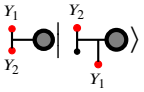 $\rangle$ for these states are derived in Ref. [58] and can also be downloaded from [200]. Based on these transition coefficients, Eqs. (5.12), (5.13), and (5.14) can be evaluated.

5.3. SRG evolution for chiral interactions

For the *ab-initio* studies of hypernuclei, we are mainly interested in results that are based on the modern chiral BB and 3B interactions described in Sections 2 and 3. It turns out that it is not possible to get converged NCSM calculations based on such interactions since even on today's supercomputers the model spaces required cannot be handled. This is already true for ordinary nuclei for $A > 4$ but becomes more pressing for hypernuclei due to the increased dimensions caused by particle conversions, like Λ-Σ or ΞN-YY. This issue can be resolved by performing unitary transformations of the underlying interactions that remove or mitigate the short range repulsion of typical nuclear interactions and reduce correlations of the baryons. In early NCSM calculations [202], the Lee-Suzuki [203] or Okubo [204] transformations were used based on a combination of the NN and HO interactions. The disadvantage of these approaches was that the procedure was only applicable to NCSM calculations for a specific nucleus. Therefore, it was difficult to compare results of calculations even when both were performed within the NCSM. Directly using the unitarily transformed interactions in few-baryon systems to obtain, e.g., scattering results was not possible. Unitary transformations that can be directly applied to the interactions like the V_{lowk} [205,206] or SRG [195] transformations are therefore preferable. Since all of these transformations induce many-baryon interactions, the SRG is nowadays the standard method for softening nuclear interactions for many-body calculations. For this approach, the calculation of three-baryon interactions is feasible and four-baryon interactions have been shown to be smaller than the expected uncertainty due to higher orders in the chiral expansion [48,207]. In the following, we give a brief introduction to SRG transformations.

The unitary SRG transformations can be obtained by solving flow equations for the Hamiltonian [195,208]. Introducing the flow parameter s, the unitary transformations $U(s)$ and the transformed Hamilton operator $H(s)$ are defined by

$$H(s) = U(s)H_0U^{\dagger}(s) \equiv T_{rel} + V(s). \tag{5.17}$$

Note that the potential $V(s)$ is defined such that the relative kinetic energy T_{rel} is not transformed. Starting point of the evolution is the bare Hamiltonian $H(0)$ for $s = 0$. s is then increased and therefore always positive. Following [195], we will utilize the more intuitive variable $\lambda = \left(\frac{4\mu^2}{s}\right)^{1/4}$ with $\mu = m_N/2$ for all BB forces. λ can be approximately identified with the width of the band

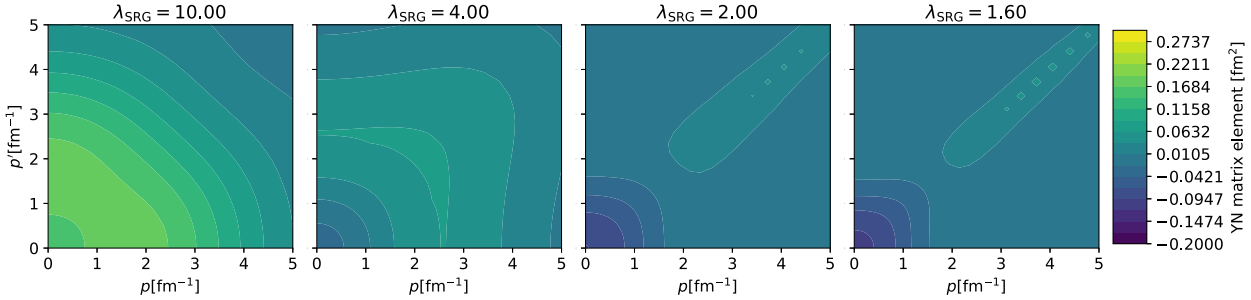

Fig. 5.1. SRG evolution of the ΛN interaction in the $^3S_1$ partial wave for (λ_{SRG} = 10, 4, 2 and 1.6 fm^{-1} (left to right) starting from the SMS N2LO(550) YN interaction. The matrix elements are given in fm^2 for ΛN relative momenta in fm^{-1}.

for which the SRG-evolved momentum space matrix elements of the interaction are non-zero. The flow equation is obtained by differentiating the transformation Eq. (5.17)

$$\frac{dH(s)}{ds} = \frac{dV(s)}{ds} = [\eta(s), H(s)] \tag{5.18}$$

where the generator

$$\eta(s) = \frac{dU(s)}{ds} U^\dagger(s) = -\eta^\dagger(s) \tag{5.19}$$

is an anti-hermitian operator. These equations can also be used to define the unitary transformation by choosing an appropriate anti-hermitian operator $\eta(s)$ and solving Eq. (5.18). Usually, $\eta(s)$ is taken as a commutator of the relative kinetic energy (without the mass shift in case of particle conversion) with the Hamiltonian: $\eta(s) = [\tilde{T}_{rel}, H(s)]$. This choice leads to a suppression of off-diagonal matrix elements in momentum space and softens the interaction. Other choices of generator have been discussed, e.g., in Refs. [191,208,209] and lead to Hamilton operators that are diagonal with respect to different quantum numbers or basis states. Note that our choice of η implies that s has the dimension [length]^2.

As usual, the unitary transformations generate higher-body interactions even when the bare interactions did not involve such many-body forces. Exact unitarity could only be achieved if all of these many-baryon interactions were generated. This is not feasible and would be even more complicated than directly solving the many-body problem using the bare interactions. The unitary transformations are nevertheless useful since it turns out that the most important contributions to the interactions generated by the transformation, so-called induced interactions, are two-baryon ones. For hypernuclei, the induced three-baryon interactions are quantitatively important. Four- and more-baryon interactions contribute much less than missing higher order terms in the chiral expansion and are therefore irrelevant, at least for light hypernuclei [48,207]. The SRG is particularly convenient since the two-baryon, three-baryon and higher-body contributions can be obtained step wise by solving the individual equations [195,210]

$$\frac{dV_{ij}(s)}{ds} = \left[\left[T_{ij}, V_{ij}(s)\right], T_{ij} + V_{ij}(s)\right] , \tag{5.20}$$

$$\begin{aligned}\frac{dV_{ijk}(s)}{ds} &= \left[\left[T_{ij}, V_{jj}(s)\right], V_{ki}(s) + V_{jk}(s) + V_{ijk}(s)\right] \\ &+ \left[\left[T_{jk}, V_{jk}(s)\right], V_{ki}(s) + V_{ij}(s) + V_{ijk}(s)\right] \\ &+ \left[\left[T_{ki}, V_{ki}(s)\right], V_{ij}(s) + V_{jk}(s) + V_{ijk}(s)\right] \\ &+ \left[\left[T_{ij} + T_k, V_{ijk}(s)\right], T_{ij} + T_k + V_{ij}(s) + V_{ij}(s) + V_{ki}(s) + V_{ijk}(s)\right] ,\end{aligned} \tag{5.21}$$

where i, j, k number the individual baryons of the pair interactions and triplets. These equations have been solved for nuclear and hypernuclear interactions either in a HO basis [193] or using momentum space [55,210]. In both cases, the matrix elements need to be expressed in the HO basis of the NCSM calculation. In the former case, this generally requires a frequency shift, the latter case, a momentum integration over HO wave functions.

Examples of the evolution in momentum space are shown in Figs. 5.1 and 5.2. In both cases, the evolution leads to a suppression of transitions from low to high momenta. For the BB interactions this can be clearly seen in the dependence of the matrix elements on the relative momenta $p_{\rm YN}$ in the YN system. For the YNN interaction, we show here the dependence on the hyper-momentum $\xi = \sqrt{p_{\rm NN}^2 + \frac{m_{\rm Y}+2m_{\rm N}}{4m_{\rm Y}} q_{\rm Y}^2}$ (Y=Λ, Σ)). For this example, we fix the hyper-angle $\cos\Phi = p_{\rm NN}/\xi = 1/2$. Fig. 5.2 shows the 3BFs for two-nucleon subsystem spin $S = 1$ with all orbital angular momenta equal to zero. In case of the YNN interaction, the ΛNN particle channel is shown. The comparison of the 3NF case (left) to the YNN case without bare YNN interaction (middle) confirms the naive expectation: for large λ_{SRG}, the 3NF is large with maximal matrix elements around 0.023 fm^5. For this SRG parameter, the interaction is almost completely given by the bare 3NFs and provides significant additional binding to typical nuclei. The further evolved 3NF to λ_{SRG} = 1.88 fm^{-1} is smaller in magnitude by a factor of almost 10. For this SRG parameter, the NN forces alone result in more binding making additional contributions of the 3NF much smaller. The middle column of Fig. 5.2 shows the opposite

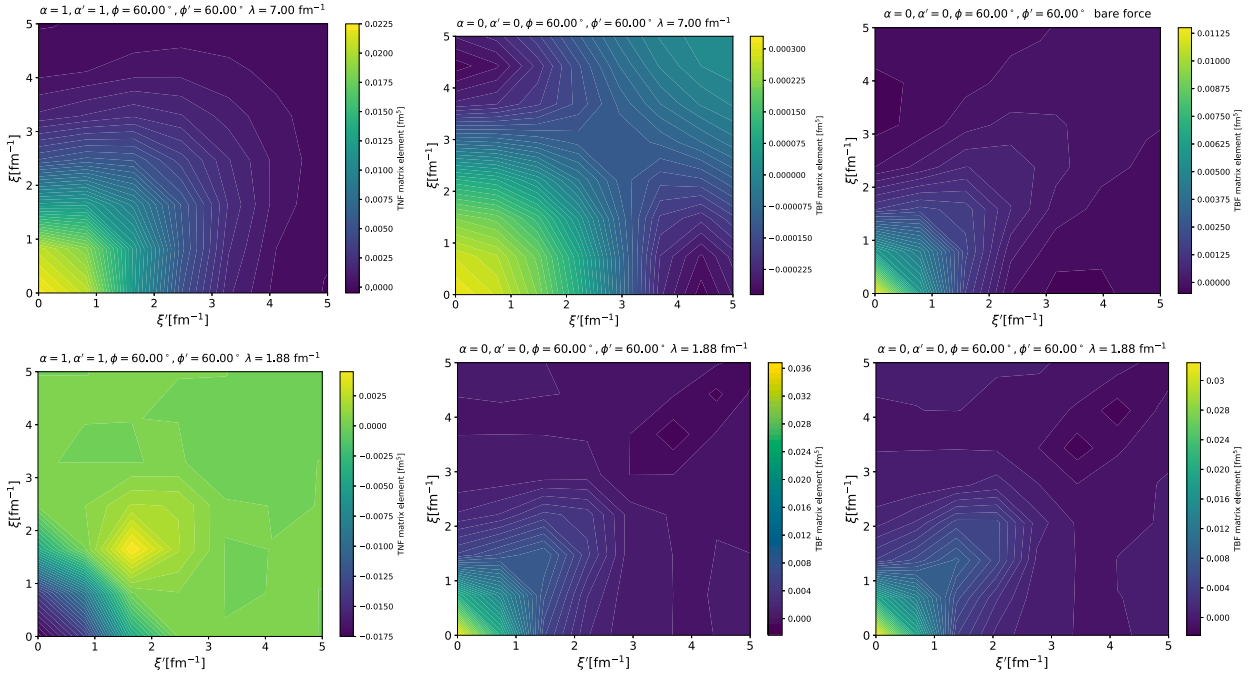

Fig. 5.2. Comparison of the SRG evolution of the 3N (left) and YNN (middle/right) interaction for 3B angular momentum and parity $J^\pi = 1/2^+$. The middle column is based on bare YN interactions only. The right one also includes chiral YNN forces. For the 3N (YNN) case, the isospin $T = 1/2$ (0) interaction is shown. The partial wave indices α are chosen such that the two-nucleon subsystem has $l_{12} = 0$ and $s_{12} = 1$. The third particle is in an s-wave. All evolutions start with the SMS N4LO$^+$(550) NN interaction and the appropriately adjusted chiral 3NF at N2LO. For the bare YN interaction, the SMS N2LO(550) one is used. In the left and middle column, λ_{SRG} is 7.0/1.88 fm^{-1} in the upper/lower panel. In the right column, the upper figure shows the bare fitted YNN force at N2LO and the lower the evolution of the combination to $\lambda_{SRG} = 1.88$ fm^{-1}. The matrix elements are given in fm^5 for hyper-momenta in fm^{-1}. The hyper-angles Φ are set to 60°.

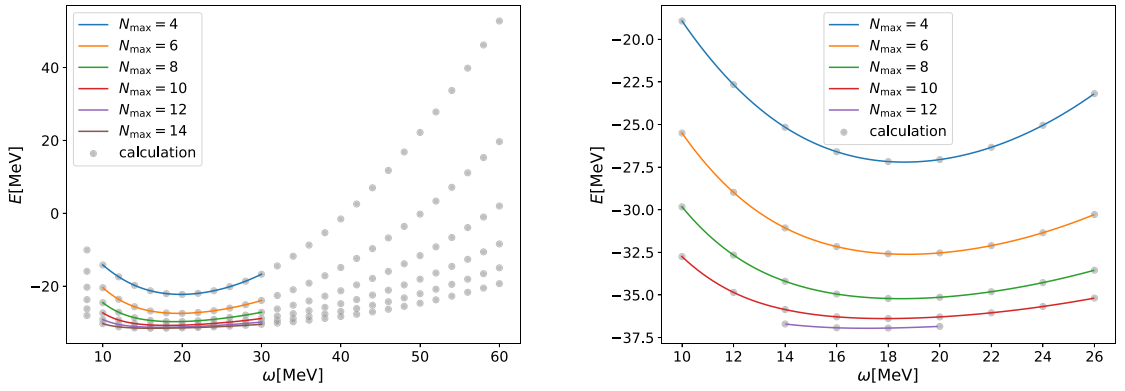

Fig. 5.3. ω and $N_{\max}$ dependence of the energy of the ground state of ^{6}Li (left) and $^7_\Lambda$Li (right) for $\lambda = 1.88$ fm^{-1} including the SRG evolved 3BF. For the bare interaction, the SMS N4LO$^+$(550) NN, the N2LO 3N and the N2LO(550^b) YN interaction was used.

trend for the YNN interaction starting without bare YNN force. At $\lambda_{SRG} = 7$ fm^{-1}, the matrix elements of the YNN force a tiny. Without evolved YNN force, the hypernuclear separation energies become very large at $\lambda_{SRG} = 1.88$ fm^{-1}. Therefore, the YNN force is even larger in magnitude than the bare 3NF. The right column exemplifies the same behavior for the case where a bare YNN force is considered. The matrix elements of the bare force are smaller but comparable to the 3NFs. The evolution then even increases the magnitude of matrix elements.

The change of the interaction leads to sufficient softening so that the NCSM calculations converge sufficiently fast to extract meaningful results. As an example, the results for $^7_\Lambda$Li are shown in Figs. 5.3 to 5.5. In Fig. 5.3, the full $N_{\max}$ and ω dependence is shown for the core nucleus ^{6}Li and $^7_\Lambda$Li. At this point, model spaces up to $N_{\max} = 12(14)$ for $^7_\Lambda$Li (^{6}Li) are feasible. The calculations have been performed for $\lambda_{\mathrm{SRG}} = 1.88$ fm^{-1} and include 3NFs and induced YNN forces. Since the 3BFs are included, the SRG

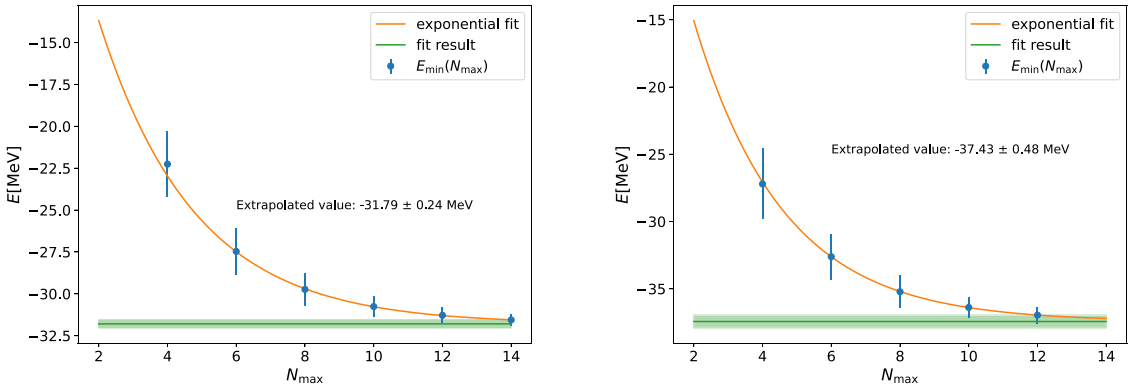

Fig. 5.4. $N_{\max}$ dependence of the minimum energy of the ground state of ^{6}Li (left) and $^{7}_{\Lambda}$Li (right). An exponential extrapolation is used to extract the binding energy results (also given in the figure together with the extrapolation uncertainty). Same interactions as in Fig. 5.3. See text for details.

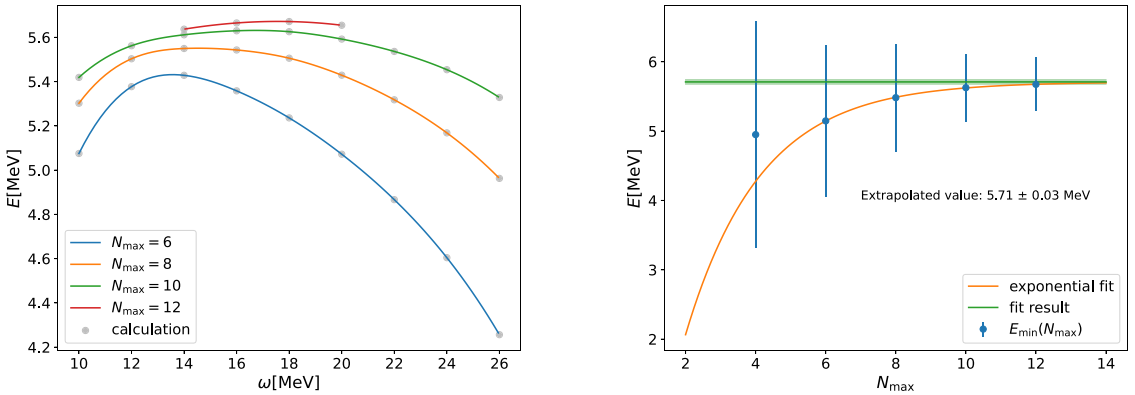

Fig. 5.5. Left: ω and $N_{\max}$ dependence of the Λ separation energy. Right: Convergence of the Λ separation energy with respect to $N_{\max}$. Both figures show results for the ground state of $^{7}_{\Lambda}$Li using the same interactions as in Fig. 5.3. See text for details.

dependence is small for SRG parameters in this range. On the other hand, the results are sufficiently converged to get results that are numerically more accurate than the expected uncertainty due to the chiral expansion.

We usually perform a simple exponential extrapolation as can be seen in Fig. 5.4. Other extrapolation methods using machine learning [211] or relating the HO frequencies and model space size to effective long and short distance cutoffs [166,212] are possible. However, we will see below that such sophisticated extractions are probably unnecessary for obtaining separation energies.

We use the minimum energies for each model space for the extrapolation to $N_{\max} \to \infty$. The uncertainty of this value is then derived from the curvature of the ω dependence in the minimum. This uncertainty is only used for a weighted exponential fit of the $N_{\max}$ dependence. The final uncertainty is conservatively estimated by the difference of the largest model space result and the extrapolated value. In this way, the energies of $^{7}_{\Lambda}$Li can be obtained with an uncertainty of approximately 500 keV. However, the dependence of the energy of the core nucleus on N_{max} is very similar as can be seen on the left hand side of Fig. 5.5. For the largest model space, the ω dependence of the difference of the ^{6}Li and $^{7}_{\Lambda}$Li energies for a specific ω and $N_{\max}$ almost becomes negligible. It is therefore much more accurate to directly extrapolate this difference.

We considered doing the extrapolation for the extrema of the ω dependence or by building the difference of the optimal energies of the core nucleus and hypernucleus for each $N_{\max}$ separately. It turns out that the latter choice allows for a more reliable extrapolation. The result of this scheme is shown on the right hand side of Fig. 5.5 leading to a determination of the separation energy with an accuracy of 30 keV. Obviously, this simple extrapolation procedure leads to quite accurate results for the separation energy even in the limited model spaces available. The numerical uncertainty is then significantly smaller than the expected chiral uncertainty and will usually be of minor importance. We note that the ω dependence can be quite efficiently calculated using the J-NCSM since the basis states have to be generated only once.

In the following sections, we present some recent results for light hypernuclei exactly for the same $\lambda_{SRG} = 1.88$ fm^{-1}. This value is a good compromise between speed of convergence and keeping induced many-body forces small.

Table 5.3
Contributions to CSB in the $A = 7$ and 8 isospin multiplets, based on the YN potentials NLO13(500) and NLO19(500) (including 3N forces and SRG-induced YNN interactions). The results are for the original potentials (without CSB force) and for the scenario CSB1, see text. Results by Gal [213] and by Hiyama et al. [214] are included for the ease of comparison. All energies are in keV. The estimated uncertainties for $A = 7$ and 8 systems are 30 and 50 keV, respectively.

		ΔT	$\Delta V_{\rm NN}$	$\Delta V_{\rm YN}$			ΔB_Λ
				$^1S_0$	$^3S_1$	total	
$^7_\Lambda$Be-$^7_\Lambda$Li*	NLO13-CSB	8	−24	−49	26	−24	−40
	NLO19-CSB	6	−41	−43	42	0	−35
	Hiyama [214]		−70			200	150
	Gal [213]	3	−70			50	−17
	experiment						−145 ± 107
$^7_\Lambda$Li*-$^7_\Lambda$He	NLO13-CSB	7	−14	−49	26	−24	−31
	NLO19-CSB	5	−21	−43	42	0	−16
	Hiyama [214]		−80			200	130
	Gal [215]	2	−80			50	−28
	experiment						−279 ± 141
$^8_\Lambda$Be-$^8_\Lambda$Li	NLO13-CSB	12	7	100	56	159	178
	NLO19-CSB	6	−11	62	79	147	143
	Hiyama [214]		40				160
	Gal [213]	11	−81			119	49
	experiment						51 ± 80

5.4. CSB for p-shell hypernuclei

In Section 4.3, we discussed the determination of the strength of CSB in YN interactions using the hypernuclear $A = 4$ isospin multiplet $^4_\Lambda$He/$^4_\Lambda$H. Although the independence of the chiral realization indicates that the approach is robust, cross checks with other available data are desirable. Such additional data can also serve to constrain the parameters more tightly in the future. Fortunately, data for more isospin multiplets are available (see Table 5.3 and Refs. [51,216]). As one can see, the uncertainty of the data is still significant. The $A = 8$ hypernuclei $^8_\Lambda$Be/$^8_\Lambda$Li form an isospin doublet and the CSB of the separation energies is defined similarly to the one for $A = 4$ hypernuclei in Eq. (4.17). In this case, both separation energies are fairly well known, based on the current Mainz evaluation [50], the CSB is 51 ± 80 keV. For $A = 7$ hypernuclei, the ground states of $^7_\Lambda$Be and $^7_\Lambda$He, and the excited isospin $T = 1$ state of $^7_\Lambda$Li form an isospin triplet. In the latter case, the separation energy is calculated with respect to the first excited $T = 1$ state in ^{6}Li. Based on the excitation energy [217] and the most recent determination of the ground state separation energy from the Mainz database [50], one obtains 5.305 ± 0.060 MeV for the separation energy of this state. The current world average for the separation energy of $^7_\Lambda$Be is 5.160 ± 0.089 MeV [50]. For $^7_\Lambda$He, the situation is more ambiguous since the old emulsion data and the new data from JLab are inconsistent with each other. Based on the new experiments at JLab [218,219], one obtains 5.584 ± 0.128 MeV [50]. The experimental values for the CSB in the table are based on these values.

The table shows our results for the CSB interactions of Section 4.3 and compares them to the experiment and the previous calculations of Refs. [213,214], performed within a cluster model and the shell model, respectively. Besides the total value ΔB_Λ for the CSB of the separation energies, also the different contributions from the kinetic energy ΔT, the NN potential $\Delta V_{\rm NN}$ and the YN potential $\Delta V_{\rm YN}$ are shown. For the latter one also the singlet and triplet contributions are separately shown. The kinetic energy contribution is small in all cases. For the NN interaction, which also includes effects from the Coulomb force, our full calculation leads to much smaller values than the previous approximate ones. (Note that the values of Gal for this part have been taken over simply from the cluster calculations of Hiyama et al.). Also the contribution from the YN force is different in all of the approaches. In $A = 7$, our full calculations predict generally smaller YN contributions sometimes even different in sign to the previous ones. Therefore, it is not surprising that the predicted CSB for the separation energies is smaller. Interestingly, we find that the sign of the contribution is different for $A = 7$ and $A = 8$. This is mainly caused by the opposite sign of the $^1S_0$ contribution. This highlights that a proper understanding of the CSB of the light hypernuclei also requires a proper representation of the spin dependence. The heavier hypernuclei have recently been investigated within a mean field approach [220]. In this case, the CSB is adjusted to $A = 12$ mirror hypernuclei and it was found that the spin dependence is small for heavier hypernuclei. Unfortunately, a direct comparison of both approaches for light hypernuclei and/or the resulting scattering lengths is not possible. It is also remarkable that the contribution from $^3S_1$ is still comparable to the one of $^1S_0$ although the effect on the corresponding scattering lengths is much larger for $^1S_0$.

The total CSB of the separation energies is also presented in Fig. 5.6. The figure shows our results for the scenario CSB1 of Ref. [54] and an additional scenario (CSB*) fitted to a recent experiment of the STAR collaboration [178]. It is reassuring to see that the predictions for NLO13 and NLO19 are very similar to each other for the CSB1 scenario. This indicates that the theory uncertainty is small once the $A = 4$ CSB is accurately determined. Using the STAR input (CSB*) for $A = 4$, also the predictions for $A = 7$ and 8 shift visibly. Given the still quite larger experimental error bars, both scenarios are more or less consistent with the experimental data. The most problematic case is certainly $^7_\Lambda$Li/$^7_\Lambda$He. As discussed above, here the experimental situation is much

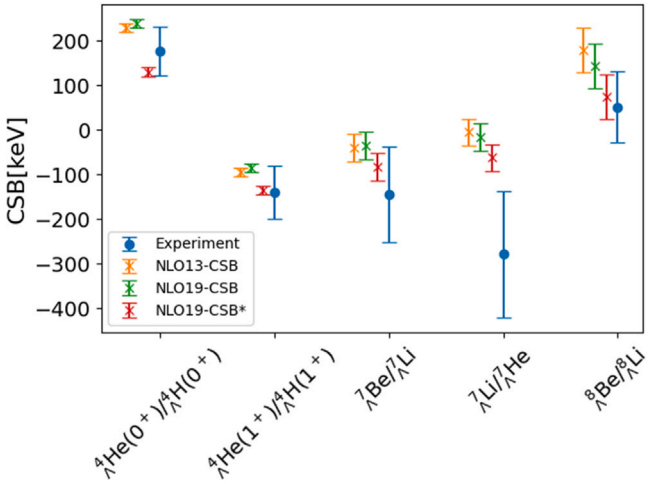

Fig. 5.6. CSB of Λ separation energies for $A = 4$ to 8 hypernuclei. Experimental values obtained as described in the text are compared to results for three CSB YN interactions: the scenario CSB1 for NLO13 (orange) and NLO19 (green) of Ref. [54] and to the alternative scenario fitted to experimental values of the STAR collaboration [178] for NLO19 (red). Error bars on the theoretical values are numerical uncertainties.

less clear. Note also that the theoretical results indicate that the CSB for those two hypernuclei is similar to $^{7}_{\Lambda}$Be/$^{7}_{\Lambda}$Li whereas the experiment suggests a larger value in the former systems. Also note that the CSB* scenario seems to be in better agreement with experiment and that both scenarios are able to reproduce the sign change of the CSB for $A = 7$ and 8. This could not be achieved within the cluster model [214].

In summary, our calculations can reproduce the non-trivial features for the CSB of $A = 7$ and $A = 8$ hypernuclei. This supports that the chiral interactions fitted to the $A = 4$ data provide a realistic description for this aspect. In the future, more accurate data for separation energies of the light isomultiplets will provide firmer constraints for the strength of the Λn interaction.

5.5. Application of chiral YNN interactions

YN interactions based on phenomenological approaches result in very different predictions even for the light hypernuclei, and even when their description of ΛN and ΣN data is quite similar [31,41]. It was therefore clear for many years that reliable predictions for the separation energies can only be obtained when including YNN interactions properly. With the chiral approach, the inclusions of consistent YN, NN, 3N and YNN forces becomes possible. The formulation of corresponding forces has already been discussed in Section 3. In this section, we discuss the first steps towards applying these interactions. The first applications of the ΛNN interaction have been done using momentum space in Refs. [221,222]. In order to check the numerical implementation of the partial waves decomposition, these results have been benchmarked in Ref. [223].

As described in Section 3, YNN forces depend on a large number of LECs which essentially need to be determined by fits to hypernuclear data. Given the scarceness of the available data, this is impossible in the foreseeable future. The probably most viable path to a realistic inclusion of YNN force is therefore making use of the decuplet saturation as described in Section 3.5. Using SU(6) symmetry, within decuplet saturation the 3BFs only depend on the two contact LECs H_1 and H_2. At the same time, the estimates discussed in Section 4.4 show that its contribution to $^{3}_{\Lambda}$H is likely negligible and that the $A = 4$ hypernuclei are the lightest ones that can be used for a determination of the YNN LECs. Therefore, in a naïve expectation one could determine H_1 and H_2 by a fit to the 0^+ and 1^+ states of the $A = 4$ hypernuclei.[5] Unfortunately, the explicit calculation showed that a consistent description of both states cannot be achieved with any combination of H_1 and H_2. In reality, the dependence of these separation energies on H_1 and H_2 is strongly correlated. These observations are easily explained when looking at the decuplet saturation for the most important ΛNN matrix elements (see Eq. (3.34)). In turns out that these matrix elements only depend on the linear combination $H_1 + 3H_2$, i.e. essentially only on one LEC. This freedom in the parameter can be used to get a consistent description of the 1^+ state in $A = 4$ and of the $A = 5$ separation energy. The 0^+ state in $A = 4$ is then not well described. In order to also improve the description of this state, it is necessary to add further terms of the YNN forces [49]. Since a full calculation without decuplet saturation involves too many unknown LECs, as already mentioned above, it was most practical to only select a simple term that promises to provide the necessary spin dependence. Such a term can be identified in the set of ΛNN contact terms of Eq. (3.20). Decuplet saturation sets the spin dependent C_2' term to zero. As shown in Ref. [49], by including this term with a non-zero LEC, a consistent description

[5] The separation energy differences of $^{4}_{\Lambda}$H/$^{4}_{\Lambda}$He is due to CSB and cannot be used to determine any parameter in the isospin conserving LO YNN forces.

Table 5.4
Separation energies for $A = 3 - 7$ hypernuclei with angular momentum and parity J^π and isospin T in MeV, calculated without and with inclusion of YNN 3BFs. The number in parenthesis indicates the estimated extrapolation uncertainties of the J-NCSM uncertainty and do not include the uncertainty due to higher order terms in the chiral expansion (see Fig. 5.7). All results are based on the N4LO$^+$(550) SMS NN potential [95], the corresponding N2LO(550) 3NF (see Table 1 of Ref. [48]) and the N2LO(550^b) YN potential and include the SRG-evolution up to the 3B level for $\lambda_{SRG} = 1.88$ fm^{-1}. In the third column (YNN(sat)) the YNN forces using properly adjusted parameters H_1 and H_2 are added. In the fourth column, the C_2' term is added additionally.

${}^A_\Lambda$Z(J^π, T)	w/o YNN	YNN(sat)	YNN(sat+C_2')	Expt. [50]
${}^3_\Lambda$H$(1/2^+, 0)$	0.121(4)	0.125(4)	0.155(3)	0.164(43)
${}^4_\Lambda$He $(0^+, 1/2)$	1.954(1)	2.027(3)	2.220(2)	2.258(55) (average) 2.169(42) (${}^4_\Lambda$H) 2.347(36) (${}^4_\Lambda$He)
${}^4_\Lambda$He $(1^+, 1/2)$	1.168(20)	1.010(11)	0.984(12)	1.011(72) (average) 1.081(46) (${}^4_\Lambda$H) 0.942(36) (${}^4_\Lambda$He)
${}^5_\Lambda$He$(1/2^+, 0)$	3.518(20)	3.152(21)	3.196(20)	3.102(30)
${}^7_\Lambda$Li$(1/2^+, 0)$	5.719(56)	5.444(57)	5.623(52)	5.619(60)
${}^7_\Lambda$Li$(3/2^+, 0)$	5.522(70)	5.042(65)	5.040(57)	4.927(60)
${}^7_\Lambda$Li$(5/2^+, 0)$	3.440(66)	3.205(65)	3.356(60)	3.568(60)

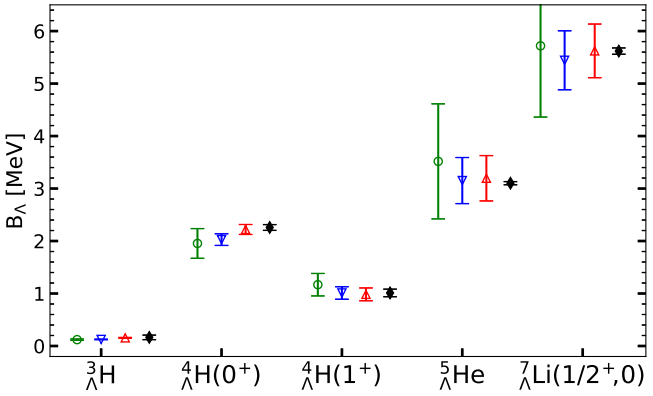

Fig. 5.7. Separation energies of $A = 3 \to 7$ hypernuclei based on the N4LO$^+$(550) SMS NN potential [95], the corresponding N2LO(550) 3NF (see Table 1 of Ref. [48]) and the N2LO(550^b) YN potential. The uncertainty is obtained as described in Section 4.4. All interactions are evolved to $\lambda = 1.88$ fm^{-1} including the induced 3BFs. The green circle is the result without chiral YNN force, and with the NLO uncertainty. The blue downward triangle is the result including the decuplet saturated YNN force and the red upward triangle also includes the C_2' term. Here, the uncertainty is given by the N2LO uncertainty. The black diamond is the experimental result [50].

of $A = 4$ and $A = 5$ states is possible. In fact, the values of H_1 and H_2 were not even changed since the main contribution of this term is to the 0^+ state. The resulting energies are shown in Table 5.4. It is interesting to look at the contribution of the individual 3BFs to ${}^3_\Lambda$H. The pure decuplet saturation (YNN(sat)) only contributes a tiny 4 keV to this energy. Only the additional C_2' term adds about 30 keV additional binding to this hypernucleus. This is only slightly larger than the estimate of Section 4.4 and still below the experimental uncertainty of 40 keV. The fit of the LECs was performed for the $A = 4$ energies. Since the interaction does not include CSB terms, the averaged values for ${}^4_\Lambda$H and ${}^4_\Lambda$He were used. For YNN(sat) this is by construction in agreement with the experimental value for the 1^+ state. Adding the C_2' term only led to changes within the uncertainties for this state, so that a refit of H_1 and H_2 was not necessary.

In Fig. 5.7, the energies are plotted together with uncertainties due to the truncation of the chiral expansion. Without YNN forces, we use the NLO uncertainty. When including the YNN force, we assume that we have included the dominant part of the YNN force and therefore use the N2LO uncertainty. The agreement of the experimental values is generally much better than expected from the uncertainty estimates which supports that our assumption is justified. Clearly, the appropriate choice of the uncertainty estimate should be investigated more systematically in the future.

It is remarkable that fixing the energy of the 1^+ state also leads to a good description of the ${}^5_\Lambda$He ground state. The only visible difference of the YNN(sat) calculation and the one with C_2' term appears for the 0^+ state. It is also reassuring to observe that adding YNN forces improves the agreement with experiment for ${}^7_\Lambda$Li. Note that the YNN force acts repulsively for all of the examples except ${}^3_\Lambda$H and the 0^+ state of $A = 4$.

Finally, in Fig. 5.8, the excitation energies for ${}^7_\Lambda$Li are shown. These energies are experimentally known with very high accuracy. Without YNN force, the doublet splitting for the lower states are too small and the ordering of states in the second doublet is

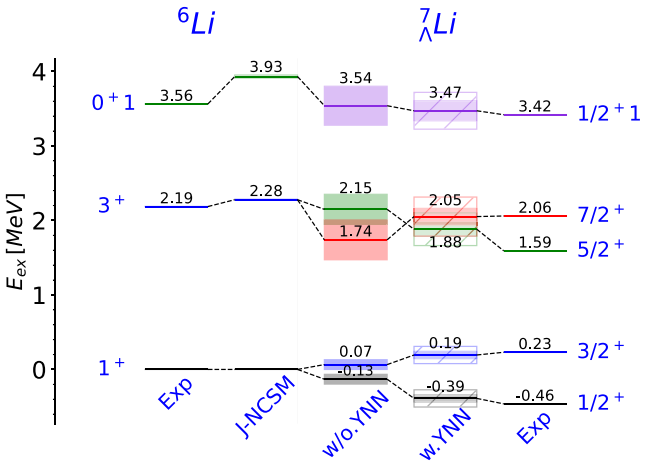

Fig. 5.8. Spectrum of excitation energies of $^7_\Lambda$Li based on the N4LO$^+$(550) SMS NN potential [95], the corresponding N2LO(550) 3NF (see Table 1 of Ref. [48]) and the N2LO(550^b) YN potential. The uncertainty is obtained as described in Section 4.4. All interactions are evolved to $\lambda = 1.88$ fm^{-1} including the induced 3BFs. Results are shown without chiral YNN forces (full band NLO uncertainty) and with chiral YNN forces (full band N2LO uncertainty, hatched band NLO uncertainty) including the C_2' term. Experimental uncertainties are almost invisible.

wrong. For the lowest doublet, the uncertainties are quite small and indicate a deviation from experiment when no YNN force is considered. This improves when including the YNN forces. In the figure, we only show the calculation including the C_2' term. Without this additional spin dependence, there is still an improvement but the increase of the splitting is somewhat smaller. The YNN force corrects the ordering within the upper doublet. For the isospin 1 state, there is almost no effect from the YNN force. In summary, the YNN force that describes the *s*-shell hypernuclei fairly well also leads to an improved description for this *p*-shell hypernucleus.

Note that our work on *p*-shell hypernuclei in general is still work in progress. It will be especially important to get more insight into the uncertainty estimates by, e.g. variation of the cutoff or by adding other YNN interaction terms that are not contributing when one resorts to the decuplet saturation approximation.

5.6. $\Lambda\Lambda$ hypernuclei and the strength of the $S = -2$ interaction

As has been discussed in Section 2.2.2, there is only very sparse direct scattering information on the $S = -2$ interaction. To determine the strength of the $\Lambda\Lambda$ interaction, it is therefore even more important than in the YN sector to take information from hypernuclei into account. But also experiments on $\Lambda\Lambda$ hypernuclei are difficult. Therefore, only a few events have been identified [50] for $A = 6$ and 10 to 13 hypernuclei. Fortunately, the lightest system, for which binding energies have been determined, is $^{\ 6}_{\Lambda\Lambda}$He and is within the reach of J-NCSM calculations. Note that the most accepted experimental result for this hypernucleus [224] has been corrected in [225,226] because the recommendation for the Ξ mass was changed.

Double Λ hypernuclei have already been investigated within the stochastical variational approach [57,227,228], using for very light systems Faddeev–Yakubovsky equations [229], and within cluster models [230–233]. These calculations have mostly been performed with simplified interactions omitting $\Lambda\Lambda$-$\Sigma\Sigma$-ΞN transitions. The common aim was to determine a reasonable strength of the underlying interactions such that all available hypernuclei could be described and use this to identify possible other bound states in $S = -2$. In Ref. [57], a pionless EFT approach was used for the interaction and it was found that $^{\ 5}_{\Lambda\Lambda}$He is most likely bound whereas $^{\ 4}_{\Lambda\Lambda}$H is probably not particle stable against decay to $^3_\Lambda$H and Λ. Note that it is mostly the experimental binding energy of $^{\ 6}_{\Lambda\Lambda}$He that determines the strength of the $\Lambda\Lambda$ interaction in such a calculation, and that, due to the Pauli principle, only the spin singlet can contribute to the *S*-wave interaction. Ambiguities because of the spin dependence are therefore suppressed in this case.

The first calculations based on realistic chiral interactions have been performed in Ref. [58]. Commonly, one defines the so-called $\Lambda\Lambda$ excess binding energy

$$\Delta B_{\Lambda\Lambda}(^{\ A}_{\Lambda\Lambda}\mathrm{X}) = B_{\Lambda\Lambda}(^{\ A}_{\Lambda\Lambda}\mathrm{X}) - 2B_\Lambda(^{A-1}_{\ \Lambda}\mathrm{X}) = 2E(^{A-1}_{\ \Lambda}\mathrm{X}) - E(^{\ A}_{\Lambda\Lambda}\mathrm{X}) - E(^{A-2}\mathrm{X}) \tag{5.22}$$

as a difference of double Λ separation energies $B_{\Lambda\Lambda}$ or binding energies $E(^{\ A}_{\Lambda\Lambda}\mathrm{X})$, the single Λ separation energies B_Λ or binding energies $E(^{A-1}_{\ \Lambda}\mathrm{X})$, and the energy of the core nucleus $E(^{A-2}\mathrm{X})$. It quantifies the contribution to the binding energy due to the $\Lambda\Lambda$ pair. In Ref. [58], the calculations have been performed neglecting all contributions of 3BFs. In order to still arrive at realistic values for the energies of these hypernuclei, the SRG evolution was done to specifically chosen λ_{SRG} parameters that lead to a realistic description for the binding energy of the core nucleus and of the single Λ core nuclei [38]. Specifically, for NN, the SMS N4LO$^+$(450) [95] evolved to $\lambda_{\mathrm{NN}} = 1.6$ fm^{-1} and, for YN, the NLO19(650) [41] evolved to $\lambda_{\mathrm{YN}} = 0.868$ fm^{-1} was used. For the $S = -2$ interaction, the LO(600) [234] and NLO(600) [104] were employed. The parameters of these interactions are consistent with the scarce YY data that is available (see Section 2.2.2).

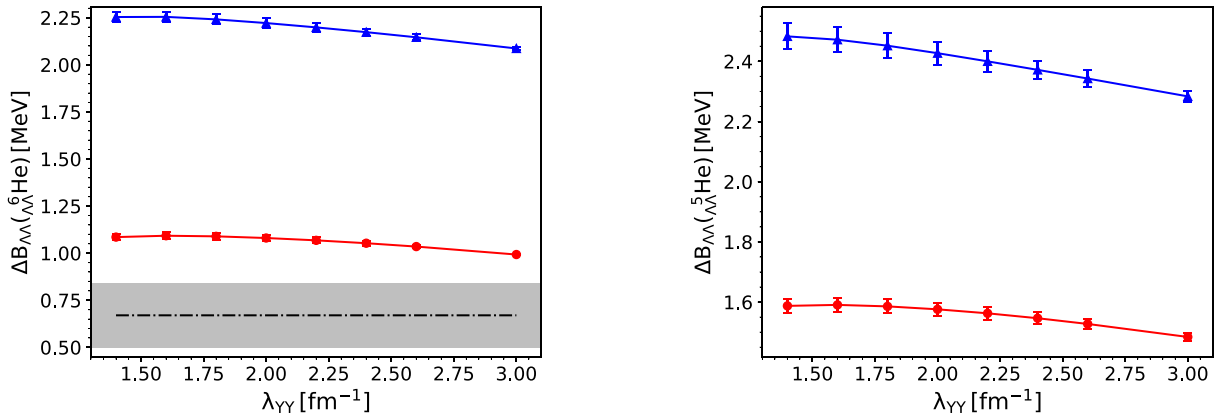

Fig. 5.9. $\Lambda\Lambda$ excess energies $\Delta B_{\Lambda\Lambda}$ of ${}^{6}_{\Lambda\Lambda}$He (left) and ${}^{5}_{\Lambda\Lambda}$He (right). depending on the SRG parameter of the YY interaction λ_{YY}. Results for the LO(600) (blue triangles) and NLO(600) (red circles) YY interactions are compared. The experimental result for ${}^{6}_{\Lambda\Lambda}$He is also shown (dashed dotted line and gray band) [224,225]. The SMS N4LO^{+}(450) [95] NN interaction evolved to $\lambda_{\rm NN} = 1.6$ fm^{-1} and the NLO19(650) [41] YN interaction evolved to $\lambda_{\rm YN} = 0.868$ fm^{-1} was used. Uncertainties of the theoretical calculations are due to extrapolation in model-space size.

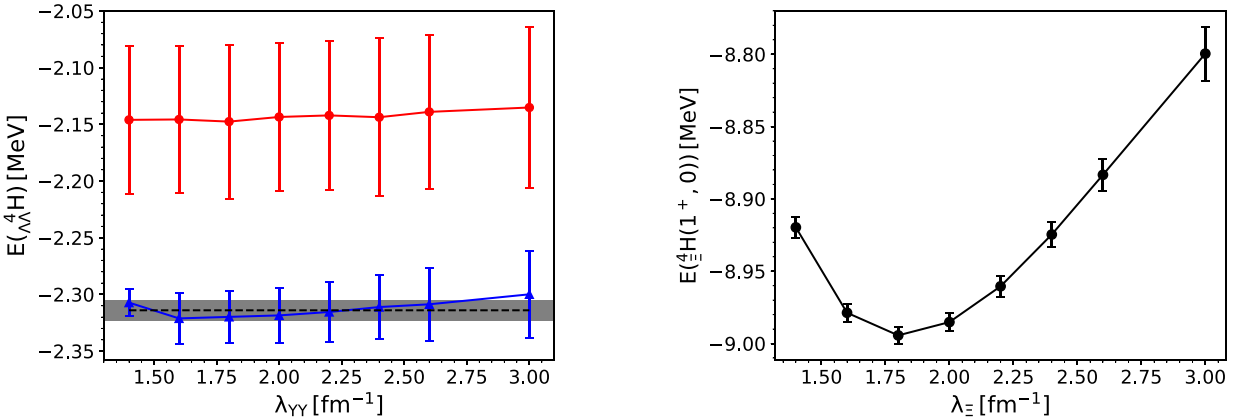

Fig. 5.10. Binding energies E of ${}^{4}_{\Lambda\Lambda}$H (left) and ${}^{4}_{\Xi}$H$(1^{+}, 0)$ (right) depending on the SRG parameter of the YY (ΞN) interaction λ_{YY} (λ_{Ξ}). The SMS N4LO^{+}(450) [95] NN interaction evolved to $\lambda_{\rm NN} = 1.6$ fm^{-1} and the NLO19(650) [41] YN interaction evolved to $\lambda_{\rm YN} = 0.868$ fm^{-1} was used. On the left, results for the LO(600) (blue triangles) and NLO(600) (red circles) YY interactions are compared to the experimental binding energy of ${}^{3}_{\Lambda}$H (dashed line and gray band) [158]. On the right, the results for the NLO ΞN interaction was used (black circles and line). Uncertainties of the theoretical calculations are due to extrapolation in model-space size.

The left hand side of Fig. 5.9 shows the result for ${}^{6}_{\Lambda\Lambda}$He in comparison to the experimental result. Fortunately, the dependence on λ_{YY} is small. LO and NLO energies are both more attractive than necessary to explain the data. Whereas the NLO one is still in fair agreement,[6] the LO result is in clear deviation from the data. We stress that these results are pure predictions and that the energies of ${}^{6}_{\Lambda\Lambda}$He have not been used to determine the YY force parameters.

Given that at least the NLO energy is quite realistic, it is now also interesting to predict energies of other s-shell double Λ hypernuclei. The results for ${}^{5}_{\Lambda\Lambda}$He are shown on the right hand side of Fig. 5.9. Again the λ_{YY} dependence is mild. First of all, the positive excess energy for LO and NLO indicate that this system is probably bound so that experimental searches seem to be promising. The results also show a significant increase of the excess energy from approximately 1 MeV to 1.5 MeV when going from $A = 6$ to $A = 5$ for the more realistic NLO interaction. It is conceivable that this increase is a signature of the transition to ΞN which should be suppressed because of isospin conservation in ${}^{6}_{\Lambda\Lambda}$He. An experimental determination of the energy for $A = 5$ will therefore provide new and independent information on the YY interaction.

Going further, we show energy results for ${}^{4}_{\Lambda\Lambda}$H on the left-hand side of Fig. 5.10. Energies below the hypertriton energy shown as a gray band imply a bound $A = 4$ double Λ hypernucleus. The LO result is close to this threshold, however, the more realistic NLO results are clearly above the threshold making a bound $A = 4$ system unlikely.

[6] Error bars are only due to the model-space extrapolation. The probably larger uncertainty due to the chiral expansion could not be quantified yet.

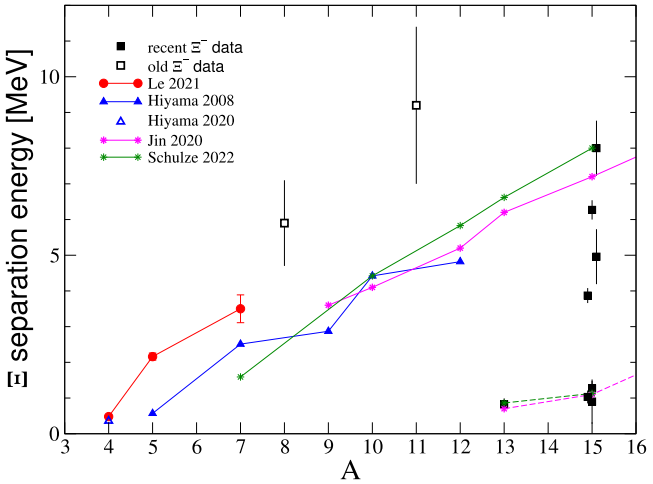

Fig. 5.11. Ξ hypernuclei: past and present experiments, predictions from theory. Shown are theoretical results by Jin et al. [248] and Schulze et al. [254] from a Skyrme model (stars), by Hiyama et al. obtained in a cluster model [251] and from a variational calculation [56] (filled and open triangles), and the NCSM results by Le et al. [59] (circles). Recent data for ${}^{15}_{\Xi}$C [244,245] and ${}^{13}_{\Xi}$B [241] are indicated by filled squares. Older but inconclusive results from the past [255] are shown as open squares. The solid and dashed lines connect *s*-shell and *p*-shell states, respectively.

In summary, we find that realistic chiral $S = -2$ interactions lead to a reasonable description of the $A = 6$ system and predict that an $A = 5$ double Λ hypernucleus likely exists. An experimental confirmation of this expectation will be most welcome in view of the possible insight into the importance for $\Lambda\Lambda$-$\Sigma\Sigma$-ΞN conversion.

5.7. Ξ-hypernuclei as a probe of the ΞN interaction

The ΞN interaction is strongly linked to the $\Lambda\Lambda$ interaction because of the importance of $\Lambda\Lambda$-$\Sigma\Sigma$-ΞN conversion. In the last section, we have therefore considered it as a byproduct of the $\Lambda\Lambda$ case. But the interaction itself is also interesting because several different S-wave channels contribute. We will see below that the different states of the light Ξ-hypernuclei reflect the freedom of spin and isospin in the ΞN channels. Moreover, the ΞN interaction could have direct impact on the EOS and the properties of neutron stars [235]. While in some scenarios Ξ hyperons appear only at fairly large density [236], others suggest a very early onset of the appearance of Ξ's (specifically of the Ξ^-) in nuclear matter [170,237,238]. As discussed in Section 2.2.2, only very scarce experimental information on the strength of the interaction is available and the lattice QCD simulations for this interaction still bear large uncertainties. In fact, the original version of the chiral $S = -2$ potential [104] leads to a repulsive interaction in the ${}^{(2I+1)(2S+1)}L_J = {}^{33}S_1$ partial wave and was too repulsive to explain observations of Ξ-hypernuclei. In Ref. [108], the potential was therefore appropriately readjusted while keeping it consistent with the available empirical constraints on the ΞN interaction. Our calculations below use this updated potential.

In order to further constrain the LECs, more detailed experimental information on Ξ-hypernuclei are highly desirable. Due to the strong conversion process to $\Lambda\Lambda$, their identification is not so easy since a decay to $\Lambda\Lambda$ can be expected. Older experimental searches were inconclusive only providing hints [239,240], but in recent years some evidence for a ${}^{13}_{\Xi}$B bound state was found [241] and, in the reaction ^{12}C(K^-, K^+), also for ${}^{12}_{\Xi}$Be [242]. In emulsion experiments several events of a possible ${}^{15}_{\Xi}$C bound state have been identified [243–245] which seem to stem from different states of this hypernucleus. Unfortunately, some of the events found are not fully consistent with each other, see the overviews in Refs. [245,246], triggering a discussion on the correct assignment and its impact on the strength of the interaction [247].

Theoretically, the Ξ-hypernuclei have been studied within mean field approaches [231,247–250] and a cluster approximation [251]. Such calculations help to clarify the assignment of the states although an unambiguous result has not been reached yet. Unfortunately, a direct calculation within the J-NCSM is not possible at this time because the interesting Ξ-hypernucleus state will be converted into a $\Lambda\Lambda$ state so that the calculations would then correspond to the related double Λ states. Fortunately, it turns out that the ΞN-$\Lambda\Lambda$ transition is accidentally weak for chiral interactions [104,108] and in lattice QCD simulations [88]. This justifies removing the $\Lambda\Lambda$ channel and readjusting the ΞN interaction so that all observables not involving the $\Lambda\Lambda$ states are well reproduced. The transition matrix elements of the interaction can then be included perturbatively for a width estimate [56,251].

Ξ-nuclear bound states have already been studied based on the ESC08c [252] potential. For this interaction several $A = 4$ bound states have been found. Based on the HAL QCD potential only the state with angular momentum, parity and isospin $(J^\pi, T) = (1^+, 0)$ could be confirmed [56]. The ΞNN system was also investigated for chiral interactions and it was found that the $A = 3$ Ξ-hypernuclei are not bound [253].

In Ref. [59], $A = 4$–7 Ξ hypernuclei have been investigated based on the modified chiral interactions. For the J-NCSM calculation, the transition to the $\Lambda\Lambda$ channels has been removed and the LECs of the ΞN $^{11}S_0$ partial wave have been readjusted so that the ΞN data is described as in the original interaction. The conversion to the $\Sigma\Sigma$ channel has not been changed since the system cannot decay into this channel. As usual, the interactions are SRG-evolved in order to improve the convergence. On the right hand side of Fig. 5.10, the Ξ separation energy $B_\Xi(^4_\Xi\mathrm{H}(1^+,0))$ of the $(J^\pi,T) = (1^+,0)$ state is shown for given SRG parameters of the NN and YN interaction. Compared to $\Lambda\Lambda$ states, the SRG-dependence is more visible but it is still small enough to gain insight into possibly bound states. For a detailed quantitative analysis in the future, the evolution probably needs to be performed up to the $A = 3$ level. Based on a specific choice of the SRG parameters ($\lambda_{\mathrm{NN}} = \lambda_{YY} = 1.6$ fm^{-1}), the explicit calculations confirm that it is likely that several ΞNNN bound states exist and that their width is often small. Ref. [59] also gave explicit analytic expressions for the contribution of s-waves channels to the different states in an s-wave approximation. Clearly, the different ΞN partial wave contribute very differently to the various s-shell Ξ-hypernuclei. The pattern for ΞNNN bound states is therefore valuable to disentangle the spin dependence of the ΞN interaction. Ref. [59] also gives the contribution of the different S-wave partial waves to the binding energy of the various $A = 4$ states and $^5_\Xi$H and $^7_\Xi$H. Also for these light systems, an important contribution to the binding is coming from the $^{33}S_1$ partial wave.

It is interesting that the chiral interactions also led to several $A = 4$ bound states although its strength is often very similar to the HAL QCD potential. The explicit calculation also showed that $^5_\Xi$H is bound and its width is rather small. This nucleus cannot provide much insight into the spin dependence since the quantum numbers of the α particle core imply that there is likely only one state bound. However, the large density of the α particle is a good example to Ξ binding with a denser environment. Finally, Ref. [59] also provides a prediction of the binding energy of $^7_\Xi$H. This hypernucleus is of special interest because one can soon expect some experimental results [256] and also because it promises to test the strength of the neutron-Ξ interaction given the large number of neutrons.

Clearly, several light Ξ-hypernuclear bound states likely exists. Experimental data of these states can provide valuable information on the spin and isospin dependence of the ΞN interaction.

In order to provide a general overview of the situation regarding light Ξ hypernuclei, in Fig. 5.11 we summarize data from past and present experiments, and results from different theoretical approaches. Besides the predictions from Ref. [59], indicated by circles, we show the result of the variational calculation of Hiyama et al. [56] (open triangle). The latter is based on an interaction derived by the HAL QCD collaboration from lattice simulations close to the physical point [88]. However, in the actual calculations the various YY channels of the original HAL QCD potential are renormalized into an effective ΞN interaction and the latter is then treated within the so-called Gaussian expansion method. Earlier results for Ξ hypernuclei with $A = 5 - 12$ by Hiyama et al. were obtained within a cluster model [251] (filled triangles). In this case, the underlying effective ΞN interaction was fixed to the single-particle potential of $U_\Xi = -14$ MeV, as suggested by the analysis in Ref. [240]. Regarding mean-field calculations we show exemplary two Skyrme model results by Jin et al. [248] and Schulze et al. [254] (stars). The former calculation (model SLX3) is rooted on the value of $B_\Xi = 1.11 \pm 0.25$ MeV, interpreted as p-state of the hypernucleus $^{15}_\Xi$C, the so-called Kiso event [243]. In the latter case, the model parameters have been fixed to produce the Ξ^- removal energies for the s- and p-states of $^{15}_\Xi$C of 8 and 1.13 MeV, respectively. Note that similar predictions were reported by Tanimura et al. within a relativistic mean field approach [249] and for the density-dependent relativistic mean-field model of Ding et al. [250]. As far as experimental results are concerned, we include here values for $^{15}_\Xi$C reported in Refs. [244,245], and for $^{13}_\Xi$B from Ref. [241] (filled squares). For purely illustrative reasons, we show also binding energies of some inconclusive Ξ hypernuclei reported in the past (open squares) [255].

One can see from Fig. 5.11 that the overall trend of the predictions based on the chiral $S = -2$ interaction, obtained within a microscopic approach, is roughly in line with results for heavier Ξ hypernuclei calculated in a phenomenological way. Nonetheless, one should keep in mind that there might be certainly some overestimation of the separation energies, given that induced three-body forces that result from the SRG transformation have not yet been properly implemented.

6. Nuclear lattice effective field theory

So far, we have considered various continuum approaches combined with forces from chiral EFT. An alternative is given by Nuclear Lattice Effective Field Theory (NLEFT), where the Euclidean space–time is discretized and the world is represented by a finite box, see Refs. [257,258] for detailed expositions. Recent results are summarized in [259]. Here, we only discuss the basic features of NLEFT and focus on its extension to hypernuclei.

6.1. Basics of NLEFT

Let us briefly summarize the main ingredients of NLEFT as a novel method to tackle the nuclear few- as well as the many-body problem:

- Space–time is discretized on a hypercubic lattice with the volume $V = L \times L \times L \times L_t$, where L is the extension in the spatial directions and L_t the extension in Euclidean time, see Fig. 6.1. L is usually taken sufficiently large so as to avoid finite volume corrections, say $L = 10$ (in lattice units given by the lattice spacing a), whereas L_t in principle tends to infinity but in practice is taken large.

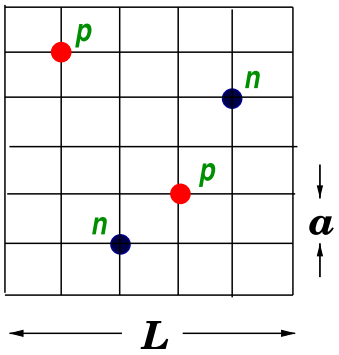

Fig. 6.1. Sketch of the lattice used in NLEFT. For details, see the text.

- The box is further characterized by finite lattice spacings a and a_t in the spatial and temporal directions, respectively. In contrast to lattice QCD, a is kept finite and is varied between 1 and 2 fm, corresponding to a fine and a coarse lattice, respectively. A finite a entails a maximum momentum,

$$p_{\max} = \frac{\pi}{a} \simeq 315 \text{ to } 630 \text{ MeV} , \tag{6.1}$$

  for $a = 2$ to 1 fm. Thus, $1/a$ serves as an UV cutoff and defines the EFT on the lattice. Quite differently, a_t is taken very small to ensure convergence as $L_t \to \infty$, typically $a_t = 0.001$ MeV^{-1}.
- The lattice spacing a is bounded from below by the nucleon size, as the EFT cannot resolve the nucleon structure. Also, it is bounded from above by not exceeding too much the average distance of nucleons in nuclei. In nuclear matter ($\rho = \rho_0 = 0.17$ fm^{-3}), the average distance between nucleons is $d \simeq 1.8$ fm. Still, physics should be independent of the choice of a, which is indeed the case if one goes to sufficiently high orders in the chiral expansion [260,261].
- Nucleons are placed on the sites as depicted in Fig. 6.1. Their interactions are given by a discretized version of the chiral NN and 3N potentials and the Coulomb interaction between protons can easily be included [262]. Note further that the masses of the nucleons (and of the pions) are given by their physical values.
- Simulations of many-baryon systems are usually plagued by sign oscillations, induced by the finite density (chemical potential). These pose a severe problem to lattice QCD calculations of the phase diagram of strongly interacting matter or calculations of atomic nuclei. In the case of NLEFT, these sign oscillations are strongly suppressed due to the approximate Wigner SU(4) (spin–isospin) symmetry of the nuclear interactions, see [263–265]. In fact, Wigner's SU(4) symmetry can be exploited to construct a minimal nuclear interaction, that can reproduce the ground state properties of light nuclei, medium-mass nuclei, and neutron matter simultaneously with no more than a few percent error in the energies and charge radii, requiring only four parameters [266]. Later, we will see how such a framework can be exploited in hypernuclear calculations.
- The central object of NLEFT is the correlation function for A nucleons,

$$Z_A(\tau) = \langle \Psi_A | \exp(-\tau H) | \Psi_A \rangle , \tag{6.2}$$

  with Ψ_A a Slater determinant for A free nucleons or a more sophisticated (correlated) initial/final state with given spin and parity, like e.g. $J^P = 0^+$ for the ^{12}C ground state (g.s.). Here, τ is the Euclidean time and H is the Hamiltonian which is expanded in terms of small momenta and pion masses (chiral expansion, with the small parameters collectively denoted as Q). From this, one calculates the transient energy $E_A(\tau) = -d \ln Z_A(\tau)/d\tau$, which allows one to extract the g.s. energy via:

$$E_A^0 = \lim_{\tau \to \infty} E_A(\tau) . \tag{6.3}$$

  In practical calculations, τ is limited due to sign oscillations, but, for large enough values of τ, one can fit to asymptotic formulas. Excited states can also be extracted, in this case Z_A becomes a matrix, which upon diagonalization delivers the first, second, third, ... state with given quantum numbers of spin and parity, like the tower of 0^+ states in the ^{12}C spectrum. The expectation value of any normal-ordered operator can be calculated in a similar fashion by inserting the operator at mid-times.
- Smearing is an important tool to enhance the simulation signals. In NLEFT, both local and non-local smearings, corresponding to velocity-independent and velocity-dependent interactions, are employed. Local smearing is performed on the level of the nucleon densities, such as for the spin- and isospin-independent density $\rho(\boldsymbol{n})$,

$$\rho(\boldsymbol{n}) = \sum_{i,j=0,1} a_{i,j}^\dagger(\boldsymbol{n})\, a_{i,j'}(\boldsymbol{n}) + s_{\rm L} \sum_{|\boldsymbol{n}-\boldsymbol{n}'|^2=1} \sum_{i,j=0,1} a_{i,j}^\dagger(\boldsymbol{n}')\, a_{i,j}(\boldsymbol{n}') , \tag{6.4}$$

  with $s_{\rm L}$ the local smearing parameter, $\boldsymbol{n}$, $\boldsymbol{n}'$ represent points on the lattice with spin $i = 0, 1$ (up, down) and isospin $j = 0, 1$ (proton, neutron) indices. The non-local smearing is done on the level of the nucleon creation/annihilation operators,

$$\tilde{a}_{i,j}^{(\dagger)}(\boldsymbol{n}) = a_{i,j}^{(\dagger)}(\boldsymbol{n}) + s_{\rm NL} \sum_{|\boldsymbol{n}'-\boldsymbol{n}|=1} a_{i,j}^{(\dagger)}(\boldsymbol{n}') , \tag{6.5}$$

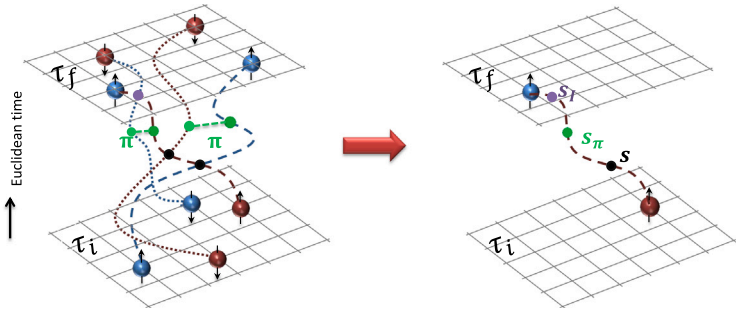

Fig. 6.2. Simulation of a ^{4}He nucleus (left panel) that decomposes into four independent worldline simulations due to the use of auxiliary fields (right panel). In the left panel, explicit interactions (pion exchanges and contact terms) are shown. In the right panel, these interactions are represented by auxiliary field insertions on the nucleon worldline.
Source: Figure courtesy of Serdar Elhatisari.

with $s_{\rm NL}$ the non-local smearing parameter. In few-body systems, these two types of smearing cannot be disentangled, quite differently to medium-mass and heavy nuclei (as discussed below). Note further that, through this smearing, one effectively accounts for a number of higher-order operators, as distances can be translated into derivatives on the lattice.

- An important ingredient in NLEFT simulations is the representation of the interactions in terms of auxiliary fields, such as

$$\exp\left[-\frac{C}{2}\left(N^\dagger N\right)^2\right] = \sqrt{\frac{1}{2\pi}}\int_{-\infty}^{+\infty} ds \exp\left[-\frac{s^2}{2} + \sqrt{C}\, s\left(N^\dagger N\right)\right] , \tag{6.6}$$

with s an auxiliary field that couples to the nucleon density, $\rho = N^\dagger N$. Similarly, spin- and isospin-dependent multi-nucleon operators and pion exchanges can be represented by labeled auxiliary fields. This makes NLEFT optimally suited for parallel computing as shown in Fig. 6.2.

- By construction, all possible initial/final states are considered in NLEFT. Often, one starts with free waves subject to the lattice boundary conditions and consistent with the quantum numbers of the state under consideration. However, different initial states can be constructed. To be specific, consider the ^{4}He nucleus. These initial states can consist of four nucleons on different lattice sites, but also doublets, triplets and even quartets, the latter consisting of two protons and two neutrons, each pair with one spin up and one spin down as allowed by the Pauli principle. Thus, NLEFT has the advantage of capturing the full set of many-body correlations, or stated differently, clustering emerges naturally. Furthermore, one can also work in a basis given by shell model states, as detailed in [267,268].
- Another important ingredient to achieve the required high precision is the recently developed method called *wavefunction matching* [269]. Despite the approximate Wigner SU(4) symmetry, NLEFT suffers from severe sign problems in its application to high-fidelity chiral forces (beyond N2LO) described by the chiral Hamiltonian H_χ. In the wavefunction matching method, the unitarily transformed $H'_\chi = U H_\chi U$ is mapped onto a simple Hamiltonian H_S, where the H_S is largely free of sign oscillations. This simple Hamiltonian consists of smeared two-nucleon SU(4) symmetric contact interactions as well as regularized one-pion exchange. If H'_χ is sufficiently close to H_S, first-order perturbation theory in $H'_\chi - H_S$ can be used efficiently to calculate the higher-order chiral forces up-to-and-including N3LO. Furthermore, smeared 3NFs are then fitted to masses of selected nuclei ranging from $A = 3$ to $A = 58$. Consequently, nuclear charge radii as well the EOS for neutron matter and for nuclear matter can be predicted, showing good agreement with the data.

6.2. Lattice Hamiltonian

Here, we briefly discuss the state-of-the-art lattice Hamiltonian for NN and 3N forces, that forms the basis of the calculations of the nuclear core of the hypernuclei. This is based on the high-fidelity chiral interaction at N3LO and the quantum many-body approach, called wavefunction matching, developed in Ref. [269]. The Hamiltonian H is,

$$H = T + V_{\rm OPE} + V_{\rm C} + V_{\rm 3N}^{\rm Q^3} + V_{\rm 2N}^{\rm Q^4} + W_{\rm 2N}^{\rm Q^4} , \tag{6.7}$$

where T is the kinetic energy term constructed using fast Fourier transforms to produce the exact dispersion relation $E_N = p^2/(2m_N)$, and $m_N = 938.92$ MeV is the nucleon mass. The one-pion-exchange potential $V_{\rm OPE}$ is given in terms of the regularization method from Ref. [95],

$$V_{\rm OPE} = -\frac{g_A^2}{8F_\pi^2} \sum_{\mathbf{n}',\mathbf{n},S',S,I} : \rho^{(0)}_{S',I}(\mathbf{n}') f_{S',S}(\mathbf{n}'-\mathbf{n}) \rho^{(0)}_{S,I}(\mathbf{n}) : -C_\pi \frac{g_A^2}{8f_\pi^2} \sum_{\mathbf{n}',\mathbf{n},S,I} : \rho^{(0)}_{S,I}(\mathbf{n}') f^\pi(\mathbf{n}'-\mathbf{n}) \rho^{(0)}_{S,I}(\mathbf{n}) : , \tag{6.8}$$

where $g_A = 1.287$ the axial–vector coupling constant (adjusted to account for the Goldberger–Treiman discrepancy [97]), $F_\pi = 92.2$ MeV the pion decay constant, and $\rho_{SI}(\boldsymbol{n})$ is the spin- and isospin-dependent density operator,

$$\rho^{(d)}_{S,I}(\boldsymbol{n}) = \sum_{i,j,i',j'=0,1} a^\dagger_{i,j}(\boldsymbol{n})\,[\sigma_S]_{ii'}\,[\tau_I]_{jj'}\,a_{i',j'}(\boldsymbol{n}) + s_{\rm L}\sum_{|\boldsymbol{n}-\boldsymbol{n}'|^2=1}^{d}\sum_{i,j,i',j'=0,1} a^\dagger_{i,j}(\boldsymbol{n}')\,[\sigma_S]_{ii'}\,[\tau_I]_{jj'}\,a_{i',j'}(\boldsymbol{n}'), \tag{6.9}$$

with $\boldsymbol{\tau},\boldsymbol{\sigma}$ the Pauli-(iso)spin matrices and annihilation (creation) operators a ($a^\dagger$). Further, $f_{S',S}$ is the locally-regulated pion correlation function,

$$f_{S',S}(\boldsymbol{n}'-\boldsymbol{n}) = \frac{1}{L^3}\sum_{\boldsymbol{q}}\frac{q_{S'}q_S\,e^{-i\boldsymbol{q}\cdot(\boldsymbol{n}'-\boldsymbol{n})-(\boldsymbol{q}^2+M_\pi^2)/\Lambda_\pi^2}}{\boldsymbol{q}^2+M_\pi^2}, \tag{6.10}$$

where f^π is a local regulator defined in momentum space,

$$f^\pi(\boldsymbol{n}'-\boldsymbol{n}) = \frac{1}{L^3}\sum_{\boldsymbol{q}} e^{-i\boldsymbol{q}\cdot(\boldsymbol{n}'-\boldsymbol{n})-(\boldsymbol{q}^2+M_\pi^2)/\Lambda_\pi^2}, \tag{6.11}$$

with $\boldsymbol{q} = \boldsymbol{p}-\boldsymbol{p}'$ the momentum transfer ($\boldsymbol{p}$ and $\boldsymbol{p}'$ are the relative incoming and outgoing momenta). In addition, C_π is the coupling constant of the OPE counter term given by,

$$C_\pi = -\frac{\Lambda_\pi(\Lambda_\pi^2-2M_\pi^2)+2\sqrt{\pi}M_\pi^3\exp(M_\pi^2/\Lambda_\pi^2)\mathrm{erfc}(M_\pi/\Lambda_\pi)}{3\Lambda_\pi^3}, \tag{6.12}$$

with

$$\mathrm{erfc}(x) = \frac{2}{\sqrt{\pi}}\int_x^\infty e^{-t^2}\,dt \tag{6.13}$$

the complementary error function, $\Lambda_\pi = 300$ MeV the regulator parameter and $M_\pi = 134.98$ MeV the pion mass. Furthermore, $V_{\rm C}$ is the Coulomb interaction, $V^{\rm Q^3}_{\rm 3N}$ denotes the 3N potential, and $V^{\rm Q^4}_{\rm 2N}$ is the 2N short-range interaction at N3LO. In addition, $W^{\rm Q^4}_{\rm 2N}$ is the required 2N Galilean invariance restoration (GIR) interaction at N3LO. For more details of the Coulomb interaction and the 2N short-range interactions, see Ref. [270]. The 3N interactions at Q^3 consist of three different topologies. These are the locally smeared contact interactions, the OPE interaction with the locally smeared two-nucleon contact terms, and the two-pion exchange potential [133,271,272]. Further, we have two additional SU(4) symmetric 3N potentials denoted by $V^{(l)}_{c_E}$ and $V^{(t)}_{c_E}$. Therefore, the 3N interaction at Q^3 is given by

$$V^{\rm Q^3}_{\rm 3N} = V^{(0)}_{c_E} + V^{(1)}_{c_E} + V^{(2)}_{c_E} + V^{(l)}_{c_E} + V^{(t)}_{c_E} + V^{(0)}_{c_D} + V^{(1)}_{c_D} + V^{(2)}_{c_D} + V^{\rm (TPE)}_{\rm 3N}. \tag{6.14}$$

The two-pion exchange potential can be separated into three parts,

$$V^{\rm (TPE1)}_{\rm 3N} = \frac{c_3}{f_\pi^2}\frac{g_A^2}{4f_\pi^2}\sum_{S,S',S'',I}\sum_{\boldsymbol{n},\boldsymbol{n}',\boldsymbol{n}''} :\rho^{(0)}_{S',I}(\boldsymbol{n}')\,f_{S',S}(\boldsymbol{n}'-\boldsymbol{n})f_{S'',S}(\boldsymbol{n}''-\boldsymbol{n})\rho^{(0)}_{S'',I}(\boldsymbol{n}'')\,\rho^{(0)}(\boldsymbol{n}):\tag{6.15}$$

$$V^{\rm (TPE2)}_{\rm 3N} = -\frac{2c_1}{f_\pi^2}\frac{g_A^2M_\pi^2}{4f_\pi^2}\sum_{S,S',I}\sum_{\boldsymbol{n},\boldsymbol{n}',\boldsymbol{n}''} :\rho^{(0)}_{S',I}(\boldsymbol{n}')\,f^{\pi\pi}_{S'}(\boldsymbol{n}'-\boldsymbol{n})f^{\pi\pi}_{S}(\boldsymbol{n}''-\boldsymbol{n})\rho^{(0)}_{S,I}(\boldsymbol{n}'')\,\rho^{(0)}(\boldsymbol{n}):,\tag{6.16}$$

$$\begin{aligned}V^{\rm (TPE3)}_{\rm 3N} = {}& \frac{c_4}{2f_\pi^2}\left(\frac{g_A}{2f_\pi}\right)^2\sum_{S_1,S_2,S_3}\sum_{I_1,I_2,I_3}\sum_{S',S''}\sum_{\boldsymbol{n},\boldsymbol{n}',\boldsymbol{n}''}\varepsilon_{S_1,S_2,S_3}\varepsilon_{I_1,I_2,I_3}\\ &\times :\rho^{(0)}_{S',I_1}(\boldsymbol{n}')\,f_{S',S_1}(\boldsymbol{n}'-\boldsymbol{n})f_{S'',S_2}(\boldsymbol{n}''-\boldsymbol{n})\rho^{(0)}_{S'',I_2}(\boldsymbol{n}'')\,\rho^{(0)}_{S_3,I_3}(\boldsymbol{n}):,\end{aligned}\tag{6.17}$$

where the locally smeared spin–isospin symmetric density operator is defined as,

$$\rho^{(d)}(\boldsymbol{n}) = \sum_{i,j=0,1} a^\dagger_{i,j}(\boldsymbol{n})\,a_{i,j}(\boldsymbol{n}) + s_{\rm L}\sum_{|\boldsymbol{n}-\boldsymbol{n}'|^2=1}^{d}\sum_{i,j=0,1} a^\dagger_{i,j}(\boldsymbol{n}')\,a_{i,j}(\boldsymbol{n}'), \tag{6.18}$$

and the LECs of two-pion exchange potentials are fixed from pion–nucleon scattering data, $c_1 = -1.10(3)$, $c_3 = -5.54(6)$ and $c_4 = 4.17(4)$ all in GeV^{-1} [273]. Next, the OPE interaction with the locally smeared 2N contact terms is given by,

$$V^{(d)}_{c_D} = -\frac{c_D^{(d)}\,g_A}{4f_\pi^4\Lambda_\chi}\sum_{\boldsymbol{n},S,I}\sum_{\boldsymbol{n}',S'} :\rho^{(0)}_{S',I}(\boldsymbol{n}')f_{S',S}(\boldsymbol{n}'-\boldsymbol{n})\rho^{(d)}_{S,I}(\boldsymbol{n})\rho^{(d)}(\boldsymbol{n}):. \tag{6.19}$$

A graphical representation of the first three terms with $d = 0,1,2$ is given in Fig. 6.3.

Furthermore, the locally smeared contact interactions take the form,

$$V^{(d)}_{c_E} = \frac{c_E^{(d)}}{6}\sum_{\boldsymbol{n},\boldsymbol{n}',\boldsymbol{n}''}\left[\rho^{(d)}(\boldsymbol{n})\right]^3, \tag{6.20}$$

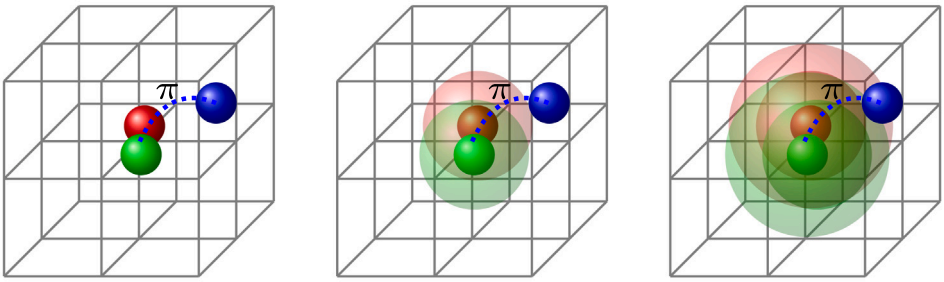

Fig. 6.3. Smearing of the LEC c_D. **Left panel:** Non-smeared case $d = 0$. **Middle panel:** Smearing with $d = 1$. **Right panel:** Smearing with $d = 2$. Note that $d = 0, 1, 2$ refers to the same, the neighboring and the next-to-neighboring lattice point, in order.

and finally two additional SU(4) symmetric potentials denoted by $V_{c_E}^{(l)}$ and $V_{c_E}^{(t)}$ are defined as,

$$V_{c_E}^{(l)} = c_E^{(l)} \sum_{\boldsymbol{n},\boldsymbol{n}',\boldsymbol{n}''} \rho^{(d)}(\boldsymbol{n})\,\rho^{(d)}(\boldsymbol{n}')\,\rho^{(d)}(\boldsymbol{n}'')\delta_{|\boldsymbol{n}-\boldsymbol{n}'|^2,1}\;\delta_{|\boldsymbol{n}-\boldsymbol{n}''|^2,1}\;\delta_{|\boldsymbol{n}'-\boldsymbol{n}''|^2,4}, \tag{6.21}$$

$$V_{c_E}^{(t)} = c_E^{(t)} \sum_{\boldsymbol{n},\boldsymbol{n}',\boldsymbol{n}''} \rho^{(d)}(\boldsymbol{n})\,\rho^{(d)}(\boldsymbol{n}')\,\rho^{(d)}(\boldsymbol{n}'')\delta_{|\boldsymbol{n}-\boldsymbol{n}'|^2,2}\;\delta_{|\boldsymbol{n}-\boldsymbol{n}''|^2,2}\;\delta_{|\boldsymbol{n}'-\boldsymbol{n}''|^2,2}\,. \tag{6.22}$$

It is important to stress that in contrast to the continuum case, where we just have two LECs, namely c_E and c_D, these are smeared here over neighboring lattice sites and appear with independent LECs $c_{D,E}^{(0)}, c_{D,E}^{(1)}, c_{D,E}^{(2)}, \ldots$. As noted before, this smearing effectively emulates a number of higher-order interactions involving derivatives. In lattice units, these LECs take the values

$$\begin{aligned}
c_D^{(0)} &= -1.2787\,, \quad c_D^{(1)} = -2.5665\,, \quad c_D^{(2)} = -0.2578\,,\\
c_E^{(0)} &= \;\;3.3724\,, \quad c_E^{(1)} = \;\;4.9896\,, \quad c_E^{(2)} = -1.0876\,,\\
c_E^{(l)} &= -0.4991\,, \quad c_E^{(t)} = \;\;0.06575\,.
\end{aligned} \tag{6.23}$$

Finally, we note that the pion–nucleon vertices are not smeared, so that we can take the values of the dimension-two LECs c_i from Ref. [273].

6.3. Lattice Hamiltonian with hyperons

Consider now interactions containing additional hyperons. At present, two different NLEFT approaches to hypernuclei exist. The first combines the high-fidelity chiral NN and 3N forces with leading order YN and YNN forces, all smeared locally and non-locally. In this framework, hypernuclei up to ${}^{16}_{\Lambda}$O have been investigated. Second, an extension of the minimal nuclear into the strangeness $S = -1, 2$ sectors also has been constructed. In this framework, some single and double Λ hypernuclei have been studied together with the EoS of nuclear matter and of (hyper)neutron matter. Clearly, these studies require improvements in the years to come.

All NLEFT studies have so far been using LO S-wave ΛN contact interactions:

$$V_{YN} = \frac{1}{4}C_{YN}^{S}(\mathbb{1} - \boldsymbol{\sigma_1}\cdot\boldsymbol{\sigma_2}) + \frac{1}{4}C_{YN}^{T}(3 + \boldsymbol{\sigma_1}\cdot\boldsymbol{\sigma_2}) \tag{6.24}$$

where $\boldsymbol{\tau}, \boldsymbol{\sigma}$ are Pauli-(iso)spin matrices and $C_{YN}^{S,T}$ are the respective LECs. In addition, contact three-body ΛNN and $N\Lambda\Lambda$ forces as derived in Ref. [43] have been utilized,

$$\begin{aligned}
V_{YNN} &= C_1(\mathbb{1} - \boldsymbol{\sigma}_2\cdot\boldsymbol{\sigma}_3)(3 + \boldsymbol{\tau}_2\cdot\boldsymbol{\tau}_3) + C_2\,\boldsymbol{\sigma}_1\cdot(\boldsymbol{\sigma}_2 + \boldsymbol{\sigma}_3)(\mathbb{1} - \boldsymbol{\tau}_2\cdot\boldsymbol{\tau}_3) + C_3(3 + \boldsymbol{\sigma}_2\cdot\boldsymbol{\sigma}_3)(\mathbb{1} - \boldsymbol{\tau}_2\cdot\boldsymbol{\tau}_3)\,,\\
V_{YYN} &= D_1\,\mathbb{1}\,\mathbb{1}\,,
\end{aligned} \tag{6.25}$$

in terms of 3 LECs for the ΛNN and 1 LEC for the $\Lambda\Lambda$N interaction (without smearing). Note that the hyperon in the YNN interaction is always counted as the first particle. As noted before, 3BFs appear at N2LO in the chiral power counting à la Weinberg. In pionless EFT, the three-body forces, however, would be LO [274]. Since in these calculations the explicit two-pion exchange interactions were not considered, but effectively simulated by the smearing discussed below, it is legitimate to promote the 3BFs in the $S = -1$ and the $S = -2$ sectors to LO (or consider the extension of the minimal interaction to include hyperons discussed below). Note further that the one-pion exchange is suppressed for the ΛN interaction due to isospin symmetry and hence not part of this effective leading order interaction. Finally, due to the fact that high-fidelity chiral interactions between nucleons are well tested, those set the smearing parameters as well as the lattice spacing for the hypernuclear interactions. Therefore, the lattice Hamiltonian is defined as,

$$H = H_{\mathrm{N3LO}} + T_Y + V_{YN} + V_{YNN} + V_{YYN}\,, \tag{6.26}$$

where H_{N3LO} is the high-fidelity Hamiltonian for nucleons [269], T_Y is the kinetic energy term for Λ hyperons defined by using fast Fourier transforms to produce the exact dispersion relations $E_\Lambda = p^2/(2m_\Lambda)$ with hyperon mass $m_\Lambda = 1115.68$ MeV, V_{YN} and

V_{YNN}, V_{YYN} are the hyperon–nucleon and hyperon–nucleon–nucleon, hyperon–hyperon–nucleon interactions given in Eqs. (6.24) and (6.25), respectively. Note that, in these calculations, no other hyperons have been considered, and thus the Σ-Λ conversion is subsumed in the fitted LECs. As so far, in this approach, only the $S = -1$ hypernuclear sector has been investigated, let us discuss the smearing of the ΛNN 3BFs. The locally smeared forms of the interactions given in Eq. (6.25) are given by,

$$
\begin{aligned}
V_1^{(d)} &= 3\sum_{\boldsymbol{n}} :\left\{[\rho^{(d)}(\boldsymbol{n})]^2 - \sum_S [\rho_S^{(d)}(\boldsymbol{n})]^2\right\}\xi^{(d)}(\boldsymbol{n}): + \sum_{\boldsymbol{n},I} :\left\{[\rho_I^{(d)}(\boldsymbol{n})]^2 - \sum_S [\rho_{SI}^{(d)}(\boldsymbol{n})]^2\right\}\xi^{(d)}(\boldsymbol{n}):,\\
V_2^{(d)} &= 2\sum_{\boldsymbol{n}} :\rho^{(d)}(\boldsymbol{n})\sum_S \rho_S^{(d)}(\boldsymbol{n})\xi_S^{(d)}(\boldsymbol{n}): -2\sum_{\boldsymbol{n},S,I} :\rho_I^{(d)}(\boldsymbol{n})\rho_{SI}^{(d)}(\boldsymbol{n})\xi_S^{(d)}(\boldsymbol{n}):,\\
V_3^{(d)} &= 3\sum_{\boldsymbol{n}} :\left\{[\rho^{(d)}(\boldsymbol{n})]^2 - \sum_I [\rho_I^{(d)}(\boldsymbol{n})]^2\right\}\xi^{(d)}(\boldsymbol{n}): + \sum_{\boldsymbol{n},S} :\left\{[\rho_S^{(d)}(\boldsymbol{n})]^2 - \sum_I [\rho_{SI}^{(d)}(\boldsymbol{n})]^2\right\}\xi^{(d)}(\boldsymbol{n}):.
\end{aligned}
\tag{6.27}
$$

in terms of the various smeared nucleon densities and $\xi^{(d)}(\boldsymbol{n}), \xi_S^{(d)}(\boldsymbol{n})$ are the locally smeared hyperon densities,

$$
\xi^{(d)}(\boldsymbol{n}) = \sum_{i=0,1} b_i^\dagger(\boldsymbol{n})\, b_i(\boldsymbol{n}) + s_{\rm L}\sum_{|\boldsymbol{n}-\boldsymbol{n}'|^2=1}^{d}\sum_{i,j=0,1} b_i^\dagger(\boldsymbol{n}')\, b_i(\boldsymbol{n}'),
\tag{6.28}
$$

$$
\xi_S^{(d)}(\boldsymbol{n}) = \sum_{i,i'=0,1} b_i^\dagger(\boldsymbol{n})\,[\sigma_S]_{i,i'}\, b_{i'}(\boldsymbol{n}) + s_{\rm L}\sum_{|\boldsymbol{n}-\boldsymbol{n}'|^2=1}^{d}\sum_{i,i'=0,1} b_i^\dagger(\boldsymbol{n}')\,[\sigma_S]_{i,i'}\, b_{i'}(\boldsymbol{n}').
\tag{6.29}
$$

Here, the $b_i, b_i^\dagger$ are hyperon annihilation and creation operators and the superscript d describes the range of the local smearing. We consider different choices up to $d = 3$ corresponding to 2.28 fm. In addition, for these interactions, we set $s_{\rm L} = 0.5$. Therefore, the locally smeared three-body interactions are labeled as $V_{C_k}^{(d=0)}$, $V_{C_k}^{(d=1)}$, $V_{C_k}^{(d=2)}$ and $V_{C_k}^{(d=3)}$ with $k = 1, 2, 3$. We also define the non-locally smeared forms of the interactions given in Eq. (6.25),

$$
\begin{aligned}
V_1^{s_{\rm NL}} &= 3\sum_{\boldsymbol{n}} :\left\{[\hat\rho(\boldsymbol{n})]^2 - \sum_S [\hat\rho_S(\boldsymbol{n})]^2\right\}\hat\xi(\boldsymbol{n}): + \sum_{\boldsymbol{n},I} :\left\{[\hat\rho_I(\boldsymbol{n})]^2 - \sum_S [\hat\rho_{SI}(\boldsymbol{n})]^2\right\}\hat\xi(\boldsymbol{n}):,\\
V_2^{s_{\rm NL}} &= 2\sum_{\boldsymbol{n}} :\hat\rho(\boldsymbol{n})\sum_S \hat\rho_S(\boldsymbol{n})\hat\xi_S(\boldsymbol{n}): -2\sum_{\boldsymbol{n},S,I} :\hat\rho_I(\boldsymbol{n})\hat\rho_{SI}(\boldsymbol{n})\hat\xi_S(\boldsymbol{n}):,\\
V_3^{s_{\rm NL}} &= 3\sum_{\boldsymbol{n}} :\left\{[\hat\rho(\boldsymbol{n})]^2 - \sum_I [\hat\rho_I(\boldsymbol{n})]^2\right\}\hat\xi(\boldsymbol{n}): + \sum_{\boldsymbol{n},S} :\left\{[\hat\rho_S(\boldsymbol{n})]^2 - \sum_I [\hat\rho_{SI}(\boldsymbol{n})]^2\right\}\hat\xi(\boldsymbol{n}):.
\end{aligned}
\tag{6.30}
$$

in terms of the non-locally smeared hyperon densities

$$
\begin{aligned}
&\hat\xi(\boldsymbol{n}) = \sum_{i=0,1}\tilde b_i^\dagger(\boldsymbol{n})\tilde b_i(\boldsymbol{n}), \quad \hat\xi_S(\boldsymbol{n}) = \sum_{i,i'=0,1}\tilde b_i^\dagger(\boldsymbol{n})[\sigma_S]_{i,i'}\tilde b_{i'}(\boldsymbol{n}),\\
&\tilde b_i(\boldsymbol{n}) = b_i(\boldsymbol{n}) + s_{\rm NL}\sum_{|\boldsymbol{n}'-\boldsymbol{n}|=1} b_i(\boldsymbol{n}'),
\end{aligned}
\tag{6.31}
$$

in terms of the strength of the non-locality of the interactions, $s_{\rm NL}$. One considers three different values of this parameter, $s_{\rm NL} = 0.1, 0.2, 0.3$, labeled $V_{C_k}^{0.1}$, $V_{C_k}^{0.2}$ and $V_{C_k}^{0.3}$, respectively, with $k = 1, 2, 3$. Now one considers all possible versions of the ΛNN interaction, constructed from the combinations of these smeared versions of V_{C_1}, V_{C_2}, and V_{C_3}, which leads to a total set of 343 combinations. By systematically analyzing each combination using hypernuclei from light to medium mass, we determine the optimal configuration for the ΛNN interaction which give a good description for hypernuclei. Such an analysis is not yet available. In the results presented later, a limited set of hypernuclei is included in the fitting procedure and one then considers the combination with the lowest Root Mean Square Deviation (RMSD) defined as follows

$$
{\rm RMSD}(S) = \sqrt{\frac{1}{M_S}\sum_{i\in S}\left(\frac{{}^iB_\Lambda^c - {}^iB_\Lambda^{\rm exp}}{{}^iB_\Lambda^{\rm exp}}\right)^2},
\tag{6.32}
$$

where ${}^iB_\Lambda^c$ is the evaluated Λ separation energy and ${}^iB_\Lambda^{\rm exp}$ is the experimental separation energy for each hypernucleus within the set S. The size of the set S of hypernuclei is given by M_S, which contains well measured hypernuclei from the light and medium mass region, starting from the four-body systems. The corresponding ${}^iB_\Lambda^{\rm exp}$ are taken from Ref. [50].

There also exists a so-called minimal hypernuclear interaction that builds upon the significant achievements of the EFT within Wigner's SU(4) spin–isospin symmetry, which is referred to as the minimal nuclear interaction. An extension of this is pionless EFT at LO for nucleons (see also [275]) derived from this minimal nuclear interaction. This approach allows us to make use of the well-established theoretical framework by the minimal nuclear interaction, providing a solid basis for calculations of hypernuclei and the equation of state of neutron matter including hyperons. This was developed in Ref. [276]. As before, we only consider Λ hyperons, so that the contributions of Λ-Σ conversion are effectively represented by ΛNN forces. For the YN and YY interactions, we also utilize minimal interactions assuming that these interactions are spin symmetric. Therefore, the minimal Hamiltonian for hypernuclear physics is defined as,

$$
H = T + \frac{c_{NN}}{2}\sum_{\boldsymbol{n}} :[\tilde\rho(\boldsymbol{n})]^2: + \frac{c_{NN}^T}{2}\sum_{I,\boldsymbol{n}} :\left[\tilde\rho_I(\boldsymbol{n})\right]^2: + c_{N\Lambda}\sum_{\boldsymbol{n}} :\tilde\rho(\boldsymbol{n})\tilde\xi(\boldsymbol{n}): + \frac{c_{\Lambda\Lambda}}{2}\sum_{\boldsymbol{n}} :\left[\tilde\xi(\boldsymbol{n})\right]^2:
$$

$$+ V_{NN}^{\rm GIR} + V_{N\Lambda}^{\rm GIR} + V_{\Lambda\Lambda}^{\rm GIR} + V_{\rm C} + V_{NNN} + V_{NN\Lambda} + V_{N\Lambda\Lambda}\,, \tag{6.33}$$

Here, T is the kinetic energy term defined by using fast Fourier transforms to produce the exact dispersion relations $E_N = p^2/(2m_N)$ and $E_\Lambda = p^2/(2m_\Lambda)$ with nucleon mass $m_N = 938.92$ MeV and hyperon mass $m_\Lambda = 1115.68$ MeV, c_{NN} is the coupling constant of the SU(4) symmetric short-range 2N interaction, c_{NN}^T is the coupling constant of the isospin-dependent short-range 2N interaction, that breaks SU(4) symmetry (see the discussion below), $c_{N\Lambda}$ ($c_{\Lambda\Lambda}$) is the LEC of the spin-symmetric short-ranged YN (YY) interaction, and $\tilde{\xi}$ is the hyperon density operator, that is smeared both locally and non-locally, as given above. Further, $V_{\rm C}$ represents the Coulomb interaction, see Ref. [270] for details. The nonlocal smearing applied on the lattice introduces an explicit dependence on the center-of-mass momentum, thereby breaking Galilean invariance. Consequently, in Eq. (6.26), we introduce $V_{NN}^{\rm GIR}$, $V_{N\Lambda}^{\rm GIR}$, and $V_{\Lambda\Lambda}^{\rm GIR}$, which denote the Galilean invariance restoration (GIR) interactions for the nucleon–nucleon, nucleon–hyperon, and hyperon–hyperon interactions, respectively. We refer the reader to Ref. [277] for further details. Finally, in this approach, the three-baryon interactions V_{NNN}, $V_{NN\Lambda}$, and $V_{N\Lambda\Lambda}$, are also given in Eq. (6.33). The 3N forces take the form

$$V_{NNN} = \sum_{i=1,2} \frac{c_{NNN}^{(d_i)}}{6} \sum_{\boldsymbol{n}} :\, \left[\rho^{(d_i)}(\boldsymbol{n})\right]^3 :\,, \tag{6.34}$$

where the parameter d_i denotes the range of local smearing with $0 \le d_1 < d_2 \le 3$ (in lattice units). In this case, the 3BFs between two nucleons and one hyperon are defined with two different choices of local smearing

$$V_{NN\Lambda} = \sum_{i=1,2} \frac{c_{NN\Lambda}^{(d_i)}}{2} \sum_{\boldsymbol{n}} :\, \left[\rho^{(d_i)}(\boldsymbol{n})\right]^2 \xi^{(d_i)}(\boldsymbol{n}) :\,, \tag{6.35}$$

and similarly for the interactions involving one nucleon and two hyperons,

$$V_{N\Lambda\Lambda} = \sum_{i=1,2} \frac{c_{N\Lambda\Lambda}^{(d_i)}}{2} \sum_{\boldsymbol{n}} :\, \rho^{(d_i)}(\boldsymbol{n}) \left[\xi^{(d_i)}(\boldsymbol{n})\right]^2 :\,, \tag{6.36}$$

where ρ (ξ) is then purely locally smeared nucleon (hyperon) density operator with annihilation and creation operators, a (b) and $a^\dagger$ ($b^\dagger$) for nucleons (hyperons),

$$\rho^{(d)}(\boldsymbol{n}) = \sum_{i,j=0,1} a_{i,j}^\dagger(\boldsymbol{n})\, a_{i,j}(\boldsymbol{n}) + s_{\rm L}^{\rm 3B} \sum_{|\boldsymbol{n}-\boldsymbol{n}'|^2=1}^{d} \sum_{i,j=0,1} a_{i,j}^\dagger(\boldsymbol{n}')\, a_{i,j}(\boldsymbol{n}')\,, \tag{6.37}$$

$$\xi^{(d)}(\boldsymbol{n}) = \sum_{i=0,1} b_i^\dagger(\boldsymbol{n})\, b_i(\boldsymbol{n}) + s_{\rm L}^{\rm 3B} \sum_{|\boldsymbol{n}-\boldsymbol{n}'|^2=1}^{d} \sum_{i=0,1} b_i^\dagger(\boldsymbol{n}')\, b_i(\boldsymbol{n}')\,. \tag{6.38}$$

Here, the parameter d gives the range of local smearing with $0 \le d \le 3$ and $s_{\rm L}^{\rm 3B}$ defines the strength of the local smearing. Note that here no nonlocal smearing is applied to the 3BFs. This is related to the fact that this approach was applied simultaneously to hypernuclei as well as dense hypernuclear matter, where it is found that for generating a stiff neutron matter EoS, only local smearing should be used.

Next, we have to discuss how to treat the Λ hyperons in the simulations. At present, there exist two different methods that we will discuss separately.

6.3.1. *Impurity lattice MC formalism*

The impurity lattice Monte Carlo (ILMC) method has been introduced in Ref. [278] in the context of a Hamiltonian theory of spin-up and spin-down fermions, and applied to the intrinsically non-perturbative physics of Fermi polarons in two dimensions in Ref. [279]. The ILMC method is particularly useful for the case where only one (or two) fermion(s) (of either species) is immersed in a "sea" of the other species. Within the standard auxiliary field Monte Carlo method, such an extreme imbalance would often lead to unacceptable sign oscillations in the Monte Carlo probability weight (except by using a certain trick, as discussed later). In the ILMC method, the minority particle is "integrated out", resulting in a formalism where only the majority species fermions appear as explicit degrees of freedom, while the minority fermion is represented by a "worldline" in Euclidean projection time. The spatial position of this worldline is updated using Metropolis moves, while the interactions between the majority fermions are described by the usual auxiliary field formalism [258].

The ILMC formalism for hypernuclei with one Λ was developed in [280]. One starts from the partition function via the Grassmann path integral

$$\mathcal{Z} = \int \left[\prod_{\substack{\boldsymbol{n},n_t \\ s=N,Y}} d\zeta_s(\boldsymbol{n}, n_t) d\zeta_s^*(\boldsymbol{n}, n_t) \right] \exp(-S[\zeta, \zeta^*]), \tag{6.39}$$

where the subscripts N and Y refer to all nucleon and hyperon degrees of freedom, respectively. For simplicity, let us assume that the YN and NN interactions are spin-independent and we neglect Coulomb interactions. Trotterizing the Euclidean action in Eq. (6.39) gives

$$S[\zeta, \zeta^*] \equiv \sum_{n_t} \Big\{ S_t[\zeta, \zeta^*, n_t] + S_Y[\zeta, \zeta^*, n_t] + S_N[\zeta, \zeta^*, n_t] + S_{YN}[\zeta, \zeta^*, n_t] + S_{NN}[\zeta, \zeta^*, n_t] \Big\}, \tag{6.40}$$

where the component due to the time derivative is

$$S_t[\zeta,\zeta^*,n_t] \equiv \sum_{\boldsymbol{n},s=N,Y} \zeta_s^*(\boldsymbol{n},n_t)\Big[\zeta_s(\boldsymbol{n},n_t+1)-\zeta_s(\boldsymbol{n},n_t)\Big], \tag{6.41}$$

while S_Y and S_N describe the kinetic energies of the hyperons and nucleons, respectively. Further, S_{YN} provides the YN interaction, and S_{NN} the NN interaction. Note that actual NLEFT calculations are performed using the transfer matrix MC method. As noted in Ref. [278], the Grassmann and transfer matrix formulations are related by

$$\begin{aligned}&\mathrm{Tr}\Big\{:\, f_{N_t-1}[a_s(\boldsymbol{n}),a_{s'}^\dagger(\boldsymbol{n}')]:\cdots:\, f_0[a_s(\boldsymbol{n}),a_{s'}^\dagger(\boldsymbol{n}')]:\Big\} = \\ &\int\left[\prod_{\substack{\boldsymbol{n},n_t\\ s=N,Y}} d\zeta_s(\boldsymbol{n},n_t)d\zeta_s^*(\boldsymbol{n},n_t)\right]\exp\left(-\sum_{n_t} S_t[\zeta,\zeta^*,n_t]\right)\prod_{n_t=0}^{N_t-1} f_{n_t}\big[\zeta_s(\boldsymbol{n},n_t),\zeta_{s'}^*(\boldsymbol{n}',n_t)\big],\end{aligned} \tag{6.42}$$

where f is an arbitrary function, $a_s^\dagger$ and a_s denote creation and annihilation operators for the fermion degrees of freedom, and colons represent normal ordering. We shall now consider the explicit forms of the YN and NN interactions, and use Eq. (6.42) to relate expressions in the Grassmann and transfer matrix formulations. To be specific, consider now the Λ hyperons. The most simple form of the action reads

$$\begin{aligned} S &= S_Y + S_{YN}\ , \\ S_Y &= h\sum_{\boldsymbol{n}}\zeta_Y^*(\boldsymbol{n},n_t)\zeta_Y(\boldsymbol{n},n_t) - h\sum_{\boldsymbol{n}}\sum_{l=1}^{3}\zeta_Y^*(\boldsymbol{n},n_t)\Big[\zeta_Y(\boldsymbol{n}+\hat{e}_l,n_t)+\zeta_Y(\boldsymbol{n}-\hat{e}_l,n_t)\Big]\ , \\ S_{YN} &= \alpha_t C_{YN}\sum_{\boldsymbol{n}}\rho_N(\boldsymbol{n},n_t)\rho_Y(\boldsymbol{n},n_t)\ , \end{aligned} \tag{6.43}$$

where m_Y is the hyperon mass, $h=\alpha_t/(2m_Y)$, and $\alpha_t = a_t/a$ is the ratio of temporal and spatial lattice spacings. The LEC C_{YN} may be fitted, for instance, to the empirical hypertriton binding energy. Using Eq. (6.42), the hyperon contributions are described by the transfer matrix operator

$$M =: \exp\left(-\alpha_t T - \alpha_t C_{YN}\sum_{\boldsymbol{n}}\rho_N(\boldsymbol{n})\rho_Y(\boldsymbol{n})\right):\ , \tag{6.44}$$

where

$$\rho_N(\boldsymbol{n}) \equiv \sum_{i,j}\rho_{i,j}(\boldsymbol{n}) \equiv \sum_{i,j} a_{i,j}^\dagger(\boldsymbol{n})a_{i,j}(\boldsymbol{n})\ , \quad \rho_Y(\boldsymbol{n}) \equiv a_Y^\dagger(\boldsymbol{n})a_Y(\boldsymbol{n})\ , \tag{6.45}$$

are density operators for nucleons and hyperons, respectively. Note that this is a simplified version of the pionless EFT calculation of Ref. [81], which also included a three-body interaction at LO. Treating the NN interactions in the usual fashion, we are now in the position to integrate out the hyperon degrees of freedom and derive a "reduced" transfer matrix, which refers to the nucleon degrees of freedom only. For simplicity (and without loss of generality), we shall neglect the NN interaction term for the purpose of the derivation, and consider the case of a single hyperon Y and nucleon N (which can be thought of as representing any of the spin–isospin combinations i,j of the full theory). Next, we write the transfer matrix element between time slices n_t and n_t+1 in terms of

$$|\chi_{n_t}^N,\chi_{n_t}^Y\rangle \equiv \prod_{\boldsymbol{n}}\left\{\Big[a_N^\dagger(\boldsymbol{n})\Big]^{\chi_{n_t}^N(\boldsymbol{n})}\Big[a_Y^\dagger(\boldsymbol{n})\Big]^{\chi_{n_t}^Y(\boldsymbol{n})}\right\}|0\rangle, \tag{6.46}$$

where the $\chi_{n_t}^s(\boldsymbol{n})$ count the occupation numbers for nucleons and hyperons on time slice n_t and spatial lattice site $\boldsymbol{n}$. Following the relations established in Ref. [278], we express the transfer matrix element as

$$\begin{aligned}&\langle\chi_{n_t+1}^N,\chi_{n_t+1}^Y|\hat{M}|\chi_{n_t}^N,\chi_{n_t}^Y\rangle = \\ &\prod_{\boldsymbol{n}}\left\{\left[\frac{\overrightarrow{\partial}}{\partial\zeta_N^*(\boldsymbol{n},n_t)}\right]^a\left[\frac{\overrightarrow{\partial}}{\partial\zeta_Y^*(\boldsymbol{n},n_t)}\right]^b\right\}X(n_t)M(n_t)\times\prod_{\boldsymbol{n}'}\left\{\left[\frac{\overleftarrow{\partial}}{\partial\zeta_N^*(\boldsymbol{n}',n_t)}\right]^c\left[\frac{\overleftarrow{\partial}}{\partial\zeta_Y^*(\boldsymbol{n}',n_t)}\right]^d\right\}\Bigg|_{\substack{\zeta_N^*=\zeta_N=0\\ \zeta_Y^*=\zeta_Y=0}},\end{aligned} \tag{6.47}$$

where

$$a=\chi_{n_t+1}^N(\boldsymbol{n})\ , \quad b=\chi_{n_t+1}^Y(\boldsymbol{n})\ , \quad c=\chi_{n_t}^N(\boldsymbol{n}')\ , \quad d=\chi_{n_t}^Y(\boldsymbol{n}')\ , \tag{6.48}$$

are integers which are either 0 or 1. Further,

$$X(n_t) \equiv \prod_{\boldsymbol{n}}\exp(\zeta_N^*(\boldsymbol{n},n_t)\zeta_N(\boldsymbol{n},n_t))\times\exp(\zeta_Y^*(\boldsymbol{n},n_t)\zeta_Y(\boldsymbol{n},n_t)), \tag{6.49}$$

and

$$M(n_t) \equiv \exp(-S_{\mathrm{kin}}[\zeta,\zeta^*,n_t])\exp(-S_{\mathrm{int}}[\zeta,\zeta^*,n_t]), \tag{6.50}$$

are Grassmann functions (to be defined below). The impurity worldline is considered static for the purposes of this derivation, although it will be updated by the Metropolis algorithm in the actual MC simulations. From one time slice to the next, the impurity

may either remain on the same lattice site, or hop to a nearest-neighbor site. For the case where the impurity remains on a given lattice site $\boldsymbol{n}''$, we have

$$\langle \chi^N_{n_t+1}, \chi^Y_{n_t+1} | M | \chi^N_{n_t}, \chi^Y_{n_t} \rangle = \prod_{\boldsymbol{n}} \left\{ \left[\frac{\overrightarrow{\partial}}{\partial \zeta^*_N(\boldsymbol{n}, n_t)} \right]^{\chi^N_{n_t+1}(\boldsymbol{n})} \right\} \mathcal{X}(n_t) \mathcal{M}_{\boldsymbol{n}'',\boldsymbol{n}''}(n_t) \prod_{\boldsymbol{n}'} \left\{ \left[\frac{\overleftarrow{\partial}}{\partial \zeta^*_N(\boldsymbol{n}', n_t)} \right]^{\chi^N_{n_t}(\boldsymbol{n}')} \right\} \Bigg|_{\zeta^*_N = \zeta_N = 0}, \tag{6.51}$$

with

$$\chi^Y_{n_t}(\boldsymbol{n}'') = 1, \quad \chi^Y_{n_t+1}(\boldsymbol{n}'') = 1, \tag{6.52}$$

and thus

$$\mathcal{X}(n_t) \mathcal{M}_{\boldsymbol{n}'',\boldsymbol{n}''}(n_t) = \frac{\overrightarrow{\partial}}{\partial \zeta^*_Y(\boldsymbol{n}'', n_t)} X(n_t) \exp(-S_{\rm kin}[\zeta, \zeta^*, n_t]) \times \exp(-S_{\rm int}[\zeta, \zeta^*, n_t]) \frac{\overleftarrow{\partial}}{\partial \zeta_Y(\boldsymbol{n}'', n_t)} \Bigg|_{\zeta^*_Y = \zeta_Y = 0}, \tag{6.53}$$

where

$$\mathcal{X}(n_t) \equiv \prod_{\boldsymbol{n}} \exp(\zeta^*_N(\boldsymbol{n}, n_t) \zeta_N(\boldsymbol{n}, n_t)). \tag{6.54}$$

and we define $\mathcal{M}(n_t)$ as the "reduced" transfer matrix. Specifically, we take $S_{\rm kin}[\zeta, \zeta^*, n_t] = S_N[\zeta, \zeta^*, n_t] + S_Y[\zeta, \zeta^*, n_t]$, with the nearest-neighbor expression for the hyperon kinetic term and also $S_{\rm int}[\zeta, \zeta^*, n_t] = S_{YN}[\zeta, \zeta^*, n_t]$ as the YN interaction. By evaluating the derivatives in Eq. (6.53), we find

$$\mathcal{M}_{\boldsymbol{n}'',\boldsymbol{n}''}(n_t) = \exp(-S_N[\zeta, \zeta^*, n_t]) \left(1 - 6h - \alpha_t C_{YN} \rho_N(\boldsymbol{n}'', n_t)\right), \tag{6.55}$$

which can be written as

$$\mathcal{M}_{\boldsymbol{n}'',\boldsymbol{n}''}(n_t) \simeq (1 - 6h) \exp\left(-S_N[\zeta, \zeta^*, n_t] - \frac{\alpha_t C_{YN}}{1 - 6h} \rho_N(\boldsymbol{n}'', n_t)\right), \tag{6.56}$$

where the last factor, which encodes the interaction between the nucleons and the single hyperon impurity, has been exponentiated. Thus, Eq. (6.56) is the reduced Grassmann transfer matrix for the case where the impurity worldline remains stationary. For the case of a long-range YN interaction, Eq. (6.56) should be replaced by an expression of the form

$$\mathcal{M}_{\boldsymbol{n}'',\boldsymbol{n}''}(n_t) \simeq (1 - 6h) \exp\left(-S_N[\zeta, \zeta^*, n_t] - \frac{\alpha_t}{1 - 6h} \sum_{\boldsymbol{n}'} G(\boldsymbol{n}' - \boldsymbol{n}'') \rho_N(\boldsymbol{n}', n_t)\right), \tag{6.57}$$

whereby the hyperon impurity now also interacts with nucleons not on the same spatial lattice site, and $G(\boldsymbol{n}' - \boldsymbol{n}'')$ is the nucleon Greens function (propagator). As a check, setting $G(\boldsymbol{n}' - \boldsymbol{n}) = C_{YN} \delta(\boldsymbol{n}' - \boldsymbol{n})$, the expression for a contact interaction is recovered. Another possibility permitted by the nearest-neighbor YN kinetic term is

$$\chi^Y_{n_t}(\boldsymbol{n}'') = 1, \quad \chi^Y_{n_t+1}(\boldsymbol{n}'' \pm \hat{e}_l) = 1, \tag{6.58}$$

such that

$$\mathcal{X}(n_t) \mathcal{M}_{\boldsymbol{n}''\pm\hat{e}_l,\boldsymbol{n}''}(n_t) = \frac{\overrightarrow{\partial}}{\partial \zeta^*_Y(\boldsymbol{n}'' \pm \hat{e}_l, n_t)} X(n_t) \exp(-S_{\rm kin}[\zeta, \zeta^*, n_t]) \times \exp(-S_{\rm int}[\zeta, \zeta^*, n_t]) \frac{\overleftarrow{\partial}}{\partial \zeta_Y(\boldsymbol{n}'', n_t)} \Bigg|_{\zeta^*_Y = \zeta_Y = 0}, \tag{6.59}$$

which gives

$$\mathcal{M}_{\boldsymbol{n}''\pm\hat{e}_l,\boldsymbol{n}''}(n_t) = h \exp\left(-S_N[\zeta, \zeta^*, n_t]\right), \tag{6.60}$$

for the reduced Grassmann transfer matrix, when the impurity hops to a neighboring lattice site. Having determined the form of the reduced Grassmann transfer matrices, these can be translated to the transfer matrix formulation. The corresponding operators are

$$\mathcal{M}_{\boldsymbol{n}'',\boldsymbol{n}''} = (1 - 6h) : \exp\left(-\alpha_t T_N - \frac{\alpha_t C_{YN}}{1 - 6h} \hat{\rho}_N(\boldsymbol{n}'')\right) :, \tag{6.61}$$

from Eq. (6.56), and

$$\mathcal{M}_{\boldsymbol{n}''\pm\hat{e}_l,\boldsymbol{n}''} = h : \exp(-\alpha_t T_N) :, \tag{6.62}$$

from Eq. (6.60), with T_N the nucleon kinetic energy. A few comments about this implementation of the ILMC formalism are in order. In the MC codes, Eq. (6.61) is evaluated as

$$\mathcal{M}_{\boldsymbol{n}'',\boldsymbol{n}''} \sim \left(1 - \alpha_t T_N - \frac{\alpha_t C_{YN}}{1 - 6h} \hat{\rho}_N(\boldsymbol{n}'') - V_{\phi N}\right), \tag{6.63}$$

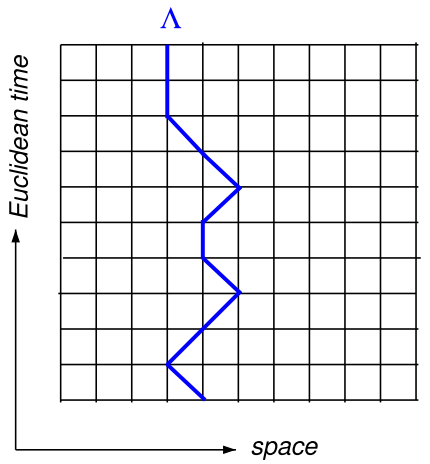

Fig. 6.4. Illustration of the hyperon worldline. In the reduced transfer matrix formalism, the hyperon (here, the Λ) has been "integrated out", and the interaction between the hyperon and the nucleons is mediated by an effective "background field" generated by the hyperon worldline.

which also includes the NN interaction through term $V_{\phi N}$ that gives the auxiliary field coupling(s) to the nucleon density. For ILMC, the nucleons are treated as distinguishable particles, and the hyperon as a classical worldline during the Euclidean time evolution, as depicted in Fig. 6.4.

This induces a three-body interaction when two nucleons and the hyperon occupy the same site, which is absent in Eq. (6.44). To be able to benchmark the ILMC codes against exact Euclidean time projection calculations of Eq. (6.44), the induced interaction

$$H_{YNN} = -\frac{\alpha_t C_{YN}^2}{2(1-6h)} \sum_{\boldsymbol{n}} \rho_N(\boldsymbol{n})\rho_N(\boldsymbol{n})\rho_Y(\boldsymbol{n}), \tag{6.64}$$

has to be added to the original transfer matrix (6.44). This induced 3BF is a lattice artifact which disappears when $\alpha_t \to 0$. Let us now discuss how ILMC calculations are performed using the Projection Monte Carlo (PMC) method. Assume first that the impurity has been fixed at a given spatial lattice site, and that no "hopping" of the impurity occurs during the Euclidean time evolution. We shall then relax this constraint, and discuss a practical algorithm for updating the configuration of the hyperon worldline.

Stationary impurity: For a stationary hyperon impurity, the reduced transfer matrix is given by Eq. (6.61), and for the purposes of the PMC calculation, we define the Euclidean projection amplitude

$$Z_{jk}(N_t) \equiv \langle \psi_j | \not{M}^{N_t} | \psi_k \rangle, \tag{6.65}$$

where j and k denote different initial cluster states. As usual, this is expressed as a determinant of single-particle amplitudes, which gives

$$Z_{jk}(N_t) = \det M^{jk}_{p\times p}, \tag{6.66}$$

where

$$M^{jk}_{p\times p} = \begin{pmatrix} \langle \phi_{0,j} | \not{M}^{N_t} | \phi_{0,k} \rangle & \langle \phi_{0,j} | \not{M}^{N_t} | \phi_{1,k} \rangle & \cdots \\ \langle \phi_{1,j} | \not{M}^{N_t} | \phi_{0,k} \rangle & \langle \phi_{1,j} | \not{M}^{N_t} | \phi_{1,k} \rangle & \cdots \\ \vdots & \vdots & \ddots \end{pmatrix}, \tag{6.67}$$

for p nucleons. By means of the projection amplitudes (6.66), we construct

$$[M^a(N_t)]_{qq'} \equiv \sum_{q''} Z^{-1}_{qq''}(N_t) Z_{q''q'}(N_t+1), \tag{6.68}$$

which is known as the adiabatic transfer matrix. If we denote the eigenvalues of (6.68) by $\lambda_i(N_t)$, we find

$$\lambda_i(N_t) = \exp(-\alpha_t E_i(N_t + 1/2)), \tag{6.69}$$

such that the low-energy spectrum is given by the transient energies

$$E_i(N_t + 1/2) = -\frac{\log(\lambda_i(N_t))}{\alpha_t}, \tag{6.70}$$

at finite temporal lattice spacing a_t. For the case of a single trial cluster state with p nucleons, Eq. (6.66) reduces to

$$Z(N_t) = \det M^{00}_{p\times p}\ . \tag{6.71}$$

The ground-state energy is obtained from

$$E_0(N_t + 1/2) = -\frac{\log(Z(N_t+1)/Z(N_t))}{\alpha_t}, \tag{6.72}$$

in the limit $N_t \to \infty$, where the exact low-energy spectrum of the transfer matrix will be recovered. Note that the argument $N_t + 1/2$ is conventionally assigned to the transient energy computed from the ratio of projection amplitudes evaluated at Euclidean time steps $N_t + 1$ and N_t. For the hypertriton, we have $p = 2$ nucleons after the impurity hyperon has been integrated out. We start the Euclidean time projection with a single initial trial cluster state ($j = k = 0$) consisting of a spin-up proton, and a spin-up neutron. As there are no terms that mix spin or isospin, the other components of each single-particle state are set to zero, and remain so during the PMC calculation. For the spatial parts of the nucleon wave functions, we may choose, for example, the zero-momentum state

$$|\phi_{0,0}\rangle = |\phi_{1,0}\rangle = \langle 0, 0, 0\rangle, \tag{6.73}$$

in the notation of Ref. [278], which denotes plane-wave orbitals in a cubic box. In principle, we may also choose any other plane-wave state with non-zero momentum (see Table 1 of Ref. [278]), or any other more complicated trial state. For the heavier nuclei, it is indeed better to choose an initial state where the nucleons are clustered together. In this case, we sum over all possible translations of the cluster in order construct an initial state with zero total momentum.

Hopping impurity: If the hyperon impurity is allowed to hop between nearest-neighbor sites (from one Euclidean time slice to the next), the Euclidean projection amplitude becomes a sum over hyperon worldline configurations. This gives

$$Z_{jk}(N_t) \equiv \sum_{\boldsymbol{n}_0,\ldots,\boldsymbol{n}_{N_t}} \langle \psi_j | \hat{M}^{N_t}_{\{\boldsymbol{n}_j\}} | \psi_k \rangle, \tag{6.74}$$

where the product

$$\hat{M}^{N_t}_{\{\boldsymbol{n}_j\}} \equiv \hat{M}_{\boldsymbol{n}_{N_t},\boldsymbol{n}_{N_t-1}} \hat{M}_{\boldsymbol{n}_{N_t-1},\boldsymbol{n}_{N_t-2}} \cdots \hat{M}_{\boldsymbol{n}_2,\boldsymbol{n}_1} \hat{M}_{\boldsymbol{n}_1,\boldsymbol{n}_0}, \tag{6.75}$$

is expressed in terms of the reduced transfer matrices (6.61) and (6.62). Here, $\boldsymbol{n}_j$ denotes the spatial position of the hyperon impurity on time slice j. The expressions for the projection amplitude and determinant are generalized to

$$Z_{jk}(N_t) = \sum_{\boldsymbol{n}_0,\ldots,\boldsymbol{n}_{N_t}} \det M^{jk}_{p\times p}, \tag{6.76}$$

where

$$M^{jk}_{p\times p} = \begin{pmatrix} \langle \phi_{0,j} | \hat{M}^{N_t}_{\{\boldsymbol{n}_j\}} | \phi_{0,k} \rangle & \langle \phi_{0,j} | \hat{M}^{N_t}_{\{\boldsymbol{n}_j\}} | \phi_{1,k} \rangle & \cdots \\ \langle \phi_{1,j} | \hat{M}^{N_t}_{\{\boldsymbol{n}_j\}} | \phi_{0,k} \rangle & \langle \phi_{1,j} | \hat{M}^{N_t}_{\{\boldsymbol{n}_j\}} | \phi_{1,k} \rangle & \cdots \\ \vdots & \vdots & \ddots \end{pmatrix}, \tag{6.77}$$

such that the determinant is now to be computed over all possible hyperon wordline configurations. We note that the worldline configuration is to be updated stochastically using a Metropolis-type algorithm. Thus, the proposed changes in the impurity worldline are accepted or rejected by importance sampling with $|Z_{jj}(N_t)|$ as the probability weight function. Here, j denotes one of the initial trial nucleon cluster states.

Worldline updates: The updating of the impurity worldline is handled in two steps: The generation of a new proposed worldline, and a Metropolis accept/reject step to determine whether to use the generated worldline. Here, the worldline $W(\boldsymbol{n}, n_t)$ is a function of only the lattice site $\boldsymbol{n}$ and the Euclidean time step n_t, and is equal to 1 where the impurity is present, and 0 at all other lattice points. From the expressions of the reduced transfer matrices, the worldline at two adjacent time steps, $W(\boldsymbol{n}', n_t)$ and $W'(\boldsymbol{n}', n_t + 1)$ must obey the relation $|\boldsymbol{n} - \boldsymbol{n}'| \leq 1$. For an illustration of the impurity (hyperon) worldline, see Fig. 6.4. For the non-interacting worldline, we can generate new configurations from the free probabilities, determined from the reduced transfer matrices. In this case, $P_h = h$ is the hopping probability, and $P_s = (1 - 6h)$ is the probability to remain stationary. When initializing the worldline at the beginning of the MC simulation, we may start from a configuration where the worldline is completely stationary ("cold start"), a configuration where the worldline either hops or remains stationary with equal probabilities ("hot start"), or one where the worldline either hops or remains stationary according to P_h and P_s ("warm start"). At the beginning of every sweep through the lattice, we propose a new worldline to use for that sweep. This is done by taking the previous worldline and choosing a random time at which we cut the worldline and regenerating it either in the forwards and backwards time direction. The new worldline is then accepted or rejected using a Metropolis accept or reject condition to preserve detailed balance associated with the absolute value of the amplitude.

In Table 6.1, we present benchmark calculations of the IMLC results for ${}^{3}_{\Lambda}\mathrm{H}$ in comparison with exact transfer matrix calculations. We present the energy versus Euclidean time.

We see that the agreement is quite good. The initial nucleon states for these calculations are chosen to be constant functions corresponding to zero momentum wave functions. The hyperon initial wave function is also taken be a constant function. These exact transfer matrix calculations include the induced three-baryon interaction described in Eq. (6.64).

In Ref. [280], results for light hypernuclei where presented using spin-independent nucleon–nucleon and hyperon–nucleon interactions to test the computational power of the method. The resulting hypertriton binding energy comes out as $B_\Lambda = 0.22$ MeV, which is reasonable given the simplified nature of the calculation. In Fig. 6.5, we show the ILMC results for the ${}^{4}_{\Lambda}\mathrm{He}/{}^{4}_{\Lambda}\mathrm{H}$ and the

Table 6.1
Impurity lattice Monte Carlo results for the energy of ${}^{3}_{\Lambda}$H versus Euclidean time in comparison with exact transfer matrix results for periodic box length 15.8 fm.

L_t	t (MeV^{-1})	ILMC (MeV)	Exact (MeV)
50	0.1667	−1.0878(6)	−1.0878
100	0.3333	−1.4598(9)	−1.4590
150	0.5000	−1.6778(11)	−1.6760
200	0.6667	−1.7975(13)	−1.7966
250	0.8333	−1.8630(17)	−1.8614
300	1.0000	−1.8971(18)	−1.8954

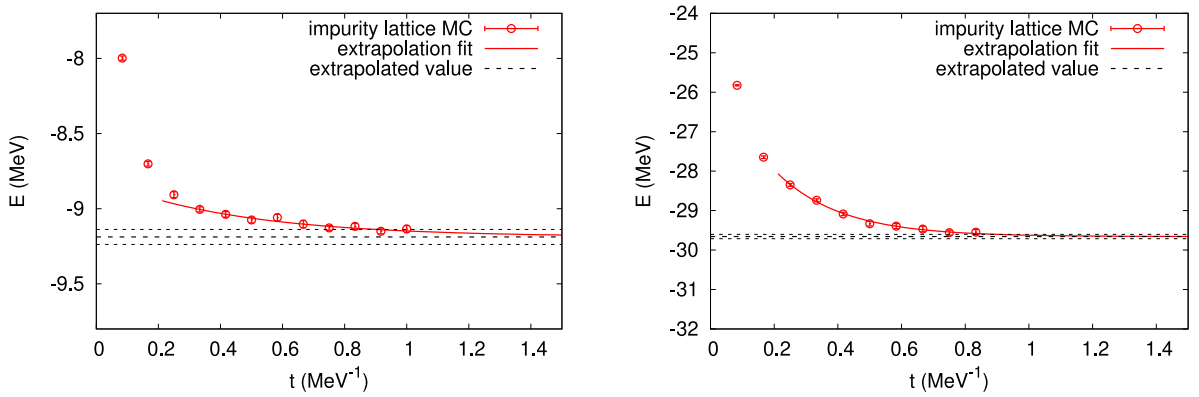

Fig. 6.5. Left panel: ILMC results for the ${}^{4}_{\Lambda}$H/${}^{4}_{\Lambda}$He energy versus Euclidean projection time in a periodic box size of $L = 15.8$ fm. **Right panel:** ILMC results for the ${}^{5}_{\Lambda}$He energy versus Euclidean time in a periodic box size of $L = 9.9$ fm. In both cases the ground state energy is extracted using an exponential ansatz for the asymptotic time dependence.

${}^{5}_{\Lambda}$He hypernuclei, which lead to the binding energies of 0.46(5) MeV and 3.96(6) MeV, where the error is mostly due to the Euclidean time extrapolation but no effort has been made to address the issue of higher orders. These values are again comparable to the experimental ones, showing that this approach is indeed capable of capturing the main features of light hypernuclei.

In Ref. [281], the ILMC formalism for the case of two distinguishable impurities in a bath of polarized fermions was developed. As before, the majority particles are treated as explicit degrees of freedom, while the impurities are described by worldlines. The latter serve as localized auxiliary fields, which affect the majority particles. The method was applied to non-relativistic three-dimensional systems of two impurities and a number of majority particles where both the impurity–impurity interaction and the impurity–majority interaction have zero range. For the case of an attractive impurity–majority interaction the formation and disintegration of bound states as a function of the impurity–impurity interaction strength was studied. This formalism could be applied to $\Lambda\Lambda$ hypernuclei, but this has so far not been done. An unsolved problem in the ILMC formalism is the smearing of the worldline, which has so far prevented further detailed applications of this approach.

6.3.2. Auxiliary field formalism

In NLEFT, the Auxiliary Field Quantum Monte Carlo (AFQMC) method is used as it leads to a significant suppression of the sign oscillations [258]. AFQMC represents a powerful computational framework within quantum many-body physics, particularly tailored for investigating strongly correlated systems. This method addresses the challenge of solving the full A-body Schrödinger equation by introducing a Hubbard–Stratonovich transformation. This transformation incorporates auxiliary fields to decouple particle densities, thereby enhancing the applicability of MC techniques. In essence, within the AFQMC formalism, individual nucleons evolve as if they are single particles in a fluctuating background of auxiliary fields. As has been shown recently [44,276], Λ hyperons can also be included in this formalism, which is a major step forward in the study of hypernuclei and hyperons in dense neutron matter.

To be concrete, let us consider a discrete auxiliary field formulation for the SU(4) symmetric short-ranged NN interaction given in Eq. (6.33),

$$: \exp\left(-\frac{a_t\, c_{NN}}{2}\,\tilde{\rho}^2\right) := \sum_{k=1}^{3} w_k \; : \exp\left(\sqrt{-a_t\, c_{NN}}\, s_k\, \tilde{\rho}\right) \; : \quad . \tag{6.78}$$

From a Taylor expansion of Eq. (6.78) one determines the constants s_k and w_k as $s_1 = -s_3 = \sqrt{3}$, $s_2 = 0$, $w_1 = w_3 = 1/6$ and $w_2 = 2/3$. This NN interaction obeys the Wigner SU(4) symmetry. Since we use minimal forces for the YN and YY interactions, it is possible to derive an auxiliary field formulation for systems including neutrons, protons and Λ hyperons. This derivation involves replacing the isospin SU$_T$(2) with flavor SU$_F$(3) within Wigner's SU(4) symmetry framework, and the combined spin (S) and flavor

(F) invariance ultimately leads to the SU(6) symmetry [282]. However, the fact that the strengths of the NN and YN interactions are different breaks this SU(6) symmetry, and there is no longer an approximate symmetry similar to Wigner's SU(4) symmetry used in Eq. (6.78). Nevertheless, one can exploit the fact that $|c_{NN}| > |c_{N\Lambda}| > |c_{\Lambda\Lambda}|$, allowing us to introduce an auxiliary field formulation with an approximate SU(6) symmetry that protects our simulations including Λ hyperons against strong sign oscillations. For that, express the spin and isospin independent two-baryon interactions in Eq. (6.33) as,

$$V_{\rm 2B} = \frac{c_{NN}}{2} \sum_{\boldsymbol{n}} \, : \, [\tilde{\rho}(\boldsymbol{n})]^2 \, : \, + c_{N\Lambda} \sum_{\boldsymbol{n}} \, : \, \tilde{\rho}(\boldsymbol{n}) \tilde{\xi}(\boldsymbol{n}) \, : \, + \frac{c_{\Lambda\Lambda}}{2} \sum_{\boldsymbol{n}} \, : \, \left[\tilde{\xi}(\boldsymbol{n})\right]^2 \, : \, , \tag{6.79}$$

and this potential (6.79) can be rewritten in the following form,

$$V_{\rm 2B} = \frac{c_{NN}}{2} \sum_{\boldsymbol{n}} \, : \, \left[\tilde{\boldsymbol{\rho}}(\boldsymbol{n})\right]^2 \, : \, + \frac{1}{2} \left(c_{\Lambda\Lambda} - \frac{c_{N\Lambda}^2}{c_{NN}} \right) \sum_{\boldsymbol{n}} \, : \, \left[\tilde{\xi}(\boldsymbol{n})\right]^2 \, : \, , \tag{6.80}$$

where $\tilde{\boldsymbol{\rho}}$ is defined as,

$$\tilde{\boldsymbol{\rho}} = \tilde{\rho} + \frac{c_{N\Lambda}}{c_{NN}} \, \tilde{\xi} \, . \tag{6.81}$$

In Eq. (6.80) the leading contribution comes from the first term on the right-hand side. It is treated non-perturbatively, while the remaining term is computed using first-order perturbation theory. Hence, we define a new Hubbard–Stratonovich transformation for the first term in Eq. (6.80), enabling the simulations of systems consisting of both arbitrary number of nucleons and arbitrary number of Λ hyperons with a single auxiliary field,

$$: \exp\left(-\frac{a_t \, c_{NN}}{2} \, \tilde{\boldsymbol{\rho}}^2 \right) := \sum_{k=1}^{3} w_k \, : \exp\left(\sqrt{-a_t \, c_{NN}} \, s_k \, \tilde{\boldsymbol{\rho}} \right) : \, . \tag{6.82}$$

It is evident that the solution for the auxiliary field variables s_k and weights w_k is consistent with systems containing only nucleons. This extension of the AFQMC method introduced here broadens hypernuclear calculations by enabling simulations with any number of hyperons. In addition, the approach can be effectively applied to a wide range of systems, see e.g. [283]. For understanding that, consider two distinct families of particles and call them A and B, and assume that all interactions are attractive. When the square of the interaction strength between particle types A and B, denoted as c_{AB}^2, is of comparable magnitude to the product of the interaction strengths within the same particle types, $c_{AA} c_{BB}$, the overall coupling of the second term in Eq. (6.80) becomes very small, enabling a perturbative treatment and calculations with a single auxiliary field. Furthermore, when $c_{AA} c_{BB} \geq c_{AB}^2$, the second term's overall coupling is attractive, so that calculations still can be performed with two auxiliary fields. However, only in the case of $c_{AA} c_{BB} \ll c_{AB}^2$, the overall coupling of the second term becomes repulsive which leads to significant sign problems.

Finally, we discuss the NN interaction $\sim c_{NN}^T$, known to break SU(4) symmetry and to induce significant sign oscillations, which was previously disregarded in minimal nuclear interaction studies. Since we aim at constraining nuclear forces by using the ground state energies of finite hypernuclei and the saturation properties of symmetric nuclear matter, this isospin interaction is treated non-perturbatively. We employ a Hubbard–Stratonovich transformation and introduce a discrete auxiliary field defined as,

$$: \exp\left(-\frac{a_t \, c_{NN}^T}{2} \sum_I \tilde{\rho}_I^2 \right) := \sum_{k=1}^{3} w_k \, : \exp\left(\sqrt{-a_t \, c_{NN}^T} \sum_I s_{k,I} \, \tilde{\rho}_I \right) : \, . \tag{6.83}$$

To minimize the occurring sign oscillations in finite nuclei, we focus on systems with equal numbers of protons and neutrons. Furthermore, in the simulations of pure neutron matter and hyper-neutron matter, this term can be omitted due to the absence of particles breaking isospin symmetry, allowing for sign oscillation-free simulations. Similarly, in the studies based on the Hamiltonian given in Eq. (6.26), the same trick is employed to include the Λ hyperon in the simulations.

6.4. Results from the minimal hypernuclear interaction

Here, we consider the results obtained from the minimal hypernuclear model. We note that in the original work on that topic [276], hypernuclei where considered together with the equation of state of nuclear as well as (hyper-)neutron matter, that is neutron matter in the absence (presence) of hyperons. In this review, we focus mostly on the results for hypernuclei and refer to a detailed discussion of the EoS of hyper-neutron matter to Ref. [276]. First, one has to give the lattice parameters. A spatial lattice spacing of $a = 1.1$ fm and a temporal lattice spacing of $a_t = 0.2$ fm are used. The local and nonlocal smearing parameters are $s_{\rm L} = 0.06$ and $s_{\rm NL} = 0.6$, respectively. For the three-baryon interaction, the local smearing parameter is set to $s_{\rm L}^{\rm 3B} = 0.06$. To compute the g.s. energies of finite nuclei and hypernuclei, various periodic cubic lattices ranging in length from 13.2 fm to 19.7 fm are used. Furthermore, for the computation of pure neutron matter and hyper-neutron matter energies one uses lattices with a length of 6.6 fm and imposes average twisted boundary conditions to efficiently eliminate finite volume effects, see Ref. [284]. Second, one must fix parameters in the nucleonic sector, i.e. the LECs c_{NN}, c_{NN}^T and $c_{NNN}^{(d_i)}$, see Eqs. (6.33),(6.34). This are determined from a fit to the $^1S_0$ and $^3S_1$ np phase shifts and to the saturation properties of symmetric nuclear matter considering all possible combinations of d_1 and d_2 with $0 \leq d_1 < d_2 \leq 3$. Through this process, one arrives at six distinct interactions, enabling one to quantify the theoretical uncertainty. The resulting EoSs for nuclear and neutron matter are shown in Fig. 6.6. Together with the binding energy of some typical nuclei, namely $E(^4{\rm He}) = 29.4(5)$ MeV, $E(^8{\rm Be}) = 58.4(9)$ MeV, $E(^{12}{\rm C}) = 87.1(10)$ MeV, and $E(^{16}{\rm 0}) = 121.8(7)$ MeV, this shows that this minimal model captures the basic features of nuclear binding. Third, we must fix the LECs in the $S = -1, -2$ sectors, which

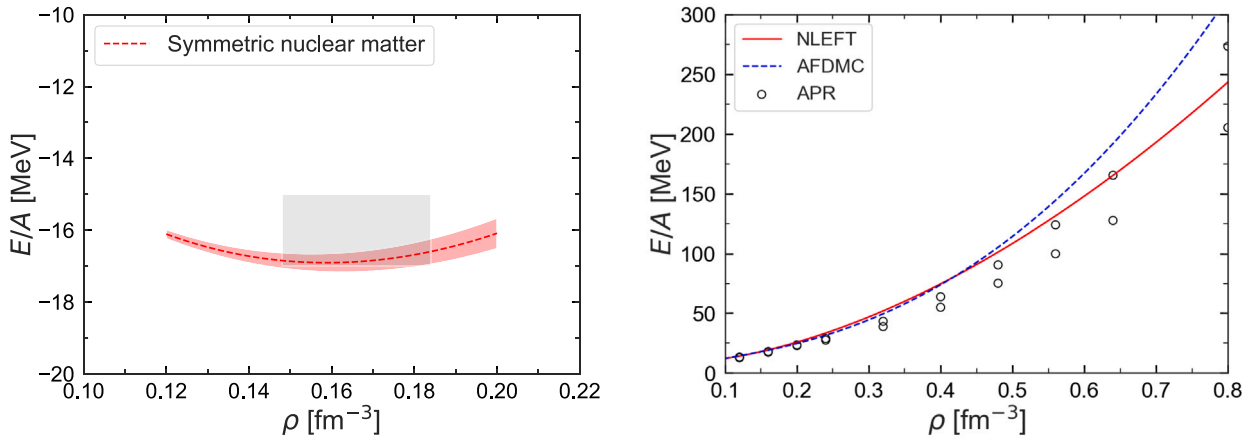

Fig. 6.6. **Left Panel:** Energy per nucleon as a function of density for symmetric nuclear matter from the NLEFT calculations. The gray shaded area indicates the empirical values. **Right Panel:** Energy per nucleon as a function of density for symmetric nuclear matter from the NLEFT calculations (red line) in comparison to the APR [286] (black circles) and AFDMC [287] (blue dashed line) calculations.

Table 6.2
Λ separation energies for single-Λ and double-Λ hypernuclei in the minimal interaction model (in MeV). The first error is the statistical one whereas the second error is the systematic one (due to the three-baryon forces). The * marks a prediction. Note that the experimental values for the two Be double-Λ hypernuclei are contested.

Nucleus	${}^{5}_{\Lambda}$He	${}^{9}_{\Lambda}$Be	${}^{13}_{\Lambda}$C	${}^{6}_{\Lambda\Lambda}$He	${}^{10}_{\Lambda\Lambda}$Be	${}^{12}_{\Lambda\Lambda}$Be
NLEFT$_{\text{min}}$	3.40(1)(1)	5.72(5)(4)	10.54(17)(29)*	6.91(1)(1)	13.30(7)(12)*	21.22(56)(21)*
Exp.	3.10(3)	6.61(7)	11.80(16)	6.91(16)	14.70(40)	21.48(121)

are $c_{N\Lambda}, c_{\Lambda\Lambda}$ in the two-particle and $c^{(d_i)}_{NN\Lambda}, c^{(d_i)}_{N\Lambda\Lambda}$ in the three-particle sector. These parameters are determined as follows: For the ΛN interaction, one fits the experimental total cross-section data $\sigma_{\text{tot}}(\Lambda N \to \Lambda N)$ for laboratory momenta below 600 MeV and in the absence of cross section data in the $= -2$ sector, the ${}^1S_0$ phase shift derived from chiral EFT at NLO [104] is also fitted. To pin down the parameters of the 3BFs, the separation energies for single-Λ and double-Λ hypernuclei are fitted as collected in Table 6.2, where also a few predictions are given. As in the nucleonic sector, one obtains an overall satisfactory description of hypernuclei. For the discussion of the neutron matter EoS in the presence of hyperons and the resulting neutron star properties, we refer to Refs. [276,285].

This work has recently been improved and more hypernuclei have been considered [288]. In fact, the LECs of the ΛNN and $\Lambda\Lambda$N interaction were determined solely from hypernuclear binding energies as shown by the open square symbols in Fig. 6.7. With that, the ground state energies of 10 single-Λ hypernuclei and of one double-Λ hypernucleus could be predicted, generally finding good agreement with the data and with calculations based on variational MC calculations [47] and the NCSM [289]. In this work, the density where Λ hyperons appear in a neutron star is predicted to be $\rho^{\text{crit}}_{\Lambda} = 0.490(0.002)(0.005)$ fm^{-3}, consistent with other approaches. This calculation also yields a neutron star maximum mass consistent with observations, predicts tidal deformabilities compatible with gravitational-wave measurements, and gives a trace anomaly in line with Bayesian constraints. The consistency with astrophysical posteriors arises from the fact that in this framework the three-body hyperonic interactions are systematically constrained by single- and double-Λ separation energies of hypernuclei, cf. Fig. 6.7. These constraints ensure that the additional hyperonic degrees of freedom soften the EoS in a controlled manner. At the same time, the repulsive components of the three-body forces counterbalance this effect. Therefore, this approach provides a solid microscopic foundation for reliable predictions of neutron star properties that incorporate hyperonic matter.

6.5. Results based on high-fidelity chiral forces

In Ref. [44], Λ-hypernuclei where considered based on the Hamiltonian Eq. (6.26) with $V_{YYN} = 0$ and the locally and non-locally smeared 3BFs given in Eqs. (6.27) and (6.30), respectively. A spacial lattice spacing of $a = 1.32$ fm and a temporal lattice spacing of $a_t = 1/1000$ MeV^{-1} were used. All interactions share a similar set of local and non-local smearing parameters of $s_{\text{L}} = 0.07$ and $s_{\text{NL}} = 0.5$, the same parameters are also used in Ref. [269] for the NN interaction. The presence of non-local smearing results

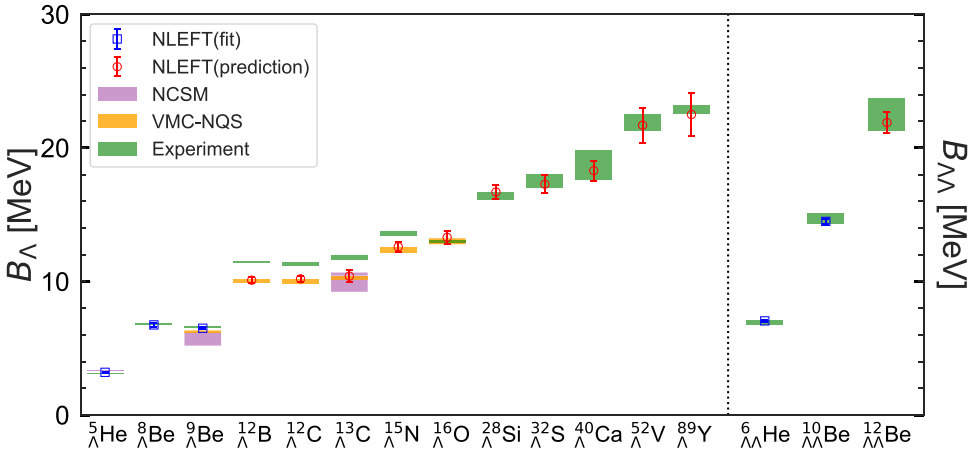

Fig. 6.7. Single-Λ separation energies and double-Λ separation energies for hypernuclei. Hypernuclei used to fit the $NN\Lambda$ and $N\Lambda\Lambda$ forces are depicted by blue squares. Predictions are shown as red circles for single-Λ hypernuclei up to $^{89}_{\Lambda}$Y and double-Λ hypernuclei up to $^{12}_{\Lambda\Lambda}$Be. Error bars represent the combined statistical and systematic uncertainties. NLEFT results are compared with experimental data from the Hypernuclear Database (green) [50], and with recent *ab initio* predictions from the variational Monte Carlo method based on neural network quantum states (VMC-NQS, orange) [47] and the no-core shell model (NCSM, purple) [289].

Table 6.3
Λ separation energies in the two different scenarios of fitting the YNN forces. The experimental values are taken from [50], where the four-body systems were averaged. *Value as of August 7, 2025, see discussion in Section 4.2.

Nucleus	Scenario 1 [MeV]	Scenario 2 [MeV]	Experiment [MeV]
$^{3}_{\Lambda}$H	0.12 ± 0.06	0.12 ± 0.06	$0.16 \pm 0.04^{*}$
$^{4}_{\Lambda}$H$^{0^+}$	2.26 ± 0.19	2.27 ± 0.19	2.25 ± 0.04
$^{4}_{\Lambda}$H$^{1^+}$	0.97 ± 0.19	1.02 ± 0.19	1.01 ± 0.05
$^{5}_{\Lambda}$He	3.10 ± 0.13	3.11 ± 0.13	3.10 ± 0.03
$^{7}_{\Lambda}$Li$^{\frac{1}{2}^+}$	5.52 ± 0.97	5.51 ± 0.97	5.62 ± 0.06
$^{7}_{\Lambda}$Li$^{\frac{3}{2}^+}$	5.36 ± 0.97	5.37 ± 0.97	4.93 ± 0.06
$^{9}_{\Lambda}$Be	6.72 ± 0.55	6.73 ± 0.56	6.61 ± 0.07
$^{13}_{\Lambda}$C	11.44 ± 0.84	11.47 ± 0.85	11.96 ± 0.07
$^{16}_{\Lambda}$O	12.72 ± 1.61	13.00 ± 1.61	13.00 ± 0.06

in an explicit dependence on the center-of-mass momentum, thus breaking Galilean invariance. As in the case of the nucleon–nucleon interactions in Ref. [269], in [44] the nucleon–hyperon GIR interaction was included. For a detailed discussion of GIR interactions on the lattice, see Ref. [277]. Having fixed the lattice parameters, the LECs of the YN interaction ($C_{YN}^{S,T}$) are determined from the unpolarized $\Lambda N \to \Lambda N$ cross section while keeping consistency with the scattering parameters of the best continuum interaction [42]. Furthermore, the hypertriton is described as a shallow bound state to be able to properly split the two S-wave channels. Then, the smeared ΛNN forces are fitted to a number of hypernuclei, more precisely, two scenarios are considered. In scenario 1, the 3BFs are constrained only by the light $A = 4$ and $A = 5$ systems, while in scenario 2 hypernuclei up to $A = 16$ are used. Note also that no CSB breaking effects are considered, so in the four-body system the average of $^{4}_{\Lambda}$H and $^{4}_{\Lambda}$He is taken.

The results of this study can be summarized as follows. As shown in Fig. 6.8, considering 2BFs alone reproduces already the observed trends, however, there is clearly room left for 3BFs. The results when including these are also shown in that figure for scenario 1. A rather good description of the g.s. energies of $^{9}_{\Lambda}$Be, $^{13}_{\Lambda}$C and $^{16}_{\Lambda}$O is found. However, the $^{7}_{\Lambda}$Li$^{\frac{1}{2}^+}$-$^{7}_{\Lambda}$Li$^{\frac{3}{2}^+}$ splitting is not well reproduced. Within scenario 2, one finds that the improvement in the final results is minimal, as the data is already well-described within uncertainties, see Table 6.3. For more details on the determination of the 3BFs, the reader is referred to Ref. [44]. However, the inclusion of heavier hypernuclei may be necessary in the future to address mid- to heavy-mass hypernuclei. Furthermore, in Ref. [44], it was shown that decuplet saturation [140], which means $C_3 = C_1$ and $C_2 = 0$, gives a fair description of the hypernuclei considered, but can certainly not be considered a precision tool. Note that similar problems for decuplet saturation were also observed in [49] and fixed by choosing $C_2 \neq 0$ (see Section 5.5).

Clearly, a number of improvements of this type of calculation are necessary, such as the inclusion of the explicit two-pion exchange in the NN interaction, the inclusion of higher order terms in the hyperon–nucleon interaction as well the Λ-Σ conversion, which could be done perturbatively as suggested in Ref. [290].

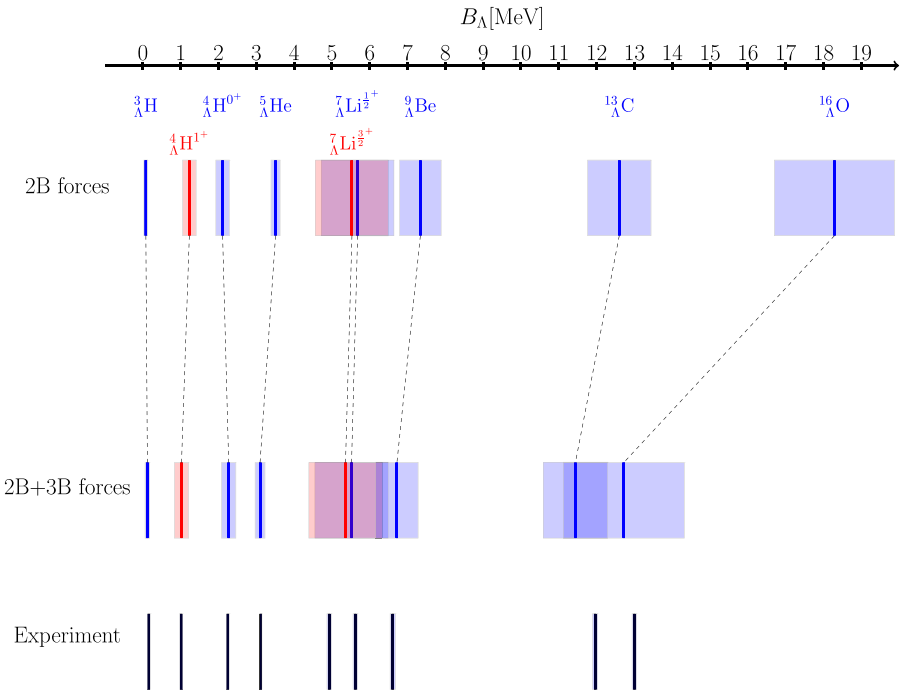

Fig. 6.8. Λ separation energies the YNN forces in scenario 1. The experimental values are taken from [50], where the four-body systems were averaged. Ground states are depicted in blue, excited states in red. The uncertainties are indicated by the shaded areas.

7. Summary and outlook

Over the past 10 years, there has been considerable progress in the treatment and in our understanding of hypernuclear physics. It could be achieved, on the one hand side, by adopting chiral effective field theory, an approach that has been rather successfully employed in studies of nuclear forces, as basis for deriving the interaction of hyperons, too. Thereby, the principal merits of chiral EFT, (i) an organizational scheme ("power counting") that allows to quantify the uncertainty of predictions, and (ii) a consistent treatment of two- and many-body forces, are likewise incorporated into hypernuclear studies. On the other hand, and again following the development in the nuclear sector, rigorous calculations with so-called *ab initio* methods have become feasible for hypernuclei as well. For example, within the no-core shell model (NCSM) computations of hypernuclei up to A=10 and beyond have been reported, based on state-of-the-art YN and YNN potentials.

In this work, we have reviewed the present status of *ab initio* calculations of light hypernuclei with interactions based on chiral effective field theory. To begin with, we have summarized the basics to derive the forces between octet baryons (N, Λ, Σ, Ξ) up to next-to-next-to-leading order in SU(3) chiral EFT. The effective baryon–baryon potentials include contributions from pure four-baryon contact terms, one-meson-exchange diagrams, and two-meson-exchange diagrams involving leading and subleading meson–baryon vertices. The leading three-baryon forces, which formally start to contribute at N2LO, consist of a three-baryon contact interaction, a one-meson exchange and a two-meson exchange component. For illustration explicit expressions of the potentials for the ΛNN interaction in the spin and isospin basis have been discussed and compared to those for the NNN system. It has also been shown how the emerging low-energy constants can be estimated via decuplet saturation, which leads to a promotion of some parts of the three-baryon forces to NLO.

Regarding the BB interaction, selective results for cross sections in the Λp, $\Sigma^- p$, $\Sigma^+ p$, and $\Xi^- p$ channels have been provided. Those testify that an excellent description of the low-energy scattering cross sections could be achieved.

In the second part of this review, we have presented the formalisms of *ab initio* methods for studies of light hypernuclei. This concerns Faddeev- and Faddeev–Yakubovsky equations on one hand side and the no-core shell model on the other side. In addition, explicit results for separation energies of light hypernuclei based on chiral NN, YN and YY potentials have been reported. In some calculations effects from charge-symmetry breaking in the ΛN interaction have been taken into account, while in others chiral three-body forces in the NNN and YNN systems have been included. Another promising approach discussed here is NLEFT, where nuclear properties can be worked out to high precision, so far up to $A = 58$ for conventional nuclei. In this review, we have concentrated on the first hypernuclear calculations in NLEFT, that offer an alternative to the NCSM.

Overall the results for Λ hypernuclei obtained with the *ab initio* approaches considered in the review are very encouraging. Obviously, despite of the incomplete knowledge of the underlying ΛN interaction and the sizeable uncertainties of the available scattering data, the spectrum of light hypernuclei is qualitatively well reproduced, up to A=7 within the NCSM and even up to

A=16 with the NLEFT method. This signals that the bulk properties of the ΛN and ΣN interactions are reasonably well reflected by the scarce two-body data and also that those properties are appropriately represented by the chiral potentials which are the starting point of the few-body calculations. Remarkably, once three-body forces are included in the calculations, in line with and of an order of magnitude that is consistent with the employed power counting, a good quantitative agreement with the empirical separation energies is achieved for essentially all considered hypernuclei. Furthermore, charge symmetry breaking in the ΛN interaction, as evidenced by the measured level splittings of several light mirror hypernuclei, can be well accounted for when, in addition to the long-established pion-exchange contribution associated with Λ-Σ^0 mixing, appropriate contact interactions are included, which arise in a proper and consistent treatment within chiral EFT.

As next step, the more subtle and detailed properties of the YN interaction have to be explored and established. On the experimental side, work in this direction has already started. Here, measurements of the Σ^+p and Σ^-p differential cross sections have been performed and reported. Corresponding measurements for Λp scattering, which are more directly relevant for studies of Λ hypernuclei, are planned for the future [291,292]. Also, as already pointed out, the actual experimental values of some of the energy levels of light Λ hypernuclei are still controversial. In particular, the uncertainty for the lightest system, the hypertriton is still uncomfortably large. Any more accurate determination if its value [293] would provide a very strong constraint on the ΛN interaction, specifically the $^1S_0$ scattering length.

The next and also straightforward step is certainly to take into account CSB in the ΛN channel of the SMS YN potentials. With CSB forces included, a direct comparison of the predicted separation energies with the measured splittings of the ${}^4_\Lambda$H/${}^4_\Lambda$He hypernuclei in the 0^+ and 1^+ states will be possible.

It is also desirable to extend the application of chiral potentials to heavier Λ hypernuclei, i.e. at least up to A=10 or so. Among other things, this would allow to investigate the possible role of ΛN P-waves on the pertinent separation energies.

The so far reported Ξ hypernuclei ${}^{13}_{\Xi}$B and ${}^{15}_{\Xi}$C are much heavier than those which have been predicated/calculated within the NCSM up to now. An extension of the calculations to those systems is desirable but computationally quite challenging. Anyway, as a first step one would need to include the SRG induced YNN 3BFs in the evaluation of the separation energies of those Ξ hypernuclei that have been already studied in the past. Though no essential change in the separation energies is expected, it is still interesting to establish reliably the predictions for the lightest bound Ξ hypernuclei and to pin down the expected energies more quantitatively.

Furthermore, it would be also interesting to explore the existence of possible light Σ hypernuclei based on the chiral YN potentials [294]. Indeed, so far there is only undisputed evidence for a single nucleus, namely a ${}^4_\Sigma$He $I = 1/2$ quasibound state, established in the experiments by Hayano et al. [295] and Nagae et al. [296], see also the review [297], and investigated theoretically by Harada et al. [298]. Recently a possible Σ^0nn state has been reported by the HALL A Collaboration at JLab [299]. Its location is 3.14 ± 0.84 MeV below the Σ^0nn threshold and the suggested quantum numbers are $I = 1$, $J^P = 1/2^+$. A corresponding theoretical study has been presented in Ref. [300].

A first Faddeev calculation of Λd scattering based on the chiral YN potentials NLO13 and NLO19 has been published recently by Kohno and Kamada [151]. There are ongoing experiments for determining Λd scattering observables by the CLAS Collaboration at JLab [301]. However, the expected Λ momentum range of 0.5 to 1.5 GeV/c is significantly higher than what has been considered in Ref. [151]. Regarding the Λd properties at low energies, measurements of correlation functions by the STAR Collaboration [302], and similar efforts by the HADES [303] and ALICE [304] Collaborations, could provide some insight [153,305]. Of course, in this context one has to keep in mind the caveats pointed out in Ref. [67].

Finally, we note that NLEFT allows to investigate much heavier hypernuclei due to the mild scaling in A. However, before performing such calculations, a more precise representation of the two- and three-baryon forces consistent with the high-fidelity two- and three-nucleons forces has to be implemented. Such work is underway.

CRediT authorship contribution statement

Johann Haidenbauer: Writing – review & editing, Writing – original draft, Visualization, Software, Methodology, Investigation, Formal analysis. **Ulf-G. Meißner:** Writing – review & editing, Writing – original draft, Validation, Supervision, Project administration, Investigation, Funding acquisition, Conceptualization. **Andreas Nogga:** Writing – review & editing, Writing – original draft, Visualization, Supervision, Software, Resources, Methodology, Investigation, Data curation, Conceptualization.

Declaration of competing interest

The authors declare that they have no known competing financial interests or personal relationships that could have appeared to influence the work reported in this paper.

Acknowledgments

It is a great pleasure to thank Shahin Bour, Serdar Elhatisari, Dillon Frame, Hans-Werner Hammer, Fabian Hildenbrand, Norbert Kaiser, Hiroyuki Kamada, Michio Kohno, Timo Lähde, Hoai Le, Dean Lee, Susanna Liebig, Kazuya Miyagawa. Stefan Petschauer, Henk Polinder, Zhengxue Ren, Xiang-Xiang Sun, Hui Tong, Isaac Vidaña and Wolfram Weise for sharing their insights into the topics discussed here. This work was supported in part by the European Research Council (ERC) under the European Union's Horizon 2020 research and innovation programme (grant agreement No. 101018170) and by the MKW NRW under the funding code NW21-024-A. The work of UGM was also supported in part by the CAS President's International Fellowship Initiative (PIFI) (Grant No. 2025PD0022).

References

[1] B. Povh, Ann. Rev. Nucl. Part. Sci. 28 (1978) 1–32, http://dx.doi.org/10.1146/annurev.ns.28.120178.000245.
[2] M. Danysz, J. Pniewski, Phil. Mag. 44 (1953) 348, http://dx.doi.org/10.1080/14786440308520318.
[3] R. Levi-Setti, W.E. Slater, V.L. Telegdi, 8th International Annual Conference on High Energy Physics, 1958, p. 328.
[4] R.H. Dalitz, B.W. Downs, Phys. Rev. 111 (1958) 967–986, http://dx.doi.org/10.1103/PhysRev.111.967.
[5] B. Sechi-Zorn, et al., Phys. Rev. Lett. 13 (1964) 282, http://dx.doi.org/10.1103/PhysRevLett.13.282.
[6] G. Alexander, et al., Phys. Rev. Lett. 13 (1964) 484, http://dx.doi.org/10.1103/PhysRevLett.13.484.
[7] R. Engelmann, H. Filthuth, V. Hepp, E. Kluge, Phys. Lett. 21 (5) (1966) 587–589, http://dx.doi.org/10.1016/0031-9163(66)91310-2.
[8] F. Eisele, H. Filthuth, W. Foehlisch, V. Hepp, G. Zech, Phys. Lett. B 37 (1971) 204–206, http://dx.doi.org/10.1016/0370-2693(71)90053-0.
[9] J.J. de Swart, Rev. Modern Phys. 35 (1963) 916–939, http://dx.doi.org/10.1103/RevModPhys.35.916; Rev. Modern Phys. 37 (1965) 326, (erratum).
[10] J.J. De Swart, M.M. Nagels, T.A. Rijken, P.A. Verhoeven, Springer Tracts Mod. Phys. 60 (1971) 138–203.
[11] M.M. Nagels, T.A. Rijken, J.J. De Swart, Ann. Phys. 79 (1973) 338–385, http://dx.doi.org/10.1016/0003-4916(73)90090-0.
[12] M.M. Nagels, T.A. Rijken, J.J. de Swart, Phys. Rev. D 15 (1977) 2547, http://dx.doi.org/10.1103/PhysRevD.15.2547.
[13] P.M.M. Maessen, T.A. Rijken, J.J. de Swart, Phys. Rev. C 40 (1989) 2226–2245, http://dx.doi.org/10.1103/PhysRevC.40.2226.
[14] T.A. Rijken, V.G.J. Stoks, Y. Yamamoto, Phys. Rev. C 59 (1999) 21–40, http://dx.doi.org/10.1103/PhysRevC.59.21, arXiv:nucl-th/9807082.
[15] M.M. Nagels, T.A. Rijken, Y. Yamamoto, Phys. Rev. C 99 (4) (2019) 044003, http://dx.doi.org/10.1103/PhysRevC.99.044003, arXiv:1501.06636.
[16] B. Holzenkamp, K. Holinde, J. Speth, Nucl. Phys. A 500 (1989) 485–528, http://dx.doi.org/10.1016/0375-9474(89)90223-6.
[17] A. Reuber, K. Holinde, J. Speth, Nucl. Phys. A 570 (1994) 543–579, http://dx.doi.org/10.1016/0375-9474(94)90073-6.
[18] J. Haidenbauer, U.-G. Meißner, Phys. Rev. C 72 (2005) 044005, http://dx.doi.org/10.1103/PhysRevC.72.044005, arXiv:nucl-th/0506019.
[19] W.R. Greenberg, E.L. Lomon, Phys. Rev. D 47 (1993) 2703–2721, http://dx.doi.org/10.1103/PhysRevD.47.2703, arXiv:nucl-th/9212004.
[20] K. Tominaga, T. Ueda, Nucl. Phys. A 693 (2001) 731–754, http://dx.doi.org/10.1016/S0375-9474(01)00882-X.
[21] Y. Fujiwara, Y. Suzuki, C. Nakamoto, Prog. Part. Nucl. Phys. 58 (2007) 439–520, http://dx.doi.org/10.1016/j.ppnp.2006.08.001, arXiv:nucl-th/0607013.
[22] H. Garcilazo, T. Fernandez-Carames, A. Valcarce, Phys. Rev. C 75 (2007) 034002, http://dx.doi.org/10.1103/PhysRevC.75.034002, arXiv:hep-ph/0701275.
[23] G. Alexander, U. Karshon, A. Shapira, G. Yekutieli, R. Engelmann, H. Filthuth, W. Lughofer, Phys. Rev. 173 (1968) 1452–1460, http://dx.doi.org/10.1103/PhysRev.173.1452.
[24] B. Sechi-Zorn, B. Kehoe, J. Twitty, R.A. Burnstein, Phys. Rev. 175 (1968) 1735–1740, http://dx.doi.org/10.1103/PhysRev.175.1735.
[25] J.A. Kadyk, G. Alexander, J.H. Chan, P. Gaposchkin, G.H. Trilling, Nuclear Phys. B 27 (1971) 13–22, http://dx.doi.org/10.1016/0550-3213(71)90076-9.
[26] J.M. Hauptman, J.A. Kadyk, G.H. Trilling, Nuclear Phys. B 125 (1977) 29–51, http://dx.doi.org/10.1016/{0550}-3213(77)90222-X.
[27] J. Rowley, et al., Phys. Rev. Lett. 127 (27) (2021) 272303, http://dx.doi.org/10.1103/PhysRevLett.127.272303, arXiv:2108.03134.
[28] M. Ablikim, et al., Phys. Rev. Lett. 132 (23) (2024) 231902, http://dx.doi.org/10.1103/PhysRevLett.132.231902, arXiv:2401.09012.
[29] K. Miyagawa, W. Glöckle, Phys. Rev. C 48 (1993) 2576–2584, http://dx.doi.org/10.1103/PhysRevC.48.2576.
[30] K. Miyagawa, H. Kamada, W. Glöckle, V.G.J. Stoks, Phys. Rev. C 51 (1995) 2905–2913, http://dx.doi.org/10.1103/PhysRevC.51.2905.
[31] A. Nogga, H. Kamada, W. Glöckle, Phys. Rev. Lett. 88 (2002) 172501, http://dx.doi.org/10.1103/PhysRevLett.88.172501, arXiv:nucl-th/0112060.
[32] E. Hiyama, M. Kamimura, T. Motoba, T. Yamada, Y. Yamamoto, Phys. Rev. C 65 (2002) 011301, http://dx.doi.org/10.1103/PhysRevC.65.011301, arXiv:nucl-th/0106070.
[33] H. Nemura, Y. Akaishi, Y. Suzuki, Phys. Rev. Lett. 89 (2002) 142504, http://dx.doi.org/10.1103/PhysRevLett.89.142504, arXiv:nucl-th/0203013.
[34] E. Hiyama, M. Kamimura, T. Motoba, T. Yamada, Y. Yamamoto, Phys. Rev. Lett. 85 (2000) 270–273, http://dx.doi.org/10.1103/PhysRevLett.85.270.
[35] E. Hiyama, Y. Yamamoto, Progr. Theoret. Phys. 128 (2012) 105–124, http://dx.doi.org/10.1143/PTP.128.105, arXiv:1205.6551.
[36] R. Wirth, D. Gazda, P. Navrátil, A. Calci, J. Langhammer, R. Roth, Phys. Rev. Lett. 113 (19) (2014) 192502, http://dx.doi.org/10.1103/PhysRevLett.113.192502, arXiv:1403.3067.
[37] R. Wirth, D. Gazda, P. Navrátil, R. Roth, Phys. Rev. C 97 (6) (2018) 064315, http://dx.doi.org/10.1103/PhysRevC.97.064315, arXiv:1712.05694.
[38] H. Le, J. Haidenbauer, U.-G. Meißner, A. Nogga, Eur. Phys. J. A 56 (12) (2020) 301, http://dx.doi.org/10.1140/epja/s10050-020-00314-6, arXiv:2008.11565.
[39] H. Polinder, J. Haidenbauer, U.-G. Meißner, Nucl. Phys. A 779 (2006) 244–266, http://dx.doi.org/10.1016/j.nuclphysa.2006.09.006, arXiv:nucl-th/0605050.
[40] J. Haidenbauer, S. Petschauer, N. Kaiser, U.-G. Meißner, A. Nogga, W. Weise, Nucl. Phys. A 915 (2013) 24–58, http://dx.doi.org/10.1016/j.nuclphysa.2013.06.008, arXiv:1304.5339.
[41] J. Haidenbauer, U.-G. Meißner, A. Nogga, Eur. Phys. J. A 56 (3) (2020) 91, http://dx.doi.org/10.1140/epja/s10050-020-00100-4, arXiv:1906.11681.
[42] J. Haidenbauer, U.-G. Meißner, A. Nogga, H. Le, Eur. Phys. J. A 59 (3) (2023) 63, http://dx.doi.org/10.1140/epja/s10050-023-00960-6, arXiv:2301.00722.
[43] S. Petschauer, N. Kaiser, J. Haidenbauer, U.-G. Meißner, W. Weise, Phys. Rev. C 93 (1) (2016) 014001, http://dx.doi.org/10.1103/PhysRevC.93.014001, arXiv:1511.02095.
[44] F. Hildenbrand, S. Elhatisari, Z. Ren, U.-G. Meißner, Eur. Phys. J. A 60 (10) (2024) 215, http://dx.doi.org/10.1140/epja/s10050-024-01427-y, arXiv:2406.17638.
[45] D. Lonardoni, S. Gandolfi, F. Pederiva, Phys. Rev. C 87 (2013) 041303, http://dx.doi.org/10.1103/PhysRevC.87.041303, arXiv:1301.7472.
[46] D. Lonardoni, F. Pederiva, S. Gandolfi, Phys. Rev. C 89 (1) (2014) 014314, http://dx.doi.org/10.1103/PhysRevC.89.014314, arXiv:1312.3844.
[47] A. Di Donna, L. Contessi, A. Lovato, F. Pederiva, Phys. Rev. Res. 8 (1) (2026) 013160, http://dx.doi.org/10.1103/wmxg-cnrg, arXiv:2507.16994.
[48] H. Le, J. Haidenbauer, U.-G. Meißner, A. Nogga, Eur. Phys. J. A 60 (1) (2024) 3, http://dx.doi.org/10.1140/epja/s10050-023-01219-w, arXiv:2308.01756.
[49] H. Le, J. Haidenbauer, U.-G. Meißner, A. Nogga, Phys. Rev. Lett. 134 (7) (2025) 072502, http://dx.doi.org/10.1103/PhysRevLett.134.072502, arXiv:2409.18577.
[50] P. Eckert, P. Achenbach, et al., Chart of hypernuclides — Hypernuclear structure and decay data, 2023, https://hypernuclei.kph.uni-mainz.de.
[51] E. Botta, T. Bressani, A. Feliciello, Nucl. Phys. A 960 (2017) 165–179, http://dx.doi.org/10.1016/j.nuclphysa.2017.02.005, arXiv:1608.07448.
[52] D. Gazda, A. Gal, Phys. Rev. Lett. 116 (12) (2016) 122501, http://dx.doi.org/10.1103/PhysRevLett.116.122501, arXiv:1512.01049.
[53] D. Gazda, A. Gal, Nucl. Phys. A 954 (2016) 161–175, http://dx.doi.org/10.1016/j.nuclphysa.2016.05.015, arXiv:1604.03434.
[54] J. Haidenbauer, U.-G. Meißner, A. Nogga, Few Body Syst. 62 (4) (2021) 105, http://dx.doi.org/10.1007/s00601-021-01684-3, arXiv:2107.01134.
[55] H. Le, J. Haidenbauer, U.-G. Meißner, A. Nogga, Phys. Rev. C 107 (2) (2023) 024002, http://dx.doi.org/10.1103/PhysRevC.107.024002, arXiv:2210.03387.
[56] E. Hiyama, K. Sasaki, T. Miyamoto, T. Doi, T. Hatsuda, Y. Yamamoto, T.A. Rijken, Phys. Rev. Lett. 124 (9) (2020) 092501, http://dx.doi.org/10.1103/PhysRevLett.124.092501, arXiv:1910.02864.
[57] L. Contessi, M. Schäfer, N. Barnea, A. Gal, J. Mareš, Phys. Lett. B 797 (2019) 134893, http://dx.doi.org/10.1016/j.physletb.2019.134893, arXiv:1905.06775.
[58] H. Le, J. Haidenbauer, U.-G. Meißner, A. Nogga, Eur. Phys. J. A 57 (7) (2021) 217, http://dx.doi.org/10.1140/epja/s10050-021-00522-8, arXiv:2103.08395.
[59] H. Le, J. Haidenbauer, U.-G. Meißner, A. Nogga, Eur. Phys. J. A 57 (12) (2021) 339, http://dx.doi.org/10.1140/epja/s10050-021-00653-y, arXiv:2109.06648.
[60] S. Acharya, et al., Phys. Lett. B 833 (2022) 137272, http://dx.doi.org/10.1016/j.physletb.2022.137272, arXiv:2104.04427.

[61] Alice Collaboration, Nature 588 (2020) 232–238, http://dx.doi.org/10.1038/s41586-020-3001-6, arXiv:2005.11495; Nature 590 (2021) E13, (erratum).
[62] S. Acharya, et al., Phys. Rev. Lett. 124 (9) (2020) 092301, http://dx.doi.org/10.1103/PhysRevLett.124.092301, arXiv:1905.13470.
[63] S. Acharya, et al., Phys. Lett. B 797 (2019) 134822, http://dx.doi.org/10.1016/j.physletb.2019.134822, arXiv:1905.07209.
[64] S. Acharya, et al., Phys. Lett. B 805 (2020) 135419, http://dx.doi.org/10.1016/j.physletb.2020.135419, arXiv:1910.14407.
[65] S. Acharya, et al., Phys. Lett. B 856 (2024) 138915, http://dx.doi.org/10.1016/j.physletb.2024.138915, arXiv:2312.12830.
[66] S. Acharya, et al., Phys. Rev. X 14 (3) (2024) 031051, http://dx.doi.org/10.1103/PhysRevX.14.031051, arXiv:2308.16120.
[67] E. Epelbaum, S. Heihoff, U.-G. Meißner, A. Tscherwon, Can the strong interactions between hadrons be determined using femtoscopy? 2025, arXiv:2504.08631.
[68] M. Albaladejo, A. Canoa, J. Nieves, J.R. Peláez, E. Ruiz-Arriola, J.R. de Elvira, Phys. Lett. B 866 (2025) 139552, http://dx.doi.org/10.1016/j.physletb.2025.139552, arXiv:2503.19746.
[69] B.F. Gibson, E.V. Hungerford, Phys. Rep. 257 (1995) 349–388, http://dx.doi.org/10.1016/0370-1573(94)00114-I.
[70] D.H. Davis, Nucl. Phys. A 754 (2005) 3–13, http://dx.doi.org/10.1016/j.nuclphysa.2005.01.002.
[71] O. Hashimoto, H. Tamura, Prog. Part. Nucl. Phys. 57 (2006) 564–653, http://dx.doi.org/10.1016/j.ppnp.2005.07.001.
[72] A. Gal, E.V. Hungerford, D.J. Millener, Rev. Modern Phys. 88 (3) (2016) 035004, http://dx.doi.org/10.1103/RevModPhys.88.035004, arXiv:1605.00557.
[73] E. Hiyama, B.F. Gibson, What is hypernuclear physics and why studying hypernuclear physics is important, 2022, pp. 1–18, http://dx.doi.org/10.1007/978-981-15-8818-1_29-1.
[74] E. Epelbaum, H.-W. Hammer, U.-G. Meißner, Rev. Modern Phys. 81 (2009) 1773–1825, http://dx.doi.org/10.1103/RevModPhys.81.1773, arXiv:0811.1338.
[75] R. Machleidt, D.R. Entem, Phys. Rep. 503 (2011) 1–75, http://dx.doi.org/10.1016/j.physrep.2011.02.001, arXiv:1105.2919.
[76] C.L. Korpa, A.E.L. Dieperink, R.G.E. Timmermans, Phys. Rev. C 65 (2002) 015208, http://dx.doi.org/10.1103/PhysRevC.65.015208, arXiv:nucl-th/0109072.
[77] D.B. Kaplan, M.J. Savage, M.B. Wise, Nuclear Phys. B 534 (1998) 329–355, http://dx.doi.org/10.1016/S0550-3213(98)00440-4, arXiv:nucl-th/9802075.
[78] K.-W. Li, X.-L. Ren, L.-S. Geng, B. Long, Phys. Rev. D 94 (1) (2016) 014029, http://dx.doi.org/10.1103/PhysRevD.94.014029, arXiv:1603.07802.
[79] X.L. Ren, E. Epelbaum, J. Gegelia, Phys. Rev. C 101 (3) (2020) 034001, http://dx.doi.org/10.1103/PhysRevC.101.034001, arXiv:1911.05616.
[80] J. Song, Z.-W. Liu, K.-W. Li, L.-S. Geng, Phys. Rev. C 105 (3) (2022) 035203, http://dx.doi.org/10.1103/PhysRevC.105.035203, arXiv:2107.04742.
[81] H.W. Hammer, Nucl. Phys. A 705 (2002) 173–189, http://dx.doi.org/10.1016/S0375-9474(02)00621-8, arXiv:nucl-th/0110031.
[82] F. Hildenbrand, H.W. Hammer, Phys. Rev. C 100 (3) (2019) 034002, http://dx.doi.org/10.1103/PhysRevC.100.034002, arXiv:1904.05818; Phys. Rev. C 102 (2020) 039901, (erratum).
[83] L. Contessi, N. Barnea, A. Gal, Phys. Rev. Lett. 121 (10) (2018) 102502, http://dx.doi.org/10.1103/PhysRevLett.121.102502, arXiv:1805.04302.
[84] S.R. Beane, W. Detmold, K. Orginos, M.J. Savage, Prog. Part. Nucl. Phys. 66 (2011) 1–40, http://dx.doi.org/10.1016/j.ppnp.2010.08.002, arXiv:1004.2935.
[85] S. Aoki, T. Doi, T. Hatsuda, Y. Ikeda, T. Inoue, N. Ishii, K. Murano, H. Nemura, K. Sasaki, PTEP 2012 (2012) 01A105, http://dx.doi.org/10.1093/ptep/pts010, arXiv:1206.5088.
[86] H. Nemura, PoS LATTICE2021 (2022) 272, http://dx.doi.org/10.22323/1.396.0272, arXiv:2203.07661.
[87] H. Nemura, et al., EPJ Web Conf. 175 (2018) 05030, http://dx.doi.org/10.1051/epjconf/201817505030, arXiv:1711.07003.
[88] K. Sasaki, et al., Nucl. Phys. A 998 (2020) 121737, http://dx.doi.org/10.1016/j.nuclphysa.2020.121737, arXiv:1912.08630.
[89] J. Haidenbauer, U.-G. Meißner, A. Nogga, H. Polinder, Lect. Notes Phys. 724 (2007) 113–140, http://dx.doi.org/10.1007/978-3-540-72039-3_4, arXiv:nucl-th/0702015.
[90] C.B. Dover, H. Feshbach, Ann. Phys. 217 (1992) 51–65, http://dx.doi.org/10.1016/0003-4916(92)90338-M.
[91] E. Epelbaum, W. Glöckle, U.-G. Meißner, Nucl. Phys. A 637 (1998) 107–134, http://dx.doi.org/10.1016/S0375-9474(98)00220-6, arXiv:nucl-th/9801064.
[92] E. Epelbaum, W. Glöckle, U.-G. Meißner, Nucl. Phys. A 747 (2005) 362–424, http://dx.doi.org/10.1016/j.nuclphysa.2004.09.107, arXiv:nucl-th/0405048.
[93] S. Petschauer, N. Kaiser, Nucl. Phys. A 916 (2013) 1–29, http://dx.doi.org/10.1016/j.nuclphysa.2013.07.010, arXiv:1305.3427.
[94] R.H. Dalitz, F. von Hippel, Phys. Lett. 10 (1964) 153–157, http://dx.doi.org/10.1016/0031-9163(64)90617-1.
[95] P. Reinert, H. Krebs, E. Epelbaum, Eur. Phys. J. A 54 (5) (2018) 86, http://dx.doi.org/10.1140/epja/i2018-12516-4, arXiv:1711.08821.
[96] J. Beringer, et al., Phys. Rev. D 86 (2012) 010001, http://dx.doi.org/10.1103/PhysRevD.86.010001.
[97] N. Fettes, U.-G. Meißner, S. Steininger, Nucl. Phys. A 640 (1998) 199–234, http://dx.doi.org/10.1016/S0375-9474(98)00452-7, arXiv:hep-ph/9803266.
[98] V. Hepp, H. Schleich, Z. Phys. 214 (1968) 71, http://dx.doi.org/10.1007/BF01380085.
[99] D. Stephen, Study of $\Sigma^- p$ Inelastic Interaction with Σ^- momentum from 0 to 650 MeV/c (Ph. D. thesis), University of Massachusetts, 1970.
[100] K. Miwa, et al., Phys. Rev. Lett. 128 (7) (2022) 072501, http://dx.doi.org/10.1103/PhysRevLett.128.072501, arXiv:2111.14277.
[101] K. Miwa, et al., Phys. Rev. C 104 (4) (2021) 045204, http://dx.doi.org/10.1103/PhysRevC.104.045204, arXiv:2104.13608.
[102] T. Nanamura, et al., PTEP 2022 (9) (2022) 093D01, http://dx.doi.org/10.1093/ptep/ptac101, arXiv:2203.08393.
[103] J. Haidenbauer, U.-G. Meißner, S. Petschauer, Eur. Phys. J. A 51 (2) (2015) 17, http://dx.doi.org/10.1140/epja/i2015-15017-0, arXiv:1412.2991.
[104] J. Haidenbauer, U.-G. Meißner, S. Petschauer, Nucl. Phys. A 954 (2016) 273–293, http://dx.doi.org/10.1016/j.nuclphysa.2016.01.006, arXiv:1511.05859.
[105] H. Machner, J. Haidenbauer, F. Hinterberger, A. Magiera, J.A. Niskanen, J. Ritman, R. Siudak, Nucl. Phys. A 901 (2013) 65–88, http://dx.doi.org/10.1016/j.nuclphysa.2013.01.031, arXiv:1301.6089.
[106] M. Röder, et al., Eur. Phys. J. A 49 (2013) 157, http://dx.doi.org/10.1140/epja/i2013-13157-{{9}}, arXiv:1305.0451.
[107] F. Hauenstein, et al., Phys. Rev. C 95 (3) (2017) 034001, http://dx.doi.org/10.1103/PhysRevC.95.034001, arXiv:1607.04783.
[108] J. Haidenbauer, U.-G. Meißner, Eur. Phys. J. A 55 (2) (2019) 23, http://dx.doi.org/10.1140/epja/i2019-12689-2, arXiv:1810.04883.
[109] M. Ablikim, et al., Phys. Rev. Lett. 130 (25) (2023) 251902, http://dx.doi.org/10.1103/PhysRevLett.130.251902, arXiv:2304.13921.
[110] M. Ablikim, et al., Study of the reaction $\Xi^0 n \to \Lambda\Lambda X$ using Ξ^0-nucleus scattering, 2025, arXiv:2512.04701.
[111] W.S. Jung, et al., PTEP 2025 (9) (2025) 091D01, http://dx.doi.org/10.1093/ptep/ptaf064, arXiv:2503.17614.
[112] J.K. Ahn, et al., Phys. Lett. B 633 (2006) 214–218, http://dx.doi.org/10.1016/j.physletb.2005.12.057, arXiv:nucl-ex/0502010.
[113] S. Aoki, et al., Nucl. Phys. A 644 (1998) 365–385, http://dx.doi.org/10.1016/S0375-9474(98)00596-X.
[114] S. Acharya, et al., Phys. Rev. Lett. 123 (11) (2019) 112002, http://dx.doi.org/10.1103/PhysRevLett.123.112002, arXiv:1904.12198.
[115] J. Haidenbauer, U.-G. Meißner, EPJ Web Conf. 271 (2022) 05001, http://dx.doi.org/10.1051/epjconf/202227105001, arXiv:2208.13542.
[116] M. Döring, J. Haidenbauer, M. Mai, T. Sato, Prog. Part. Nucl. Phys. 146 (2026) 104213, http://dx.doi.org/10.1016/j.ppnp.2025.104213, arXiv:2505.02745.
[117] G. 't Hooft, Nuclear Phys. B 72 (1974) 461, http://dx.doi.org/10.1016/0550-3213(74)90154-0.
[118] E. Witten, Nuclear Phys. B 160 (1979) 57–115, http://dx.doi.org/10.1016/0550-3213(79)90232-3.
[119] T.H.R. Skyrme, Proc. Roy. Soc. Lond. A 260 (1961) 127–138, http://dx.doi.org/10.1098/rspa.1961.0018.
[120] T.H.R. Skyrme, Nucl. Phys. 31 (1962) 556–569, http://dx.doi.org/10.1016/0029-5582(62)90775-7.
[121] E. Witten, Nuclear Phys. B 223 (1983) 433–444, http://dx.doi.org/10.1016/0550-3213(83)90064-0.
[122] J.-L. Gervais, B. Sakita, Phys. Rev. D 30 (1984) 1795, http://dx.doi.org/10.1103/PhysRevD.30.1795.
[123] J.-L. Gervais, B. Sakita, Phys. Rev. Lett. 52 (1984) 87, http://dx.doi.org/10.1103/PhysRevLett.52.87.
[124] R.F. Dashen, A.V. Manohar, Phys. Lett. B 315 (1993) 425–430, http://dx.doi.org/10.1016/0370-2693(93)91635-Z, arXiv:hep-ph/9307241.
[125] R.F. Dashen, E.E. Jenkins, A.V. Manohar, Phys. Rev. D 51 (1995) 3697–3727, http://dx.doi.org/10.1103/PhysRevD.51.3697, arXiv:hep-ph/9411234.
[126] D.B. Kaplan, M.J. Savage, Phys. Lett. B 365 (1996) 244–251, http://dx.doi.org/10.1016/0370-2693(95)01277-X, arXiv:hep-ph/9509371.
[127] D.B. Kaplan, A.V. Manohar, Phys. Rev. C 56 (1997) 76–83, http://dx.doi.org/10.1103/PhysRevC.56.76, arXiv:nucl-th/9612021.

[128] X. Liu, V. Limkaisang, D. Samart, Y. Yan, Phys. Lett. B 789 (2019) 530–537, http://dx.doi.org/10.1016/j.physletb.2018.12.044, arXiv:1710.10068.
[129] T. Vonk, U.-G. Meißner, Eur. Phys. J. A 61 (6) (2025) 135, http://dx.doi.org/10.1140/epja/s10050-025-01602-9, arXiv:2412.13677.
[130] D. Lee, et al., Phys. Rev. Lett. 127 (6) (2021) 062501, http://dx.doi.org/10.1103/PhysRevLett.127.062501, arXiv:2010.09420.
[131] R.F. Dashen, E.E. Jenkins, A.V. Manohar, Phys. Rev. D 49 (1994) 4713, http://dx.doi.org/10.1103/PhysRevD.51.2489, arXiv:hep-ph/9310379; Phys. Rev. D 51 (1995) 2489, (erratum).
[132] S. Petschauer, J. Haidenbauer, N. Kaiser, U.-G. Meißner, W. Weise, Nucl. Phys. A 957 (2017) 347–378, http://dx.doi.org/10.1016/j.nuclphysa.2016.09.010, arXiv:1607.04307.
[133] E. Epelbaum, A. Nogga, W. Glöckle, H. Kamada, U.G. Meißner, H. Witala, Phys. Rev. C 66 (2002) 064001, http://dx.doi.org/10.1103/PhysRevC.66.064001, arXiv:nucl-th/0208023.
[134] C.B. Dover, H. Feshbach, Ann. Phys. 198 (1990) 321–357, http://dx.doi.org/10.1016/0003-4916(90)90254-L.
[135] A. Krause, Helv. Phys. Acta 63 (1990) 3–70, http://dx.doi.org/10.5169/seals-116214.
[136] J.A. Oller, M. Verbeni, J. Prades, J. High Energy Phys. 09 (2006) 079, http://dx.doi.org/10.1088/1126-6708/2006/09/079, arXiv:hep-ph/0608204.
[137] M. Frink, U.-G. Meißner, J. High Energy Phys. 07 (2004) 028, http://dx.doi.org/10.1088/1126-6708/2004/07/028, arXiv:hep-lat/0404018.
[138] M. Mai, P.C. Bruns, B. Kubis, U.-G. Meißner, Phys. Rev. D 80 (2009) 094006, http://dx.doi.org/10.1103/PhysRevD.80.094006, arXiv:0905.2810.
[139] S.K. Petschauer, Baryonic Forces and Hyperons in Nuclear Matter from SU(3) Chiral Effective Field Theory (Ph. D. thesis), Munich, Tech. U., 2016.
[140] S. Petschauer, J. Haidenbauer, N. Kaiser, U.-G. Meißner, W. Weise, Front. Phys. 8 (2020) 12, http://dx.doi.org/10.3389/fphy.2020.00012, arXiv:2002.00424.
[141] V. Bernard, N. Kaiser, U.-G. Meißner, Nucl. Phys. A 615 (1997) 483–500, http://dx.doi.org/10.1016/S0375-9474(97)00021-3, arXiv:hep-ph/9611253.
[142] T.R. Hemmert, B.R. Holstein, J. Kambor, J. Phys. G 24 (1998) 1831–1859, http://dx.doi.org/10.1088/0954-3899/24/10/003, arXiv:hep-ph/9712496.
[143] N. Kaiser, S. Gerstendorfer, W. Weise, Nucl. Phys. A 637 (1998) 395–420, http://dx.doi.org/10.1016/S0375-9474(98)00234-6, arXiv:nucl-th/9802071.
[144] H. Krebs, E. Epelbaum, U.-G. Meißner, Eur. Phys. J. A 32 (2007) 127–137, http://dx.doi.org/10.1140/epja/i2007-10372-y, arXiv:nucl-th/0703087.
[145] E. Epelbaum, H. Krebs, U.-G. Meißner, Nucl. Phys. A 806 (2008) 65–78, http://dx.doi.org/10.1016/j.nuclphysa.2008.02.305, arXiv:0712.1969.
[146] U.-G. Meißner, AIP Conf. Proc. 1011 (1) (2008) 49–58, http://dx.doi.org/10.1063/1.2932307.
[147] K. Sasaki, E. Oset, M.J. Vicente Vacas, Phys. Rev. C 74 (2006) 064002, http://dx.doi.org/10.1103/PhysRevC.74.064002, arXiv:nucl-th/0607068.
[148] T.E.O. Ericson, W. Weise, Pions and Nuclei, Clarendon Press, Oxford, UK, 1988.
[149] R.C. Herndon, Y.C. Tang, Phys. Rev. 153 (1967) 1091–1099, http://dx.doi.org/10.1103/PhysRev.153.1091.
[150] R.H. Dalitz, R.C. Herndon, Y.C. Tang, Nuclear Phys. B 47 (1972) 109–137, http://dx.doi.org/10.1016/0550-3213(72)90105-8.
[151] M. Kohno, H. Kamada, Phys. Rev. C 110 (4) (2024) 044005, http://dx.doi.org/10.1103/PhysRevC.110.044005, arXiv:2406.13899.
[152] J.H. Hetherington, L.H. Schick, Phys. Rev. 139 (1965) B1164–B1169, http://dx.doi.org/10.1103/PhysRev.139.B1164.
[153] J. Haidenbauer, Phys. Rev. C 102 (3) (2020) 034001, http://dx.doi.org/10.1103/PhysRevC.102.034001, arXiv:2005.05012.
[154] A. Nogga, Few Body Syst. 43 (2008) 137–142, http://dx.doi.org/10.1007/s00601-008-0222-x.
[155] A. Nogga, H. Kamada, W. Glöckle, B.R. Barrett, Phys. Rev. C 65 (2002) 054003, http://dx.doi.org/10.1103/PhysRevC.65.054003, arXiv:nucl-th/0112026.
[156] A. Nogga, A. Kievsky, H. Kamada, W. Glöckle, L.E. Marcucci, S. Rosati, M. Viviani, Phys. Rev. C 67 (2003) 034004, http://dx.doi.org/10.1103/PhysRevC.67.034004, arXiv:nucl-th/0202037.
[157] V.G.J. Stoks, R.A.M. Klomp, C.P.F. Terheggen, J.J. de Swart, Phys. Rev. C 49 (1994) 2950–2962, http://dx.doi.org/10.1103/PhysRevC.49.2950, arXiv:nucl-th/9406039.
[158] M. Juric, et al., Nuclear Phys. B 52 (1973) 1–30, http://dx.doi.org/10.1016/0550-3213(73)90084-9.
[159] R. Kino, et al., Precise measurement of the Λ-binding energy difference between ${}^{3}_{\Lambda}$H and ${}^{4}_{\Lambda}$H via decay-pion spectroscopy at MAMI, 2026, arXiv:2601.08694.
[160] T. Akaishi, et al., Phys. Lett. B 873 (2026) 140163, http://dx.doi.org/10.1016/j.physletb.2026.140163, arXiv:2509.16967.
[161] D.L. Mihaylov, J. Haidenbauer, V. Mantovani Sarti, Phys. Lett. B 850 (2024) 138550, http://dx.doi.org/10.1016/j.physletb.2024.138550, arXiv:2312.16970.
[162] Y. Fujiwara, Y. Suzuki, M. Kohno, K. Miyagawa, Phys. Rev. C 77 (2008) 027001, http://dx.doi.org/10.1103/PhysRevC.77.027001, arXiv:0710.0047.
[163] J. Adam, et al., Nat. Phys. 16 (4) (2020) 409–412, http://dx.doi.org/10.1038/s41567-020-0799-7, arXiv:1904.10520.
[164] S. Acharya, et al., Phys. Rev. Lett. 131 (10) (2023) 102302, http://dx.doi.org/10.1103/PhysRevLett.131.102302, arXiv:2209.07360.
[165] T.Y. Htun, D. Gazda, C. Forssén, Y. Yan, Few Body Syst. 62 (4) (2021) 94, http://dx.doi.org/10.1007/s00601-021-01675-4, arXiv:2109.09479.
[166] D. Gazda, T.Y. Htun, C. Forssén, Phys. Rev. C 106 (5) (2022) 054001, http://dx.doi.org/10.1103/PhysRevC.106.054001, arXiv:2208.02176.
[167] S. Ghosh, B.K. Pradhan, D. Chatterjee, J. Schaffner-Bielich, Front. Astron. Space Sci. 9 (2022) 864294, http://dx.doi.org/10.3389/fspas.2022.864294, arXiv:2203.03156.
[168] D. Chatterjee, I. Vidaña, Eur. Phys. J. A 52 (2) (2016) 29, http://dx.doi.org/10.1140/epja/i2016-16029-x, arXiv:1510.06306.
[169] S. Weissenborn, D. Chatterjee, J. Schaffner-Bielich, Nucl. Phys. A 881 (2012) 62–77, http://dx.doi.org/10.1016/j.nuclphysa.2012.02.012, arXiv:1111.6049.
[170] S. Weissenborn, D. Chatterjee, J. Schaffner-Bielich, Phys. Rev. C 85 (6) (2012) 065802, http://dx.doi.org/10.1103/PhysRevC.85.065802, arXiv:1112.0234; Phys. Rev. C 90 (2014) 019904, (erratum).
[171] H. Djapo, B.-J. Schaefer, J. Wambach, Phys. Rev. C 81 (2010) 035803, http://dx.doi.org/10.1103/PhysRevC.81.035803, arXiv:0811.2939.
[172] M. Raymund, Il Nuovo Cimento 32 (3) (1964) 555–587, http://dx.doi.org/10.1007/BF02735882.
[173] A.R. Bodmer, Q.N. Usmani, Phys. Rev. C 31 (1985) 1400–1411, http://dx.doi.org/10.1103/PhysRevC.31.1400.
[174] A. Nogga, Nucl. Phys. A 914 (2013) 140–150, http://dx.doi.org/10.1016/j.nuclphysa.2013.02.053.
[175] M. Bedjidian, et al., Phys. Lett. B 83 (1979) 252–256, http://dx.doi.org/10.1016/0370-2693(79)90697-X.
[176] T.O. Yamamoto, et al., Phys. Rev. Lett. 115 (22) (2015) 222501, http://dx.doi.org/10.1103/PhysRevLett.115.222501, arXiv:1508.00376.
[177] F. Schulz, et al., Nucl. Phys. A 954 (2016) 149–160, http://dx.doi.org/10.1016/j.nuclphysa.2016.03.015.
[178] M. Abdallah, et al., Phys. Lett. B 834 (2022) 137449, http://dx.doi.org/10.1016/j.physletb.2022.137449, arXiv:2207.00778.
[179] M. Schäfer, N. Barnea, A. Gal, Phys. Rev. C 106 (3) (2022) L031001, http://dx.doi.org/10.1103/PhysRevC.106.L031001, arXiv:2202.07460.
[180] E. Epelbaum, PoS CD2018 (2019) 006, http://dx.doi.org/10.22323/1.317.0006.
[181] J.A. Melendez, S. Wesolowski, R.J. Furnstahl, Phys. Rev. C 96 (2) (2017) 024003, http://dx.doi.org/10.1103/PhysRevC.96.024003, arXiv:1704.03308.
[182] J.A. Melendez, R.J. Furnstahl, D.R. Phillips, M.T. Pratola, S. Wesolowski, Phys. Rev. C 100 (4) (2019) 044001, http://dx.doi.org/10.1103/PhysRevC.100.044001, arXiv:1904.10581.
[183] B.D. Carlsson, A. Ekström, C. Forssén, D.F. Strömberg, G.R. Jansen, O. Lilja, M. Lindby, B.A. Mattsson, K.A. Wendt, Phys. Rev. X 6 (1) (2016) 011019, http://dx.doi.org/10.1103/PhysRevX.6.011019, arXiv:1506.02466.
[184] B.R. Barrett, P. Navratil, J.P. Vary, Prog. Part. Nucl. Phys. 69 (2013) 131–181, http://dx.doi.org/10.1016/j.ppnp.2012.10.003.
[185] R. Roth, P. Navratil, Phys. Rev. Lett. 99 (2007) 092501, http://dx.doi.org/10.1103/PhysRevLett.99.092501, arXiv:0705.4069.
[186] P. Navratil, G.P. Kamuntavicius, B.R. Barrett, Phys. Rev. C 61 (2000) 044001, http://dx.doi.org/10.1103/PhysRevC.61.044001, arXiv:nucl-th/9907054.
[187] S. Liebig, U.-G. Meißner, A. Nogga, Eur. Phys. J. A 52 (4) (2016) 103, http://dx.doi.org/10.1140/epja/i2016-16103-5, arXiv:1510.06070.
[188] S. Baroni, P. Navratil, S. Quaglioni, Phys. Rev. Lett. 110 (2) (2013) 022505, http://dx.doi.org/10.1103/PhysRevLett.110.022505, arXiv:1210.1897.
[189] A.M. Shirokov, A.I. Mazur, I.A. Mazur, J.P. Vary, Phys. Rev. C 94 (6) (2016) 064320, http://dx.doi.org/10.1103/PhysRevC.94.064320, arXiv:1608.05885; Phys. Rev. C 98 (2018) 039901, (erratum).
[190] A.T. Kruppa, N. Michel, X.-l. Shang, W. Zuo, Phys. Rev. C 113 (1) (2026) 014316, http://dx.doi.org/10.1103/7q75-9bbx, arXiv:2501.11294.

[191] R. Wirth, R. Roth, Phys. Rev. Lett. 117 (2016) 182501, http://dx.doi.org/10.1103/PhysRevLett.117.182501, arXiv:1605.08677.
[192] R. Wirth, R. Roth, Phys. Lett. B 779 (2018) 336–341, http://dx.doi.org/10.1016/j.physletb.2018.02.021, arXiv:1710.04880.
[193] R. Wirth, R. Roth, Phys. Rev. C 100 (4) (2019) 044313, http://dx.doi.org/10.1103/PhysRevC.100.044313, arXiv:1902.03324.
[194] A. Pérez-Obiol, D. Gazda, E. Friedman, A. Gal, Phys. Lett. B 811 (2020) 135916, http://dx.doi.org/10.1016/j.physletb.2020.135916, arXiv:2006.16718.
[195] S.K. Bogner, R.J. Furnstahl, R.J. Perry, Phys. Rev. C 75 (2007) 061001, http://dx.doi.org/10.1103/PhysRevC.75.061001, arXiv:nucl-th/0611045.
[196] H. Le, J. Haidenbauer, U.-G. Meißner, A. Nogga, Phys. Lett. B 801 (2020) 135189, http://dx.doi.org/10.1016/j.physletb.2019.135189, arXiv:1909.02882.
[197] M. Moshinsky, Nucl. Phys. 13 (1) (1959) 104–116, http://dx.doi.org/10.1016/0029-5582(59)90143-9.
[198] L. Trlifaj, Phys. Rev. C 5 (1972) 1534–1539, http://dx.doi.org/10.1103/PhysRevC.5.1534.
[199] G.P. Kamuntavicius, R.K. Kalinauskas, B.R. Barrett, S. Mickevicius, D. Germanas, Nucl. Phys. A 695 (2001) 191–201, http://dx.doi.org/10.1016/S0375-9474(01)01101-0, arXiv:nucl-th/0105009.
[200] A. Nogga, et al., jncsmcoeff: library to access to CPF and transition coefficients, 2024, https://jugit.fz-juelich.de/a.nogga/jncsmcoeff.
[201] X.-X. Sun, H. Le, U.-G. Meißner, A. Nogga, Phys. Rev. C 112 (2) (2025) 024317, http://dx.doi.org/10.1103/j4ky-tn1j, arXiv:2502.03989.
[202] P. Navratil, B.R. Barrett, Phys. Rev. C 57 (1998) 3119–3128, http://dx.doi.org/10.1103/PhysRevC.57.3119, arXiv:nucl-th/9804014.
[203] K. Suzuki, S.Y. Lee, Progr. Theoret. Phys. 64 (1980) 2091–2106, http://dx.doi.org/10.1143/PTP.64.2091.
[204] S. Okubo, Progr. Theoret. Phys. 12 (1954) 603, http://dx.doi.org/10.1143/PTP.12.603.
[205] E. Epelbaum, W. Glöckle, A. Krüger, U.-G. Meißner, Nucl. Phys. A 645 (1999) 413–438, http://dx.doi.org/10.1016/S0375-9474(98)00585-5, arXiv:nucl-th/9809084.
[206] S.K. Bogner, T.T.S. Kuo, A. Schwenk, Phys. Rep. 386 (2003) 1–27, http://dx.doi.org/10.1016/j.physrep.2003.07.001, arXiv:nucl-th/0305035.
[207] P. Maris, H. Le, A. Nogga, R. Roth, J.P. Vary, Front. Phys. 11 (2023) 1098262, http://dx.doi.org/10.3389/fphy.2023.1098262, arXiv:2305.19648.
[208] F. Wegner, Ann. Phys. 506 (2) (1994) 77–91, http://dx.doi.org/10.1002/andp.19945060203.
[209] R. Wirth, Ab-Initio Approach to Hypernuclei (Ph. D. thesis), Darmstadt, Tech. Hochsch., 2018.
[210] K. Hebeler, Phys. Rev. C 85 (2012) 021002, http://dx.doi.org/10.1103/PhysRevC.85.021002, arXiv:1201.0169.
[211] T. Wolfgruber, M. Knöll, R. Roth, Phys. Rev. C 110 (1) (2024) 014327, http://dx.doi.org/10.1103/PhysRevC.110.014327, arXiv:2310.05256.
[212] K.A. Wendt, C. Forssén, T. Papenbrock, D. Sääf, Phys. Rev. C 91 (6) (2015) 061301, http://dx.doi.org/10.1103/PhysRevC.91.061301, arXiv:1503.07144.
[213] A. Gal, Phys. Lett. B 744 (2015) 352–357, http://dx.doi.org/10.1016/j.physletb.2015.04.009, arXiv:1503.01687.
[214] E. Hiyama, Y. Yamamoto, T. Motoba, M. Kamimura, Phys. Rev. C 80 (2009) 054321, http://dx.doi.org/10.1103/PhysRevC.80.054321, arXiv:0911.4013.
[215] A. Gal, JPS Conf. Proc. 17 (2017) 011006, http://dx.doi.org/10.7566/JPSCP.17.011006, arXiv:1609.00229.
[216] E. Botta, AIP Conf. Proc. 2130 (1) (2019) 030003, http://dx.doi.org/10.1063/1.5118393.
[217] H. Tamura, et al., Phys. Rev. Lett. 84 (2000) 5963, http://dx.doi.org/10.1103/PhysRevLett.84.5963.
[218] T. Gogami, et al., Phys. Rev. C 94 (2) (2016) 021302, http://dx.doi.org/10.1103/PhysRevC.94.021302, arXiv:1606.09157.
[219] S.N. Nakamura, et al., Phys. Rev. Lett. 110 (1) (2013) 012502, http://dx.doi.org/10.1103/PhysRevLett.110.012502, arXiv:1207.0571.
[220] T.-T. Sun, Y. Tanimura, H. Sagawa, E. Hiyama, Phys. Lett. B 865 (2025) 139460, http://dx.doi.org/10.1016/j.physletb.2025.139460, arXiv:2502.21161.
[221] H. Kamada, M. Kohno, K. Miyagawa, Phys. Rev. C 108 (2) (2023) 024004, http://dx.doi.org/10.1103/PhysRevC.108.024004, arXiv:2304.06352; Phys. Rev. C 110 (2024) 019907, (erratum).
[222] M. Kohno, H. Kamada, K. Miyagawa, Phys. Rev. C 109 (2) (2024) 024003, http://dx.doi.org/10.1103/PhysRevC.109.024003, arXiv:2311.10923; Phys. Rev. C 110 (2024) 019908, (erratum).
[223] H. Le, J. Haidenbauer, H. Kamada, M. Kohno, U.-G. Meißner, K. Miyagawa, A. Nogga, Eur. Phys. J. A 61 (2) (2025) 21, http://dx.doi.org/10.1140/epja/s10050-024-01474-5, arXiv:2407.02064.
[224] H. Takahashi, et al., Phys. Rev. Lett. 87 (2001) 212502, http://dx.doi.org/10.1103/PhysRevLett.87.212502.
[225] K. Nakazawa, Nucl. Phys. A 835 (2010) 207–214, http://dx.doi.org/10.1016/j.nuclphysa.2010.01.195.
[226] K. Nakazawa, H. Takahashi, Progr. Theoret. Phys. Suppl. 185 (2010) 335–343, http://dx.doi.org/10.1143/PTPS.185.335.
[227] H. Nemura, Y. Suzuki, Y. Fujiwara, C. Nakamoto, Progr. Theoret. Phys. 103 (2000) 929–958, http://dx.doi.org/10.1143/PTP.103.929, arXiv:nucl-th/9912065.
[228] H. Nemura, S. Shinmura, Y. Akaishi, K.S. Myint, Phys. Rev. Lett. 94 (2005) 202502, http://dx.doi.org/10.1103/PhysRevLett.94.202502, arXiv:nucl-th/0407033.
[229] I.N. Filikhin, A. Gal, Phys. Rev. Lett. 89 (2002) 172502, http://dx.doi.org/10.1103/PhysRevLett.89.172502, arXiv:nucl-th/0209003.
[230] E. Hiyama, M. Kamimura, T. Motoba, T. Yamada, Y. Yamamoto, Progr. Theoret. Phys. 97 (1997) 881–899, http://dx.doi.org/10.1143/PTP.97.881.
[231] E. Hiyama, K. Nakazawa, Ann. Rev. Nucl. Part. Sci. 68 (2018) 131–159, http://dx.doi.org/10.1146/annurev-nucl-101917-021108.
[232] I.N. Filikhin, A. Gal, V.M. Suslov, Phys. Rev. C 68 (2003) 024002, http://dx.doi.org/10.1103/PhysRevC.68.024002, arXiv:nucl-th/0303028.
[233] I.N. Filikhin, A. Gal, Nucl. Phys. A 707 (2002) 491–509, http://dx.doi.org/10.1016/S0375-9474(02)01008-4, arXiv:nucl-th/0203036.
[234] H. Polinder, J. Haidenbauer, U.-G. Meißner, Phys. Lett. B 653 (2007) 29–37, http://dx.doi.org/10.1016/j.physletb.2007.07.045, arXiv:0705.3753.
[235] J. Schaffner-Bielich, Compact Star Physics, Cambridge University Press, 2020, http://dx.doi.org/10.1017/9781316848357.
[236] I. Vidaña, V. Mantovani Sarti, J. Haidenbauer, D.L. Mihaylov, L. Fabbietti, Eur. Phys. J. A 61 (3) (2025) 59, http://dx.doi.org/10.1140/epja/s10050-025-01539-z, arXiv:2412.12729.
[237] M. Oertel, C. Providência, F. Gulminelli, A.R. Raduta, J. Phys. G 42 (7) (2015) 075202, http://dx.doi.org/10.1088/0954-3899/42/7/075202, arXiv:1412.4545.
[238] D.D. Ofengeim, M.E. Gusakov, P. Haensel, M. Fortin, Phys. Rev. D 100 (10) (2019) 103017, http://dx.doi.org/10.1103/PhysRevD.100.103017, arXiv:1911.08407.
[239] T. Fukuda, et al., Phys. Rev. C 58 (1998) 1306–1309, http://dx.doi.org/10.1103/PhysRevC.58.1306.
[240] P. Khaustov, et al., Phys. Rev. C 61 (2000) 054603, http://dx.doi.org/10.1103/PhysRevC.61.054603, arXiv:nucl-ex/9912007.
[241] S. Aoki, et al., Nucl. Phys. A 828 (2009) 191–232, http://dx.doi.org/10.1016/j.nuclphysa.2009.07.005.
[242] Y. Ichikawa, et al., PTEP 2024 (9) (2024) 091D01, http://dx.doi.org/10.1093/ptep/ptae133.
[243] K. Nakazawa, et al., PTEP 2015 (3) (2015) 033D02, http://dx.doi.org/10.1093/ptep/ptv008.
[244] S.H. Hayakawa, et al., Phys. Rev. Lett. 126 (6) (2021) 062501, http://dx.doi.org/10.1103/PhysRevLett.126.062501, arXiv:2010.14317.
[245] M. Yoshimoto, et al., PTEP 2021 (7) (2021) 073D02, http://dx.doi.org/10.1093/ptep/ptab073, arXiv:2103.08793.
[246] K. Nakazawa, Experimental aspect of $S = -2$ hypernuclei, 2023, pp. 1–60, http://dx.doi.org/10.1007/978-981-15-8818-1_33-1.
[247] E. Friedman, A. Gal, Phys. Lett. B 837 (2023) 137640, http://dx.doi.org/10.1016/j.physletb.2022.137640, arXiv:2209.01606.
[248] Y. Jin, X.-R. Zhou, Y.-Y. Cheng, H.J. Schulze, Eur. Phys. J. A 56 (5) (2020) 135, http://dx.doi.org/10.1140/epja/s10050-020-00143-7, arXiv:1910.05884.
[249] Y. Tanimura, H. Sagawa, T. Sun, E. Hiyama, Phys. Rev. C 105 (4) (2022) 044324, http://dx.doi.org/10.1103/PhysRevC.105.044324, arXiv:2202.04276.
[250] S.Y. Ding, B.Y. Sun, T.-T. Sun, Phys. Rev. C 111 (1) (2025) 014301, http://dx.doi.org/10.1103/PhysRevC.111.014301, arXiv:2406.10980.
[251] E. Hiyama, Y. Yamamoto, T. Motoba, T.A. Rijken, M. Kamimura, Phys. Rev. C 78 (2008) 054316, http://dx.doi.org/10.1103/PhysRevC.78.054316, arXiv:0811.3156.
[252] M.M. Nagels, T.A. Rijken, Y. Yamamoto, Phys. Rev. C 102 (5) (2020) 054003, http://dx.doi.org/10.1103/PhysRevC.102.054003, arXiv:1504.02634.
[253] K. Miyagawa, M. Kohno, Few Body Syst. 62 (3) (2021) 65, http://dx.doi.org/10.1007/s00601-021-01650-z, arXiv:2105.11258.
[254] H.-J. Schulze, J. Guo, X.-R. Zhou, EPJ Web Conf. 271 (2022) 03003, http://dx.doi.org/10.1051/epjconf/202227103003.

[255] C.B. Dover, A. Gal, Ann. Phys. 146 (1983) 309–348, http://dx.doi.org/10.1016/0003-4916(83)90036-2.
[256] H. Fujioka, et al., Decay pion spectroscopy of ${}^{5}_{\Lambda\Lambda}$H produced by Ξ-hypernuclear decay, 2019, J-PARC proposal P75. https://j-parc.jp/researcher/Hadron/en/pac_1901/pdf/P75_2019-09.pdf.
[257] D. Lee, Prog. Part. Nucl. Phys. 63 (2009) 117–154, http://dx.doi.org/10.1016/j.ppnp.2008.12.001, arXiv:0804.3501.
[258] T.A. Lähde, U.-G. Meißner, Nuclear Lattice Effective Field Theory: An Introduction, vol. 957, Springer, 2019, http://dx.doi.org/10.1007/978-3-030-14189-9.
[259] D. Lee, Ann. Rev. Nucl. Part. Sci. 75 (1) (2025) 109–128, http://dx.doi.org/10.1146/annurev-nucl-101918-023343, arXiv:2501.03303.
[260] J.M. Alarcón, D. Du, N. Klein, D. Lee T.A. Lähde, N. Li, B.-N. Lu, T. Luu, U.-G. Meißner, Eur. Phys. J. A 53 (5) (2017) 83, http://dx.doi.org/10.1140/epja/i2017-12273-x, arXiv:1702.05319.
[261] N. Klein, S. Elhatisari, T.A. Lähde, D. Lee, U.-G. Meißner, Eur. Phys. J. A 54 (7) (2018) 121, http://dx.doi.org/10.1140/epja/i2018-12553-y, arXiv:1803.04231.
[262] E. Epelbaum, H. Krebs, D. Lee, U.-G. Meißner, Eur. Phys. J. A 45 (2010) 335–352, http://dx.doi.org/10.1140/epja/i2010-11009-x, arXiv:1003.5697.
[263] E. Wigner, Phys. Rev. 51 (1937) 106–119, http://dx.doi.org/10.1103/PhysRev.51.106.
[264] T. Mehen, I.W. Stewart, M.B. Wise, Phys. Rev. Lett. 83 (1999) 931–934, http://dx.doi.org/10.1103/PhysRevLett.83.931, arXiv:hep-ph/9902370.
[265] J.-W. Chen, D. Lee, T. Schäfer, Phys. Rev. Lett. 93 (2004) 242302, http://dx.doi.org/10.1103/PhysRevLett.93.242302, arXiv:nucl-th/0408043.
[266] B.-N. Lu, N. Li, S. Elhatisari, D. Lee, E. Epelbaum, U.-G. Meißner, Phys. Lett. B 797 (2019) 134863, http://dx.doi.org/10.1016/j.physletb.2019.134863, arXiv:1812.10928.
[267] S. Shen, T.A. Lähde, D. Lee, U.-G. Meißner, Eur. Phys. J. A 57 (9) (2021) 276, http://dx.doi.org/10.1140/epja/s10050-021-00586-6, arXiv:2106.04834.
[268] S. Shen, S. Elhatisari, T.A. Lähde, D. Lee, B.-N. Lu, U.-G. Meißner, Nat. Commun. 14 (1) (2023) 2777, http://dx.doi.org/10.1038/s41467-023-38391-y, arXiv:2202.13596.
[269] S. Elhatisari, et al., Nature 630 (8015) (2024) 59–63, http://dx.doi.org/10.1038/s41586-024-07422-z, arXiv:2210.17488.
[270] N. Li, S. Elhatisari, E. Epelbaum, D. Lee, B.-N. Lu, U.-G. Meißner, Phys. Rev. C 98 (4) (2018) 044002, http://dx.doi.org/10.1103/PhysRevC.98.044002, arXiv:1806.07994.
[271] J.L. Friar, D. Huber, U. van Kolck, Phys. Rev. C 59 (1999) 53–58, http://dx.doi.org/10.1103/PhysRevC.59.53, arXiv:nucl-th/9809065.
[272] E. Epelbaum, H. Krebs, D. Lee, U.-G. Meißner, Eur. Phys. J. A 41 (2009) 125–139, http://dx.doi.org/10.1140/epja/i2009-10764-y, arXiv:0903.1666.
[273] M. Hoferichter, J. Ruiz de Elvira, B. Kubis, U.-G. Meißner, Phys. Rev. Lett. 115 (19) (2015) 192301, http://dx.doi.org/10.1103/PhysRevLett.115.192301, arXiv:1507.07552.
[274] P.F. Bedaque, H.W. Hammer, U. van Kolck, Phys. Rev. Lett. 82 (1999) 463–467, http://dx.doi.org/10.1103/PhysRevLett.82.463, arXiv:nucl-th/9809025.
[275] S. König, H.W. Grießhammer, H.W. Hammer, U. van Kolck, Phys. Rev. Lett. 118 (20) (2017) 202501, http://dx.doi.org/10.1103/PhysRevLett.118.202501, arXiv:1607.04623.
[276] H. Tong, S. Elhatisari, U.-G. Meißner, Sci. Bull. 70 (2025) 825–828, http://dx.doi.org/10.1016/j.scib.2025.01.008, arXiv:2405.01887.
[277] N. Li, S. Elhatisari, E. Epelbaum, D. Lee, B. Lu, U.-G. Meißner, Phys. Rev. C 99 (6) (2019) 064001, http://dx.doi.org/10.1103/PhysRevC.99.064001, arXiv:1902.01295.
[278] S. Elhatisari, D. Lee, Phys. Rev. C 90 (6) (2014) 064001, http://dx.doi.org/10.1103/PhysRevC.90.064001, arXiv:1407.2784.
[279] S. Bour, D. Lee, H.W. Hammer, U.-G. Meißner, Phys. Rev. Lett. 115 (18) (2015) 185301, http://dx.doi.org/10.1103/PhysRevLett.115.185301, arXiv:1412.8175.
[280] D. Frame, T.A. Lähde, D. Lee, U.-G. Meißner, Eur. Phys. J. A 56 (10) (2020) 248, http://dx.doi.org/10.1140/epja/s10050-020-00257-y, arXiv:2007.06335.
[281] F. Hildenbrand, S. Elhatisari, T.A. Lähde, D. Lee, U.-G. Meißner, Eur. Phys. J. A 58 (9) (2022) 167, http://dx.doi.org/10.1140/epja/s10050-022-00821-8, arXiv:2206.09459.
[282] F. Gursey, L.A. Radicati, Phys. Rev. Lett. 13 (1964) 173–175, http://dx.doi.org/10.1103/PhysRevLett.13.173.
[283] A. Sedrakian, J. Mur-Petit, A. Polls, H. Muther, Phys. Rev. A 72 (2005) 013613, http://dx.doi.org/10.1103/PhysRevA.72.013613, arXiv:cond-mat/0504511.
[284] B.-N. Lu, N. Li, S. Elhatisari, D. Lee, J.E. Drut, T.A. Lähde, E. Epelbaum, U.-G. Meißner, Phys. Rev. Lett. 125 (19) (2020) 192502, http://dx.doi.org/10.1103/PhysRevLett.125.192502, arXiv:1912.05105.
[285] H. Tong, S. Elhatisari, U.-G. Meißner, Astrophys. J. 982 (2) (2025) 164, http://dx.doi.org/10.3847/1538-4357/adba47, arXiv:2502.14435.
[286] A. Akmal, V.R. Pandharipande, D.G. Ravenhall, Phys. Rev. C 58 (1998) 1804–1828, http://dx.doi.org/10.1103/PhysRevC.58.1804, arXiv:nucl-th/9804027.
[287] S. Gandolfi, J. Carlson, S. Reddy, A.W. Steiner, R.B. Wiringa, Eur. Phys. J. A 50 (2014) 10, http://dx.doi.org/10.1140/epja/i2014-14010-5, arXiv:1307.5815.
[288] H. Tong, S. Elhatisari, U.-G. Meißner, Z. Ren, Multi-strangeness matter from ab initio calculations, 2025, arXiv:2509.26148.
[289] M. Knöll, R. Roth, Phys. Lett. B 846 (2023) 138258, http://dx.doi.org/10.1016/j.physletb.2023.138258, arXiv:2307.11577.
[290] S.R. Beane, P.F. Bedaque, A. Parreno, M.J. Savage, Nucl. Phys. A 747 (2005) 55–74, http://dx.doi.org/10.1016/j.nuclphysa.2004.09.081, arXiv:nucl-th/0311027.
[291] K. Miwa, et al., EPJ Web Conf. 271 (2022) 04001, http://dx.doi.org/10.1051/epjconf/202227104001.
[292] K. Miwa, K. Nakazawa, H. Tamura, E. Hiyama, T. Takahashi, Eur. Phys. J. A 61 (6) (2025) 128, http://dx.doi.org/10.1140/epja/s10050-025-01571-z.
[293] J.-H. Chen, L.-S. Geng, E. Hiyama, Z.-W. Liu, J. Pochodzalla, Chin. Phys. Lett. 42 (10) (2025) 100101, http://dx.doi.org/10.1088/0256-307X/42/10/100101, arXiv:2506.00864.
[294] R. Lazauskas, A. Deltuva, D. Gazda, M. Schäfer, Phys. Lett. B 874 (2026) 140214, http://dx.doi.org/10.1016/j.physletb.2026.140214.
[295] R.S. Hayano, et al., Phys. Lett. B 231 (1989) 355–358, http://dx.doi.org/10.1016/0370-2693(89)90675-8.
[296] T. Nagae, et al., Phys. Rev. Lett. 80 (1998) 1605–1609, http://dx.doi.org/10.1103/PhysRevLett.80.1605.
[297] T. Nagae, Σ hypernuclei, 2022, pp. 27–41, http://dx.doi.org/10.1007/978-981-15-8818-1_32-1.
[298] T. Harada, Phys. Rev. Lett. 81 (1998) 5287–5290, http://dx.doi.org/10.1103/PhysRevLett.81.5287.
[299] B. Pandey, et al., Phys. Rev. C 105 (5) (2022) L051001, http://dx.doi.org/10.1103/PhysRevC.105.L051001.
[300] H Garcilazo, A Valcarce, Symmetry 14 (11) (2022) 2381, http://dx.doi.org/10.3390/sym14112381, arXiv:2211.13970.
[301] K. Miwa, private communication.
[302] STAR Collaboration, First observation of deuteron-Λ correlations at RHIC, 2025, arXiv:2511.15493.
[303] D. Pawlowska-Szymanska, Femtoscopy measurements of the d-Λ system as a tool for studying the strong interaction parameters, 2024, presentation at the WPCF 2024, https://indico.in2p3.fr/event/32030/contributions/144123/attachments/88390/133641/WPCF_DPS_final.pdf.
[304] R. Del Grande, Understanding hadronic interactions from femtoscopic correlation function measurements, 2025, presentation at Lepton Interactions with Nucleons and Nuclei, https://agenda.infn.it/event/44828/contributions/262366/attachments/137715/207072/DelGrande_Elba2025_v4.pdf.
[305] M. Kohno, H. Kamada, Phys. Rev. C 112 (4) (2025) 044005, http://dx.doi.org/10.1103/gdnr-hrrc, arXiv:2507.03792.